Doctoral Dissertation in Fluid Mechanics

SIAMM, SHU & LOG, USTL – CNRS

ARBITRARY ORDER HILBERT SPECTRAL ANALYSIS DEFINITION AND APPLICATION TO FULLY DEVELOPED TURBULENCE AND ENVIRONMENTAL TIME SERIES

By

Yongxiang HUANG (黄永祥)

TO OBTAIN THE GRADE OF DOCTEUR DE L'UNIVERSITÉ DE LILLE 1 - SCIENCES ET TECHNOLOGIES

AND

DOCTOR OF SHANGHAI UNIVERSITY

JULY 2009

In front of the jury composed of:

Prof. Shiqiang DAI	member
Prof. Patrick FLANDRIN	reviewer
Prof. Song FU	member
Prof. Norden E. HUANG	reviewer
Prof. Yulu LIU	supervisor
Prof. Gilmar MOMPEAN	member
Prof. Yuehong QIAN	member
Prof. François G. SCHMITT	supervisor
Prof. Heng ZHOU	member

To My Mother and Father.

My Best Memory in Wimereux.

Email: yongxianghuang@gmail.com

Table of Contents

List of Tables

List of Figures

摘要

经验模态分解(Empirical Mode Decomposition–EMD,又被称作Hilbert-Huang变换(Hilbert-Huang Transform)–HHT) 是由黄锷等人 (Huang *et al.*, 1998, 1999)于十年前提出的一种新的分析非平稳和非线性数据的时频分析方法。在过去的十余年中，有超过1000篇文献报道在工程应用及科学研究的不同领域中使用该方法。本论文首次使用该方法分析湍流数据以及环境观测数据。在对湍流的数据分析中发现EMD类似于一类二分滤波器(dyadic filter bank)。为了能使之刻画所分析信号中的间歇性，我们将经典的Hilbert谱分析(Hilbert Spectral Analysis–HSA) 方法推广为任意阶Hilbert谱分析。对HSA方法提供的联合概率密度分布函数$p(\omega, \mathcal{A})$ 对幅值$\mathcal{A}$ 进行边际积分，就为我们提供了在幅值-频率空间中对尺度不变特性刻画的新框架，其中ω 是瞬时频率，$\mathcal{A}$ 为幅值。我们首先对构造的分形布朗运动时间序列以及多分形非平稳时间序列进行分析，从而来验证该方法的可行性和有效性。通过和结构函数的结果相对比，我们发现新方法对间歇性参数提供了更加有效的预测。

通过统计平稳假设，我们提出了速度增量时间序列$\Delta u_\ell(t)$ 自相关函数的解析模型，速度增量定义为$\Delta u_\ell(t) = u(t+\ell) - u(t)$。通过这个模型，我们解析证明了当原始变量具有标度行为时，其速度增量的自相关函数将在相应的时间分隔ℓ 位置取得最小值。同时该模型还表明该最小值存在标度行为，并被分形布朗运动以及湍流实验数据所证明。通过定义自相关的累积函数，在傅立叶谱空间里对不同的尺度贡献进行了刻画。我们发现对于自相关函数的主要贡献来自于大尺度部分。同样的分析过程被应用于二阶结构函数。分析结果表明二阶结构函数强烈受到大尺度部分影响，这表明结构函数并不适合用来提取标度指数，特别是当所分析的数据中含有大尺度的含能结构的时候。

我们然后将该方法应用于均匀、近似各向同性的湍流实验数据来刻画湍流的间

歇性，发现速度的联合概率密度分布函数$p(\omega, \mathcal{A})$ 本身具有标度趋势，相应的标度值很接近Kolmogorov值。我们随后在幅值-频率空间里对结果函数所提供的标度指数进行了重复。我们对局部各向同性假设在幅值-频率空间里进行检验，发现拓展的各向同性比值随着统计阶数q 线性减小。

我们还使用该方法分析了射流实验中的一段温度数据，该数据有着较强的峭壁结构(ramp-cliff)。对于该数据，传统的结构函数方法不再适用。但是新方法在统计阶数高达8的时候仍然给出了清晰的标度行为，相应的标度指数$\xi_\theta(q) - 1$ 非常接近充分发展湍流中的流向速度的标度指数。

最后，我们用该方法分析了河流数据以及近海海洋湍流数据，在Hilbert框架下刻画了其中的尺度不变特性。

Abstract

Empirical Mode Decomposition (EMD), or Hilbert-Huang Transform (HHT) is a novel general time-frequency analysis method for nonstationary and nonlinear time series, which was proposed by Huang *et al.* (1998, 1999) more than ten years ago. During the last ten years, there have been more than 1000 papers applying this new method to various applications and research fields. In this thesis we apply this method to turbulence time series for the first time, and to environmental time series. It is found that the EMD acts a dyadic filter bank for fully developed turbulence. To characterize the intermittent properties of a scaling time series, we generalize the classical Hilbert spectral analysis to arbitrary order q, performing what we denoted "arbitrary order Hilbert spectral analysis". This provides a new frame to characterize scale invariance directly in an amplitude-frequency space, by taking a marginal integral of a joint pdf $p(\omega, \mathcal{A})$ of instantaneous frequency ω and amplitude $\mathcal{A}$. We first validate the method by analyzing a simulated fractional Brownian motion time series, and by analyzing a synthesized multifractal nonstationary time series respectively for monofractal and multifractal processes. Compared with the classical structure function approach, it is found numerically that the Hilbert-based methodology provides a more precise estimator for the intermittency parameter.

Assuming statistical stationarity, we propose an analytical model for the autocorrelation function of velocity increments time series $\Delta u_\ell(t)$, where $\Delta u_\ell(t) = u(t+\ell) - u(t)$, and ℓ is the time increment. With this model, we prove analytically that, if a power law behaviour holds for the original variable, the location of the minimum values of the autocorrelation function is equal exactly to the time separation

ℓ when ℓ belongs to scaling range. A power law behaviour for the minimum values is suggested by this model, and verified by a fractional Brownian motion simulation and a turbulent database. By defining a cumulative function for the autocorrelation function, the scale contribution is then characterized in the Fourier frequency space. It is found that the main contribution to the autocorrelation function comes from the large scale part. The same idea is applied to the second order structure function. It is found the second order structure function is strongly influenced by the large scale part, showing that it is not a good approach to extract the scaling exponent from a given scaling time series when the data possess energetic large scales.

We then apply this Hilbert-based methodology to an experimental homogeneous and nearly isotropic turbulent database to characterize multifractal scaling properties of the velocity time series in fully developed turbulence. We obtain a scaling trend in the joint pdf $p(\omega, \mathcal{A})$ with a scaling exponent close to the Kolmogorov value. We recover the structure function scaling exponents $\zeta(q)$ in amplitude-frequency space for the first time. The isotropy hypothesis is then checked scale by scale in amplitude-frequency space. It is found that the generalized isotropy ratio decreases linearly with the order q.

We also perform the analysis on a temperature (passive scalar) time series with strong ramp-cliff structures. For these data, the traditional structure function fails. However, the new method extracts a clear power law up to $q = 8$. The scaling exponents $\xi_\theta(q) - 1$ is quite close to the scaling exponents $\zeta(q)$ of the longitudinal velocity in fully developed turbulence.

We then consider the traditional Extended Self-Similarity (ESS) (Benzi *et al.*, 1993b) and the hierarchy model (She & Lévêque, 1994) under the Hilbert frame. For the case of ESS, we have here two special cases $q = 0$ and $q = 3$ to define the ESS in the Hilbert frame. Both of them work for the fully developed turbulence providing the same scaling exponents. Based on the turbulent database we have, it seems that the lognormal model with a proper chosen intermittency parameter μ provides a better prediction of the scaling exponents.

We finally apply the new method to daily river flow discharge and surf zone marine turbulence to characterize the scale invariance under the Hilbert frame.

Résumé

La Décomposition Modale Empirique (Empirical Mode Decomposition - EMD) ou la Transformation de Hilbert-Huang (HHT) est une nouvelle méthode d'analyse temps-fréquence qui est particulièrement adaptée pour des séries temporelles nonlinéaires et non stationnaires. Cette méthode a été proposée par Huang *et al.* (1998, 1999) il y a plus de dix ans. Pendant les dix dernières années, plus de 1000 articles ont appliqué cette méthode dans le cadre de diverses applications ou domaines de recherche. Dans cette thèse, nous appliquons cette méthode à des séries temporelles de turbulence, pour la première fois, et à des séries temporelles environnementales. Nous avons obtenu comme résultat le fait que la méthode EMD correspond à un banc de filtre dyadique (ou quasi-dyadique) pour la turbulence pleinement développée. Pour caractériser les propriétés intermittentes d'une série temporelle invariante d'échelle, nous avons généralisé l'analyse spectrale de Hilbert-Huang classique à des moments d'ordre arbitraire q, pour effectuer ce que nous avons appelé "analyse spectrale de Hilbert d'ordre arbitraire". Ceci fournit un nouveau cadre pour analyser l'invariance d'échelle directement dans un espace amplitude-fréquence, en estimant une intégrale marginale d'une pdf jointe $p(\omega, \mathcal{A})$ de la fréquence instantanée ω et de l'amplitude $\mathcal{A}$. Nous validons tout d'abord la méthode en analysant des séries temporelles de mouvement Brownien fractionnaire, et en analysant des séries temporelles multifractales synthétiques, en tant que modèle respectivement de processus monofractals et multifractals. Nous comparons les résultats obtenus avec la nouvelle méthode, à l'analyse classique utilisant les fonctions de structure: nous trouvons numériquement que la méthodologie utilisant l'approche de Hilbert fournit un estimateur plus précis pour

le paramètre d'intermittence.

Avec une hypothèse de stationarité, nous proposons un modèle analytique pour la fonction d'autocorrélation des incréments de séries temporelles de vitesse $\Delta u_\ell(t)$, où $\Delta u_\ell(t) = u(t+\ell) - u(t)$, et ℓ est l'incrément temporel. Dans le cadre de ce modèle, nous prouvons analytiquement que, si une loi de puissance est valide pour la série d'origine, la position minimisant la fonction d'autocorrélation de la variable d'origine est égale exactement au temps de séparation ℓ lorsque ℓ appartient à la zone invariante d'échelle. Ce modèle prédit une loi de puissance pour la valeur minimum, comportement vérifié par une simulation de mouvement Brownien fractionnaire et à partir de données expérimentales de turbulence. En introduisant une fonction cumulative pour la fonction d'autocorrélation, la contribution en échelle est alors caractérisée dans l'espace de fréquence de Fourier. Nous observons que la contribution principale à la fonction d'autocorrélation provient des grandes échelles. La même idée est appliquée à la fonction de structure d'ordre 2. Nous obtenons que celle-ci est également fortement influencée par les grandes échelles, ce qui montre que ceci n'est pas une bonne approche pour extraire les exposants invariants d'échelle d'une série temporelle lorsque les données sont caractérisées par des grandes échelles énergétiques.

Nous appliquons ensuite cette méthodologie Hilbert-Huang à une base de données de turbulence homogène et presque isotrope, pour caractériser les propriétés multifractales invariantes d'échelle des série temporelles de vitesse en turbulence pleinement développée. Nous obtenons un comportement invariant d'échelle pour la pdf jointe $p(\omega, \mathcal{A})$ avec un exposant proche de la valeur de Kolmogorov. Nous estimons les exposants $\zeta(q)$ dans un espace amplitude-fréquence, pour la première fois. L'hypothèse d'isotropie est testée échelle par échelle dans l'espace amplitude-fréquence. Nous obtenons que le rapport d'isotropie généralisé décroit linéairement avec le moment q.

Nous effectuons également l'analyse d'une série temporelle de température (scalaire passif) possédant un effet de rampe marqué (ramp-cliff). Pour ces données, l'approche traditionnelle utilisant les fonctions de structure ne fonctionne pas. Mais la nouvelle méthode développée dans cette thèse fournit un net régime invariant d'échelle jusqu'au

moment $q = 8$. Les exposants $\xi_\theta(q) - 1$ sont très proches des exposants $\zeta(q)$ obtenus par l'approche des fonctions de structure pour la vitesse longitudinale.

Nous nous intéressons ensuite à l'auto-similarité étendue (Extended Self Similarity - ESS) (Benzi *et al.*, 1993b) dans le cadre Hilbert-Huang. En ce qui concerne la méthode ESS, qui est devenue classique en turbulence, nous adaptons l'approche pour le cas Hilbert-Huang dans un espace de fréquence, et nous constatons que le modèle lognormal, avec un coefficient adéquat, fournit une très bonne estimation des exposants invariants d'échelle.

Finalement nous appliquons la nouvelle méthodologie à des données environnementales: des débits de rivières, et des données de turbulence marine dans la zone de surf. Dans ce dernier cas, la méthode ESS permet de séparer les ondes de vent de la turbulence à petite échelle.

Acknowledgements

I would like to thank my two supervisors, Prof. François G. Schmitt from CNRS and Prof. Yulu Liu in Shanghai University, for their many suggestions and constant support during my Ph.D research. I also thank to Prof. Zhiming Lu for useful discussion. I thank Prof. Y. Gagne in Joseph Fourier University for providing the experimental temperature data. I appreciate Prof. P. Flandrin in Lyon to share his EMD MATLAB® codes, which are available at web page: http://perso.ens-lyon.fr/patrick. flandrin/emd.html. I appreciate Prof. C. Meneveau in Johns Hopkins University to share the experimental data. The data are available for download at his web page: http://www.me.jhu.edu/~meneveau/datasets.html.

During my whole three years Ph.D research, I was financed in part by a Ph.D grant from the French Ministry of Foreign Affairs, by part from Lille 1 University and Shanghai University.

Finally, I want to thank my supervisor, Prof. François G. Schmitt, again for his very valuable comments on this thesis.

Yongxiang HUANG (黄永祥)
May 8, 2009
Email: yongxianghuang@gmail.com

Laboratory of Oceanology and Geosciences
Wimereux, France

Part I

Methodology Empirical Mode Decomposition and Hilbert Spectral Analysis

Chapter 1

An Informal Introduction to Time-Frequency Analysis

In this chapter, we recall some general ideas of the time-frequency analysis, such as decomposition and representation, characteristic scale, nonlinear and nonstationary effects, etc.

1.1 Decomposition and representation

There are plenty of time-frequency analysis methods (Cohen, 1995; Flandrin, 1998). Their basic idea can be interpreted as representing a given signal/function, $f(x)$, by a given basis

$$f(x) = \int_{-\infty}^{+\infty} \psi(\nu, x')\varphi(x, x', \nu)\,\mathrm{d}\nu\,\mathrm{d}x' \tag{1.1.1}$$

where φ is a given basis (function), and ψ is the coefficient (function) which can be determined by

$$\psi(x, \nu) = \int_{-\infty}^{+\infty} f(x)\varphi(x, x', \nu)\,\mathrm{d}x' \tag{1.1.2}$$

Here the basis function φ also can be interpreted as an integral kernel of the above equation (Cohen, 1995). It is an asymptotic approximation: the signal is asymptotically approximated by the chosen basis (function) φ. The property of the chosen

basis are usually well known. Then we check φ to see how the given signal looks like with the chosen basis (function) φ. For example, when the trigonometric function is chosen, we obtain the classical Fourier transform

$$\psi(f) = \int_{-\infty}^{+\infty} f(x) e^{i2\pi fx} \, \mathrm{d}x \tag{1.1.3}$$

Another example is the Wavelet transform

$$\psi(a, x) = |a|^{-1/2} \int_{R^n} f(x') \varphi(\frac{x' - x}{a}) \, \mathrm{d}x' \tag{1.1.4}$$

where n is the dimension of the space, $\varphi(x)$ is the so-called mother wavelet and a is a dilatation parameter[1]. This is the traditional approach for time-frequency analysis: the basis are chosen before the decomposition. Therefore once we choose a basis (function), the information that can be extracted from the data is determined. They are also energy based approaches: only when the component contains enough energy, it then can be detected by such methods (Huang *et al.*, 1998; Huang, 2005).

Moreover, most *a priori* basis are defined in the global sense and they require that the signal satisfies stationary and linearity assumptions (Cohen, 1995; Flandrin, 1998; Huang *et al.*, 1998). Here the stationarity means that the statistical properties are identical for different samples[2]. Many modifications, such as short-time Fourier transform with various windows, Wigner-Ville distribution, have been designed to overcome these obstacles (Cohen, 1995; Flandrin, 1998). However, they inherit more or less the shortcoming of the Fourier transform (Huang *et al.*, 1998, 1999).

[1] To be a mother wavelet, $\varphi(x)$ should satisfy some conditions. For details on wavelet theory see Daubechies (1992). We may also consider the wavelet transform approach as an adaptive-windows Fourier transform (Huang *et al.*, 1998).

[2] The mathematical definition of stationarity is more rigorous. In practice, if some statistical quantities of a given time series do not change beyond a certain size of sample and are identical for different samples, then the time series is called stationary process.

1.2 Characteristic scale

The power of a time-frequency analysis method is determined by the chosen basis φ. Indeed, for a certain time-frequency analysis method, a characteristic scale (CS) is always defined explicitly or implicitly. Once we choose a definition of the characteristic scale for a certain method, then the ability and property of this method is determined/fixed. We compare here three different definitions of the CS, corresponding to Fourier transform, Wavelet transform and Hilbert-Huang transform (HHT) (see chapter 2 for more details of HHT).

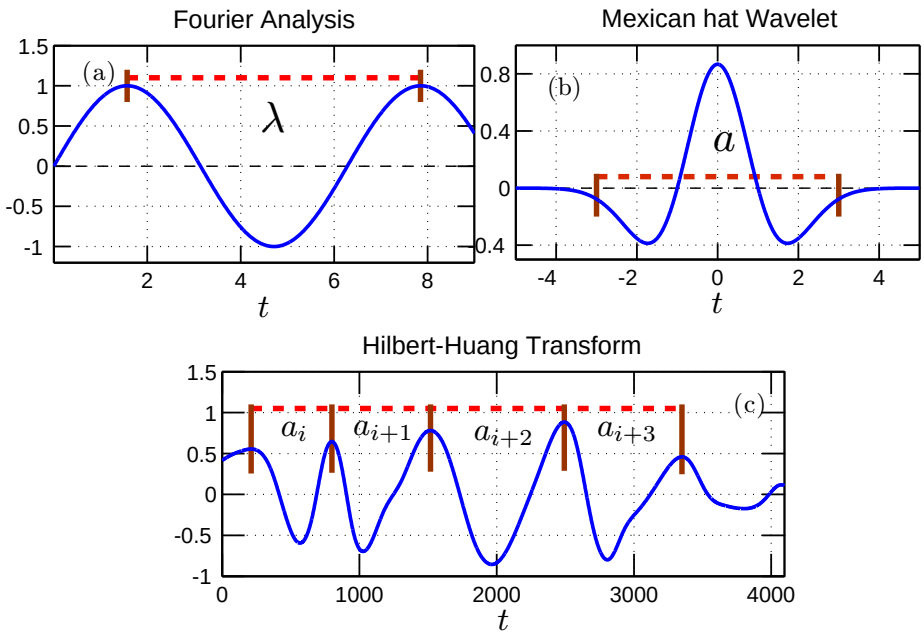

Figure 1.1: Demonstration of the characteristic scale of (a) Fourier analysis, (b) Wavelet transform and (c) Hilbert-Huang transform, respectively.

- Fourier Transform:

  The length of one period of sine or cosine wave.

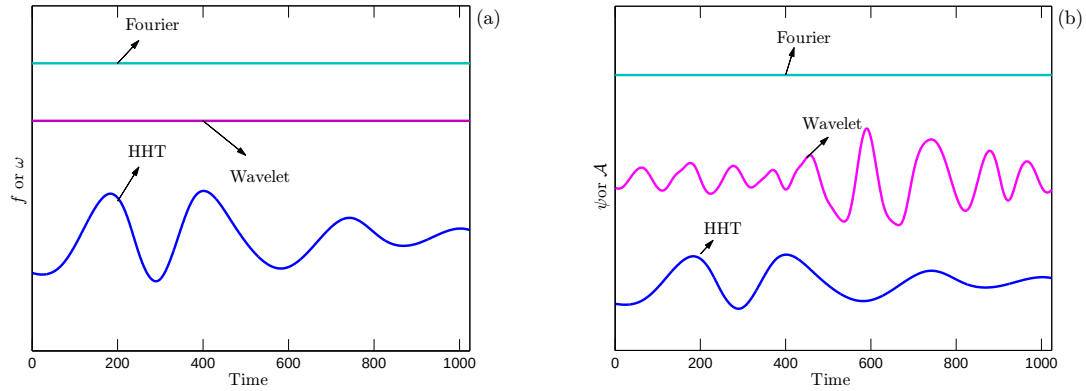

Figure 1.2: The characteristic scale in (a) frequency-time space, and (b) amplitude-time space.

- Wavelet Transform:

  The shape of the mother wavelet together with the dilation factor.

- Hilbert-Huang Transform:

  The distance between successive local extrema maxima (resp. minima) points.

We illustrate the corresponding CS in Fig. 1.1: (a) Fourier analysis, (b) Mexican hat wavelet, and (c) Hilbert-Huang transform (HHT). As we have mentioned above, for an *a priori* approach, once the basis (function) φ is chosen, the shape of CS is then fixed. We illustrate here two examples for *a priori* approach: the Fourier transform and Mexican hat wavelet. However, the shape of the CS of HHT can be varied from time to time. In other words, these three time frequency analysis methods describe the characteristic scale globally, regionally, and locally, respectively (Huang, 2005).

Frequency-Modulation

Figure 1.2 shows the CS in both frequency-time view and amplitude-time view. The difference among them are clear. For further discussion convenience, we introduce

here the concepts of frequency-modulation and amplitude-modulation. Let us consider here a monochromatic wave

$$x(t) = a\cos 2\pi\nu_o t \tag{1.2.1}$$

where the constants a and ν_o are the amplitude and the frequency. It is natural to extend this point of view to evolutionary situations

$$x(t) = a(t)\cos 2\pi\nu_o(t)t \tag{1.2.2}$$

where the amplitude a and the frequency ν_o now may vary in time. Let us first keep the amplitude a as a constant, and let the frequency ν_o vary in time. We call this "frequency modulation".

Definition 1.2.1 (Frequency-Modulation)**.** Frequency ν_o may vary in time.

Both the Fourier analysis and Wavelet transform[3] do not allow the frequency modulation, since the frequency for each component is fixed, see Fig. 1.2 (a). On the contrary, the HHT does allow frequency-modulation, since the idea of the instantaneous frequency (Cohen, 1995; Flandrin, 1998) is employed to describe the frequency. We will see this point in chapter 2, the fact that frequency modulation may be further termed into two different types: interwave-frequency-modulation and intrawave-frequency-modulation. The latter one can be associated to a nonlinear mechanism (Huang *et al.*, 1998, 1999).

Amplitude-Modulation

Now we consider another situation, the so-called amplitude-modulation. Let us keep the frequency ν_o constant, and let the amplitude a vary in time. It is then called

[3]In fact, Wavelet may detect the so-called interwave-frequency-modulation (Huang *et al.*, 1998, 1999). However, this ability comes from the amplitude-modulation: the wavelet coefficient $\varphi(x, a)$ may be zero at some locations and scales.

amplitude-modulation.

Definition 1.2.2 (Amplitude Modulation)**.** Amplitude a may vary in time.

Figure 1.2 (b) shows the amplitude of the above mentioned three approaches in amplitude-time view. Here again, the Fourier representation does not allow the amplitude-modulation, since it describes the scale in a global sense. Due to a compact support property of the wavelet in physical domain, it allows the amplitude-modulation (Daubechies, 1992). HHT allows the amplitude-modulation mechanism. Therefore, it allows the frequency-modulation and amplitude-modulation simultaneously (Huang *et al.*, 1998, 1999; Huang, 2005).

Potential Shortcoming of Fourier-Based Approach

We then reproduce the main properties of the Fourier analysis, Wavelet transform and HHT in Table 1.1 from Huang (2005). These properties determine the power of each method and also the potential shortcoming of each one. We then list the main potential shortcoming of the Fourier-based approach here

- *a priori*

  The basis φ are given before decomposition.

- Stationary

  They require that the data satisfy the stationarity assumption.

- Asymptotical approximation

  They are a linear asymptotical approximation to the original data.

- Global uncertainty

They are limited by the so-called Heisenberg-Gabor uncertainty principle[4].

Due to the above mentioned properties of the Fourier-based time-frequency analysis methods, they require high order harmonic component to mimic a transit signal, in which both the amplitude and the frequency may vary in time.

For more details on the time-frequency analysis and potential shortcomings of the Fourier-based approach, we suggest Cohen (1995) and Flandrin (1998).

Table 1.1: Comparison of the main properties of the Fourier analysis, Wavelet transform and Hilbert-Huang transform.

	Frequency-Modulation		Amplitude-Modulation
	Interwave	Intrawave	
Fourier analysis	No	No	No
Wavelet transform	Yes	No	Yes
Hilbert-Huang transform	Yes	Yes	Yes

1.3 Nonstationary and nonlinear effects

In the real world, most data are nonlinear, nonstationary and noisy. A general method to deal with nonlinear and nonstationary time series is required. The terminology 'nonlinear' here means that the underling mechanism is nonlinear. Below, we illustrate the nonstationary and nonlinear effects on both the Fourier analysis and Hilbert-Huang transform.

[4]The Heisenberg-Gabor uncertainty principle (Cohen, 1995; Flandrin, 1998) means that the time resolution δt and the frequency resolution δf are restricted by the following relation

$$\delta t \, \delta f \geq \frac{1}{4\pi} \tag{1.2.3}$$

Nonstationary Effect

Definition 1.3.1 (Stationarity)**.** A time series $x(t)$ is stationary in the weak sense, if, for all t

$$E(|x(t)|^2) < \infty \tag{1.3.1a}$$

$$E(x(t)) = m \tag{1.3.1b}$$

$$C(x(t_1), x(t_2)) = C(x(t_1) + \tau, x(t_2) + \tau) = C(t_1 - t_2) \tag{1.3.1c}$$

where $E(\cdot)$ is the expected value, and $C(\cdot)$ is the covariance function.

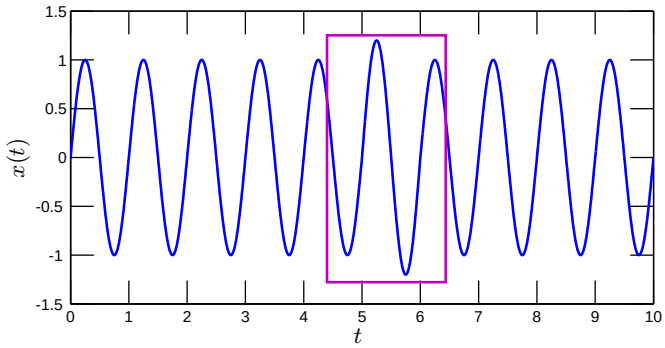

Figure 1.3: Example of a nonstationary event $x(t)$: the amplitude on range $5 \leq t \leq 6$ is 20% higher, which is marked by a rectangle.

In practice, we only have a finite size sample. Obviously, the data we have may not satisfy the above condition, which means it is nonstationary. We give an example of a nonstationary effect here. We produce a sine wave $x(t)$ on the range $0 < t < 10$

$$x(t) = \begin{cases} \sin(2\pi t) & t < 5 \\ 1.2\sin(2\pi t) & 5 \leq t \leq 6 \\ \sin(2\pi t) & 6 < t < 10 \end{cases} \tag{1.3.2}$$

where a nonstationary event with 20% higher amplitude is superposed on range $5 \leq t \leq 6$, see Fig. 1.3, in which the nonstationary event is marked by a rectangle. The sampling frequency is set as 100 Hz. Figure 1.4 shows the intrinsic mode

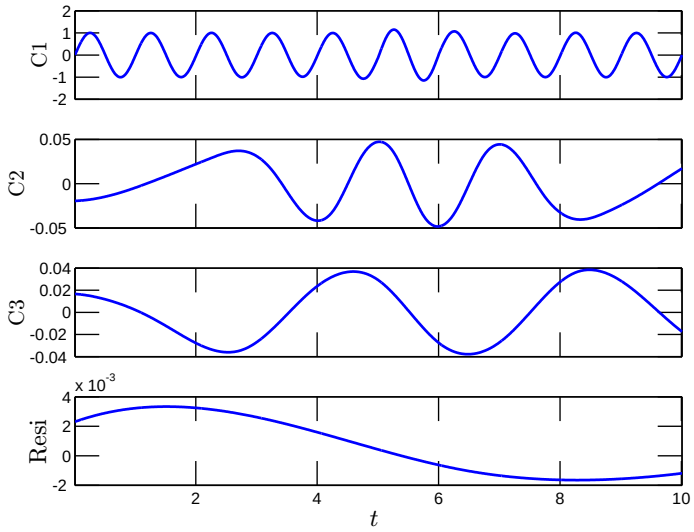

Figure 1.4: Intrinsic mode functions from empirical mode decomposition.

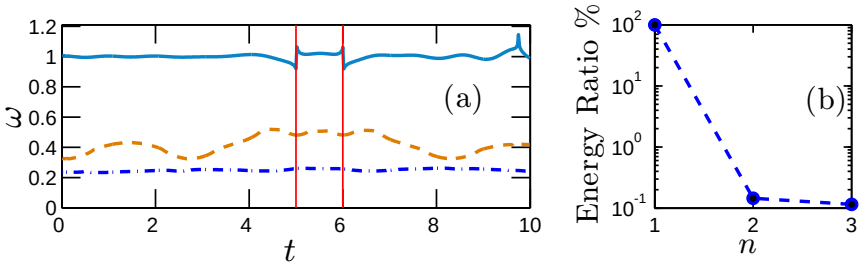

Figure 1.5: Instantaneous frequency of each mode: (a) instantaneous frequency, (b) the relative energy. The vertical solid lines indicate the location of the nonstationary event.

functions (IMF) from the empirical mode decomposition (EMD)[5]. Figure 1.5 shows the corresponding (a) instantaneous frequency, and (b) energy ratio, where the vertical solid lines indicate the location of nonstationary event. The nonstationary event is well captured by HHT in a very local level. We compare the Hilbert marginal spectrum with the Fourier spectrum in Fig. 1.6, where the thin solid line is the Fourier power spectrum of the signal without perturbation. The Fourier power spectrum is

[5]The concept of intrinsic mode function and the empirical mode decomposition methodology will be presented in chapter 2.

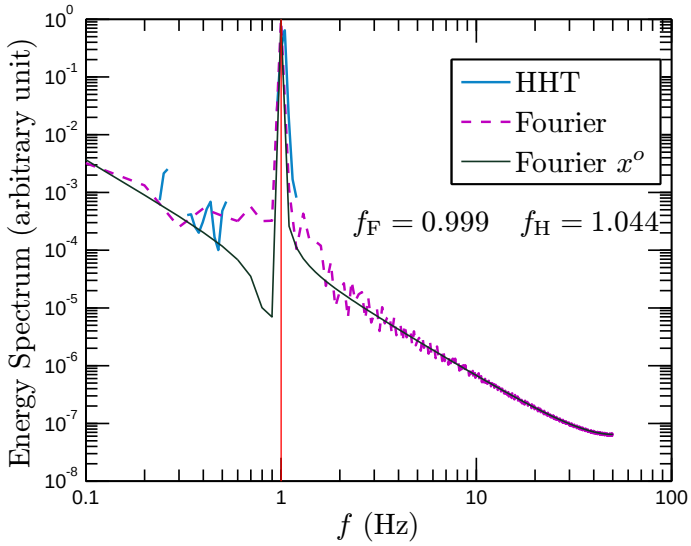

Figure 1.6: Comparison of the Hilbert marginal spectrum and Fourier spectra.

directly estimated by a Fourier transform without any window. All these three curves detect the domain frequency. For the Fourier power spectrum, there are some fluctuation on the high frequency range, indicating the presence of high order harmonic component. For the Hilbert marginal spectrum, we note that it does not require any high order harmonic component to mimic the nonstationary effect, since it allows amplitude-modulation. We also note some energy leakage on the low frequency, which may be the end-point effect in the empirical mode decomposition.

Nonlinear Effect

We turn to nonlinear effect. There is no general definition of nonlinearity for a discrete time series, since we may represent it by a linear asymptotical approximation way. Therefore, we propose here a definition of the nonlinearity for a discrete time series:

Definition 1.3.2 (Nonlinearity)**.** If the underlying mechanism behind a time series is nonlinear, we then call the dataset itself nonlinear.

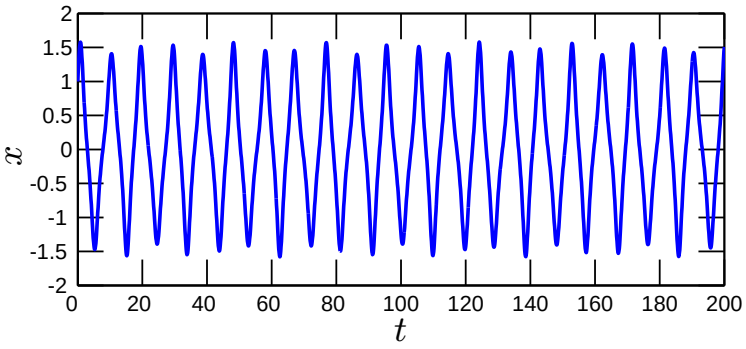

Figure 1.7: A 5th order Runge-Kutta numerical solution of the Duffing equation.

Here we consider the classical Duffing equation with a periodic forcing. The Duffing equation is written as

$$\frac{\mathrm{d}^2x}{\mathrm{d}t^2} + x(1 - \varepsilon x^2) = b\cos\omega t \tag{1.3.3}$$

where ϵ is a nonlinear parameter, $b\cos\omega t$ is a periodic forcing. It can be considered as a nonlinear spring system with a nonlinear spring $(1 - \varepsilon x^2)$, and a periodic forcing $b\cos(\omega t)$. The parameter and inertial condition are taken as $b = 0.1$, $\varepsilon = 1$, $\omega = 2\pi/25$, and $[x(0), x'(0)] = [1, 1]$. A 5th order Runge-Kutta scheme is performed to integrate the equation numerically with $\Delta t = 0.1$. Figure 1.7 shows the corresponding numerical solution. Due to the nonlinear mechanism, the wave profile of the numerical solution departures from a sine wave. We show the corresponding intrinsic mode functions from EMD decomposition in Fig. 1.8. The original time series is separated into five modes with one residual. Figure 1.9 shows the corresponding instantaneous frequency for each mode. A frequency-modulation is clearly observed for the first mode. As we will show in chapter 2, it belongs to the intrawave frequency-modulation family. We compare the corresponding Hilbert marginal spectrum and the Fourier

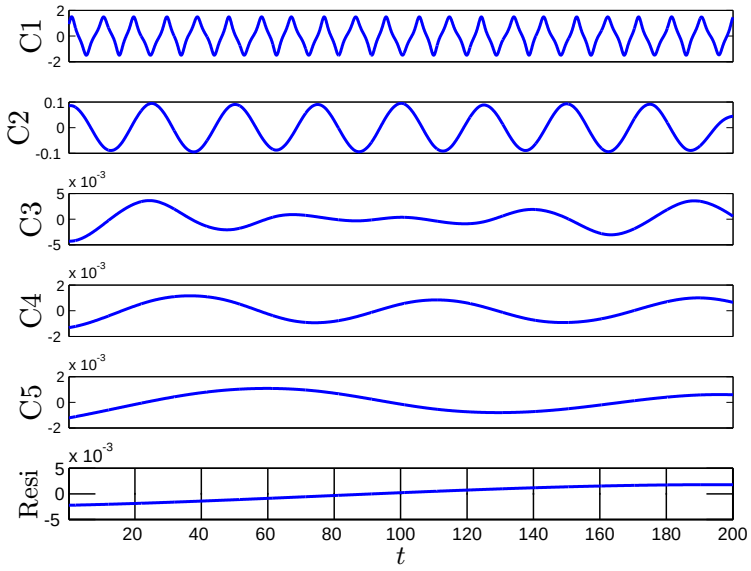

Figure 1.8: Intrinsic mode functions from empirical mode decomposition for numerical solution of the Duffing equation.

power spectrum in Fig. 1.10. They are significantly different. Both approaches capture the domain frequency and the periodic forcing. However, the Fourier analysis needs high order harmonic components to mimic the nonlinear process, which is indeed a requirement of mathematics without physics sense. It stems from the linear asymptotic representation of the nonlinear process. As we already have pointed out previously, due to the nonlinear mechanism, the wave profile of the Duffing equation

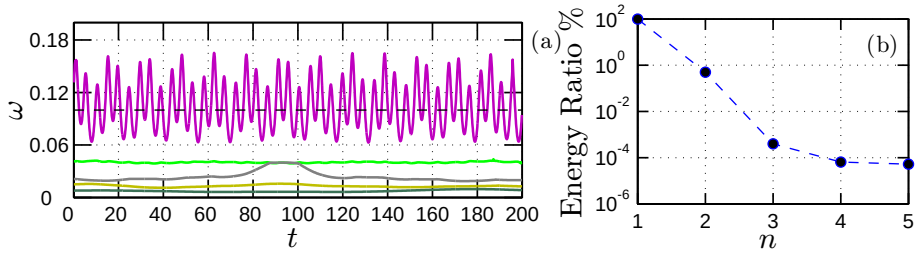

Figure 1.9: Instantaneous frequency for the Duffing equation: (a) instantaneous frequency, (b) the relative energy. Frequency modulation is observed for the first IMF mode.

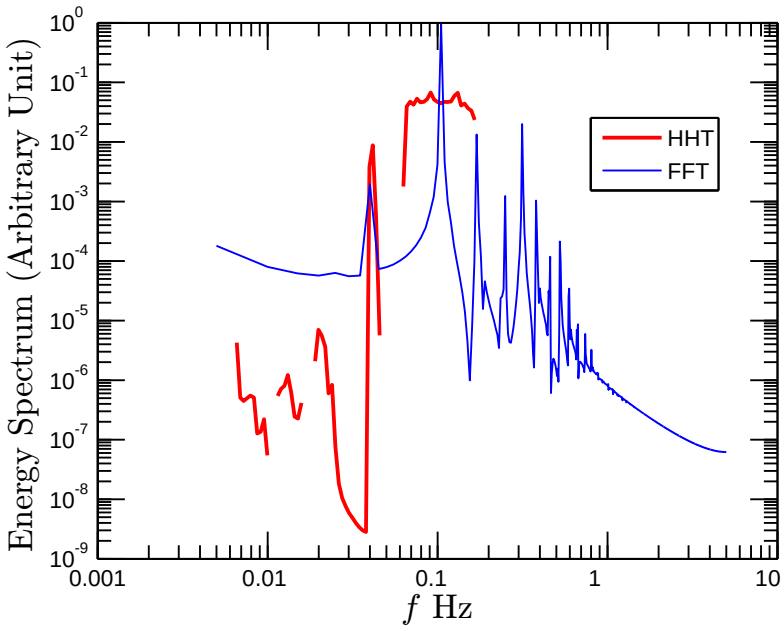

Figure 1.10: Comparison of the Hilbert marginal spectrum and Fourier power spectrum for Duffing equation. High order harmonic components are required by Fourier analysis to mimic the nonlinear distortion of the nonlinear wave.

solution is in far deviation from a pure sine wave. High order harmonic components are thus required by the Fourier analysis to mimic this deviation, namely nonlinear distortion. For HHT, since it allows frequency- and amplitude-modulation simultaneously, it does not need the high order harmonic component any more to describe the nonlinear distortion (Huang *et al.*, 1998, 1999).

1.4 Alternative Approach?

About ten year ago, Huang *et al.* (1998, 1999) introduced a novel time-frequency analysis method, the Hilbert-Huang transform, or Empirical Mode Decomposition called by some authors[6], to deal with general nonstationary and nonlinear time series. This

[6]In fact, a complete Hilbert-Huang transform has two steps. They are the empirical mode decomposition and Hilbert spectral analysis. However, we note that some authors call the empirical

method has a very local level ability both in physical domain and spectral domain. It also possesses fully self-adaptiveness ability, since there is no basis assumption *a priori* (Huang *et al.*, 1998, 1999; Flandrin & Gonçalvès, 2004). As an alternative method to the Fourier-based approach, we will apply this methodology on turbulent and environmental time series in this thesis.

* * * * * * * * * * * * * * *

This thesis is organized as follows. In chapter 2, we present more details on the traditional Hilbert-Huang transform, including Empirical Mode Decomposition, the classical Hilbert Spectral Analysis. We generalize the latter one into arbitrary order to consider the scale invariant properties of intermittent multifractal time series in an amplitude-frequency space with validation in chapter 3.

In chapter 4, we recall the classical Kolmogorov's 1941 theory on local homogenous and isotropic turbulence together with intermittency and multifractal cascade ideas. In chapter 5, we present an analytical model of the classical structure function analysis to show its potential shortcoming. A similar analytical model is proposed to the autocorrelation function of the velocity increment time series. It is found that the autocorrelation function is a better inertial range indicator than structure functions. In chapter 6, we apply the new Hilbert-based methodology to a turbulent database from an experimental homogeneous and nearly isotropic turbulence experiment. We recover the classical structure function scaling exponents $\zeta(q)$ in spectral space for the first time. In chapter 7, we analyze a passive scalar (temperature) turbulence data with very strong ramp-cliff structure, in which the classical structure function analysis

mode decomposition as Hilbert-Huang transform.

fails. In chapter 8, we generalize the Extended-Self-Similarity (ESS) into Hilbert frame to compare the scaling property of turbulent velocity with various turbulent intermittency models. We finally apply the new methodology to environmental time series: river flow discharge data in chapter 9, and surf zone marine turbulence data in chapter 10, to characterize the scale invariant properties in amplitude-frequency space. In chapter IV, we draw the main conclusions of this thesis.

Chapter 2

Norden Huang's 1998 Proposal: Hilbert-Huang Transform

About ten year ago, Huang *et al.* (1998, 1999) introduced a new method, namely Hilbert-Huang transform or Empirical Mode Decomposition, to deal with time series analysis that was claimed to be well adapted for nonlinear and nonstationary data. During the last ten years, there have been more than 1000 papers devoted to apply this new method to various engineering applications and many different science research fields. For example, waves (Hwang *et al.*, 2003; Veltcheva & Soares, 2004; Schmitt *et al.*, 2009), biological applications (Echeverria *et al.*, 2001; Balocchi *et al.*, 2004; Ponomarenko *et al.*, 2005), financial studies (Huang *et al.*, 2003b), meteorology and climate studies (Coughlin & Tung, 2004; Jánosi & Müller, 2005; Molla *et al.*, 2006; Solé *et al.*, 2007; Wu *et al.*, 2007; Huang *et al.*, 2009b), mechanical engineering (Loh *et al.*, 2001; Chen *et al.*, 2004), acoustics (Loutridis, 2005), aquatic environment (Schmitt *et al.*, 2007), and turbulence (Huang *et al.*, 2008), to quote a few. In this chapter, we introduce this method in detail.

2.1 Empirical mode decomposition

The most innovative part of the HHT is the Empirical Mode Decomposition. The starting point of the EMD is that most of the signal are multi-component, which means that there exist different scales simultaneously (Cohen, 1995; Huang *et al.*, 1998, 1999). This may be considered as faster oscillations superposed to slower ones at very local levels (Rilling *et al.*, 2003; Flandrin & Gonçalvès, 2004). We illustrate this idea in Fig. 2.1.The characteristic scale is taken, for EMD method, as the distance between two successive maxima positions. This idea was at the original of the introduction of Intrinsic Mode Function (IMF in the following). The definition of an IMF is: (i) the difference between the number of local extrema and the number of zero-crossings must be zero or at most one; (ii) the running mean value of the envelope defined by the local maxima and the envelope defined by the local minima is zero. Figure 2.2 shows an example of IMF. The next step is to consider how IMFs can be extracted from time series.

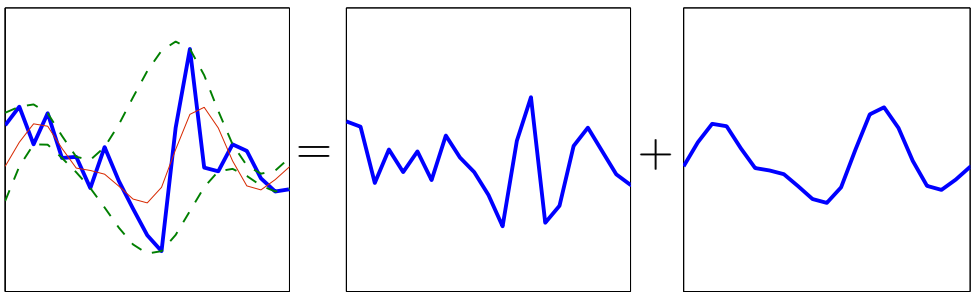

Figure 2.1: A schematic illustration of the basic idea of EMD. The original signal (thick line in the left diagram) is considered as the superposition of a faster oscillation (middle diagram) on a slower oscillation (right diagram).

Norden Huang *et al.* (1998, 1999) introduced the Empirical Mode Decomposition algorithm, called by himself "sifting process", to decompose a given signal into several

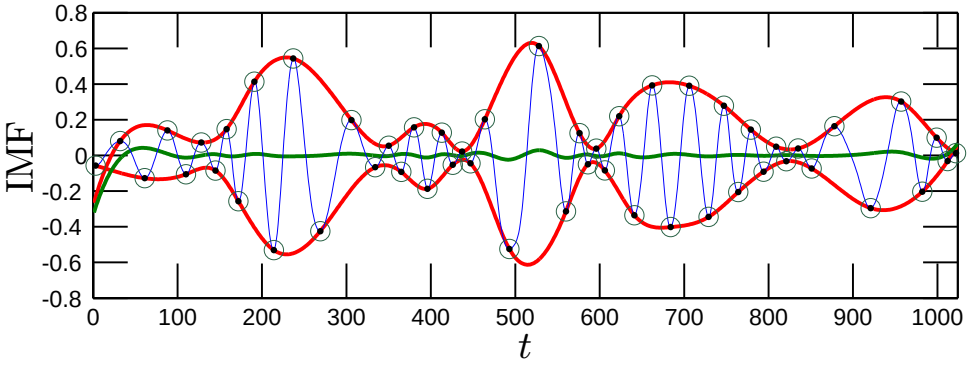

Figure 2.2: An example of IMF from EMD decomposition.

IMF modes (Flandrin *et al.*, 2004). The corresponding flow chart of this sifting process is shown in Fig. 2.3.

The first step of sifting process is to identify all the local extrema maxima (resp. minima) points for a given time series $x(t)$. Once all the local extrema maxima points are identified, the upper envelope $e_{\max}(t)$ is constructed by a cubic spline. The the procedure is repeated for the local extrema minima points to produce the lower envelope $e_{\min}(t)$. Then the mean between these two envelope is defined as

$$m_1(t) = \frac{e_{\max}(t) + e_{\min}(t)}{2} \tag{2.1.1}$$

The first component is then estimated by

$$h_1(t) = x(t) - m_1(t) \tag{2.1.2}$$

The procedure is illustrated in Fig. 2.4, where the the original data $x(t)$ are shown as thin solid line. Ideally, $h_1(t)$ should be an IMF as expected. In reality, however, $h_1(t)$ may not satisfy the condition to be an IMF. We thus take $h_1(t)$ as a new time series and repeat the sifting process j times, until $h_{1j}(t)$ is an IMF

$$h_{1j}(t) = h_{1(j-1)}(t) - m_{1j}(t) \tag{2.1.3}$$

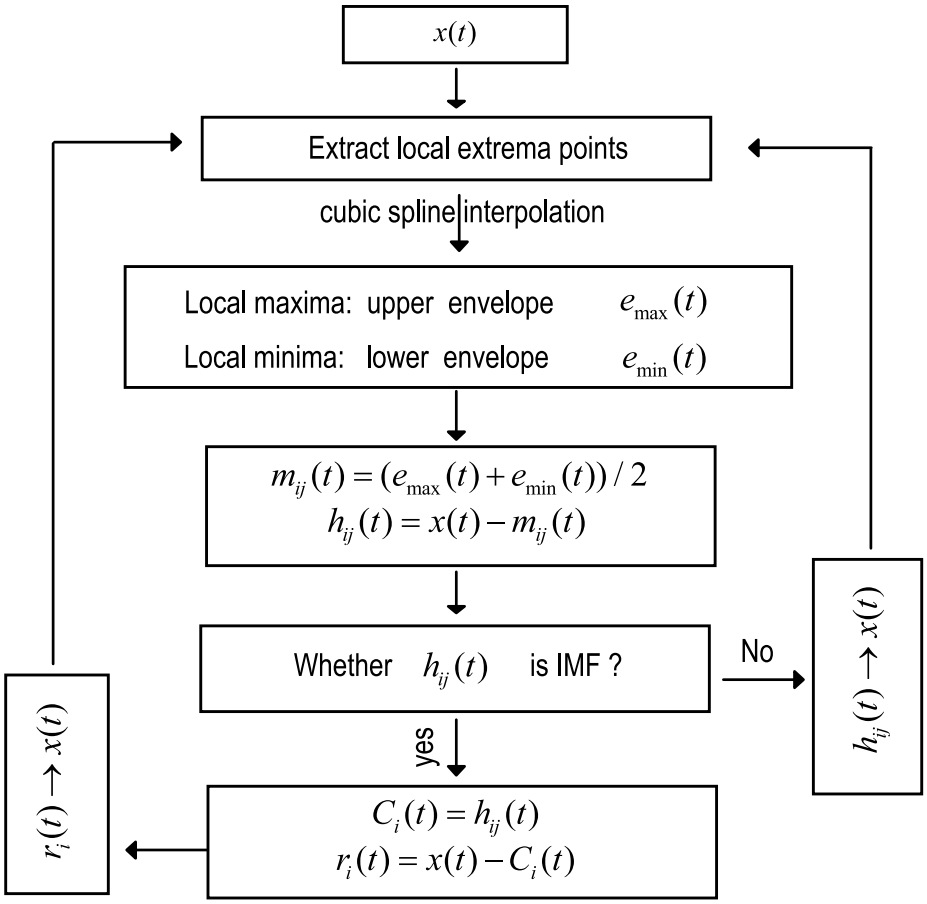

Figure 2.3: The flowchart of sifting process for EMD algorithm.

We thus extract the first IMF component $C_1(t)$

$$C_1(t) = h_{1j}(t) \tag{2.1.4}$$

and the residual $r_1(t)$

$$r_1(t) = x(t) - C_1(t) \tag{2.1.5}$$

from the data $x(t)$. An illustration of the first sifting process for a real time series is shown in Fig. 2.4. The sifting procedure is then repeated on residual until $r_n(t)$ becomes monotonic function or at most has one local extreme point. This means no more IMF can be extracted from $r_n(t)$. We finally have $n-1$ IMF modes with one

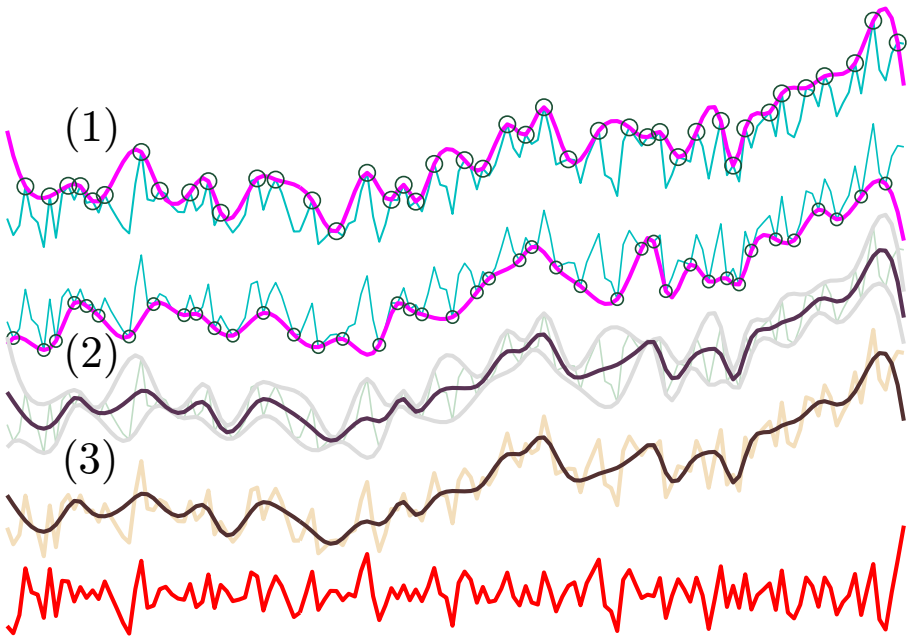

Figure 2.4: Illustration of the sifting process of EMD algorithm: (1) identify all the local extrema points (○), and construct the upper envelop $e_{\max}(t)$, and the lower envelop $e_{\min}(t)$, (2) calculate the running average $m_1(t)$, and (3) get the local detail $h_1(t)$ after 1st sifting. The original time series $x(t)$ is shown as thin solid line.

residual $r_n(t)$. The original data $x(t)$ is then rewritten as

$$x(t) = \sum_{i=1}^{n-1} C_i(t) + r_n(t) \tag{2.1.6}$$

Due to a dyadic filter bank property of the EMD algorithm (Wu & Huang, 2004; Flandrin *et al.*, 2004; Huang *et al.*, 2008), usually in practice, the number of IMF modes is less than $\log_2(N)$, where N is the length of the data set.

The above sifting process severs as two purposes: (i) to eliminate the riding wave, (ii) to make the wave profiles more symmetric. Therefore, the sifting process should be repeated enough times. However, if too many times sifting are performed, the amplitude of the IMF modes will become constant, and the nonlinear wave profiles is then distorted, which means the modes lose their physical meaning (Huang *et al.*,

1998, 1999). To guarantee that the IMF modes retain enough physical sense for both amplitude and frequency modulations, a stopping criterion has to be introduced to stop the sifting process. Different types of stopping criteria have been introduced by several authors (Huang *et al.*, 1998, 1999; Rilling *et al.*, 2003; Huang *et al.*, 2003a; Huang, 2005). We only describe here what we used in this thesis. The first stop criterion is a Cauchy-type convergence criterion. In this we introduce the standard deviation (SD), which is defined for two successive sifting process as

$$\mathrm{SD} = \frac{\sum_{t=0}^{T} |h_{i(j-1)}(t) - h_j(t)|^2}{\sum_{t=0}^{T} h_{i(j-1)}^2(t)} \tag{2.1.7}$$

If a calculated SD is smaller than a given value, then the sifting stops and gives an IMF. A typical value proposed by Huang *et al.* (1998) is $0.2 \sim 0.3$, proposed based on their experience (Huang *et al.*, 1998). Another widely used criterion is based on 3 thresholds α, θ_1 and θ_2, which are designed to guarantee globally small fluctuations in the mean while taking into account locally large excursions (Rilling *et al.*, 2003). Mode amplitude and evaluation functions are then given by

$$a(t) = \frac{e_{\max}(t) - e_{\min}(t)}{2} \tag{2.1.8}$$

and

$$\sigma(t) = |m(t)/a(t)| \tag{2.1.9}$$

The sifting is iterated until $\sigma(t) < \theta_1$ for some prescribed fraction $1 - \alpha$ of the total duration, while $\sigma(t) < \theta_2$ for the remaining fraction. The typical values proposed by Rilling *et al.* (2003) are $\alpha \approx 0.05$, $\theta_1 \approx 0.05$ and $\theta_2 \approx 10\,\theta_1$, respectively based on their experience. We also set the maximal iteration number, for example 300, to avoid to over-decompose the time series. In practice, if one of these criteria is satisfied, then the sifting process stops to give an IMF.

The above described EMD algorithm does the decomposition in a very local level in physical domain without *a priori* basis. It also means that it is an *a posteriori* method, since the basis (function) is induced by the data itself (Huang *et al.*, 1998, 1999; Flandrin & Gonçalvès, 2004). The fully adaptiveness ability of this method explains that it can be considered to be well adapted for nonlinear and nonstationary data. However, the main drawback of this method is that it is not mathematically proved (Huang, 2005). More detail about the EMD algorithm can be found in Refs. Huang *et al.* (1998, 1999); Rilling *et al.* (2003); Flandrin *et al.* (2004); Flandrin & Gonçalvès (2004); Huang (2005).

2.2 Hilbert spectral analysis

After having extracted the IMF modes, one can apply the associated Hilbert spectral analysis to each IMF component C_i in order to extract the energy-time-frequency information from the data (Long *et al.*, 1995; Huang *et al.*, 1998, 1999). The Hilbert transform of a function $C(t)$ is written as

$$\tilde{C}(t) = \frac{1}{\pi} P \int_0^{+\infty} \frac{C(t')}{t - t'} \, \mathrm{d}t' \tag{2.2.1}$$

where 'P' means the Cauchy principle value (Cohen, 1995; Long *et al.*, 1995; Huang *et al.*, 1998). It is a singularity integration, which means that it should have a very local ability to denoting fluctuations. For each IMF mode, one can construct the analytic signal (Cohen, 1995), $\mathbb{C}_i(t)$, as

$$\mathbb{C}_i(t) = C_i(t) + j\tilde{C}_i(t) = \mathcal{A}_i(t) \mathrm{e}^{j\theta_i(t)} \tag{2.2.2}$$

where

$$\mathcal{A}_i(t) = |\mathbb{C}_i(t)| = [C_i(t)^2 + \tilde{C}_i^2(t)]^{1/2}, \quad \theta_i(t) = \arctan\left(\frac{\tilde{C}_i(t)}{C_i(t)}\right) \tag{2.2.3}$$

Hence the instantaneous frequency can be defined by using the information of phase function $\theta_i(t)$, which is written as

$$\omega_i = \frac{\mathrm{d}\theta_i(t)}{\mathrm{d}t} \tag{2.2.4}$$

The original signal is finally represented (excluding the residual $r_n(t)$) as

$$x(t) = \mathrm{RP}\sum_{i=1}^{N} \mathcal{A}_i(t) e^{j\theta_i(t)} = \mathrm{RP}\sum_{i=1}^{N} \mathcal{A}_i(t) e^{j\int \omega_i(t)\,\mathrm{d}t} \tag{2.2.5}$$

where 'RP' means real part. The Hilbert-Huang transform can be taken as a generalization of Fourier transform, see Eq. (1.1.3): it allows a frequency-modulation and amplitude-modulation simultaneously. A Hilbert spectrum, $H(\omega, t) = \mathcal{A}^2(\omega, t)$, is thus designed to represent the energy in time-frequency representation (Long *et al.*, 1995; Huang *et al.*, 1998). We further can define the Hilbert marginal spectrum as

$$h(\omega) = \int_0^{+\infty} H(\omega, t)\,\mathrm{d}t \tag{2.2.6}$$

This is similar with the Fourier spectrum, and can be interpreted as the energy associated to each frequency. We however underline the fact that the definition of frequency here is different from the definition in the Fourier frame (Huang *et al.*, 1998, 1999).

We do not give the validation and calibration detail of the Hilbert-Huang transform here. For details of the validation and calibration, we suggest Refs. Huang *et al.* (1998, 1999).

2.3 Intrawave frequency modulation and nonlinear mechanism

We have mentioned in chapter 1 that the the frequency modulation can be further termed into two different types, intrawave frequency modulation and interwave frequency modulation. Indeed, the former one may be linked to the nonlinear distortion. More precisely, it may be considered as a signature of nonlinear mechanism. We show this by an example.

Intrawave Frequency Modulation

We have taken Duffing equation as an example to show the nonlinear distortion of Fourier representation. Figure 2.5 (a) reproduces the instantaneous frequency ω of the

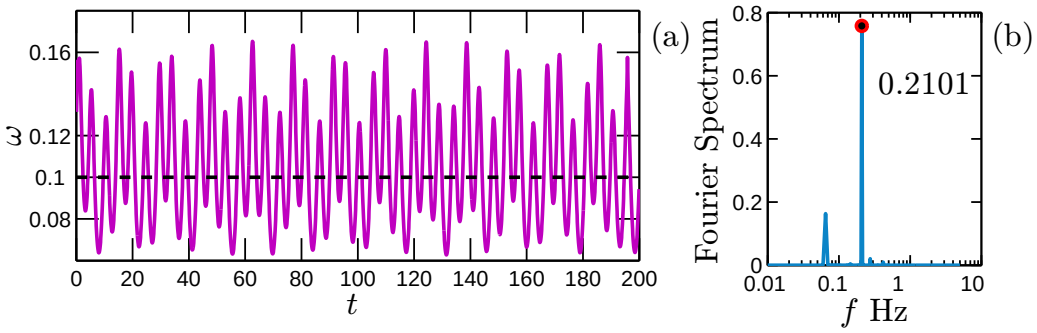

Figure 2.5: Illustration of the Intrawave Frequency Modulation by using Duffing equation: (a) instantaneous frequency of the 1st mode, (b) the Fourier energy spectrum of the instantaneous frequency of 1st mode, respectively.

first IMF mode of the numerical solution of the Duffing equation. One can find that the instantaneous frequency ω itself varies with the time t between $0.05 \sim 0.15$ Hz, with a mean value of 0.1 Hz. This corresponds to frequency-modulation. We take ω as a new time series and calculate it Fourier power spectrum. The corresponding Fourier power spectrum is shown Fig. 2.5 (b). The dominant frequency is 0.21 Hz, twice of the

mean frequency of the 1st IMF mode. This means that the instantaneous frequency does vary within one period. This is an intrawave type of frequency modulation. We argue that it corresponds to a nonlinear mechanism behind the time series.

Interwave Frequency Modulation

We consider another type of FM here, interwave frequency modulation. We construct a linear chirp signal as (Flandrin, 1998):

$$x(t) = \sin(\frac{\pi}{20}t + \frac{\pi}{100}t^2), \quad 0 \leq t \leq 50 \tag{2.3.1}$$

The corresponding instantaneous frequency is written

$$\omega(t) = \frac{1}{40} + \frac{1}{200}t \tag{2.3.2}$$

Figure 2.6 shows (a) the constructed chirp signal and (b) the corresponding instantaneous frequency. As a comparison with Fig. 2.5, one can immediately find the difference between them: the instantaneous frequency ω here is linearly increasing with time t.

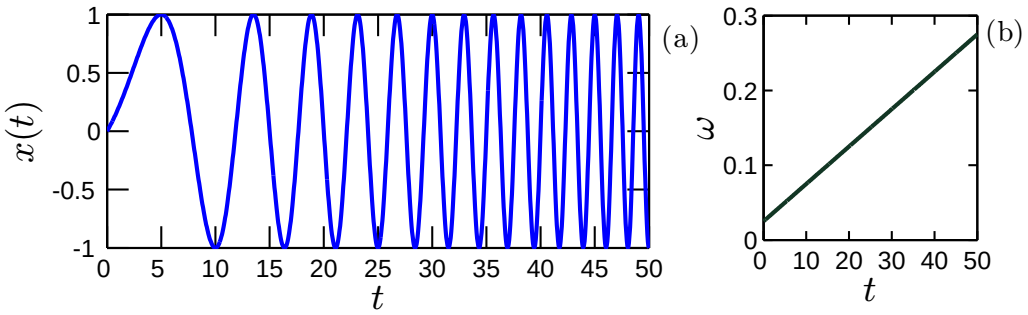

Figure 2.6: Illustration of the Interwave Frequency Modulation: (a)a chirp $x(t) = \sin(\frac{\pi}{20}t + \frac{\pi}{100}t^2)$, (b) the instantaneous frequency $\omega(t) = \frac{1}{40} + \frac{1}{200}t$, respectively.

Nonlinear Mechanism

For comparison convenience, we replot the first IMF mode of Duffing equation (top) and the chirp signal (bottom) in Fig. 2.7. This illustrates the difference between them. The former one provides a departure from the sine wave due to a nonlinear mechanism. The latter still keeps sine wave profile from period to period. Thus, any nonlinear distorted waveform has been referred to as "harmonic distortions for Fourier based methods".

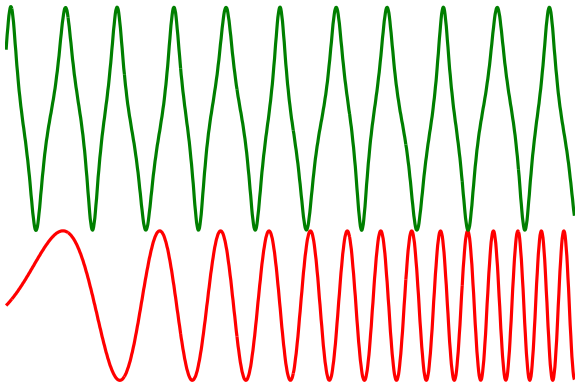

Figure 2.7: Comparison of the wave profiles of the first IMF mode of Duffing equation (top) and the chirp signal (bottom). The former one deviates from a pure sine wave profile with nonlinear distortion. The latter still keeps sine wave profile.

2.4 Summary

We introduced the Hilbert-Huang transform above, including the empirical mode decomposition and the Hilbert spectral analysis. The combination of EMD and HSA also is called Hilbert-Huang transform (HHT). It is have been shown that the HHT has fully self-adaptiveness and very local ability in both physical and spectral domains. It is particular suitable for nonstationary time series analysis.

The main drawback of the HHT is its lack of solid theoretical ground, since the EMD part is almost empirical (Huang, 2005). Recently, Flandrin *et al.* have obtained new theoretical results on the EMD method (Flandrin & Gonçalvès, 2004; Rilling & Flandrin, 2006, 2008, 2009). However, more theoretical work is still needed to fully mathematically understand this method.

Chapter 3

Our Generalization: Arbitrary Order Hilbert Spectral Analysis

We consider here the main contribution of our work: the generalization of the classical Hilbert-Huang approach for arbitrary order moments, in order to deal with scaling intermittent multifractal time series. The results presented in this chapter are published in Huang *et al.* (2008, 2009a, 2010a) [Y. Huang, *et al. Europhy. Lett.*, 84, 40010, 2008.; Y. Huang, *et al. Traitement du Signal*, 25, 481-492, 2008; Y. Huang, *et al. Phys. Rev. E*, 2010 (submitted).]

3.1 Definition

The Hilbert marginal spectrum is defined as a marginal integration of the Hilbert spectrum $H(\omega, t)$ over t, which is written as

$$h(\omega) = \int_0^{+\infty} H(\omega, t)\, \mathrm{d}t \tag{3.1.1}$$

where $H(\omega, \mathcal{A})$ is the Hilbert spectrum. There is another equivalent definition, which is based on the joint probability density function $p(\omega, \mathcal{A})$ of the instantaneous frequency ω and the amplitude $\mathcal{A}$ (Long *et al.*, 1995; Huang *et al.*, 2008, 2009a). The

Hilbert marginal spectrum is thus rewritten as the marginal integral of the joint pdf $p(\omega, \mathcal{A})$ over $\mathcal{A}^2$

$$h(\omega) = \int_0^{+\infty} p(\omega, \mathcal{A})\mathcal{A}^2 \, \mathrm{d}\mathcal{A} \tag{3.1.2}$$

One can find that the above definition is no more than a second order statistical moment. This constatation leads us to generalize this approach to arbitrary order moment

$$\mathcal{L}_q(\omega) = \int_0^{+\infty} p(\omega, \mathcal{A})\mathcal{A}^q \, \mathrm{d}\mathcal{A} \tag{3.1.3}$$

where $q \geq 0$[1] (Huang *et al.*, 2008, 2009a). In case of scale invariance, we expect a power law of the form

$$\mathcal{L}_q(\omega) \sim \omega^{-\xi(q)} \tag{3.1.4}$$

where $\xi(q)$ is the corresponding Hilbert-based scaling exponent. Due to the integration operator, $\xi(q) - 1$ can be associated to the classical $\zeta(q)$ from structure function analysis: $\langle \Delta x_\ell^q \rangle \sim \ell^{\zeta(q)}$. Therefore, the generalized Hilbert spectral analysis provides a new methodology to characterize the scale invariance in an amplitude-frequency space (Huang *et al.*, 2008, 2010a, 2009a).

In the following context, we validate and calibrate the idea of the arbitrary order HSA methodology by fractional Brownian motion simulations and a synthesized multifractal nonstationary time series.

[1] In fact here q can be take as $q \geq -1$. However, we only consider the case $q \geq 0$ in this thesis.

3.2 Calibration and validation

3.2.1 Fractional Brownian motion and multifractal time series

Fractional Brownian Motion

Fractional Brownian motion (fBm) is a continuous-time random process proposed by Kolmogorov (1940) in the 1940s and Yaglom (1957) and later named 'fractional Brownian motion' by Mandelbrot & Van Ness (1968). It consists in a fractional integration of a white Gaussian process and is therefore a generalization of Brownian motion, which consists simply in a standard integration of a white Gaussian process (Mandelbrot & Van Ness, 1968; Flandrin, 1992; Samorodnitsky & Taqqu, 1994; Beran, 1994; Rogers, 1997; Doukhan *et al.*, 2003; Gardiner, 2004; Biagini *et al.*, 2008). Because it presents deep connections with the concepts of self-similarity, fractal, long-range dependence or $1/f$-process, fBm quickly became a major tool for various fields where such concepts are relevant, such as in geophysics, hydrology, turbulence, economics, communications, etc (Samorodnitsky & Taqqu, 1994; Gardiner, 2004; Biagini *et al.*, 2008).

For a fBm $X(t)$ process, the autocorrelation is well known to be the following

$$R_H(t,t') = \frac{\sigma^2}{2}\left(|t|^{2H} + |t'|^{2H} - |t-t'|^{2H}\right) \tag{3.2.1}$$

where σ is the variance of $X(t)$, and H is the so-called Hurst number (Samorodnitsky & Taqqu, 1994; Beran, 1994; Gardiner, 2004; Biagini *et al.*, 2008). The process is said to be self-similar, since in terms of distributions for any real a

$$X(at) \sim |a|^H X(t) \tag{3.2.2}$$

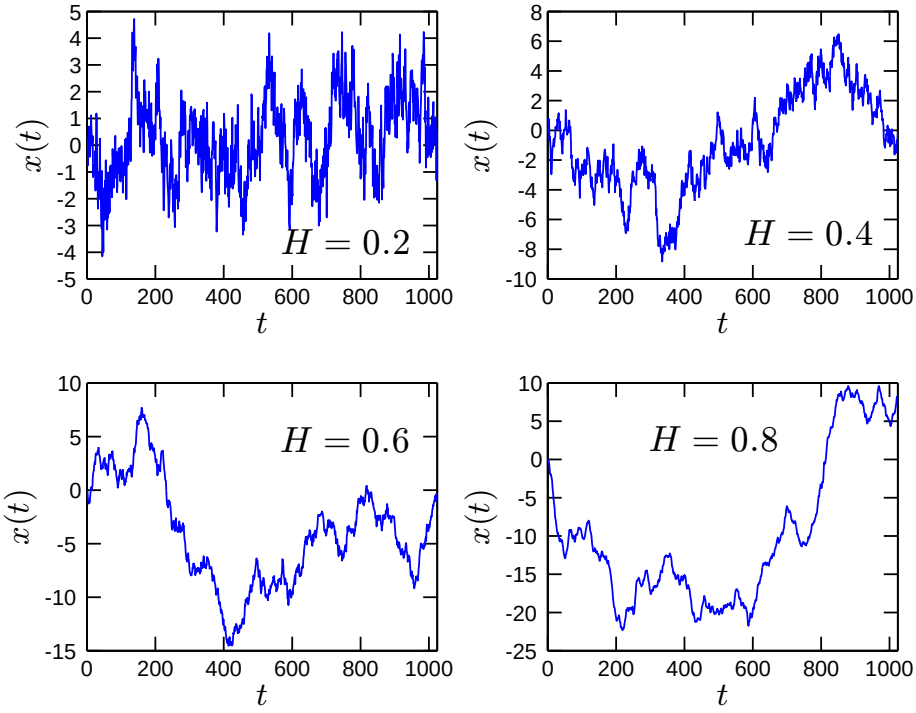

Figure 3.1: Illustration of fractional Brownian motion with various Hurst number H.

It is also well known for its stationary increments

$$X(t) - X(\tau) \sim X(t - \tau) \tag{3.2.3}$$

For the case $H > 1/2$, the process exhibits long-range dependence, which means that

$$\int_0^{+\infty} C(\tau)\,\mathrm{d}\tau = \infty \tag{3.2.4}$$

where the autocorrelation function is written as

$$C(\tau) = \langle X(t)X(t+\tau)\rangle \tag{3.2.5}$$

in which $\langle\,\rangle$ means ensemble average.

The fBm is a classical monofractal process. It requires only one parameter, the

Hurst number H, to characterize the stochastic process. For structure function analysis, the scaling exponents is well known to be the following

$$\langle |X(t+\tau) - X(t)|^q \rangle \sim \tau^{\zeta_H(q)},\ \zeta_H(q) = qH \tag{3.2.6}$$

where $\zeta_H(q)$ is the scaling exponent from structure functions. We thus expect for the HSA approach the corresponding scaling exponents $\xi_H(q)$ to be the following

$$\mathcal{L}_{q,H}(\omega) \sim \omega^{-\xi_H(q)},\ \xi_H(q) = qH + 1 \tag{3.2.7}$$

where the '+1' corresponds to the integration operator in Eq. (3.1.3).

We consider here a Wavelet based algorithm to simulate the fBm process, which was first proposed by Meyer (n.d.) and Sellan (1995), then developed by Abry & Sellan (1996). Starting from the expression of the fBm process as a integral of the fractional Gaussian noise process, the idea of the algorithm is to build a biorthogonal wavelet depending on a given orthogonal one and adapted to the parameter H. Then the generated sample path is obtained by the reconstruction using the new wavelet starting from a wavelet decomposition at a given level designed as follows: details coefficients are independent random Gaussian realizations and approximation coefficients come from a fractional Autoregressive Integrated Moving Average (ARIMA) process. A MATLAB® code, namely wfbm, to realize this algorithm can be found in the Wavelet toolbox of MATLAB®.

Figure 3.1 illustrates a 2^{12} data points portion of fBm with various Hurst numbers H by using above mentioned algorithm with db2 wavelet. One can find that for the long-range dependence case, $H > 1/2$, an increasing pattern in the previous steps is likely to be followed by the current increasing step as well.

The validation of the new arbitrary order Hilbert spectral analysis using this data series will be considered below.

Nonstationary Multifractal Time Series

Since the introduction of multifractal concepts in the 1980s (Parisi & Frisch, 1985; Grassberger & Procaccia, 1983; Benzi *et al.*, 1984; Grassberger, 1986) in the field of turbulence and chaos, this approach has met huge success.

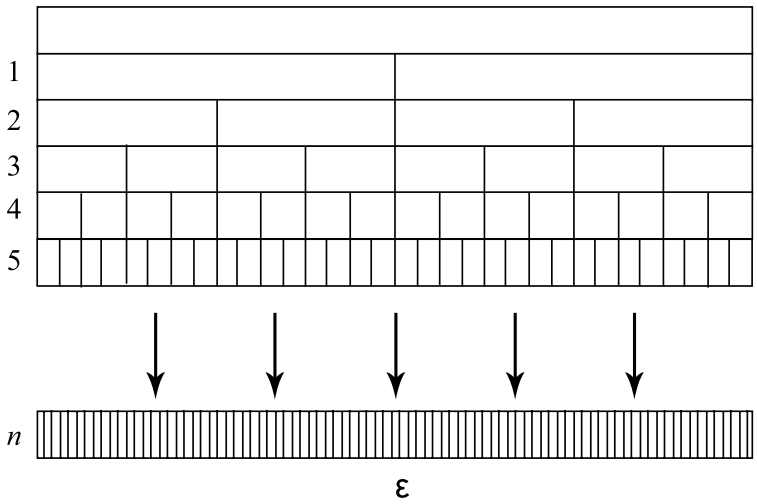

Figure 3.2: Illustration of the discrete cascade process. Each step is associated to a scale ratio of 2. After n steps, the total scale ratio is 2^n.

Multifractal properties have been found in may fields, such as, turbulence (Anselmet *et al.*, 1984; Frisch, 1995), financial time series (Ghashghaie & Dodge, 1996; Schmitt *et al.*, 1999; Lux, 2001; Calvet & Fisher, 2002), physiology (Ivanov *et al.*, 1999), rainfall (Schertzer & Lovejoy, 1987; Schmitt *et al.*, 1998; De Lima & Grasman, 1999; Venugopal *et al.*, 2006), etc. A multifractal process is a generalization of monofractal process, in which a single exponent, such as Hurst number H, is not enough to describe its dynamics; instead, a continuous spectrum of exponents is

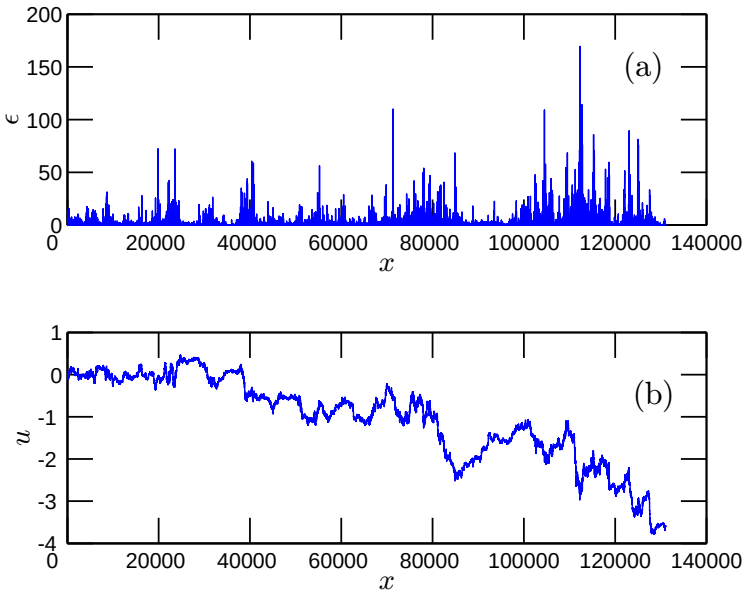

Figure 3.3: A sample for one realization 2^{17} points with $\mu = 0.25$: (a) the multifractal measure (b) the constructed multifractal nonstationary process.

needed.

For a few years now, new methods to generate nonstationary multifractal time series mimicking turbulent velocity or passive scalar time series have been proposed (Muzy & Bacry, 2002). Here we adapt the idea of multifractal random walks using discrete multiplicative cascades (Schmitt, 2003).

We consider here a synthesized multifractal nonstationary time series, which is constructed based on a multiplicative discrete cascades (Schmitt, 2003). Figure 3.2 illustrates the cascade process algorithm. The larger scale corresponds to a unique cell of size $L = \ell_0 \lambda_1^n$, where ℓ_0 is a fixed scale and $\lambda_1 > 1$ is dimensional scale ratio. For discrete model, this ratio is often taken as $\lambda_1 = 2$. The model being discrete, the next scale involved corresponds to λ_1 cells, each of size $L/\lambda_1 = \ell_0 \lambda_1^{n-1}$. This is iterated and at step p $(1 \leq p \leq n)$ there are λ_1^p cells, each of size $L/\lambda_1^p = \ell_0 \lambda_1^{n-p}$.

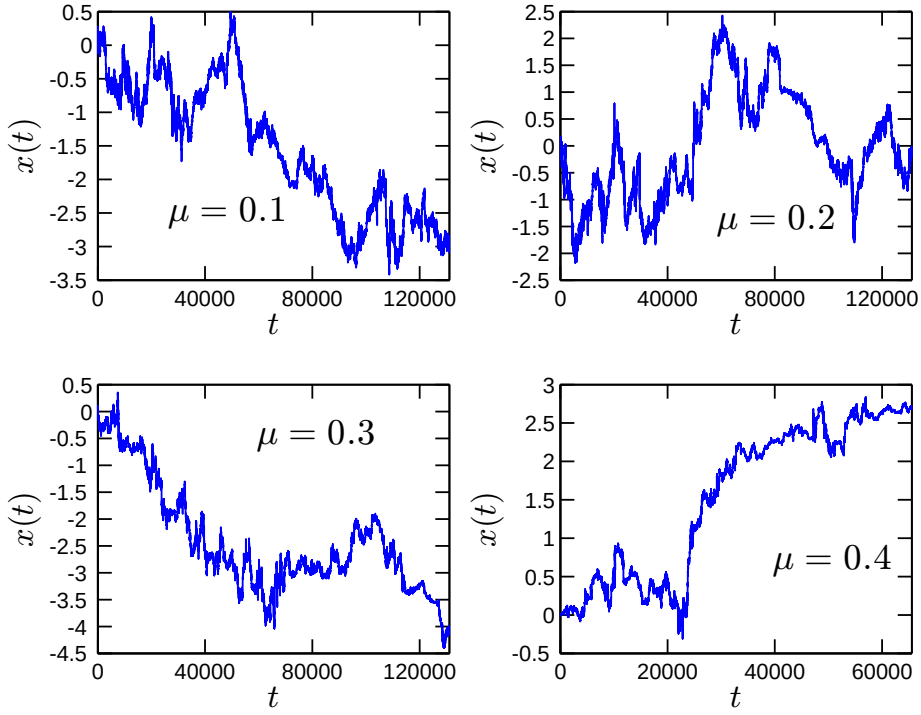

Figure 3.4: Illustration of synthesized nonstationary multifractal time series with various intermittent parameters μ.

There are n cascade steps, and at step n there are λ_1^n cells, each of size ℓ_0, which is the smallest scale of the cascade. To reach this scale, all intermediate scales have been involved. Finally, at each point the multifractal measure writes as the product of n cascade random variables

$$\epsilon(x) = \prod_{p=1}^{n} W_{p,x} \tag{3.2.8}$$

where $W_{p,x}$ is the random variable corresponding to position x and level p in the cascade (Schmitt, 2003). Following multifractal random walk ideas (Bacry *et al.*, 2001; Muzy & Bacry, 2002), we generate a nonstationary multifractal time series as

$$u(x) = \int_0^x \epsilon(x')^{1/2} dB(x') \tag{3.2.9}$$

where $B(x)$ is Brownian motion. Taking lognormal statistic for ϵ, the scaling exponent

$\zeta(q)$ such as $\langle|\Delta u_\tau(t)|^q\rangle \sim \tau^{\zeta(q)}$ is written as

$$\zeta(q) = \frac{q}{2} - \frac{\mu}{2}(\frac{q^2}{4} - \frac{q}{2}) \tag{3.2.10}$$

where μ is the intermittency parameter ($0 \leq \mu \leq 1$) characterizing the lognormal multifractal cascade (Huang *et al.*, 2010a).

A sample for one realization is shown in Fig. 3.3 (a) the multifractal measure, and (b) the nonstationary multifractal time series, with $\mu = 0.25$, and $n = 17$ levels, corresponding to data sets with data length 2^{17} points. Figure 3.4 shows the synthesized nonstationary multifractal time series with various intermittent parameters μ.

As for fBm time series, these multifractal synthetic time series are analyzed below using our new method.

3.2.2 Calibration and validation

Monofractal Processes: Fractional Brownian Motions

For the fBm process, we simulate 500 segments of length 2^{12} data points each, using above mentioned wavelet based algorithm (Abry & Sellan, 1996), with db2 wavelet and various Hurst values from 0.1 to 0.9. The Hilbert transform is numerically estimated by using a FFT based method (Marple Jr, 1999). Figure 3.5 shows the first six order Hilbert marginal spectrum for $H = 0.4$ and 0.6. Power law is observed for each curve as expected. The scaling exponent $\xi(q)$ is then estimated on the corresponding power law range by a first order least square fitting algorithm. We then represent the corresponding scaling exponents $\xi(q)$ for various value of q from 0 to 6 in Fig. 3.6, in which perfect straight lines of equation $1 + qH$ confirms the usefulness of the new method to estimate $\xi(q)$.

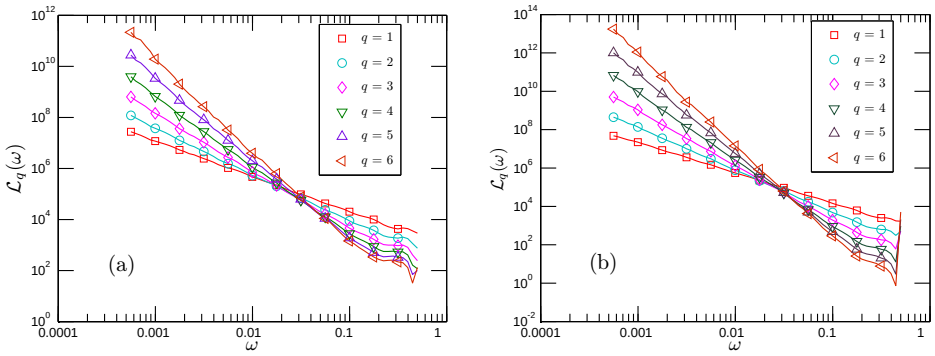

Figure 3.5: The first six order Hilbert marginal amplitude spectra of fractional Brownian motion with Hurst number (a) $H = 0.4$, and (b) $H = 0.6$. Power law behaviour is observed for each curve as expected.

We then consider estimation of the H value. For this, we consider different estimators. They involve the first and second order moment. These estimators are

$$H^{\dagger} = \xi(1) - 1 \tag{3.2.11a}$$

$$H^{\star} = (\xi(2) - 1)/2 \tag{3.2.11b}$$

and using the least square fitting for all q

$$H^{\diamond} = (\xi(q) - 1)/q \tag{3.2.11c}$$

The estimated H_{est} are shown in Fig. 3.7 for $H^{\dagger}$ ($\triangleright$), $H^{\star}$ ($\bigcirc$) and $H^{\diamond}$ ($\square$). They are good agreement with the theoretical H. The mean error for each estimator are 5.3%, 3.1% and 9.4%. For comparison, we reproduce the estimated value H from Ref. Rilling *et al.* (2005), in which two estimators $\hat{H}_1$ ($\bigtriangledown$), $\hat{H}_2$ ($\bigtriangleup$) based on IMF modes and one estimator based on discrete wavelet transform H_W ($\diamondsuit$) are presented. We also show the absolute error $|H_{est} - H|$, the estimated values departure from the given Hurst number H as inset, where the gray patch indicates the deviation less than 5%. We underline that Rilling *et al.* (2005) simulated the fractional Gaussian

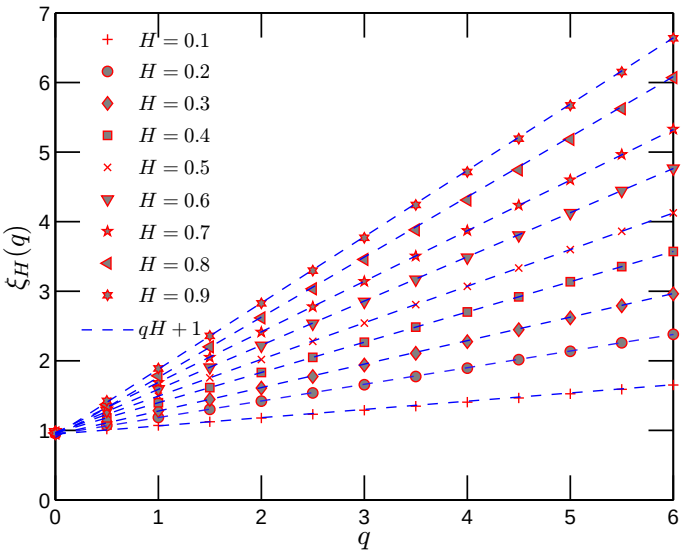

Figure 3.6: Scaling exponents $\xi_H(q)$ for fractional Brownian motion simulations with H from 0.1 to 0.9.

noise by using the algorithm proposed by Wood & Chan (1994). Their proposed estimators $\hat{H}_1$ and $\hat{H}_2$ are based on the assumption of a dyadic filter bank for the EMD method (Rilling *et al.*, 2005). If the absolute error is less than 5%, then there is no significant difference between estimators. Their results show two different range for $H < 1/2$ and $1/2 < H$, see Fig. 3.7, in which it is indicated by the vertical dashed line. They argued that for the case where $H < 1/2$, the dyadic filter bank property which underlies the EMD approach is only an approximation that has to be refined further (Rilling *et al.*, 2005). The estimators $H^{\dagger}$, $H^{\star}$ and $H^{\diamond}$ we proposed here may provide more precise estimators, since they do not require the dyadic property.

The above numerical experiment confirms the usefulness of the arbitrary order Hilbert spectral analysis methodology for the monofractal case.

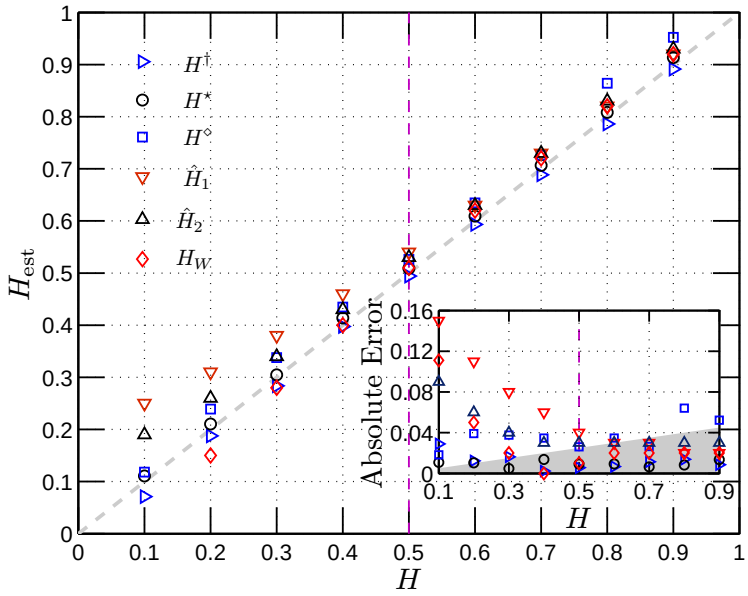

Figure 3.7: Representation of the estimation Hurst number $H^\dagger$ ($\triangleright$), $H^\star$ ($\bigcirc$) and $H^\diamond$ ($\square$) with the theoretical values H used for simulations. For comparison, the values from Ref. Rilling *et al.* (2005) are also presented, using the estimator $\hat{H}_1$ ($\bigtriangledown$), $\hat{H}_2$ ($\bigtriangleup$) and discrete wavelet transform H_W ($\diamondsuit$). The inset shows the absolute error for each estimator. The gray patch indicates when the absolute error $|H_{\text{est}} - H|$ is less than 5%.

Multifractal Process: Nonstationary Multifractal Time Series

We then validate the Hilbert-based methodology for intermittent time series by considering the synthesized nonstationary multifractal time series, and quantify the error parameter estimation. For each realization, we choose $n = 17$ levels with data length 2^{17} points each. We estimated the structure function on the range $2 < \tau < 10000$. The corresponding scaling exponents $\zeta(q)$ are then estimated on the range $10 < \tau < 1000$. For the HSA approach, the 2^{17} points are divided into several segments, each one with 2^{14} points. This averaged Hilbert marginal spectrum is taken for each realization. Power law behaviour is found on the range $0.0002 < \omega < 0.3$, corresponding to $3 < \tau < 5000$. The corresponding scaling exponents $\xi(q)$ are then estimated on this

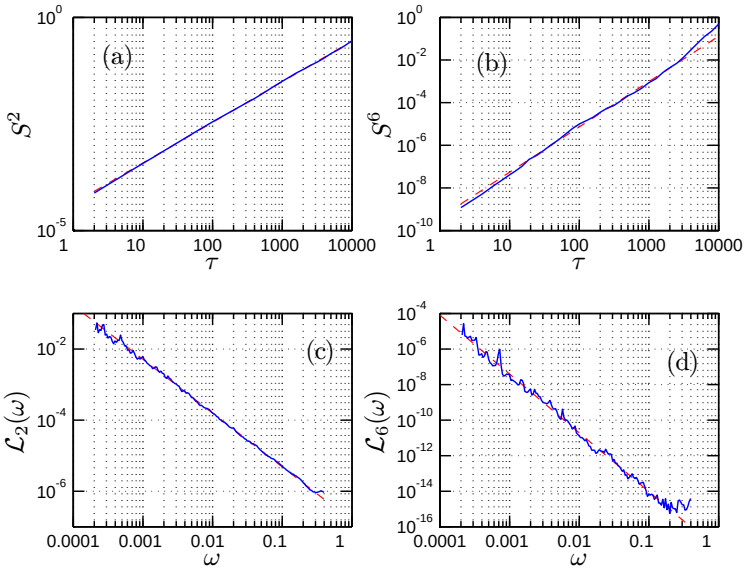

Figure 3.8: Structure function and Hilbert marginal spectra for one 2^{17} points realization (a) the second order structure function, (b) the six order structure function, (c) the second order Hilbert marginal spectrum and (d) the six order Hilbert marginal spectrum, where the dashed line in each figure is the best fit in least square sense.

range. Figure 3.8 shows the second and the sixth order structure functions and the corresponding Hilbert marginal spectra for one realization, where the dashed line is the least square fitting of the power law. For comparison convenience, we consider in the following $\xi(q) - 1$.

We then consider the convergence of the scaling exponents. For this we consider the number of realization n and for each n, for $i \in [1, n]$, we estimate separately each value ζ_i (or ξ_i). We also take

$$\overline{\zeta}(q) = \lim_{n\to\infty} \frac{1}{n} \sum_{i=1}^{n} \zeta_i(q) \tag{3.2.12}$$

Then the convergence is characterized by the ratio

$$\mathcal{R}_n(q) = \frac{1}{n} \frac{\sum_{i=1}^{n} \zeta_i(q)}{\overline{\zeta}(q)} \tag{3.2.13}$$

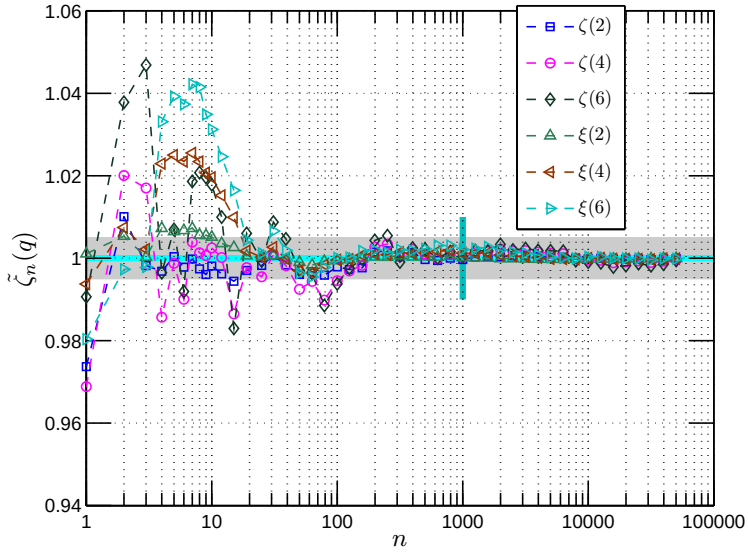

Figure 3.9: The n-dependence of the average estimator $\tilde{\zeta}_n(q)$ for various q, where n is the number of realization. The vertical solid line indicates the number $n = 1000$.

where $\lim_{n\to\infty} \mathcal{R}_n(q) = 1$. Figure 3.9 shows the convergence of this ratio for n between 1 and 70,000 for the case $\mu = 0.25$. It shows that if one wants an error of 1% in the estimation of ζ, $n = 100$ realizations are enough. In the following we consider 70,000 realizations corresponding in average to an error $100 \times |1 - \mathcal{R}_n|$ in the estimation of $\overline{\zeta}(q)$ (resp. $\overline{\xi}(q)$) of 0.02% for $q = 2$, 0.07% for $q = 4$ and 0.13% for $q = 6$ for structure functions, and 0.03% for $q = 2$, 0.04% for $q = 4$ and 0.05% for $q = 6$ for HSA. This shows that we obtain very precise estimates of $\overline{\zeta}(q)$ (resp. $\overline{\xi}(q)$).

Fig. 3.10 shows the pdf of the scaling exponents provided by structure functions and the HSA approach for $q = 2$ and 6 estimated for individual realizations, where the solid line is the Gaussian distribution fitting. These graphics show the spreading of the scaling exponents estimates. The number $n = 70,000$ of realizations considered here is rather huge compared to other multifractal studies, and represents a rather consequent numerical effort. Graphically, for small values of q, the variability in the

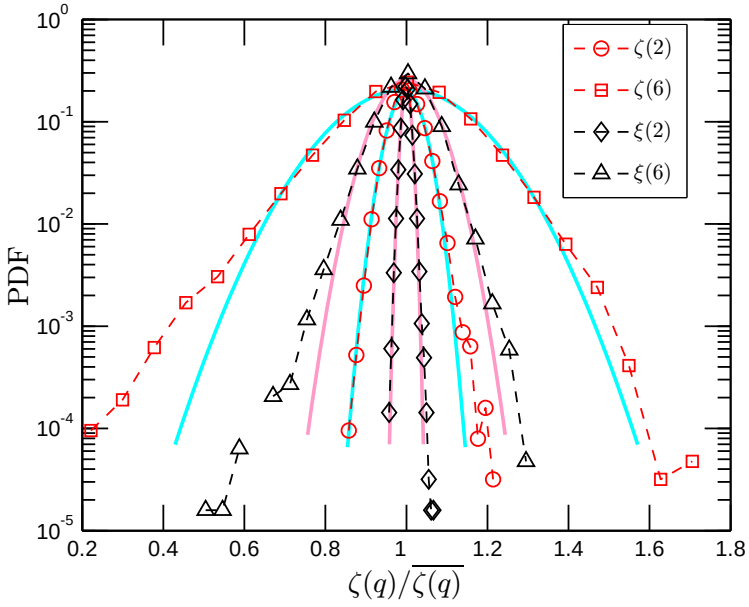

Figure 3.10: pdf of scaling exponents $\zeta(q)$ (resp. $\xi_n(q) - 1$) for 70,000 realizations with $\mu = 0.25$. The solid line is the Gaussian fitting.

estimation of scaling exponents provided by both approaches are quite close to the Gaussian distribution. We also note that the shape of the pdf corresponding to the HSA approach is narrower, which indicates that this approach provides a more precise estimator of multifractal parameters.

We show the scaling exponents predicted by the structure functions (□) and the HSA approach (○) in Fig. 3.11 for the cases $\mu = 0.25$ with $n = 70,000$, where the inset shows the departure from $q/2$. The curves provided by the two methods are in good agreement with each other.

We synthesized the multifractal time series with various intermittent parameter μ from 0.1 to 0.5, and 1000 realizations for each case (except the case $\mu = 0.25$). We estimate μ by considering the first order derivative of Eq. (3.2.10). We then have the

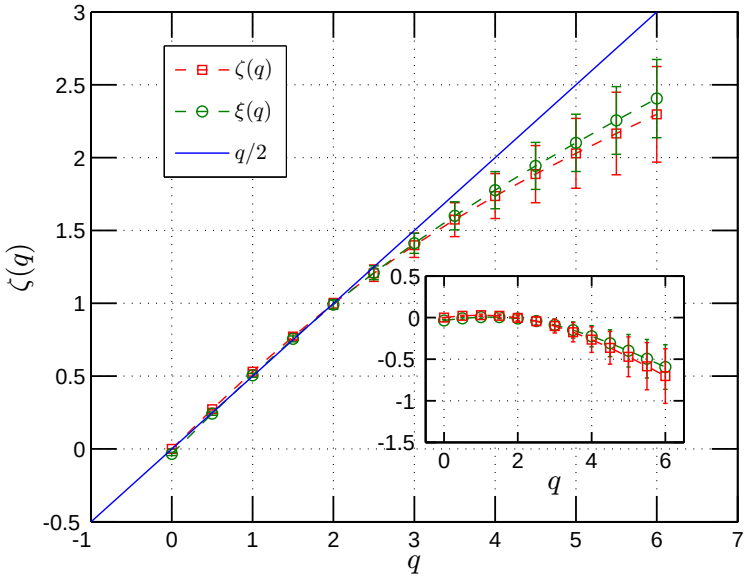

Figure 3.11: Representation of scaling exponents $\zeta(q)$ (resp. $\xi(q) - 1$) for 70000 realizations with $\mu = 0.25$.

estimator $\mu^\star$ given by

$$\mu^\star = \frac{2 - 4\zeta'(q)}{q - 1} \tag{3.2.14}$$

where $\zeta'(q)$ is the first derivative of $\zeta(q)$. The first order derivative can be estimated by the central finite difference algorithm with a second order accuracy

$$\zeta'(q) \simeq \frac{\zeta(q + \delta q) - \zeta(q - \delta q)}{2\delta q} \tag{3.2.15}$$

where δq is the increment of the order q. To estimate the first order derivative more accurately, we may firstly fit the scaling exponents $\zeta(q)$ by a quadratic polynomial, which is suggested by Eq. (3.2.10)

$$\zeta(q) \simeq p_1 q^2 + p_2 q + p_3 \tag{3.2.16}$$

where p_1, p_2 and p_3 are fitting coefficients in least square sense. We thus have

$$\zeta'(q) \simeq 2p_1 q + p_2 \tag{3.2.17}$$

We show the estimated $\mu^\star$ with $q = 2$ in Fig. 3.12, where the inset shows the relative error (in %) from the theoretical μ values. It seems that both methods slightly overestimate μ; however, the HSA provides a better estimation of μ, which may be linked to the local ability of the method both in the physical and frequency domains (Huang *et al.*, 1998, 2008). We thus have shown above the usefulness of the present new methodology to extract multifractal exponents with values consistent with structure functions.

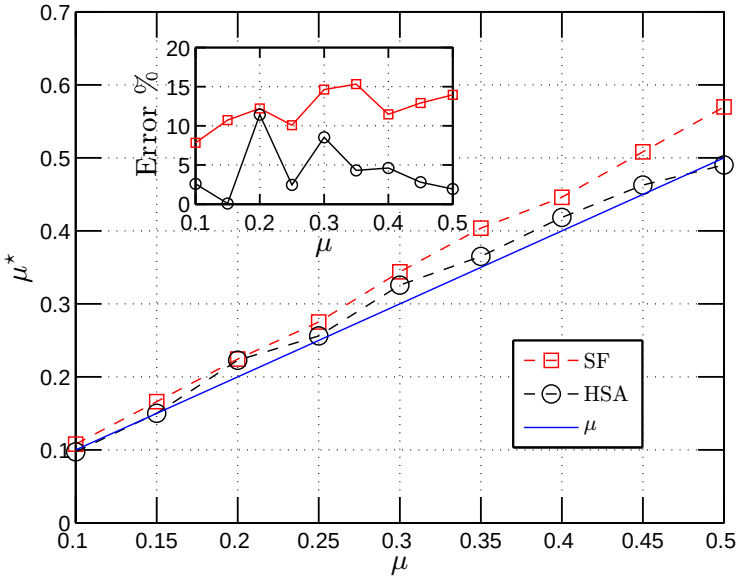

Figure 3.12: Representation $\mu^\star$, which is estimated by $\mu^\star = 2 - 4\zeta'(2)$. We first fit the corresponding scaling exponent by a quadratic polynomial. Then the first order derivative is estimated by Eq. (3.2.17).

3.3 Marginal pdf of the Instantaneous Frequency

We consider here a special case, the zeroth order Hilbert marginal spectrum, which is written as

$$\mathcal{L}_0(\omega) = \int_0^{+\infty} p(\omega, \mathcal{A})\, \mathrm{d}\mathcal{A} \tag{3.3.1}$$

a marginal integration over $\mathcal{A}$. More precisely, it is the marginal pdf of the instantaneous frequency ω. We note that the scaling exponent $\xi(0) \simeq 1$ for all H and μ, for example, see Fig. 3.6 and Fig. 3.11[2]. Figure 3.13 shows the corresponding zeroth order Hilbert marginal spectra $\mathcal{L}_{H,0}(\omega)$ for various H, where the dashed line indicates the line with slope -1. The scaling exponents are then estimated on each power law range. The mean scaling exponent is calculated as $\xi_H(0) = 0.967 \pm 0.007$. A '-1' like

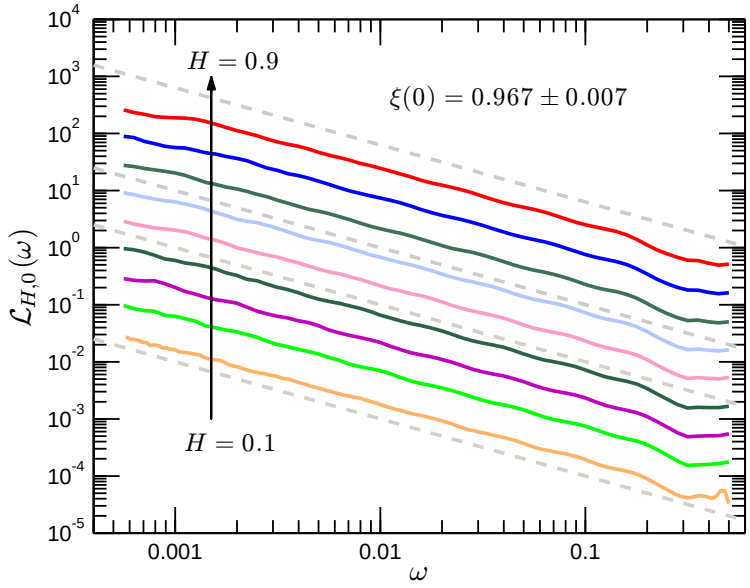

Figure 3.13: The zeroth order Hilbert marginal spectrum $\mathcal{L}_{H,0}(\omega)$ for various H. It is also the marginal pdf for the instantaneous frequency ω. The value of the scaling exponent is found as $\xi_H(0) = 0.967 \pm 0.007$. The slope of the dashed line is -1.

[2]For the other μ, the zeroth scaling exponents are also quite close to 1.

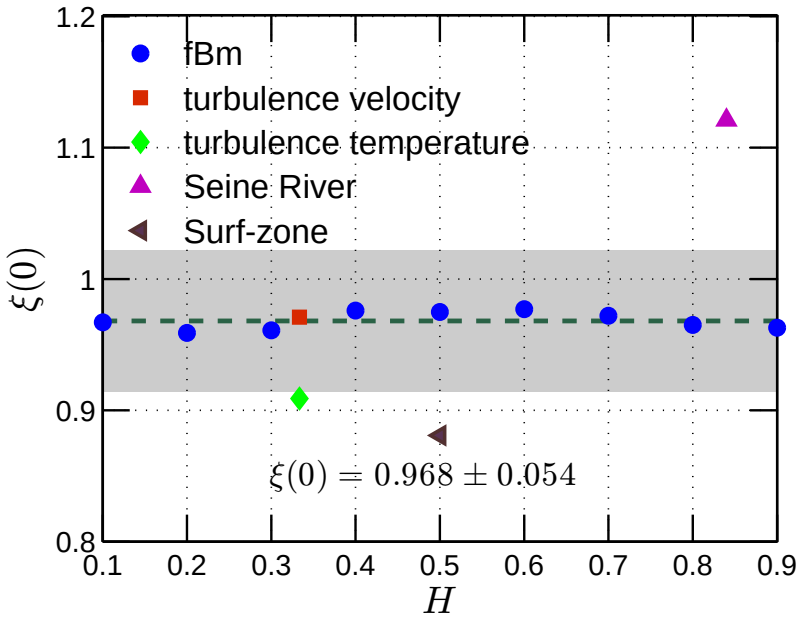

Figure 3.14: The scaling exponent $\xi(0)$ of the zeroth order Hilbert marginal spectrum $\mathcal{L}_0(\omega)$ for different types data: fractional Brownian motion (●), velocity turbulence (■), temperature turbulence (♦), the Seine river discharge (▲), and marine surf-zone (◄). The value $\xi(q)$ is found to be close to 1: 0.968 ± 0.054, which is marked as the gray patch. The dashed line indicates the mean value of $\xi(0)$.

power law for the zeroth order Hilbert marginal spectrum is also found in various experimental data, for example, turbulence velocity (Huang *et al.*, 2008) (■), turbulence temperature (♦), Seine river flow discharge (Huang *et al.*, 2009b) (▲), surf-zone fluctuation (◄), etc. Figure 3.14 represents the corresponding $\xi(0)$ for different types data. A mean scaling exponent is then estimated as

$$\langle \xi(0) \rangle = 0.968 \pm 0.054 \tag{3.3.2}$$

It seems that the zeroth order scaling exponent $\xi(0) \simeq 1$ is a quite general property of the present Hilbert-based methodology (Huang *et al.*, 2008). This brings us a question: whether this exponent $\xi(0) = 1$ for the zeroth order Hilbert marginal spectral $\mathcal{L}_0(\omega)$ is physically meaningful? If yes, what does it really mean? It should

be a subject of further studies for future work.

3.4 Summary

In this chapter we have proposed a new methodology, namely arbitrary order Hilbert spectral analysis, to characterize the scale invariance directly in amplitude-frequency space (Huang *et al.*, 2008, 2010a, 2009a). We have calibrated and validated the new method by fractional Brownian motion simulation for the monofractal case and by synthesized multifractal time series for the multifractal intermittent case. We found that the Hilbert-based methodology provides a better Hurst estimator for $0 < H < 1$. The numerical experiments, performed for $n = 70,000$ realizations each of size 2^{17} for multifractal time series, have shown that the HSA approach provides a better estimator than structure function. We have also found that the scaling exponent for the zeroth order Hilbert marginal spectrum or the marginal pdf of the instantaneous frequency is quite close to 1. It seems that it is a general property of the present method, still to be further understood.

We provide some comments on the present methodology, that we called "Arbitrary Order Hilbert Spectral Analysis". The arbitrary order Hilbert spectral analysis is an extended version of the Hilbert-Huang transform. Therefore, it inherits all the advantages and shortcomings of the HHT. The main drawback of the HHT method is its lack of solid mathematical ground, since the EMD part is almost empirical (Huang, 2005). It has been found experimentally that the method, especially for the HSA, is statistically stable with different stopping criteria (Huang *et al.*, 2003a). Furthermore, the present method measures the scale invariant properties directly in an amplitude-frequency space (Huang *et al.*, 2008, 2010a, 2009a). For the joint pdf, it seems that it

requires a large sample size to get a good statistical quantities. We find that the joint pdf itself may be scattered, but the Hilbert marginal spectrum may converge (Huang *et al.*, 2008). However, we need more theoretical/experimental work to help us to fully understand the present Hilbert-based method.

Part II

Application to Fully Developed Turbulence

Chapter 4

Homogeneous Turbulence and Intermittency: Velocity and Passive Scalar

It is well-known that turbulence is the "last great unsolved problem of the classical physics" (Feynman, 1964). Let us recall the problem of turbulence here.

Since Reynolds' very famous experiment and seminal paper of 1894 (Reynolds, 1883, 1894), turbulence has attracted many researchers interest. However, even after long time studies (Navier-Stokes equations date back to 1821), the problem of turbulence is still open. It is often believed that turbulence researches are still in their infancy (Lumley, 1992; L'vov & Procaccia, 1997; Yaglom, 2001; Lumley & Yaglom, 2001; Tsinober, 2001). Let us quote Sir Lamb's famous story here (L'vov & Procaccia, 1997). In 1932, in an address to the British Association for the Advancement of Science, he wittily expressed the difficulty of explaining and studying turbulence in fluids. He said

> " I am an old man now, and when I die and go to Heaven there are two matters on which I hope enlightenment. One is quantum electro-dynamics and the other is turbulence of fluids. About the former, I am really rather

optimistic. ”

Soon after this Kolmogorov's 1941 (K41) phenomenological theory of turbulence was one of the main successful phenomenological theories to help us quantitatively understanding the turbulence. In this chapter, we will recall the classical framework of K41 and its continuation dealing with intermittency and multifraction cascade

The Navier-Stokes equations for the velocity field u of an incompressible fluid are

$$\partial_t u + (u \cdot \bigtriangledown)u = \frac{\bigtriangledown p}{\rho} + \nu \triangle u + f, \quad \bigtriangledown \cdot u = 0 \tag{4.0.1}$$

where p is the pressure, ρ the density, f an external force and ν the kinematic viscosity. The flow is controlled by the Reynolds number

$$Re = \frac{UL}{\nu} \tag{4.0.2}$$

where U and$L$ are the characteristic velocity and length scale of the fluid. It measures the ratio between the inertial forces and the viscous forces. The number of degrees of freedom may link to the Reynolds number as $Re^{9/4}$ by a dynamical arguments (Bohr *et al.*, 1998). As a consequence, for high Reynolds number turbulent flows, it is impossible to produce a direct numerical analysis/simulation of Navier-stokes equations. Furthermore, a numerical simulation just reproduces the turbulent flow phenomena numerically. It does not reveal the underlying mechanisms. The difficulties also come from the fact that the Navier-Stokes equations are nonlinear, nonintegrable and nonlocal simultaneously (Tsinober, 2001). We still need a statistical theory to describe the turbulent flows, and more experiments to accumulate knowledge about the turbulent flows (Lumley & Yaglom, 2001; Yaglom, 2001; Tsinober, 2001). Here we consider the homogeneous and locally isotropic turbulence and focus on 1D turbulent time series.

4.1 Kolmogorov's 1941 theory

Richardson Cascade

We quote Richardson's famous words here (Richardson, 1922):

> Big whirls have little whirls
>
> that feed on their velocity
>
> and little whirls have lesser whirls
>
> and so on to viscosity in the molecule sense.

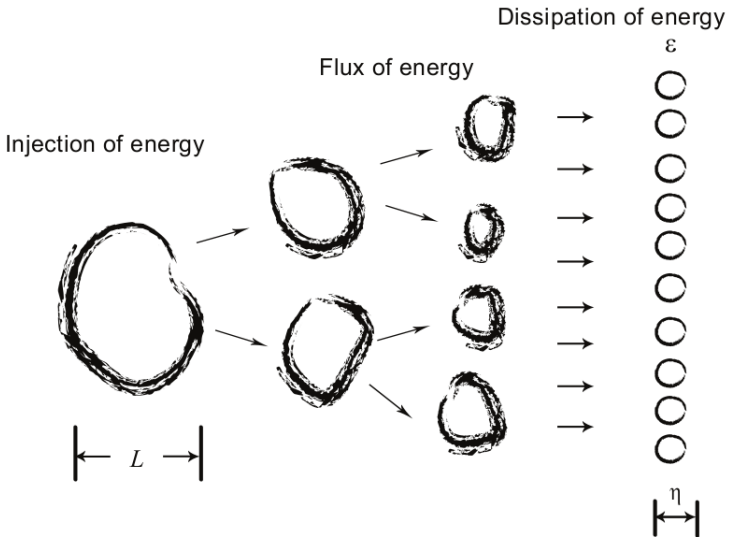

Figure 4.1: Illustration of the cascade process: the eddy is broken from integral scale L, where the energy injects into turbulent flow, to Kolmogorov scale η, where energy converts into heat.

It describes qualitatively a picture of an energy flux from large vortices to small ones. It is often believed that the energy injects into the flow from large forcing scale L, called integral scale. The energy transforms the energy from a large scale to a small scale on the inertial subrange, $\eta \ll \ell \ll L$, until one reaches the finest scale η, namely

Kolmogorov scale. Due to the fluid viscosity, the energy is then converted into heat at this finest scale. Figure 4.1 demonstrates this procedure.

Kolmogorov's 1941 Phenomenological Theory

In 1935, Sir G.I. Taylor postulated the concept of homogeneous and isotropic turbulence behind a grid, which is an ideal model of turbulence (Taylor, 1935). In the same time, he introduced the powerful Fourier analysis into turbulence research (Taylor, 1935, 1938). In 1941, Kolmogorov proposed a different version of homogeneous and locally isotropic turbulence (Kolmogorov, 1941a), in which the statistical properties of turbulent quantities of the velocity field are independent of the position and rotation of the axes. Based on the Richardson cascade, he postulated the famous two universality hypotheses (Kolmogorov, 1941a; Monin & Yaglom, 1971; Frisch, 1995):

Hypothesis 4.1.1 (Kolmogorov's First Universality Hypothesis)**.** At very high, but not infinite Reynolds numbers, all the small scale statistical properties are uniquely and universally determined by the scale ℓ, the mean energy dissipation rate ϵ and the viscosity ν.

Hypothesis 4.1.2 (Kolmogorov's Second Universality Hypothesis)**.** At very high, but not infinite Reynolds numbers, if $\eta \ll \ell \ll L$, then the statistical properties at scale ℓ are uniquely and universally determined by the scale ℓ, and the mean energy dissipation rate ϵ.

In his original paper Kolmogorov considered only the second order structure function

$$B_{dd}(r) = \langle \Delta u(r)^2 \rangle \tag{4.1.1}$$

where $\Delta u(r) = u(x+r) - u(x)$ is the velocity increment and r is the separation scale. Kolmogorov's second universality hypothesis together with dimensional consideration gives

$$B_{dd}(r) \sim c\bar{\epsilon}^{2/3} r^{2/3} \tag{4.1.2}$$

where c is the Kolmogorov constant and is believed to be universal (Kolmogorov, 1941a; Monin & Yaglom, 1971; Frisch, 1995). Independently from Kolmogorov, Obukhov (1941) used the power spectrum of the velocity field and obtained the -5/3 power law

$$E_{11}(k) = C_0 \bar{\epsilon}^{2/3} k^{-5/3} \tag{4.1.3}$$

where C_0 is the Kolmogorov constant and k is the wavenumber. These two 2/3 and -5/3 laws are mathematically equivalent and have since been verified by many experiments (Grant *et al.*, 1962; Anselmet *et al.*, 1984).

4.2 Intermittency and Kolmogorov's 1962 theory

Energy Dissipation and Intermittency

In his original postulation, Kolmogorov assumed that the energy dissipation rate of each unite ϵ is almost constant. The energy dissipation ratio ϵ is defined as

$$\epsilon = \frac{\nu}{2} \sum_{i,j} \left(\frac{\partial u_i}{x_j} + \frac{\partial u_j}{x_i} \right)^2 \tag{4.2.1}$$

where ν is the kinematic viscosity. Soon after Kolmogorov's K41 theory, Landau gave his famous remark that the energy dissipation can not be a constant[1] (Landau

[1] The Russian edition of the book on Fluid Mechanics was published in 1944. In the later versions, the footnote was moved to the main text.

& Lifshitz, 1987). Batchelor & Townsend (1949) also found by experiments that the energy dissipation is intermittent.

Kolmogorov's 1962 (K62) Theory

In order to take into account intermittency, K41 theory had to be revised. This was done in 1962 by Obukhov and Kolmogorov. Concerning intermittent of the energy dissipation, Obukhov (1962) suggested to replace the mean energy dissipation rate $\bar{\epsilon}$ by a local space averaged energy dissipation rate

$$\epsilon_\ell(x) = \frac{6}{\pi \ell^3} \int_{r' < \ell/2} \epsilon(x + r')\, \mathrm{d}r' \tag{4.2.2}$$

where ℓ is radius of the sphere. Following Obukhov (1962), Kolmogorov (1962) further proposed the hypothesis that fluctuations of the energy dissipation rate $\epsilon(x)$ satisfy a lognormal distribution or have a scaling representation. Denoting σ_ℓ^2 the variance of $\log \epsilon_\ell$, he assumed

$$\sigma_\ell^2 = A + \mu \ln(\ell_0/\ell) \tag{4.2.3}$$

where A and μ are constants (μ is often called the intermittency exponent). He then postulated two refined hypotheses[2] (Kolmogorov, 1962; Monin & Yaglom, 1971; Stolovitzky & Sreenivasan, 1994; Frisch, 1995; Sreenivasan & Antonia, 1997).

Hypothesis 4.2.1 (Kolmogorov's First Refined Hypothesis)**.** If $r \ll L$ then the conditional probability distribution function for the dimensionless relative velocities

$$V = \frac{\Delta u(\ell)}{(\ell \epsilon_\ell)^{1/3}} \tag{4.2.4}$$

depends only on the local Reynolds number $Re_\ell = \ell(\ell\epsilon_\ell)^{1/3}/\nu$.

[2] In fact, in Kolmogorov's 1962 paper, there are three hypotheses. We only consider the first two here. The third hypothesis is "Two subsets of values in the set (11) (the first hypothesis) are stochastically independent, if in the first set $|X^{(k)} - X| \geq r_1$, in the second $|X^{(k)} - X| \leq r_2$, and $r_1 \gg r_2$".

Hypothesis 4.2.2 (Kolmogorov's Second Refined Hypothesis)**.** If $Re_\ell \gg 1$ then the conditional probability distribution function indicated in the first hypothesis of V does not depend on Re_ℓ, i.e., it is universal.

Following the above two refined hypotheses, the structure function is then rewritten as

$$S^q(\ell) = \langle \Delta u_\ell(x)^q \rangle = C_q \langle \epsilon_\ell^{q/3} \rangle \ell^{q/3} \tag{4.2.5}$$

where $\Delta u_\ell(x) = u(x+\ell) - u(x)$ is the velocity increment with separation scale ℓ. Assuming the lognormal distribution of the energy dissipation ϵ, one can obtain the scaling exponent $\zeta(q)$ of the lognormal model

$$\zeta(q) = \frac{q}{3} - \frac{\mu}{18}\left(q^2 - 3q\right) \tag{4.2.6}$$

4.3 Multifractality

A few years after K62 theory, Gurvich & Zubkovskii (1963); Pond & Stewart (1965) shown that the dissipation field possesses long-range power-law correlations

$$\langle \epsilon(x)\epsilon(x+\ell) \rangle \sim \ell^{-\mu} \tag{4.3.1}$$

This was not included in the K62 proposal. It leads Yaglom (1966) to attempt to conciliate his "Master" Kolmogorov and experiment results: the lognormal distribution of the energy dissipation ϵ and the long-range correlations of the energy dissipation, by building a recursively nested cascade model, see also Schmitt (2003).

Let us consider a multiplicative discrete cascades process to simulate a multifractal measure $\epsilon(x)$. Fig. 4.2 illustrates the multiplicative discrete cascade process. The larger scale corresponds to a unique cell of size $L = \ell_0 \lambda_1^n$, where ℓ_0 is a fixed scale

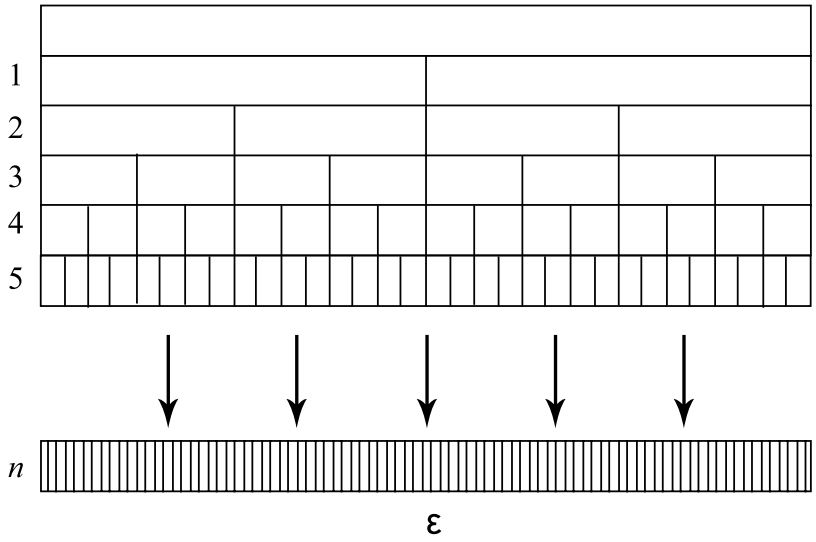

Figure 4.2: Illustration of the discrete cascade process. Each step is associated to a scale ratio of 2. After n steps, the total scale ratio is 2^n .

and $\lambda_1 > 1$ is dimensional scale ratio. For discrete models, this ratio is often taken as $\lambda_1 = 2$. The model being discrete, the next scale involved corresponds to λ_1 cells, each of size $L/\lambda_1 = \ell_0 \lambda_1^{n-1}$. This is iterated and at step p ($1 \leq p \leq n$) there are λ_1^p cells, each of size $L/\lambda_1^p = \ell_0 \lambda_1^{n-p}$. There are n cascade steps, and at step n there are λ_1^n cells, each of size ℓ_0, which is the smallest scale of the cascade. To reach this scale, all intermediate scales have been involved. Finally, at each point the multifractal measure writes as the product of n cascade random variables

$$\epsilon(x) = \prod_{p=1}^{n} W_{p,x} \tag{4.3.2}$$

where $W_{p,x}$ is the random variable corresponding to position x and level p in the cascade (Schmitt, 2003). Since each $W_{p,x}$ for different cells are assumed independent, their moment of order $q > 0$ can be estimated as

$$\langle \epsilon(x)^q \rangle = \prod_{i=0}^{n} \langle W_{p,x}^q \rangle = \langle W^q \rangle^n \tag{4.3.3}$$

This gives

$$\langle \epsilon_\lambda^q \rangle \sim \lambda^{K(q)} \tag{4.3.4}$$

where $\lambda = L/\ell = 2^n$ is the scale ratio, $K(q) = \log_2\langle W^q \rangle$. The conservative property $\langle W \rangle = 1$ gives $K(1) = 0$ and also $\langle \epsilon \rangle = 1$. One can obtain finally for the scaling exponents $\zeta(q)$

$$\zeta(q) = \frac{q}{3} - K(\frac{q}{3}) \tag{4.3.5}$$

where $K(q) = \frac{\mu}{2}(q^2 - q)$ for lognormal model.

Later, to explain Anselmet *et al.* (1984) results, Parisi & Frisch (1985) proposed a multifractal formalism. The multifractal idea have been proposed in parallel by several authors in turbulence (Parisi & Frisch, 1985; Benzi *et al.*, 1984) and chaos (Hentschel & Procaccia, 1983; Halsey *et al.*, 1986). The early Yaglom (1966) paper, together with Mandelbrot (1974) cascades, were recognized as belonging to the multifractal framework.

These papers also gave a link between fractal singularities, their dimensions, and the moment functions through a Legendre transform (Parisi & Frisch, 1985; Benzi *et al.*, 1984; Halsey *et al.*, 1986).

Now, the accepted approach for multifractal cascades using singularities can be written as (Schertzer & Lovejoy, 1987)

$$\epsilon_\ell \sim \ell^{-\gamma}, \quad p(\gamma) \sim \ell^{c(\gamma)}, \quad c(\gamma) = d - d(\gamma) \tag{4.3.6}$$

where γ is a singularity, $d(\gamma)$ its dimension, $c(\gamma)$ the codimension. Singularities and codimensions can be related to moments through a Legendre transform

$$\langle \epsilon_\ell^q \rangle \sim \ell^{-K(q)}, \quad K(q) = \max_\gamma(q\gamma - c(\gamma)) \tag{4.3.7}$$

This expresses a one-to-one relation between singularities $(\gamma, c(\gamma))$ and moments $(\zeta(q), K(q))$. This is for the cascading quantity ϵ representing the flux, becoming the dissipation ϵ at small scales. For the velocity fluctuations, the framework is the same: locally, velocity are singular, $\Delta u(\ell) \sim \ell^h$ (where h can be < 0, but is most of the time > 0) with codimension on the form

$$p(h) \sim \ell^{c(h)} \tag{4.3.8}$$

and momemts

$$\langle \Delta u(\ell)^q \rangle \sim \ell^{\zeta(q)} \tag{4.3.9}$$

where $\zeta(q) = \min\{qh + c(h)\}$. In the multifractal framework, one usually considers the scaling properties of fluctuations using the dimension or codimension, or more frequently, the moment functions $K(q)$ or $\zeta(q)$.

4.4 Intermittency models

Many statistical models have been proposed since the introduction of the multifractal formalism or even before. Let us only recall the most well known here. The debate still exists to known which one is the closest to the data for turbulent fluctuations.

- The β model: This model was introduced by Frisch *et al.* (1978) but already presented by Mandelbrot (1974) or Novikov (1969)

$$K(q) = \mu(q-1), \quad \zeta(q) = \frac{q}{3} - \mu(\frac{q}{3} - 1) \tag{4.4.1}$$

  This model is monofractal $K(q)$ or $\zeta(q)$ are liner and there is only one fractal dimension.

- The lognormal model: This model is introduced by Kolmogorov (1962) and Obukhov (1962)

$$K(q) = \frac{\mu}{2}(q^2 - q), \quad \zeta(q) = \frac{q}{3} - \frac{\mu}{18}(q^2 - 3q) \tag{4.4.2}$$

where μ is the intermittent exponent. For this model, the most famous multifractal model, the moment functions are quadratic.

- The log-Poisson model: This model was introduced by She & Lévêque (1994), Dubrulle (1994) and She & Waymire (1995)

$$K(q) = c[(1-\gamma)q - 1 + \gamma^q], \quad \zeta(q) = \frac{q}{3} - c\left[(1-\gamma)\frac{q}{3} - 1 + \gamma^{q/3}\right] \tag{4.4.3}$$

where c is the codimension and γ is linked to the maximum singularity events. She & Lévêque (1994) original proposed $c = 2$ and $\gamma = 2/3$ providing a relation without adjustable parameters

$$\zeta(q) = \frac{q}{9} + 2 - 2(2/3)^{q/3} \tag{4.4.4}$$

For this model, the nonlinear part is exponential.

- The log-stable model: This model was proposed Schertzer & Lovejoy (1987) and Kida (1991); see also Schertzer *et al.* (1997)

$$K(q) = \frac{C_1}{\alpha - 1}(q^\alpha - q), \quad \zeta(q) = \frac{q}{3} - \frac{C_1}{\alpha - 1}\left[\left(\frac{q}{3}\right)^\alpha - \frac{q}{3}\right] \tag{4.4.5}$$

where C_1 is the codimension of the mean events ($0 \leq C_1 \leq d$, where d is the dimension of the observation space), and α is the Lévy index, bounded between 0 and 2. When $\alpha = 2$ one recovers the lognormal model and when $\alpha = 0$ the β model. For $\alpha = 1$ one has a log-Cauchy model. For this model the nonlinear term is a power law.

The log-Poisson and log-stable (including lognormal) belong to the log-1D (infinitely divisible) models, whereas the log-stable is based on a stable property. Let us note that the $\zeta(q)$ is concave and has two fixed points $\zeta(0) = 0$ by its definition and $\zeta(3) = 1$ (Kolmogorov, 1941c), but there are no more result on $\zeta(q)$, and the precise analytical form depend on the model. The best model for turbulence intermittency is still a matter of debate.

4.5 Passive scalar

Another important topic in turbulence research is the passive scalar turbulence (Sreenivasan, 1991; Shraiman & Siggia, 2000; Warhaft, 2000). We recall the Kolmogorov-Obukhov-Corrsin theory here.

Governing Equation

The advection/diffusion equation for a scalar Θ reads as

$$\partial_t \Theta(x,t) + u(x,t) \cdot \bigtriangledown \Theta(x,t) = \kappa \bigtriangledown^2 \Theta(x,t) \tag{4.5.1}$$

where Θ is the scalar field (for example, temperature or dye concentration), $u(x,t)$ is the velocity field, and κ is molecular diffusivity. We consider here only the case of passive scalar, in which it has a negligible back effect on the flow (Shraiman & Siggia, 2000; Warhaft, 2000).

Kolmogorov-Obukhov-Corrsin Theory

Following Kolmogorov's argument (Kolmogorov, 1941a), Obukhov (1949); Corrsin (1951) extended the K41 theory for passive scalar. It is well-known now as Kolmogorov-Obukhov-Corrsin (KOC) theory. The KOC theory prediction of 1D spectrum of scalar is

$$F_\theta(k) = C_\theta \langle \epsilon \rangle^{-1/3} \langle \epsilon_\theta \rangle k^{-5/3} \tag{4.5.2}$$

where ϵ is the energy dissipation rate, and

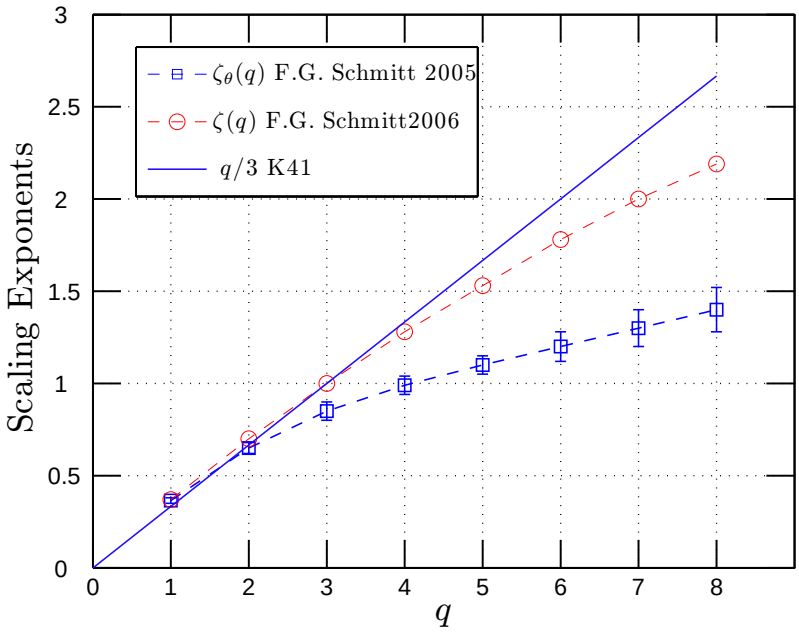

Figure 4.3: Comparison of the scaling exponents $\zeta(q)$ and $\zeta_\theta(q)$. It is notable that $\zeta(q) > \zeta_\theta(q)$ for $q > 2$. The data are compiled by Schmitt (2005) and Schmitt (2006).

$$\epsilon_\theta = 2\kappa(\partial\Theta/\partial x_i)(\partial\Theta/\partial x_i) \tag{4.5.3}$$

is the scalar dissipation rate. It also implies for the structure functions

$$S_\theta^q(r) = \langle \Delta\Theta(r)^q \rangle \sim \langle \epsilon^{-1/6} \epsilon_\theta^{1/3} \rangle^q r^{q/3} \sim r^{\zeta_\theta(q)} \tag{4.5.4}$$

where $\Delta\Theta(r) = \Theta(x+r) - \Theta(x)$ is the scalar increment with scale separation r, and $\zeta_\theta(q)$ is the corresponding scaling exponent. Let us note that we have the only fixed point $\zeta_\theta(0) = 0$ but we do not have $\zeta_\theta(3) = 1$ as in velocity because of the nonlinear mixing of the two fluxes (or dissipations) ϵ and ϵ_θ. We should note that structure functions for velocity and passive scalar are quite stable experimentally and seem to such $\zeta(q) > \zeta_\theta(q)$ for $q > 2$, see Fig. 4.3.

Intermittency and Ramp-cliff Structures

For a time, people thought that the passive scalar field is just a complementary of the velocity field (Shraiman & Siggia, 2000; Warhaft, 2000). Thus the statistical properties of the passive scalar field should be determined by the velocity field. However, experimental and numerical experiments indicate a more intermittent field than the velocity field (Celani *et al.*, 2000; Shraiman & Siggia, 2000; Warhaft, 2000; Moisy *et al.*, 2001; Gylfason & Warhaft, 2004). It is usually believed that the so-called ramp-cliff structures play an important role in the passive scalar field. Ramp-cliffs are large scale structures with sharp frontiers. Thus there is a coupling with the small scales by this frontier (Shraiman & Siggia, 2000; Warhaft, 2000), see more discussion in chapter 5 and chapter 7.

4.6 Summary

In this chapter, we recalled the classical Kolmogorov's 1941 and 1962 phenomenological theories of turbulence. Historically, Kolmogorov 1941 theory is the first successful phenomenological theories about the turbulence, and provides a quantitative description of the turbulent phenomena. In his theory, the structure functions play an

important role to characterize the scale invariant properties of intermittency in the physical domain. We will emphasize on the structure functions analysis in chapter 5.

Chapter 5

Structure Functions and Autocorrelation Functions of Increments

Since Kolmogorov's 1941 milestone work, the structure function analysis is widely used to extract scaling exponents in turbulent research (Monin & Yaglom, 1971; Anselmet *et al.*, 1984; Frisch, 1995). In his original proposal, Kolmogorov considered a tensor $\Delta V_{\alpha\beta}$ in space, whereas we consider here a 1D process: we do not consider the tensor and analyze time series. For this, we implicitly involve Taylor's hypothesis to consider scaling 1/3 properties of turbulent time series (Taylor, 1938; Frisch, 1995).

The structure function itself is seldom investigated (Nichols Pagel *et al.*, 2008; Podesta *et al.*, 2009). In this chapter, based on statistical stationary assumption, we present an analytical analysis of the structure function to characterize the scale contribution and the influence of a single scale (Huang *et al.*, 2010a, 2009a, 2010b). The results presented in this chapter are for most of them are published in Huang *et al.* (2009a, 2010a,b). [Y. Huang, *et al. Traitement du Signal*, 25, 481-492, 2008 ; Y. Huang, *et al. Phys. Rev. E*, 2010 (submitted); Y. Huang, *et al. Phys. Rev. E*, 2010 (submitted).]

5.1 Second order structure function

We investigate here the second order structure function of velocity increments in fully developed turbulence. For this, we use some properties of the Fourier transform. We will obtain results about the scale contribution and an influence of single scale to the second order structure function.

Statistical Stationary Assumption

Considering the statistical stationarity assumption (Monin & Yaglom, 1971; Frisch, 1995), the velocity $u(t)$ may represent in Fourier space as

$$\hat{U}(f) = \mathcal{F}(u(t)) = \int_{-\infty}^{+\infty} u(t) e^{-i2\pi ft}\,\mathrm{d}t \tag{5.1.1}$$

where $\mathcal{F}$ means Fourier transform. Then the velocity $u(t)$ may be reconstructed by

$$u(t) = \mathcal{F}^{-1}(\hat{U}_t(f)) = \int_{-\infty}^{+\infty} \hat{U}(f) e^{i2\pi ft}\,\mathrm{d}f \tag{5.1.2}$$

and $u(t+\ell)$ as

$$u(t+\ell) = \mathcal{F}^{-1}(\hat{U}_{t+\ell}(f)) = \int_{-\infty}^{+\infty} \hat{U}(f) e^{i2\pi f(t+\ell)}\,\mathrm{d}f \tag{5.1.3}$$

where $\mathcal{F}^{-1}$ means inverse Fourier transform, and ℓ is a separation time scale. Therefore the velocity increment $\Delta u_\ell(t) = u(t+\ell) - u(t)$ in structure functions may be represent as

$$\Delta u_\ell(t) = \int_{-\infty}^{\infty} \hat{U}(f)(e^{i2\pi f(t+\ell)} - e^{i2\pi ft})\,\mathrm{d}f \tag{5.1.4}$$

This means that $\hat{U}(f)(e^{i2\pi f\ell} - 1)$ is the inverse Fourier transform of $\Delta u_\ell(t)$. The Fourier transform of the velocity increment is thus written as

$$S_\ell(f) = \mathcal{F}(\Delta u_\ell(t)) = \hat{U}(f)(e^{i2\pi f\ell} - 1) \tag{5.1.5}$$

The corresponding Fourier power spectrum is expressed as

$$E_\Delta(f) = |S_\ell(f)|^2 = E_v(f)(1 - \cos(2\pi f \ell)) \tag{5.1.6}$$

where $E_v(f) = 2|\hat{U}(f)|^2$ is the Fourier power spectrum of original velocity (Frisch, 1995; Hou *et al.*, 1998; Huang *et al.*, 2009c, 2010b). When $f_\Delta = n/\ell$, where $n = 0, 1, 2\cdots$, we have

$$1 - \cos(2\pi f_\Delta \ell) \equiv 0 \tag{5.1.7}$$

showing that the contributions of frequency sequences f_Δ are cancelled. In other

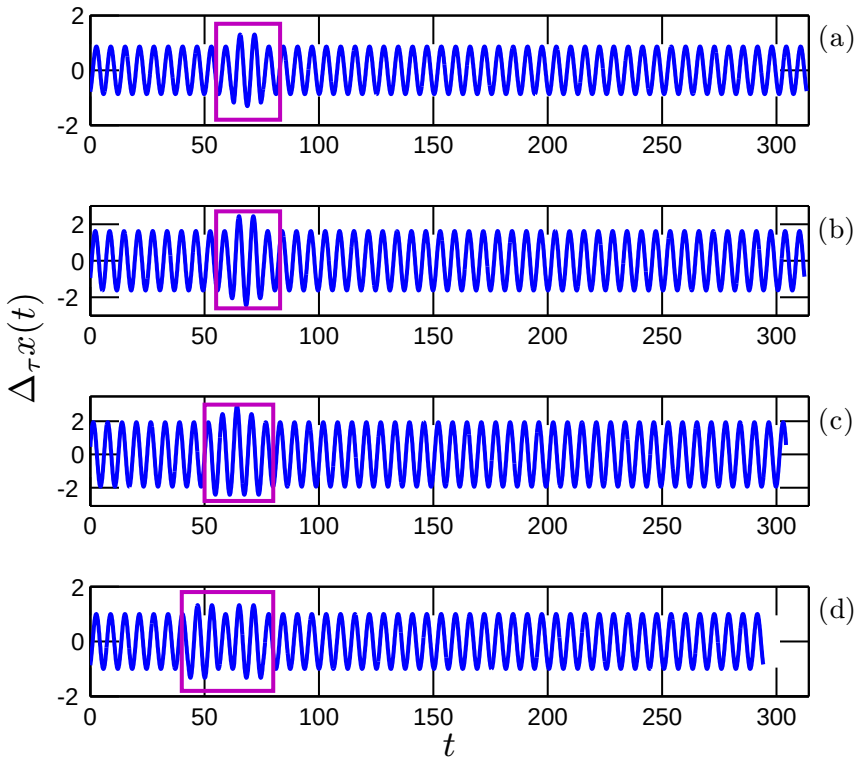

Figure 5.1: Illustration of the nonstationary effect on velocity increments: the velocity increment $\Delta x(\tau) = x(t) - x(t+\tau)$ with different time delay, (a) $\tau = 1$, (b) $\tau = 2$, (c) $\tau = 10$, and (d) $\tau = 20$ points, respectively. The nonstationary effect is marked as a rectangle. Here $x(t)$ is taken from Eq. (5.1.8).

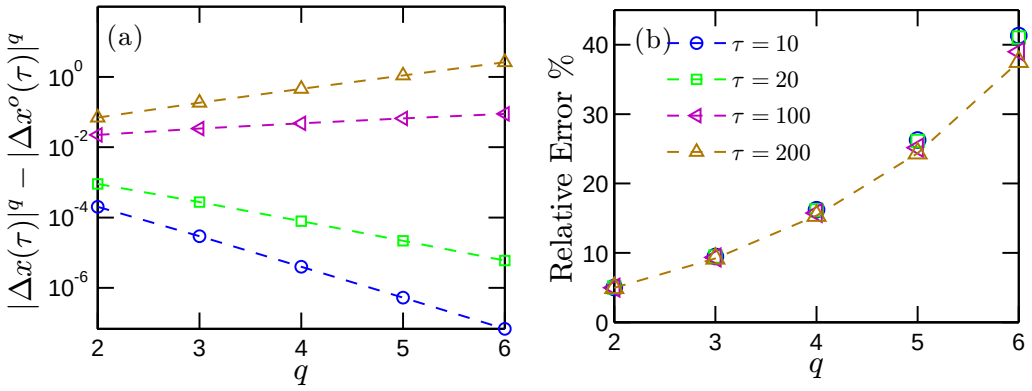

Figure 5.2: Estimation of the statistical moments for $q = 2$, 3, 4, 5 and 6: (a) the absolute error $|\Delta x(\tau)|^q - |\Delta x^o(\tau)|^q$, (b) the relative error $(|\Delta x(\tau)|^q - |\Delta x^o(\tau)|^q)/|\Delta x^o(\tau)|^q$, respectively. The time delay τ is taken as 10 ($\circ$), 20 ($\square$), 100 ($\triangleleft$) and 200 ($\triangle$) points.

words, the difference operator acts as a kind of filter operator, where the corresponding frequencies f_Δ are filtered. This means that the structure function analysis provides a statistical information without taking into account the corresponding scales $1/f_\Delta$. The scale invariance properties are indirectly measured. Furthermore, the structure function analysis is a global operator in physical space, since the difference operator is manipulated on the same data for each separation scale (Huang *et al.*, 2010a,b).

We illustrate the nonstationary effect on structure functions by constructing a signal $x(t)$ with a nonstationary perturbation as following

$$x(t) = \begin{cases} \sin(t) & 0 \leq t < 20\,\pi \\ 1.5\sin(t) & 20\,\pi \leq t \leq 24\,\pi \\ \sin(t) & 24\,\pi < t < 100\,\pi \end{cases} \tag{5.1.8}$$

where the sampling frequency is set as 10 Hz. Figure 5.1 shows the increments for various time delay (a) $\tau = 1$ point, (b) $\tau = 2$ points, (c) $\tau = 10$ points, and (d) $\tau = 20$ points, where the nonstationary effect is marked by the rectangle. Graphically, the nonstationary event does have influence on all scales, since the increment operator is

manipulated on the same data for each time delay. We then compare the statistical moments with non-perturbation case

$$x^o(t) = \sin(t)\,, \quad 0 \leq t \leq 100\,\pi \tag{5.1.9}$$

Figure 5.2 shows (a) the absolute error $\langle|\Delta x(\tau)|^q\rangle - \langle|\Delta x^o(\tau)|^q\rangle$, (b) the relative error $\langle|\Delta x(\tau)|^q\rangle/\langle|\Delta x^o(\tau)|^q\rangle - 1$ for various time lag τ. The influence increases with the order q. The relative error shows the same evolution trend with q. This shows experimentally that the difference operator is still a global operator in the physical domain.

Cumulative function

The mean kinetic energy (one-half of the variance of the random function) is the integral of the energy spectrum over all frequencies

$$\frac{1}{2}\langle u^2\rangle = \int_0^{+\infty} E_v(f)\,\mathrm{d}f \tag{5.1.10}$$

where $E_v(f)$ is the Fourier power spectrum of the velocity u (Frisch, 1995). Assuming statistical stationarity, the second order is thus rewritten as

$$\langle \Delta u_\ell(t)^2\rangle = 2\langle u^2\rangle - 2\langle u(t)u(t+\ell)\rangle = 2\langle u^2\rangle - 2\Gamma(\ell) \tag{5.1.11}$$

where $\Gamma(\ell)$ is the autocorrelation function of the velocity u. The Wiener-Khinchin theorem shows that (Percival & Walden, 1993; Frisch, 1995),

$$\Gamma(\ell) = \int_{-\infty}^{+\infty} E_v(f) e^{2i\pi f\ell}\,\mathrm{d}f \tag{5.1.12}$$

Here, $E(f)$ is extended to negative frequencies by $E(-f) = E(f)$. Thus the the second order structure function is finally rewritten as (Monin & Yaglom, 1971; Frisch,

1995)

$$\langle \Delta u_\ell(t)^2 \rangle = 4 \int_0^{+\infty} E_v(f)(1 - e^{i2\pi f\ell})\,\mathrm{d}f \tag{5.1.13}$$

Let us introduce here a cumulative function for the second order structure function

$$\mathcal{P}(f,\ell) = \frac{\int_0^f E_\Delta(f')\,\mathrm{d}f'}{\int_0^{+\infty} E_\Delta(f')\,\mathrm{d}f'} \tag{5.1.14}$$

where $E_\Delta(f) = E_v(f)(1-\cos(2\pi f\ell))$. It is increasing 0 and 1, and measures the relative contribution to the second order structure function from 0 to f. When $f = 1/\ell$, the cumulative function $\mathcal{P}_1(f) = \mathcal{P}(1/\ell, \ell)$ thus characterizes the contribution from the large scale part for frequencies larger than the one associated to the increment time scale ℓ. We further assume a pure power law for the original velocity Fourier power spectrum

$$E_v(f) = cf^{-\beta},\ c > 0 \tag{5.1.15}$$

where the value of β will be specified later. When substituted into Eq. (5.1.13), this gives an integral which is divergent for some values of β. The convergence condition requires $1 < \beta < 3$ (Frisch, 1995; Hou *et al.*, 1998; Huang *et al.*, 2010b). A scaling calculation (Frisch, 1995; Huang *et al.*, 2010b) leads to

$$\langle \Delta u_\ell(t)^2 \rangle \sim \ell^{\beta-1} \tag{5.1.16}$$

For fully developed turbulence, the Kolmogorov spectrum corresponds to $\beta = 5/3$.

Experimental Results

We apply here the above arguments to an homogeneous and nearly isotropic turbulent flow[1] at downstream $x/M = 20$, where M is the mesh size. The flow is characterized

[1] We will present more analysis results using these data in chapter 6 and chapter 8.

by the Taylor microscale based Reynolds number $Re_\lambda = 720$ (Kang *et al.*, 2003). Details about the experiment can be found in chapter 6. Let us note here $T_s = 1/f_s$ the time resolution of these measurements, where $f_s = 40000\,\mathrm{Hz}$ is the sampling frequency. Figure 5.3 shows the compensated spectra $E(f)f^\beta$ for both longitudinal (thick line, $\beta \simeq 1.63$) and transverse (thin line, $\beta \simeq 1.62$) velocity components, showing a more than two decades inertial range. The Fourier spectra are taken from Ref. Kang *et al.* (2003), which are estimated by a window Fourier transform, see Kang *et al.* (2003) for more information. The scaling exponent β is estimated from each spectrum by a least square fitting algorithm.

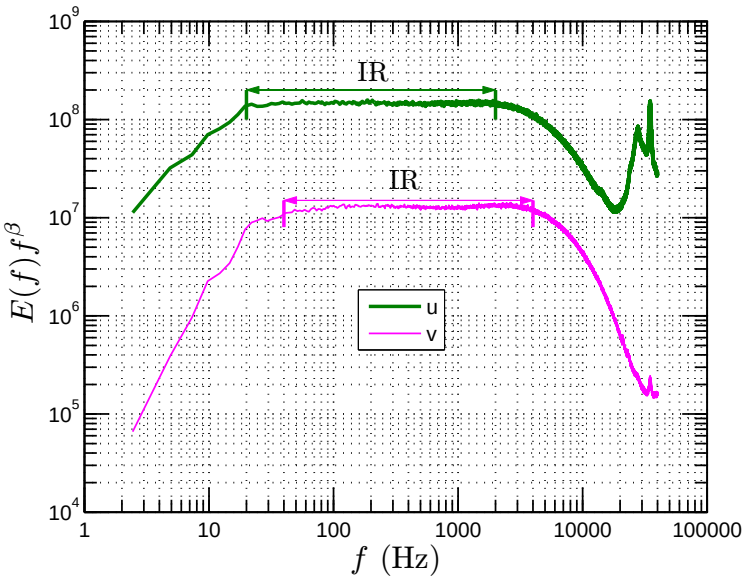

Figure 5.3: Compensated spectrum $E(f)f^\beta$ of longitudinal ($\beta \simeq 1.63$) and transverse ($\beta \simeq 1.62$) velocity at $x/M = 20$, where β is the corresponding power law estimated from the power spectrum. The plateau is observed on the range $20 < f < 2000$ Hz and $40 < f < 4000$ Hz for longitudinal and transverse velocity, respectively.

To avoid the effect of measurement noise, see Fig. 5.3, we only consider the transverse velocity here. Figure 5.4 shows the cumulative function $\mathcal{P}$ estimated from the

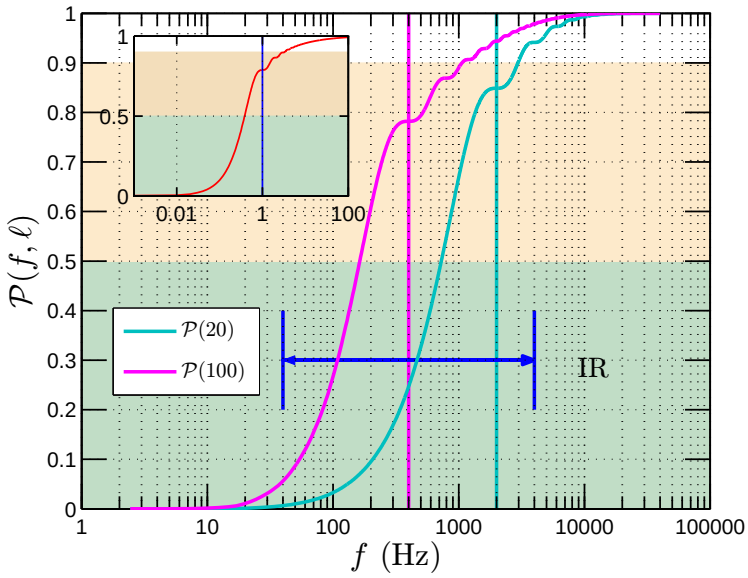

Figure 5.4: Cumulative function $\mathcal{P}(f,\ell)$ estimated from turbulent experimental data for transverse velocity with ℓ in the inertial range, where the numerical solution is shown as inset with $\ell = 1$. The inertial range is denoted as IR. Vertical solid lines demonstrate the corresponding scale in spectral space.

f	0.01	0.04	0.1	0.2	0.5	1	10	100
$\mathcal{P}$ (%)	0.5	3.0	10.0	24.1	62.9	78.8	95	99

Table 5.1: A numerical solution of cumulative function $\mathcal{P}(f,\ell)$ with $\beta = 5/3$ and $\ell = 1$, which corresponds to the Kolmogorov scaling.

transverse velocity data, in which the spectrum $E_v(f)$ is directly estimated from the data. The inertial range is marked as IR. We choose two time scales $\ell/T_s = 20$ and $\ell/T_s = 100$ in the inertial range. The large scale contribution range is more than 1.4 decades wide. A numerical solution of Eq. (5.1.14) for a pure power law by taking $E_v(f) = f^{-5/3}$ is performed on range $10^{-4} < f < 10^4$ with $\ell = 1$ and the step $\Delta f = 10^{-6}$ by using a fourth order accurate Simpson rule. The numerical solution is shown as inset in Fig. 5.4, where the vertical solid line indicates the location of

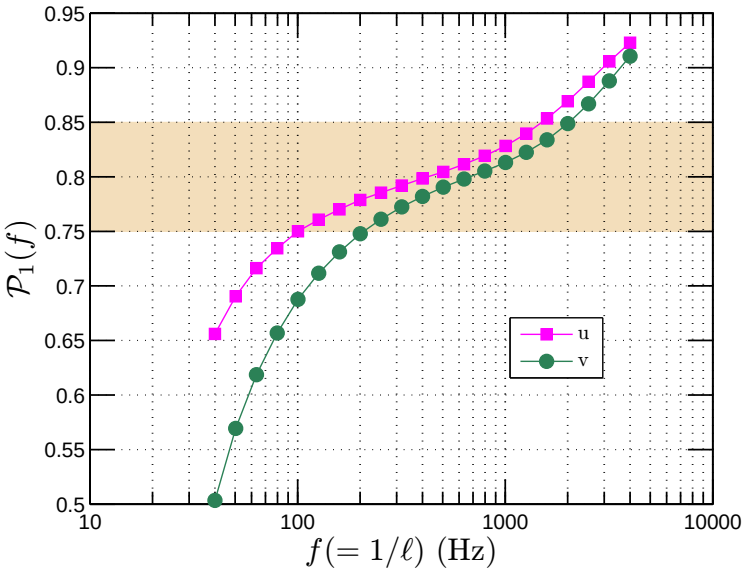

Figure 5.5: Cumulative function $\mathcal{P}_1(f)$ estimated from turbulent experimental data for both longitudinal and transverse velocity with various ℓ.

1. The shape of the numerical solution is the same as the experimental one. We list various value of $\mathcal{P}$ in Tab. 5.1. Not surprisingly, the large scale contribution $\mathcal{P}_1(1)$ is about 79%, which is consistent with experimental result, see Fig. 5.5. One can find that the contribution from the first decade large scale, $0.1 < f < 1$, is about 69%. Even for the second decade part, $0.01 < f < 0.1$, the contribution is about 9.5%. These results show the important contribution of the large scales to the second order structure function statistic. Figure 5.5 shows the corresponding $\mathcal{P}_1(f)$ directly estimated from turbulent experimental data for longitudinal (■) and transverse (●) velocity on range $40 < f(= 1/\ell) < 4000\,\mathrm{Hz}$, where the spectrum $E_v(f)$ is taken the Fourier power spectrum of each velocity component. Both curves have a similar evolution trend, which may be termed into three terms: i) near forcing scale range, in which the large scale contribution is less than 0.75, ii) unaffected inertial range, in which the large scale contribution is on range $0.75 < \mathcal{P}_1(f) < 0.85$, close to the value

0.79 indicated by the numerical solution, and iii) near dissipation range, in which the large scale contribution is larger than 0.85. Taking the transverse velocity as example, the unaffected range is found around 1 decade, on range $200 < f < 2000\,\mathrm{Hz}$. It is good agreement with the observation in Fig. 5.18, see next section. In the first and the third terms of the cumulative function $\mathcal{P}_1(f)$, the large scale contribution significantly deviates from the pure power law value 0.79. This indicates that these two range are strongly influenced by either the large forcing scales or dissipation scales. Furthermore, we note that the deviation may come from the following reasons: (i) the finite power law range (Hou *et al.*, 1998), (ii) the spectrum of the original velocity is not a pure power law (Nelkin, 1994; Frisch, 1995) and (iii) the violation of the statistical stationary assumption. In any case, the above results indicate that structure functions are strongly influenced by the large scales.

Influence by a Single Scale: Deterministic Forcing

We then consider the influence of a single scale both on the structure function and the arbitrary order Hilbert spectral analysis.

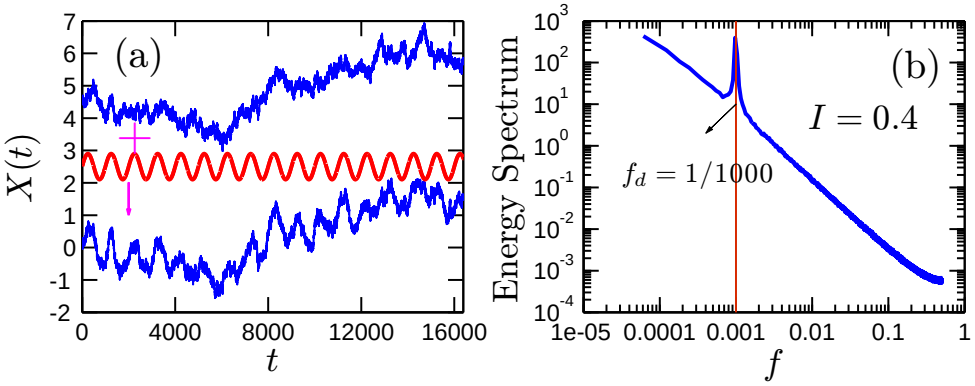

Figure 5.6: (a) A portion of fBm data with (bottom) and without (top) a sine wave perturbation (middle), and (b) the corresponding Fourier power spectrum.

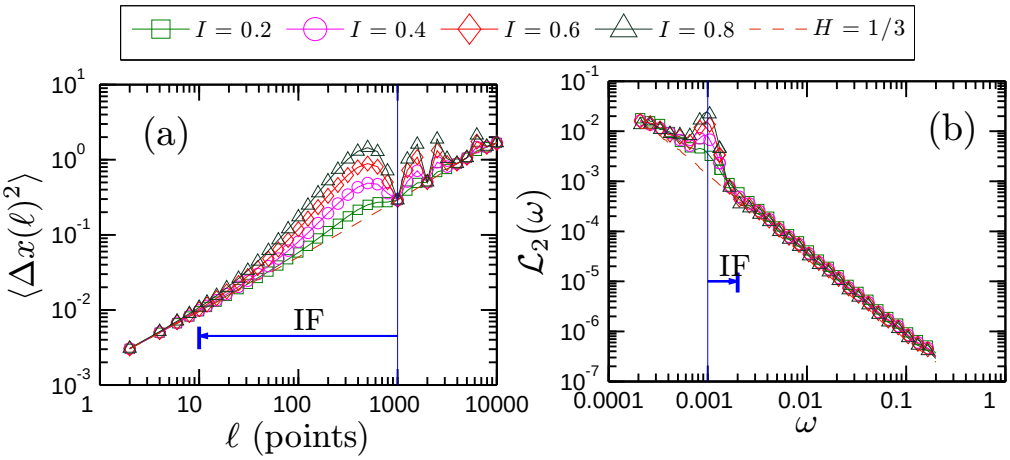

Figure 5.7: Influence of a single scale on (a) the second order structure function, and (b) the second order Hilbert marginal spectrum with various intensities I. The vertical solid line indicates location of disturbance.

We simulate a fBm time series $X(t)$ with Hurst number $H = 1/3$, corresponding to the Hurst value of turbulent velocity. We first normalize the time series by its variance and then add on these data a pure sine wave with a disturbance frequency $f_0 = 0.001$ and various intensities I. This is written as

$$X(t) = X(t)/\sigma + I\sin(2\pi f_0 t) \tag{5.1.17}$$

where σ is the variance of $X(t)$. We show a 2^{14} points portion of the simulated fBm data in Fig. 5.6 (a) fBm data with (bottom) and without (top) a sine wave perturbation (middle) with intensity $I = 0.4$, and (b) its corresponding Fourier power spectrum. We then apply the structure function analysis and the arbitrary order Hilbert spectral analysis on these data with various intensities I. For the former approach, we consider time lags on the range $0 < \tau < 10000$ points. For the original fBm data, a power law behaviour is found on the range $5 < \tau < 10000$ points. The latter methodology is performed on each realization and the ensemble averaged spectrum is taken as final spectrum. For the original fBm data, we find that a power

law behaviour holds on the range $0.0002 < \omega < 0.2$, corresponding to $5 < \tau < 5000$ points. Figure 5.7 shows (a) the second order structure function, and (b) the second order Hilbert marginal spectrum, where the solid vertical line indicates the location of the disturbance frequency f_0. The second order structure function is strongly influenced by the single scale. An influence range down to the small scale is found to be as large as 2 decades, which is marked by IF in Fig. 5.7. However, for the Hilbert-based method, the influence range down to the small scale is constrained to 0.3 decades, which might be link to the fact that the EMD acts a dyadic filter bank for several types of time series (Wu & Huang, 2004; Flandrin *et al.*, 2004; Flandrin & Gonçalvès, 2004; Huang *et al.*, 2008).

We may also consider here the single scale as a periodic component (Huang *et al.*, 2010a). A quite general common property of multifractal time series (turbulent-like stochastic dynamics) in the nature and geophysical sciences is superposed to a deterministic forcing associated to astronomical events (tide, daily cycle, annual cycle, etc). This may pose a problem for the estimation of scaling exponents. This is the case, for example, for river flow time series (Tessier *et al.*, 1996; Kantelhardt *et al.*, 2003; Huang *et al.*, 2009b), oceanic monitoring time series (Dur *et al.*, 2007; Schmitt *et al.*, 2008), etc, also see chapter 9. As already noticed by several authors, the structure function may fail when a periodic component is present in the data (Kantelhardt *et al.*, 2003, 2006). Thus, we show here numerically that this influence on the structure function. We also show that the Hilbert-based methodology can constrain this effect in an amplitude-frequency space (Huang *et al.*, 2010a).

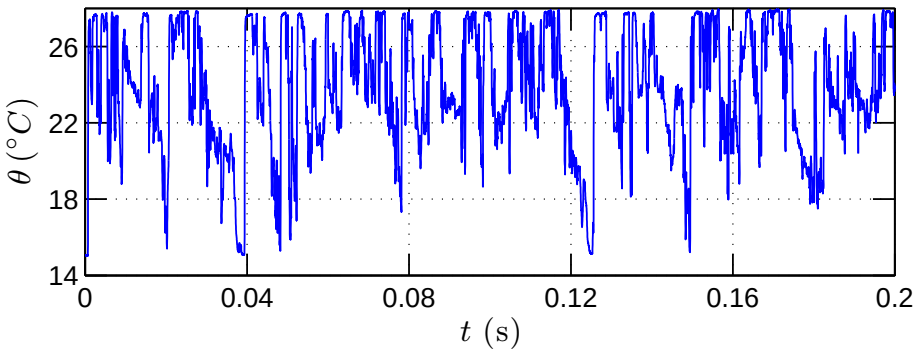

Figure 5.8: One 0.2s portion of the temperature time series, showing strong ramp-cliff structure.

Passive Scalar: An Example of Ramp-Cliff Structures

The above arguments and results indicate that the structure function may not considered a proper tool for scaling exponent extraction when the data possess energetic large scales. This is the case of ramp-cliff structure in scalar turbulence (Sreenivasan, 1991; Shraiman & Siggia, 2000; Warhaft, 2000; Celani *et al.*, 2000): the structure induced by shear effect (Staicu & van de Water, 2003; Xia *et al.*, 2008). To show this experimentally, we consider a temperature time series with strong ramp-cliff structure. The data is obtained in a shear layer of the mixing between a jet flow and a cross flow, provided by Prof. Y. Gagne. The bulk Reynolds number is about $Re = 60000$. The initial temperature of the two flows are $T_J = 27.8°C$ and $T = 14.8°C$. The measurement location is close to the nozzle of the jet. For more detail about this experiment, see chapter 7. Figure 5.8 shows a 0.2s portion temperature data, showing strong ramp-cliff structures. Figure. 5.9 shows the compensated spectra directly estimated by the Fourier analysis (solid line), the second order structure function (□), the Hilbert spectral analysis (○) and the autocorrelation function

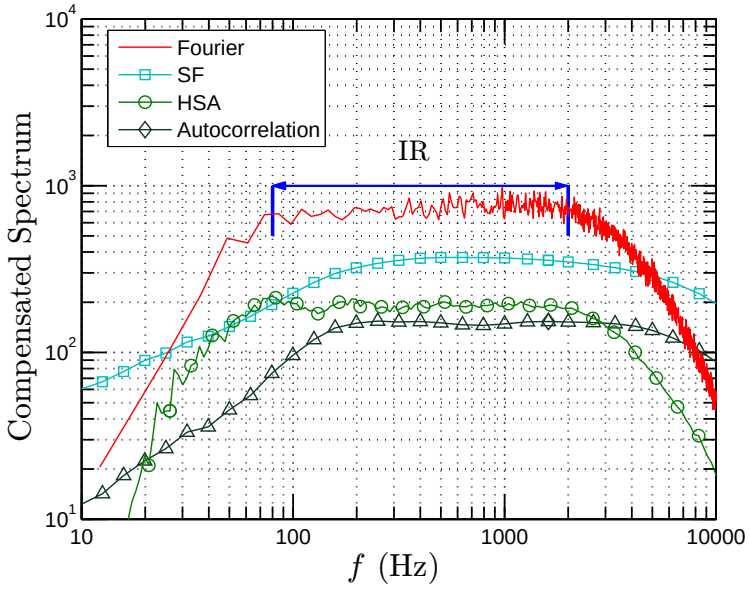

Figure 5.9: Compensated spectrum of transverse velocity. Plateau is observed on range $80 < f < 2000$ Hz for both Fourier spectrum (solid line) and Hilbert spectrum (□). For comparison, the compensated spectra estimated from the second order structure function (○) and the autocorrelation function (♢) are also shown.

(♢) (see Eq. (5.2.10) in next section). Both the structure function and the autocorrelation function are converted from from physical domain to spectral domain by taking $f = 1/\ell$. Except for the structure function, the others show a clear plateau, on the range $100 < f < 2000$ Hz. For the structure function, an ambiguous plateau is found on the range $300 < f < 2000$ Hz; for higher order structure function, we even cannot find an ambiguous inertial range, see chapter 7. However, the Hilbert spectral analysis shows a clear inertial range even for q up to 8. We reproduce the scaling exponent estimated by the Hilbert methodology (○) in Fig. 5.10. It seems that the scaling exponent $\xi(q) - 1$ is quite close to the scaling exponent $\zeta(q)$ for the velocity by using the extended self-similarity approach (dash line) (Arneodo *et al.*, 1996). The scaling exponent provided directly by the structure function (♢) seems to saturate

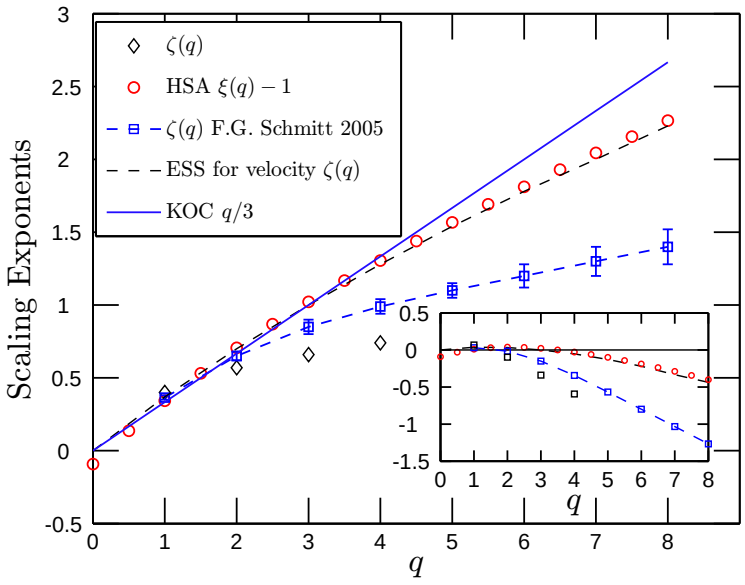

Figure 5.10: Representation of the scaling exponents, which is estimated by HSA (○), and structure function (◇). For comparison, the scaling exponent from Ref. Schmitt (2005) (□) for passive scalar and from Ref. Arneodo *et al.* (1996) for the velocity (dashed-line) are also shown.

when $q > 3$.

The comparison between scaling exponents for temperature and velocity shows that for $q > 2$

$$\zeta_\theta(q) < \zeta_v(q) \tag{5.1.18}$$

this is interpreted as an evidence that the scalar turbulence is more intermittent than the velocity field (Frisch, 1995; Warhaft, 2000). The experimental results shown here indicate that the effect of ramp-cliff structures for passive turbulence may be given more attention. The passive turbulent field may be less intermittent than what we believed before. We will present more detail and discussion in chapter 7.

5.2 Autocorrelation function of velocity increments

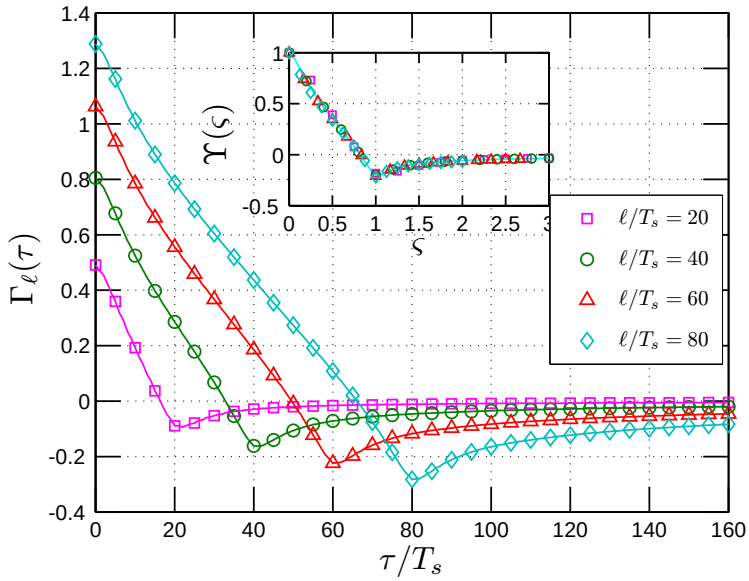

Figure 5.11: Autocorrelation function $\Gamma_\ell(\tau)$ of the velocity increment $\Delta u(\ell)$ estimated from an experimental homogeneous and nearly isotropy turbulence time series with various increments ℓ. The location of the minimum value is very close to the separation time ℓ. The inset shows the rescaled autocorrelation function $\Upsilon(\varsigma)$.

We consider in this section the autocorrelation of velocity increments (without absolute value), inspired by a remark found in Anselmet *et al.* (1984). In this reference, it is found that the location of the minimum value of the autocorrelation function $\Gamma(\tau)$ of velocity increment $\Delta u_\ell(t)$ of fully developed turbulence with time separation ℓ is approximately equal to ℓ. The autocorrelation function of the increment $V_\ell(t) = \Delta u_\ell(t)$ time series is defined as

$$\Gamma_\ell(\tau) = \langle (V_\ell(t+\tau) - \overline{\mu})(V_\ell(t) - \overline{\mu}) \rangle \tag{5.2.1}$$

where $\overline{\mu}$ is the mean value of $V_\ell(t)$, and $\tau \geq 0$ is the time lag.

We show the autocorrelation function $\Gamma_\ell(\tau)$ of the velocity increments $\Delta u_\ell(t)$ for

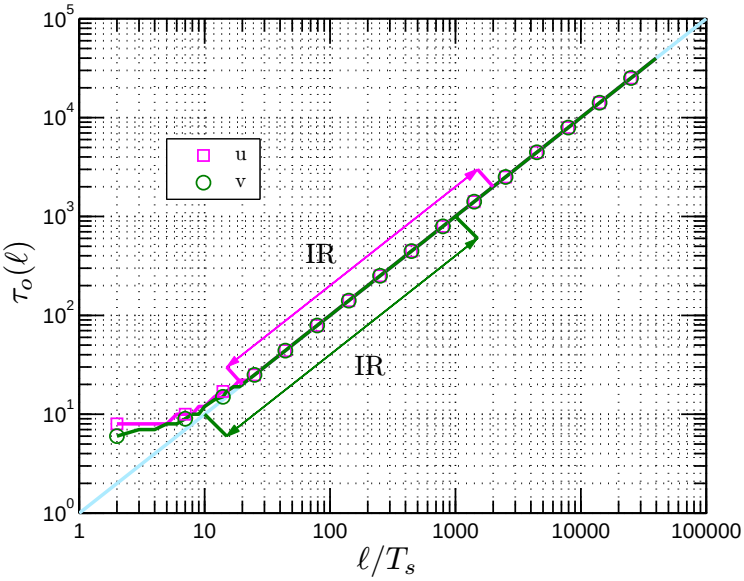

Figure 5.12: Location $\tau_o(\ell)$ of the minimum value of the autocorrelation function estimated from experimental data, where the inertial range is marked as IR. The solid line indicates $\tau_o(\ell) = \ell$.

the longitudinal velocity in Fig. 5.11, where the rescaled autocorrelation function is shown as inset. The location τ_o of the minimum value of each curve is graphically very close to ℓ, which confirms Anselmet's observation (Anselmet *et al.*, 1984).

Let us define the minimum value of an autocorrelation function

$$\Gamma_o(\ell) = \min_{\tau}\{\Gamma_\ell(\tau)\} \tag{5.2.2}$$

and τ_o the location of the minimum value

$$\Gamma_o(\ell) = \Gamma_\ell(\tau_o(\ell)) \tag{5.2.3}$$

We show the estimated $\tau_o(\ell)$ for both longitudinal and transverse velocity on the range $2 < \ell/T_s < 40000$ in Fig. 5.12, where the inertial range is indicated by IR. The solid line illustrates $\tau_o(\ell) = \ell$. When ℓ is larger than $20T_s$, τ_o is very close to ℓ even

when ℓ is in the large forcing scale range, in agreement with the remark of Anselmet *et al.* (1984). We prove this observation analytically in the following.

An Analytical Model

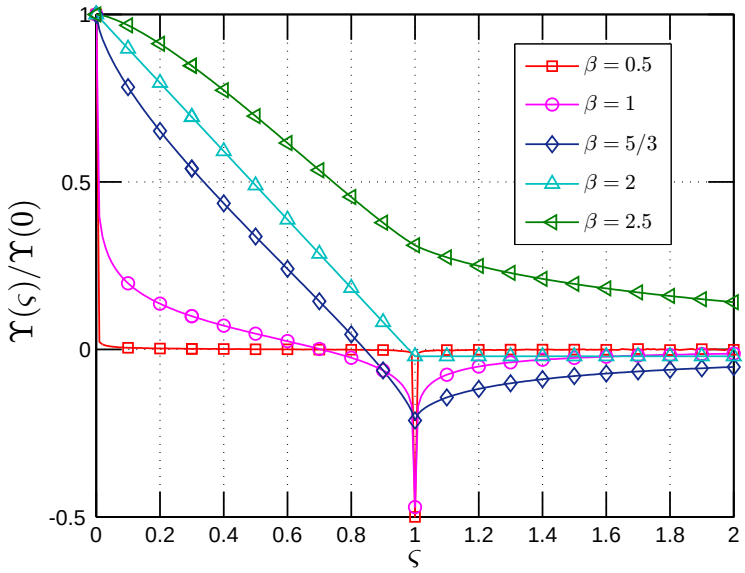

Figure 5.13: Numerical solution of the rescaled autocorrelation function $\Upsilon(\varsigma)$ with various β from 0.5 to 2.5 estimated from Eq. (5.2.8).

We have shown previously that the Fourier transform of the velocity increment $\Delta u(\ell)$ is written as

$$S_\ell(f) = \mathcal{F}(\Delta u(\ell)) = \hat{U}(f)(e^{2\pi i f \ell} - 1)$$

where $\Delta u(\ell) = u(x+\ell) - u(x)$ and $\hat{U}(f)$ is the Fourier transform of the original velocity. Hence, the 1D power spectral density function of velocity increments $E_\Delta(f)$ is expressed as

$$E_\Delta(f) = |S_\ell(f)|^2 = E_v(f)(1 - \cos(2\pi f \ell)) \tag{5.2.4}$$

where $E_v(f) = 2|\hat{U}(f)|^2$ is the velocity power spectrum (Frisch, 1995).

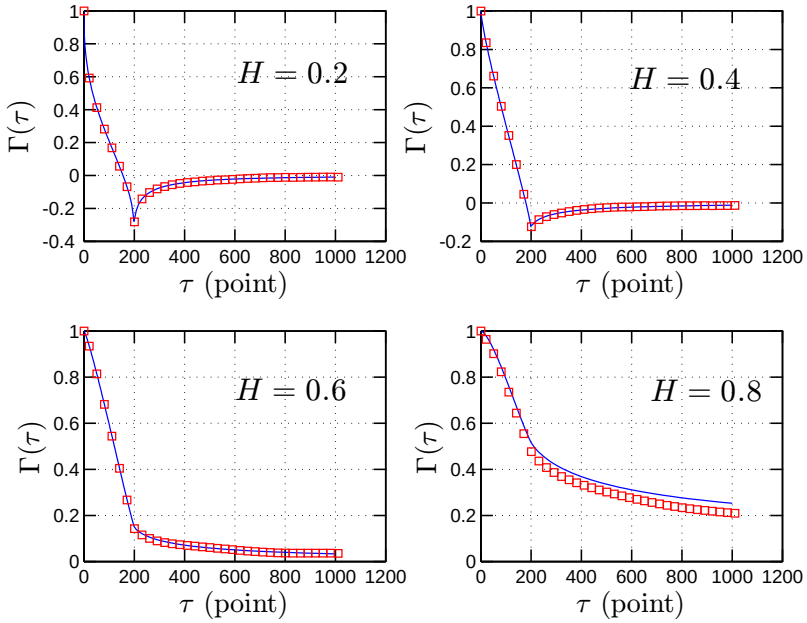

Figure 5.14: Comparison of the autocorrelation function, which is predicted by Eq. (5.2.19) (solid line) and estimated from fBm simulation (□) with $\ell = 200$ points.

Let us consider now the autocorrelation function of the increment. The Wiener-Khinchin theorem relates the autocorrelation function to the power spectral density via the Fourier transform (Percival & Walden, 1993; Frisch, 1995)

$$\Gamma_\ell(\tau) = \int_0^{+\infty} E_\Delta(f)\cos(2\pi f\tau)\,\mathrm{d}f \tag{5.2.5}$$

The theorem can be applied to wide-sense-stationary random processes, signals whose Fourier transforms may not exist, using the definition of autocorrelation function in terms of expected value rather than an infinite integral (Percival & Walden, 1993). Substituting Eq. (5.2.4) into the above equation, we thus have

$$\Gamma_\ell(\tau) = \int_0^{+\infty} E_v(f)(1-\cos(2\pi f\ell))\cos(2\pi f\tau)\,\mathrm{d}f \tag{5.2.6}$$

Assuming a power law for 1D velocity spectrum (a hypothesis of similarity)

$$E_v(f) = cf^{-\beta}, \quad c > 0 \tag{5.2.7}$$

we obtain

$$\Gamma_\ell(\tau) = c\int_0^{+\infty} f^{-\beta}(1-\cos(2\pi f\ell))\cos(2\pi f\tau)\,\mathrm{d}f \tag{5.2.8}$$

The convergence condition requires $0 < \beta < 3$. It implies a rescaled relation, using scaling transformation inside the integral. This can be estimated by taking $\ell' = \lambda\ell$, $f' = f\lambda$, $\tau' = \tau/\lambda$ for $\lambda > 0$, providing the identity directly from Eq. (5.2.8)

$$\Gamma_{\lambda\ell}(\tau) = \Gamma_\ell(\tau/\lambda)\lambda^{\beta-1} \tag{5.2.9}$$

If we take $\ell = 1$ and replace λ by ℓ, we then have

$$\Gamma_\ell(\tau) = \Gamma_1(\tau/\ell)\ell^{\beta-1} \tag{5.2.10}$$

Thus, we have a universal autocorrelation function for each ℓ

$$\Gamma_\ell(\ell\varsigma)\ell^{1-\beta} = \Upsilon(\varsigma) = \Gamma_1(\varsigma) \tag{5.2.11}$$

This universal autocorrelation function is shown as inset in Fig. 5.11. A derivative of Eq. (5.2.9) gives $\Gamma'_{\lambda\ell}(\tau) = \Gamma'_\ell(\tau/\lambda)\lambda^{\beta-2}$. The minimum value of the left-hand side is $\tau = \tau_o(\lambda\ell)$, verifying $\Gamma'_{\lambda\ell}(\tau_o(\lambda\ell)) = 0$ and for this value we have also $\Gamma'_\ell(\tau_o(\lambda\ell)/\lambda) = 0$. This shows that $\tau_o(\ell) = \tau_o(\lambda\ell)/\lambda$. Taking again $\ell = 1$ and $\lambda = \ell$, we have

$$\tau_o(\ell) = \ell\tau_o(1) \tag{5.2.12}$$

Showing that $\tau_o(\ell)$ is proportional to ℓ in the scaling range (when ℓ belongs to the inertial range). With the definition of $\Gamma_o(\ell) = \Gamma_\ell(\tau_o(\ell))$ we have, also using Eq. (5.2.9), for $\tau = \tau_o(\lambda\ell)$:

$$\begin{aligned}\Gamma_{\lambda\ell}(\tau_o(\lambda\ell)) &= \Gamma_\ell(\tau_o(\lambda\ell)/\lambda)\lambda^{\beta-1}\\ &= \Gamma_\ell(\tau_o(\ell))\lambda^{\beta-1}\end{aligned} \tag{5.2.13}$$

Hence $\Gamma_o(\lambda\ell) = \lambda^{\beta-1}\Gamma_o(\ell)$ or

$$\Gamma_o(\ell) = \Gamma_o(1)\ell^{\beta-1} \tag{5.2.14}$$

We consider the location $\tau_o(1)$ of the autocorrelation function for $\ell = 1$. We take the first derivative of Eq. (5.2.8), written for $\ell = 1$

$$\mathcal{R}(\tau) = \frac{\mathrm{d}\Gamma_1(\tau)}{\mathrm{d}\tau} = -\int_0^{+\infty} f^{1-\beta}(1-\cos(2\pi f))\sin(2\pi f\tau)\,\mathrm{d}f \tag{5.2.15}$$

where we left out the constant in the integral. The same rescaling calculation leads to the following expression

$$\begin{aligned} &\mathcal{R}(\tau) = \left[(1+1/\tau)^{\beta-2} + (1-1/\tau)^{\beta-2} - 2\right] M/2, \tau \neq 1 \\ &\mathcal{R}(\tau) = \left(2^{\beta-3} - 1\right) M, \qquad \tau = 1 \end{aligned} \tag{5.2.16}$$

where $M = \int_0^{+\infty} x^{1-\beta}(1-\cos(2\pi x))\sin(2\pi x\tau)\,\mathrm{d}x$ and $M > 0$ (Samorodnitsky & Taqqu, 1994). The convergence condition requires $1 < \beta < 4$. When $\beta < 2$, one can find that both left and right limits of $\mathcal{R}(1)$ are infinite, but the definition of $\mathcal{R}(1)$ in Eq. (5.2.15) is finite. Thus $\tau = 1$ is a second type discontinuity point of Eq. (5.2.15) (Malik & Arora, 1992). It is easy to show that

$$\begin{cases} \mathcal{R}(\tau) < 0, \tau \leq 1 \\ \mathcal{R}(\tau) > 0, \tau > 1 \end{cases} \tag{5.2.17}$$

It means that $\mathcal{R}(\tau)$ changes its sign from negative to positive when τ is increasing from $\tau < 1$ to $\tau > 1$. In other words the autocorrelation function will take its minimum value at location where τ is exactly equal to 1. We thus see that $\tau_o(1) = 1$ and hence from Eq. (5.2.12) we proved that

$$\tau_o(\ell) = \ell \tag{5.2.18}$$

For the fBm, the autocorrelation function of the increments is known to be the following (Biagini *et al.*, 2008)

$$\Gamma_\ell(\tau) = \frac{1}{2}\left\{(\tau+\ell)^{2H} + |\tau-\ell|^{2H} - \tau^{2H}\right\} \tag{5.2.19}$$

where H is Hurst number, and $\tau \geq 0$. We compare the autocorrelation (coefficient) function estimated from fBm simulation ($\square$) with Eq. (5.2.19) (solid line) in Fig. 5.14, where $\ell = 200$ points. Eq. (5.2.19) provides a very good agreement with numerical simulation. Based on this model, it is not difficult to find that $\Gamma_o(\ell) \sim \ell^{2H}$ when $0 < H < 1$, corresponding to $1 < \beta < 3$, and $\tau_o(\ell) = \ell$ when $0 < H < 0.5$, corresponding to $1 < \beta < 2$. One can find that the validity range found here for the scaling exponent β is only a subset of the validity range for Wiener-Khinchin theorem.

Experimental Results

There is no analytical solution for Eq. (5.2.8). Above we could only give a rescaling property of this function, and also give its explicit form for the fBm. It can also be solved by a proper numerical algorithm. We perform this here using a fourth order accurate Simpson rule of Eq. (5.2.8) on range $10^{-4} < f < 10^4$ with $\ell = 1$ for various β with $\Delta f = 10^{-6}$. We show the rescaled numerical solutions for various β values $\Upsilon(\varsigma)$ in Fig. 5.13. We can verify that the location $\tau_o(1)$ of the minimum autocorrelation function is exactly equal to 1 when $0 < \beta < 2$.

We then check the power law for the minimum value of autocorrelation function given in Eq. (5.2.10). We simulate 100 segments of fBm with length 10^6 data points each, by performing a Wavelet based algorithm (Abry & Sellan, 1996). We take db2 wavelet with $H = 1/3$ (corresponding to the Hurst number of turbulent velocity). We

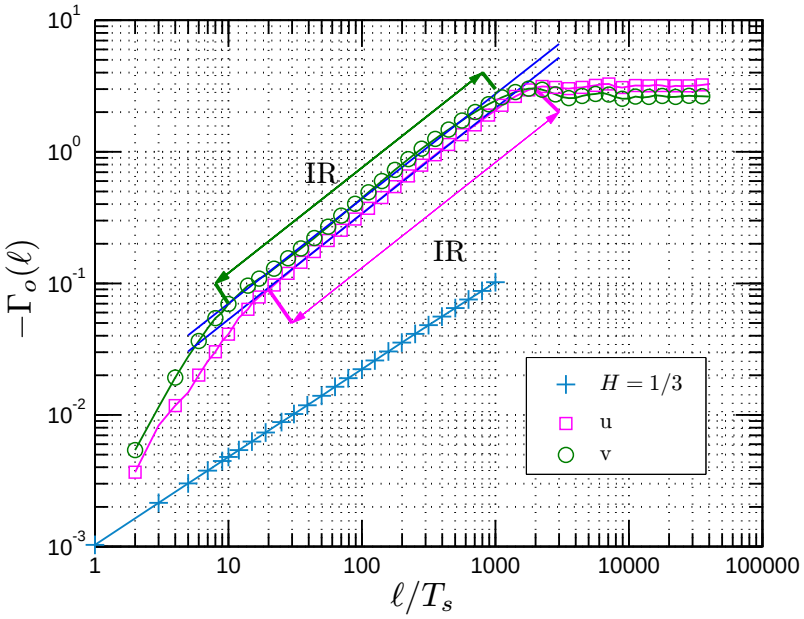

Figure 5.15: Representation of the minima value $\Gamma_o(\ell)$ of the autocorrelation function estimated from synthesized fBm time series with $H = 1/3$ (+), and the experimental data for longitudinal (□) and transverse (○) turbulent velocity components, where the corresponding inertial range is denoted as IR. Power law behaviour is observed with scaling exponent $\beta - 1 = 2/3$ and $\beta - 1 = 0.78 \pm 0.04$ for fBm and turbulent velocity, respectively.

plot the estimated minima value $\Gamma_o(\ell)$ (+) of the autocorrelation function in Fig. 5.15, where the solid line demonstrates $\Gamma_o(\ell) \sim \ell^{2/3}$. A power law behaviour is observed with the scaling exponent $\beta - 1 = 2/3$ as expected. It confirms Eq. (5.2.10) for fBm, the monofractal case. We also plot $\Gamma_o(\ell)$ estimated from turbulent experimental data for both longitudinal (□) and transverse (○) velocity component in Fig. 5.15, where the inertial range is marked by IR, which is provided by the Fourier power spectrum of the original velocity. Power law behaviour is observed on the corresponding inertial range, with scaling exponent $\beta - 1 = 0.78 \pm 0.04$. This scaling exponent is larger than 2/3, which may be an effect of intermittency. The exact relation between this scaling exponent with intermittent parameter should be investigated in future work.

The power law range is almost the same as the inertial range estimated by Fourier power spectrum. It indicates that autocorrelation function can be used to determine the inertial range. Indeed, as we show later, it seems to be a better inertial range indicator than structure function.

Cumulative function

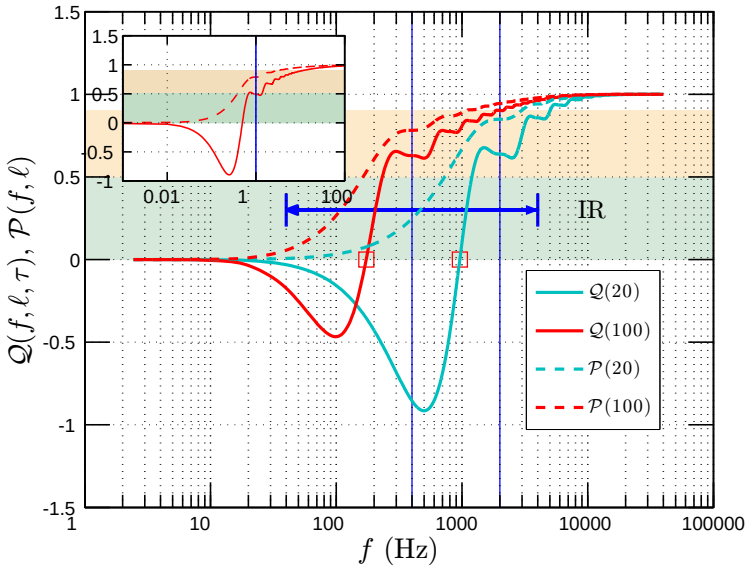

Figure 5.16: Cumulative function $\mathcal{Q}(f,\ell,\tau)$ estimated from turbulent experimental data for transverse velocity with $\tau = \ell$ in the inertial range, where the numerical solution is shown as inset with $\ell = 1$. The inertial range is denoted as IR. Vertical solid lines demonstrate the corresponding scale in spectral space. For comparison, we also show the cumulative function $\mathcal{P}(f,\ell)$ for the second order structure function.

As we have done for the second order structure function, we define here a cumulative function

$$\mathcal{Q}(f,\ell,\tau) = \frac{\int_0^f K(f',\ell,\tau)\,\mathrm{d}f'}{\int_0^{+\infty} K(f',\ell,\tau)\,\mathrm{d}f'} \tag{5.2.20}$$

where

$$K(f,\ell,\tau) = E_v(f)(1-\cos(2\pi f\ell))\cos(2\pi f\tau) \tag{5.2.21}$$

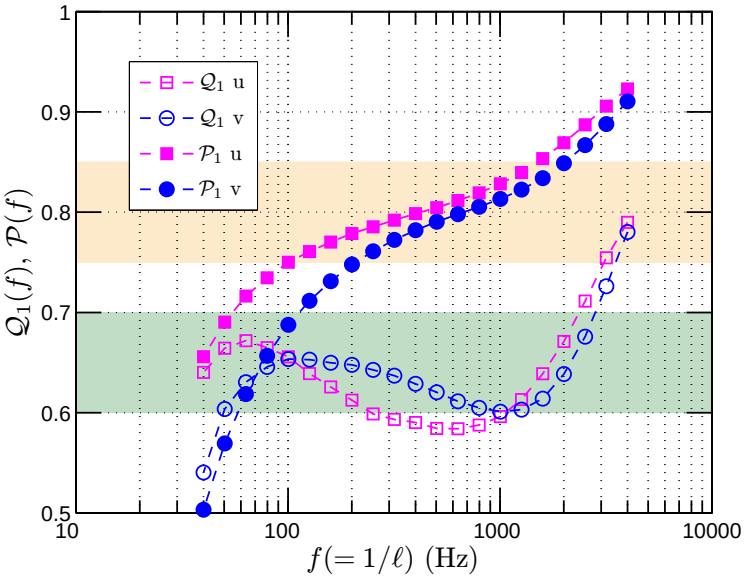

Figure 5.17: Cumulative function $\mathcal{Q}_1(f)$ estimated from turbulent experimental data for both longitudinal and transverse velocity with various ℓ. The numerical solution shows $\mathcal{Q}_1 \simeq 0.49$. For comparison, we reproduce the cumulative function $\mathcal{P}_1(f)$ for the second order structure function.

is the integration kernel of Eq. (5.2.6). It measures the contribution of the frequency from 0 to f at a given time scale ℓ and time delay τ. We are particularly concerned by the case $\tau = \ell$. To avoid the measurement noise, we only consider here the transverse velocity. We show the estimated $\mathcal{Q}$ in Fig. 5.16 for two scales $\ell/T_s = 20$ and $\ell/T_s = 100$ (solid line) in the inertial range, in which the spectrum $E_v(f)$ in Eq. (5.2.21) is directly estimated for the transverse velocity from the experimental turbulent data. The vertical solid line illustrates the location of the corresponding time scale in spectral space by taking $f = 1/\ell$. The corresponding inertial range is denoted by IR. We show the numerical solution of Eq. (5.2.20) for a pure power law with $\ell = 1$ (solid line) as inset, in which the spectrum $E_v(f)$ in Eq. (5.2.21) is taken as $E_v(f) = f^{-5/3}$ for a pure Kolmogorov power law. We notice that both curves cross

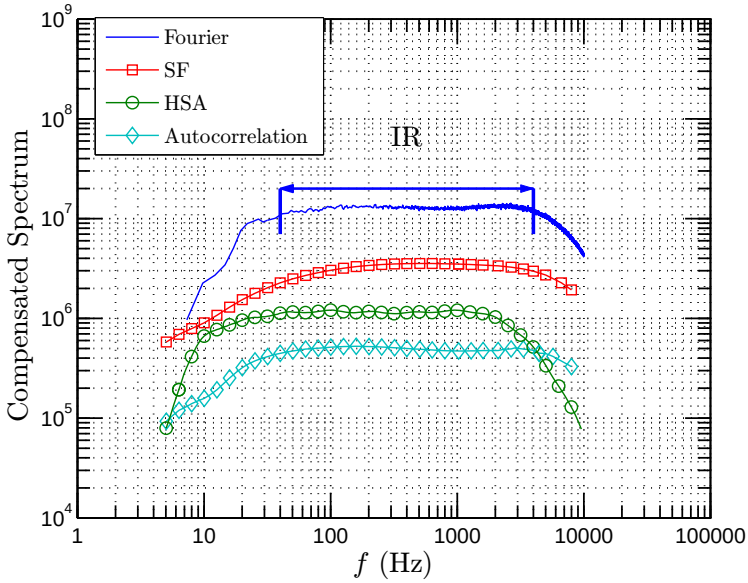

Figure 5.18: Compensated spectrum of transverse velocity. A plateau is observed on the range $40 < f < 4000$ Hz and $20 < f < 2000$ Hz for Fourier spectrum (solid line) and Hilbert spectrum (○), respectively. For comparison, the compensated spectra for the second order structure function (□) and the autocorrelation function (◇) are also shown.

the line $\mathcal{Q} = 0$, which is marked by □. We denote f_o such as $\mathcal{Q}(f_o) = 0$. It has the advantage that the contribution from the large scale part, $\ell > 1/f_o$, is canceled by itself, and the small-scale and large-scale contributions are equal (Huang *et al.*, 2009c). In the inertial range, the distance between f_o and the corresponding scale ℓ is less than 0.3 decade. The numerical solution indicates that this distance is about 0.3 decade. We then separate the contribution into a large scale part and a small scale part. We denote the contribution from the large scale part as $\mathcal{Q}_1(f) = \mathcal{Q}(1/\ell, \ell, \ell)$. The experimental result is shown in Fig. 5.17 for both longitudinal (□) and transverse (○) velocity components. The mean contribution from the large scale is found graphically to be 0.64. It is significantly larger than 0.5, the value indicated by the numerical solution. It means that the autocorrelation function is influenced more by large scales

than by small scales.

For comparison, we reproduce the cumulative function $\mathcal{P}(f, \ell)$ and $\mathcal{P}_1(f)$ for the second order structure function in Fig. 5.16 (dash line) and Fig. 5.17 (filled symbol). The contribution range from the large scale part to the second order structure function is much larger than the contribution range of the autocorrelation function. It is also confirmed by Fig. 5.17 that the large scale contribution of the second order structure function is larger than the large scale contribution of the autocorrelation function, which can be linked to the cancellation property of the large scale part $f < f_o$ of the autocorrelation function. This explains that the autocorrelation function is a **better inertial range indicator than the second order structure function** (Huang *et al.*, 2009c).

We now consider the inertial range provided by the different methods. We replot the corresponding compensated spectra estimated directly by Fourier power spectrum (solid line), the second order structure function ($\square$), the Hilbert spectral analysis ($\bigcirc$) and the autocorrelation function ($\diamondsuit$) in Fig. 5.18 for transverse velocity. For comparison convenience, both the second order structure function and the autocorrelation function are converted from physical space into spectral space by taking $f = 1/\ell$. Graphically, except for the second order structure function, the others show a clear plateau more than two decades wide. The similar shape for the compensated second order structure function can be found in Refs. Anselmet *et al.* (1984, Figure 10 and Figure 11) and Frisch (1995, P128, Figure 8.6). We have focused here on the existence of the power law, not the value of the scaling exponent or the range of the plateau. Thus we do not compare the scaling exponents here. Based on this observation, we state that the autocorrelation function is a better inertial range indicator

than structure functions (Huang *et al.*, 2009c).

5.3 Summary

In this chapter, we considered the second order structure function and the autocorrelation function of the velocity increment time series $\Delta u_\ell(t)$, where ℓ is a time scale. Taking statistical stationary assumption, we proposed an analytical model of the second order structure function and the autocorrelation function. Within this model, for the second order structure function, we found that it is strongly influenced by the large scale part. Furthermore, the influence range down to the small scale part is as large as two decades. However, the Hilbert-based methodology seems to constrain the periodic effect in 0.3 decade, which may be linked to the fact that EMD acts a dyadic filter bank. We thus argued that the widely used structure function method is not a good method to extract the scaling exponents from a given time series when the data possess energetic large scales. We showed this experimentally by analyzing a passive turbulence data, a temperature time series obtained from a jet experiment.

For the autocorrelation function, we proved analytically that the location of the minimum autocorrelation function is exactly equal to the separation time scale ℓ when the scaling of power spectrum of the original variable belongs to the range $0 < \beta < 2$. In fact, this property was found experimentally to be valid outside the scaling range, but our demonstration here concerns only the scaling range. This model also suggests a power law expression for the minimum autocorrelation $\Gamma_o(\ell)$. Considering the cumulative integration of the autocorrelation function, it was shown that the autocorrelation function is influenced more by the large scale part. We thus argued that the autocorrelation function is a better indicator of the inertial range

than second order structure function. These results have been illustrated using fully developed turbulence data; however, they are of more general validity since we only assumed that the considered time series is stationary and possesses scaling statistics.

Chapter 6

Experimental Homogeneous and Locally Isotropic Turbulence

Since Kolmogorov (1941c,a,b) proposed his very famous K41 turbulence theory, the studies to extract the scaling exponents from various turbulent flows becomes one central problem in turbulent research (Monin & Yaglom, 1971; Anselmet *et al.*, 1984; Antonia *et al.*, 1984; Kraichnan, 1991; Frisch, 1995; Kahalerras *et al.*, 1998; van de Water & Herwijer, 1999; Sreenivasan & Antonia, 1997; Tsinober, 2001; Moisy *et al.*, 2001; Tsuji, 2004; Chevillard *et al.*, 2005). The structure function scaling exponent $\zeta(q)$ extracted from various turbulent flows are well documented (Frisch, 1995; Sreenivasan & Antonia, 1997). In this chapter, we apply the arbitrary order Hilbert spectral analysis on an experimental homogeneous and nearly isotropy turbulent data to characterize the scale invariant properties in amplitude-frequency space for the first time. The results presented in this chapter are for part of them published in Huang *et al.* (2008) [Y. Huang, *et al.Europhy. Lett.*, 84, 40010, 2008.].

6.1 Experimental data

The database we consider here is the same database we used in chapter 5. Here we present it on more details.

Conventional passive grid wind tunnels of normal laboratory size allow to generate only moderate Reynolds number turbulent flow, with Taylor microscale based Reynolds numbers typically less than 150. The main reason is that the root-mean-square (r.m.s.) velocity downstream of a passive grid is relatively low (Kang *et al.*, 2003). As an alternative, the 'active grid' technique, which allows to achieve higher Reynolds number turbulent flow, has been studied by several authors (Makita, 1991; Mydlarski & Warhaft, 1996, 1998; Kang *et al.*, 2003).

Table 6.1: Some parameters of the turbulent flow consider here at four different locations: mean velocity $\langle u \rangle$, r.m.s velocity $u_{\text{r.m.s.}}(\langle (u - \langle u \rangle)^2 \rangle^{1/2})$, isotropy ratio I, turbulence intensity (%), Kolmogorov scale η $((\nu^3/\epsilon)^{1/4})$, Taylor microscale λ $((15u^2_{\text{1r.m.s.}}\nu/\epsilon)^{1/2})$ and corresponding Reynolds number Re_λ. The details about this experiment and data can be found in Kang *et al.* (2003).

	$x_1/M = 20$	$x_1/M = 30$	$x_1/M = 40$	$x_1/M = 48$
$\langle u_1 \rangle$ (ms^{-1})	12.0	11.2	11.0	10.8
$u_{\text{1r.m.s.}}$ (ms^{-1})	1.85	1.43	1.19	1.08
$u_{\text{2r.m.s.}}$ (ms^{-1})	1.64	1.25	1.04	0.932
$I = u_{\text{1r.m.s.}}/u_{\text{2r.m.s.}}$	1.13	1.14	1.14	1.16
$u_{\text{1r.m.s.}}/\langle u_1 \rangle$ (%)	15.4	12.8	10.8	10.0
η (mm)	0.11	0.14	0.16	0.18
λ (mm)	5.84	7.13	8.25	8.78
$Re_\lambda = u_{\text{1r.m.s.}}\lambda/\nu$	716	676	650	626

Experiments are performed downstream of an active grid in the return-type Corrsin wind tunnel (Comte-Bellot & Corrsin, 1966, 1971) in the Johns Hopkins University's Corrsin wind tunnel (Kang *et al.*, 2003). The wind tunnel has primary and secondary

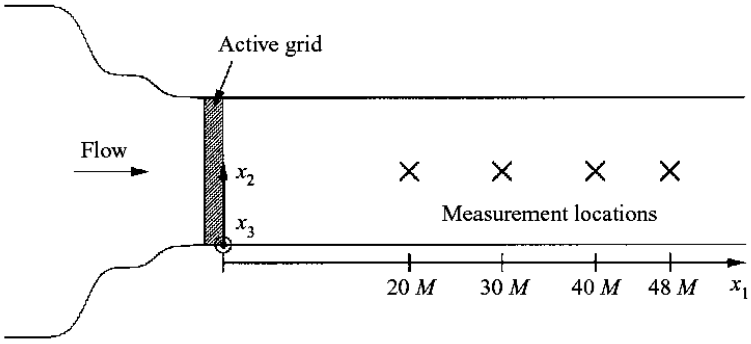

Figure 6.1: Schematic representation of the wind tunnel. Taken from Ref. Kang *et al.* (2003).

contraction ratios of 25:1 and 1.27:1, respectively. The active grid is placed downstream of the secondary contraction, see the schematic of the wind tunnel in Fig. 6.1. The test section length is 10 m and the cross-section is 1.22 m by 0.91 m. The spanwise width of the wind tunnel gradually increases along the test section to account for boundary layer growth. Figure 6.1 demonstrates the schematic of the wind tunnel, where the measurement locations are marked by $\times$.

The design of the active grid follows that of Makita (1991) and Mydlarski & Warhaft (1996, 1998). The active grid is composed of five horizontal and seven vertical rotating shafts to which diamond-shaped winglets are attached. The shafts are made of 19.05 mm square aluminium channel with 3.18 mm-thick walls. The horizontal and vertical shafts have eight and six winglets, respectively, so that the grid size, M, is 0.152 m. The $0.102\times0.102\,\mathrm{m}^2$ square winglets are made of 3.18 mm-thick aluminium plate. Along each shaft, the winglets are attached to opposite sides in an alternating fashion to help reduce vibrations (Kang *et al.*, 2003). A schematic diagram of the active grid is shown in Fig. 6.2. Each shaft is independently driven by a 1/4 hp AC motor (Baldor Industrial Motor, CNM20252) and each motor is controlled by an

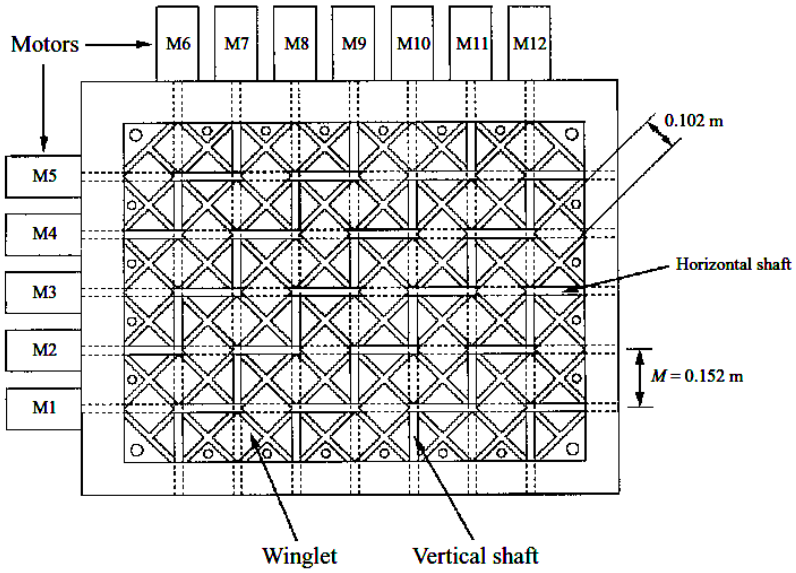

Figure 6.2: Schematic representation of the active grid. Taken from Ref. Kang *et al.* (2003).

inverter (ABB Industrial Systems Inc., ACS 140). The control signal is generated by a PC and sent to the twelve inverters through two six-node RS-485 serial networks, using a National Instruments AT-485 card. Each motor is set to randomly change rotational speed and direction once every second. The speed is selected from a uniform distribution in the range of about 210-420 r.p.m., in both directions.

Figure 6.1 shows the schematic of the experimental wind-tunnel setup, in which the active grid is located at the beginning of the test section. The measurement locations in the streamwise (longitudinal) direction (x_1) are at x_1/M = 20, 30, 40 and 48 and marked by $\times$. An X-wire probe array described in Kang & Meneveau (2001) is used for measuring two velocity components in the (x_1 , x_2)-plane. The probe array is composed of four custom-made miniature X-type hot-wire probes. The signals are sampled at $f_s = 40\,\mathrm{kHz}$, low-pass filtered at a frequency of 20 kHz and digitized with

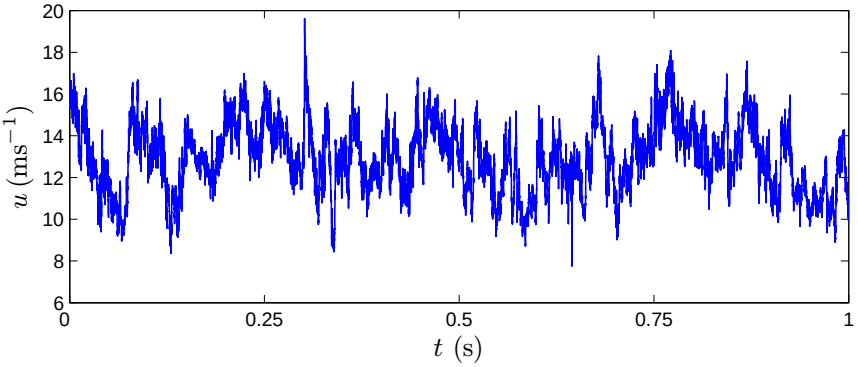

Figure 6.3: One 1s portion of longitudinal velocity at location $x/M = 48$, showing the intermittency nature of turbulent velocity field.

a 12-bit simultaneous sample and hold A/D converter (United Electronic Industries, WIN-30DS). The sampling time is 30×30 s, so the total number of data points per channel for each measurement location is 36×10^6. The array is located at the centre of the wind tunnel and is moved manually to various downstream locations. The data are recorded in the central core region (0.25 m$<x_2<$0.65 m and 0.25 m$<x_3<$0.95 m). To obtain the spatial quantities in the streamwise direction from the temporal data, Taylor's hypothesis is invoked.

Table 6.1 shows the main parameters of each experimental data set, including the mean longitudinal velocity $\langle u_1\rangle$, the r.m.s. velocities $u_{1\text{r.m.s.}}$ and $u_{2\text{r.m.s.}}$, the isotropy ratio $I = u_{1\text{r.m.s.}}/u_{2\text{r.m.s.}}$, the turbulence intensity $u_{1\text{r.m.s.}}/\langle u_1\rangle$, the Kolmogorov scale $\eta = (\nu^3/\epsilon)^{1/4}$, the Taylor microscale $\lambda = (15u^2_{1\text{r.m.s.}}\nu/\epsilon)^{1/2}$, and the Taylor microscale based Reynolds number $Re_\lambda = u_{1\text{r.m.s.}}\lambda/\nu$. A 1 s portion of velocity at downstream $x/M = 48$, where M is the mesh size, is displayed in Fig. 6.3 to demonstrate the intermittency and stochastic natural of the turbulent velocity field. We then show the Fourier spectrum and the corresponding second order Hilbert marginal spectrum at the downstream $x/M = 48$ in Fig. 6.4, where the compensated spectrum $E(f)f^{5/3}$

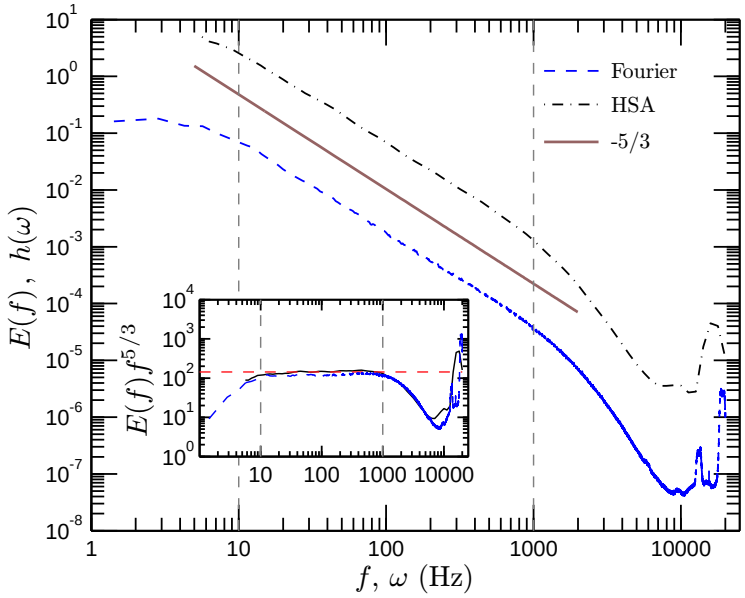

Figure 6.4: Comparison of the Hilbert marginal spectrum (dashed-dotted line) and Fourier spectrum (dashed line) at downstream $x/M = 48$. Both of them predict the inertial subrange on the range $10 \leq \omega \leq 1000\,\mathrm{Hz}$. The inset shows the corresponding compensated spectra $E(f)\,f^{5/3}$.

is shown as inset. The Hilbert marginal spectrum which is shown here is the first experimental estimate of a Kolmogorov 5/3 spectrum in Hilbert spectral frame that we published in a recent work (Huang *et al.*, 2008). We can find that both spectra predict an almost two decades inertial subrange on the range $10 \leq f(\mathrm{or}\,\omega) \leq 1000\,\mathrm{Hz}$, which is illustrated as vertical dashed line. Therefore, the data we have chosen here have a sufficient inertial subrange to test our new Hilbert-based methodology. For more details about the experiment and the data see Kang *et al.* (2003); the data can be found at http://www.me.jhu.edu/~meneveau/datasets.html.

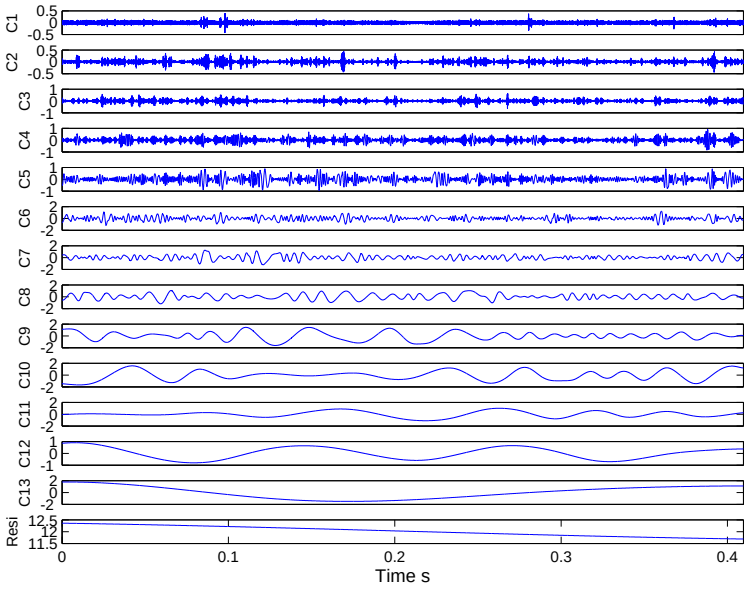

Figure 6.5: IMF modes of one 2^{14} points segment from EMD.

6.2 EMD decomposition of turbulent data

The original velocity time series is divided into 73 segments (without overlapping) of 2^{14} points each. After decomposition, the original velocity series is decomposed into several IMFs, from 11 to 13 modes with one residual. Figure 6.5 shows the IMF modes of one segment from EMD algorithm. The time scale increases with the mode index n. We note that the number of IMF modes is deduced by the data themselves, and depends on the length and the complexity of the data. In practice, based on the dyadic filter bank property of the EMD algorithm, this number is usually less than $\log_2(N)$, where N is the length of the database (Flandrin & Gonçalvès, 2004; Flandrin *et al.*, 2004; Wu & Huang, 2004; Huang *et al.*, 2008).

The time scale is increasing with the mode index n; and each mode can be characterized by its mean frequency, which is estimated by considering the Fourier energy

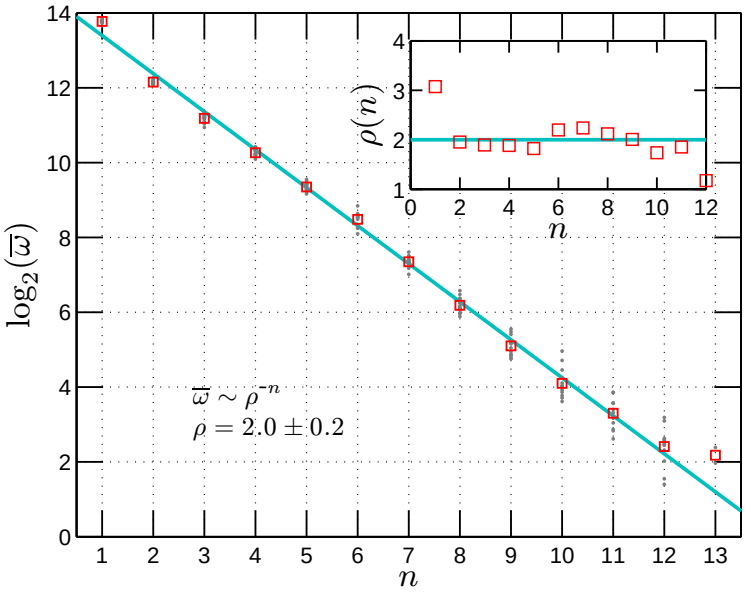

Figure 6.6: Mean frequency $\overline{\omega}$ vs mode index n for the longitude velocity time series. There is an exponential decrease with a slope very close to 1, which indicates that EMD acts as a dyadic filter bank. The inset shows the local slope $\rho(n)$.

weighted mean frequency, $\overline{\omega}$. The mean frequency $\overline{\omega}$ is defined as

$$\overline{\omega}_i = \frac{\int f|S_i(f)|^2 \, \mathrm{d}f}{\int |S_i(f)|^2 \, \mathrm{d}f} \tag{6.2.1}$$

where $S_i(f)$ is the Fourier power spectrum of each IMF mode $C_i(t)$. Figure 6.6 shows the mean frequency $\overline{\omega}(n)$, where the inset shows local slope. The straight line in log-linear plot suggests the following relation

$$\overline{\omega}(n) = \omega_o \rho^{-n} \tag{6.2.2}$$

where $\omega_o \simeq 22000$, and $\rho = 2.0 \pm 0.1$, very close to 2. This implies that the EMD algorithm acts as a dyadic filter bank in the frequency domain. An analogous property was obtained using stochastic simulations of Gaussian noise and fractional Gaussian noise (Wu & Huang, 2004; Flandrin & Gonçalvès, 2004), and it is interesting to note here that the same result holds for fully developed turbulence time series.

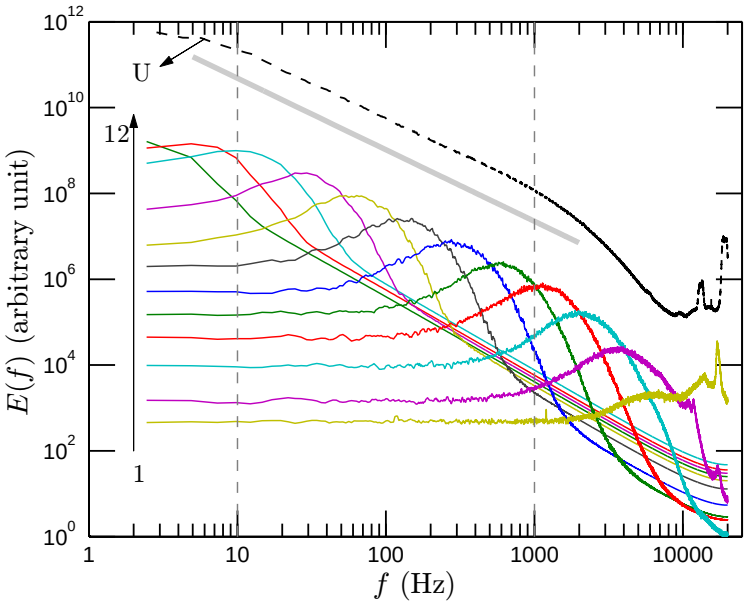

Figure 6.7: Fourier spectra for IMF modes. The vertical dashed lines indicate the inertial subrange $10 \leq f \leq 1000$ Hz. One can find that the modes belonging to the inertial range have a similar shape.

We then interpret each mode according to their characteristic time scale. When compared with the original Fourier spectrum of the turbulent time series, see Fig. 6.7, these modes can be termed as follows: the first mode, which has the smallest time scale, corresponds to the measurement noise; modes 2 and 3 are associated with the dissipation range of turbulence. Mode 4 corresponds to the Kolmogorov scale, which is the scale below which dissipation becomes important; it is a transition scale between inertial range and dissipation range. Modes 5 to 10 all belong to the inertial range, corresponding to the scale-invariant Richardson-Kolmogorov energy cascade (Frisch, 1995); larger modes belong to the large forcing scales. Figure 6.7 represents the Fourier power spectra of each mode. It shows that each mode in the inertial range is narrow-banded. This confirms that the EMD approach acts as a filter bank for turbulence time series and that each mode can be associated to a given part of the different

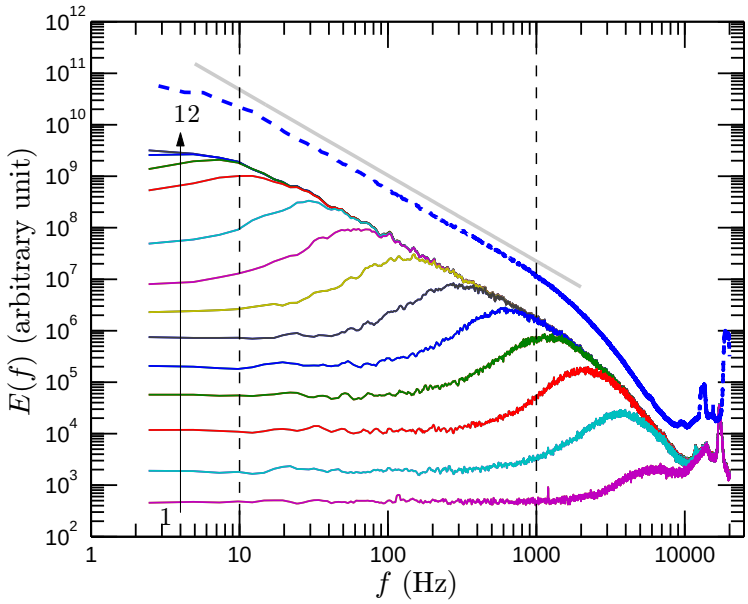

Figure 6.8: Fourier spectra for successive sums of IMF modes $\sum C_i$. The lope of the reference line is -5/3. The vertical dashed lines indicate the corresponding inertial subrange $10 \leq f \leq 1000$ Hz. With the mode index increasing, the spectrum is then asymptotic approached to the original spectrum.

zones of turbulence (injection scales, inertial range, dissipation scales) (Huang *et al.*, 2008). We then plot the Fourier spectrum of the cumulative sum of these IMF modes in Fig. 6.8. For comparison, we also represent the Fourier spectrum of the original longitude velocity u. The addition of more and more modes in the decomposition is a progressive reconstruction of the original time series as can been seen from the spectrum which asymptotically reaches the -5/3 behaviour.

6.3 Joint pdf and dimensional analysis

Here we consider the joint pdf in amplitude-frequency space, and obtain experimentally new scaling result, for which we give some interpretation using dimensional

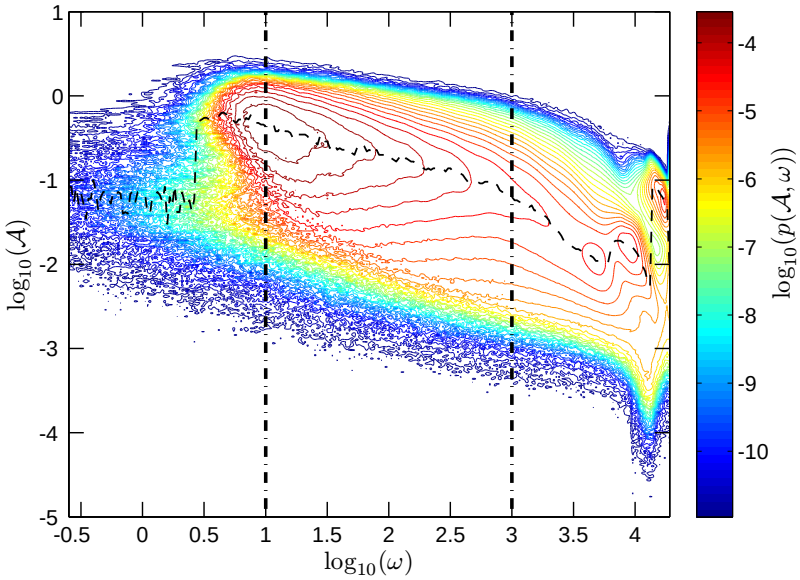

Figure 6.9: Representation of the joint pdf $p(\omega, \mathcal{A})$ (in log scale) of turbulent fluctuations in an amplitude-frequency space. The scaling range $10 < \omega < 1000\,\text{Hz}$ for frequencies is shown as vertical dashed-dotted lines. The dashed line shows the skeleton $\mathcal{A}_\text{s}(\omega)$ of the joint pdf, which is the amplitude for which the conditional pdf $p(\mathcal{A}|\omega)$ is maximum.

analysis.

Joint pdf $p(\omega, \mathcal{A})$

The arbitrary order HSA methodological framework provides a way to represent turbulent fluctuations in an amplitude-frequency space (Huang *et al.*, 2008, 2010a, 2009a). We represent the joint pdf $p(\omega, \mathcal{A})$ in Fig. 6.9 in a log-log view, where the vertical dashed-dotted lines demonstrate the inertial subrange, $10 \leq \omega \leq 1000\,\text{Hz}$. It can be seen that the joint pdf $p(\omega, \mathcal{A})$ decrease with increasing frequencies, with a scaling trend. We show in the same graph the skeleton $\mathcal{A}_\text{s}(\omega)$ of the joint pdf which

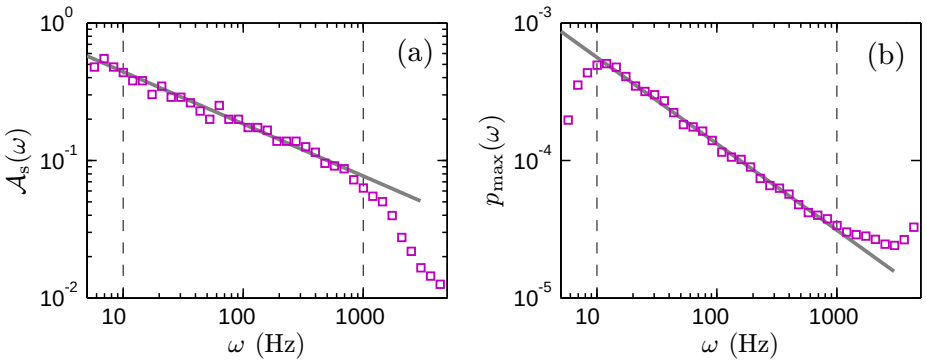

Figure 6.10: The skeleton of the joint pdf (a) $\mathcal{A}_s(\omega)$ in log-log plot. A power law behaviour is observed in the inertial subrange with scaling exponent 0.38, which is close to the Kolmogorov value 1/3, and (b) $p_{max}(\omega)$ in log-log plot. A power law behaviour is observed in the inertial subrange with scaling exponent 0.63. The vertical dashed lines show the corresponding inertial subrange $10 < \omega < 1000$ Hz.

corresponds to the amplitude for which the conditional pdf $p(\mathcal{A}|\omega)$ is maximum

$$\mathcal{A}_s(\omega) = \mathcal{A}_0 \,;\, p(\mathcal{A}_0, \omega) = \max_{\mathcal{A}}\{p(\mathcal{A}|\omega)\} \tag{6.3.1}$$

We then reproduce the skeleton in Fig. 6.10 in two different views: (a) $\mathcal{A}_s(\omega)$ in a log-log plot; (b) skeleton pdf $p_{max}(\omega) = p(\mathcal{A}_s(\omega), \omega) = \max_{\mathcal{A}}\{p(\mathcal{A}|\omega)\}$ in a log-log plot, where the vertical dashed line indicates the inertial subrange. It is interesting to note that a power law behaviour is found for both representations

$$\mathcal{A}_s(\omega) \sim \omega^{-\beta_1} \tag{6.3.2a}$$

where $\beta_1 \simeq 0.38$, and

$$p_{max}(\omega) \sim \omega^{-\beta_2} \tag{6.3.2b}$$

where $\beta_2 \simeq 0.63$. Dimensional analysis to interpret these results is provided below.

Table 6.2: The dimension of several physical quantities: wave number, k, arbitrary order Hilbert marginal spectrum $\mathcal{L}_q(k)$ and mean energy dissipation rate $\overline{\epsilon}$.

Quantity		Dimension	
Wave number	k	1/length	(L^{-1})
arbitrary order HMS	$\mathcal{L}_q(k)$	length^{q+1} /time^q	$(\mathrm{L}^{q+1}\mathrm{T}^{-q})$
Energy dissipation rate	$\overline{\epsilon}$	energy/time	$(\mathrm{L}^2\mathrm{T}^{-3})$

Dimensional Analysis

We rewrite here the arbitrary order Hilbert marginal spectrum in a wavenumber form

$$\mathcal{L}_q(k) = \int p(k, \mathcal{A})\mathcal{A}^q \, \mathrm{d}\mathcal{A} \tag{6.3.3}$$

where k is the instantaneous wavenumber in the spatial domain, which corresponds to the instantaneous frequency ω in the temporal domain, and $\mathcal{A}$ is the instantaneous amplitude. We list the dimensions for the arbitrary order Hilbert spectrum $\mathcal{L}_q(k)$, the instantaneous wavenumber k, and the mean energy dissipation rate $\overline{\epsilon}$ in Table 6.2. The amplitude $\mathcal{A}$ has the same dimension as the velocity u

$$[\mathcal{A}_\mathrm{s}] = [\mathcal{A}] = [u] = \mathrm{LT}^{-1} \tag{6.3.4}$$

in which [ ] means dimension of a variable. The dimension of the arbitrary order Hilbert marginal spectrum by its physical meaning is

$$[\mathcal{L}_q(k)] = \frac{[\mathcal{A}]^q}{[k]} = \mathrm{L}^{q+1}\mathrm{T}^{-q} \tag{6.3.5}$$

The dimension balance requires

$$[\mathcal{L}_q(k)] = [p(k, \mathcal{A})][\mathcal{A}]^{q+1} \tag{6.3.6}$$

We thus have the dimension of $p(k, \mathcal{A})$

$$[p(k, \mathcal{A})] = \mathrm{T} \tag{6.3.7}$$

If we take the mean energy dissipation rate $\overline{\epsilon}$ and the wavenumber k as basic dimensions, then we have

$$[\mathcal{L}_q(k)] = [\overline{\epsilon}]^{q/3}[k]^{-(q/3+1)} \tag{6.3.8a}$$

$$[\mathcal{A}_s] = [\overline{\epsilon}]^{1/3}[k]^{-1/3} \tag{6.3.8b}$$

$$[p_{\max}(k)] = [p(k,\mathcal{A})] = [\overline{\epsilon}]^{-1/3}[k]^{-2/3} \tag{6.3.8c}$$

Considering the Kolmogorov's first and second universality similarity hypothesis (Kolmogorov, 1941a; Monin & Yaglom, 1971; Frisch, 1995), we thus have the following power law in the so-called inertial subrange

$$\mathcal{L}_q(k) = C_q\,\overline{\epsilon}^{q/3}k^{-(q/3+1)} \sim k^{-(q/3+1)} \tag{6.3.9a}$$

$$\mathcal{A}_s = D_0\,\overline{\epsilon}^{1/3}k^{-1/3} \sim k^{-1/3} \tag{6.3.9b}$$

$$p_{\max}(k) = P_0\,\overline{\epsilon}^{-1/3}k^{-2/3} \sim k^{-2/3} \tag{6.3.9c}$$

where C_q, D_0 and P_0 are Kolmogorov constant[1]. The argument presented above indicates that the arbitrary order HSA methodology can be used to characterize the intermittent properties of turbulence. We will further consider this topic in the next section.

We notice that the difference between the estimated values β and the Kolmogorov nonintermittent values may be an effect of the turbulent intermittency. We also note that the value $\beta_1 = 0.38$ is comparable with $\zeta(1) = 0.37$ estimation given in Ref van de Water & Herwijer (1999).

[1]However, these Kolmogorov constants may depend on the detail of the turbulent flow. There is no reason to require them to be universal.

Maxima Amplitude

Inspired by the log-Poisson model (She & Lévêque, 1994; Dubrulle, 1994; She & Waymire, 1995), Vainshtein (2003) studied the most dissipative, most intense structures using a high Reynolds number experimental data. He found that the most

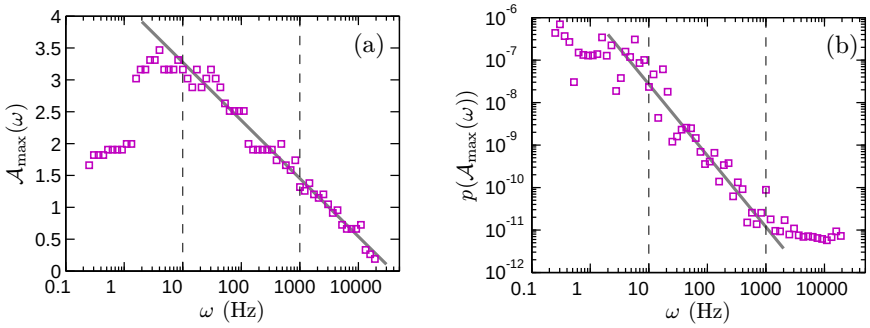

Figure 6.11: Representation of the maxima amplitude (a) $\mathcal{A}_{\max}(\omega)$ in log-linear plot, and (b) the corresponding $p(\mathcal{A}_{\max}(\omega))$ in log-log plot, respectively.

intense of the dissipation field $\max(\epsilon_r)$ satisfies a power law

$$\max(\epsilon_r) \sim \left(\frac{r}{\ell}\right)^{-\gamma} \tag{6.3.10}$$

The scaling value γ is found 0.61 ± 0.01, only slightly small than $2/3$ (Vainshtein, 2003). We are here interested in the maxima amplitude $\mathcal{A}_{\max}$ at given frequency ω

$$\mathcal{A}_{\max}(\omega) = \max\{\mathcal{A}|_{p(\mathcal{A}|\omega)\neq 0}\} \tag{6.3.11}$$

Figure 6.11 shows the maxima amplitude $\mathcal{A}_{\max}(\omega)$ in two views: (a) $\mathcal{A}_{\max}$ vs ω in a log-linear, and (b) $p(\mathcal{A}_{\max})$ vs ω in a log-log view, where the vertical dashed line demonstrates the inertial subrange $10 < \omega < 1000\,\mathrm{Hz}$. We obtain a law

$$\mathcal{A}_{\max}(\omega) = a\log_{10}(\omega) + b \tag{6.3.12}$$

in which $a \simeq -0.91$ and $b \simeq 4.19$ are obtained by using a least square fitting. We also observe a power law behaviour for $p(\mathcal{A}_{\max})$, which is written as

$$p(\mathcal{A}_{\max}) \sim \omega^{-\chi} \tag{6.3.13}$$

where $\chi \simeq 1.68$. Here the plot is quite scattered, but nevertheless the straight line trend in each representation is clear. We have no theoretical or dimensional explanation to propose for these relations. However, these findings may be linked to the nature of turbulence: this will be checked using more databases in the future studies.

Rescaled Conditional pdf

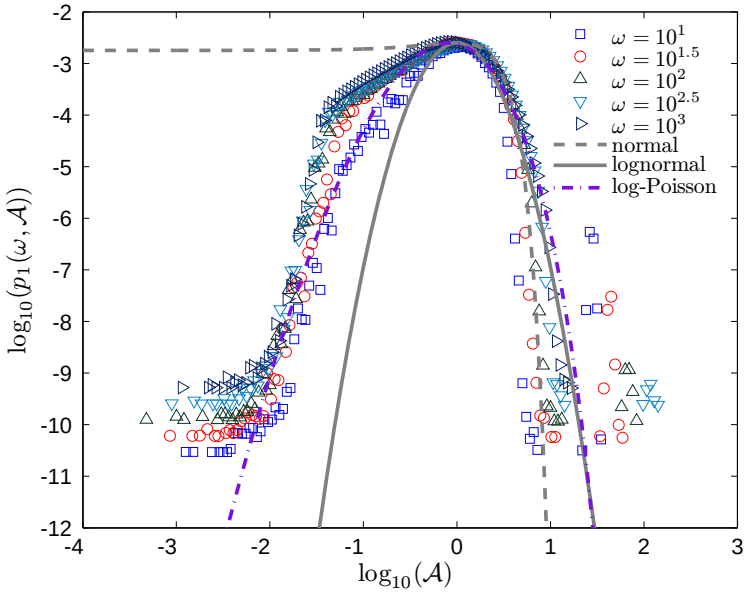

Figure 6.12: Representation of the rescaled conditional pdf $p_1(\mathcal{A},\omega)$ in the inertial range, for fixed values of $\omega = 10$ (□), $10^{1.5}$ (○), 10^2 (△), $10^{2.5}$ (▽) and 10^3 Hz (▷). For comparison, we also plot the normal distribution (dash line), log-normal distribution (solid line) and log-Poisson distribution (dashed-dotted line).

The power law relation for the skeleton indicates a rescaling relation for the pdf $p_1(\mathcal{A},\omega) = \omega^{\beta_2} p(\mathcal{A}/\omega^{\beta_1},\omega)$. We plot it in Fig. 6.12 for various fixed values of ω

in the inertial subrange, where $\omega = 10$ ($\square$), $10^{1.5}$ ($\bigcirc$), 10^2 ($\triangle$) and 10^3 ($\triangleright$) Hz, respectively. In case of monoscaling, these pdfs should superpose perfectly; here the plot is scattered, but nevertheless we note that the lack of superposition of these rescaled pdfs is a signature of intermittency. Moments of this pdf are less noisy as will be visible below. For comparison, we plot the normal distribution (dashed line), lognormal distribution (solid line) and log-Poisson distribution (dashed-dotted line) in the same figure. It seems that the log-Poisson distribution provides a better fit to the pdf than the lognormal distribution for the left-hand part, whereas the lognormal fit is better for the right-hand part.

6.4 Intermittency

Figure 6.13 shows $\mathcal{L}_q(\omega)$ for various orders of Hilbert marginal spectra (0, 1, 3, 4, 5 and 6). The moment of order 0 is the marginal pdf of the instantaneous frequency ω, see Eq. (3.3.1) and the discussion in section 3.3. It is interesting to note that this pdf is extremely "wild", having a behaviour close to $\mathcal{L}_0(\omega) \sim \omega^{-1}$, corresponding to a "sporadic" process whose probability density is not normalizable ($\int p(\omega)\, \mathrm{d}\omega$ diverges). This result is only obtained when all modes are considered together; such pdf is not found for the frequency pdf of an individual mode. This property seems to be rather general: we observed such pdf for moment of order zero using several other time series: for example surf-zone turbulence data, fBm (Huang *et al.*, 2010a, 2009a), river flow discharge data (Huang *et al.*, 2009b). Hence it does not seems to be linked to turbulence itself, but to be a main property of the HSA method, see discussion in section 3.3. Such pdf indicates in fact that high frequencies have a smaller probability than low frequencies, but still the decrease is very slow with a

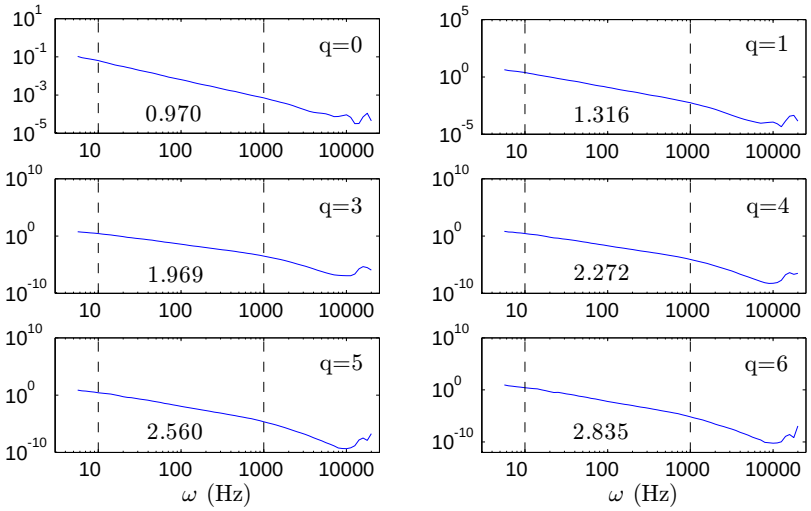

Figure 6.13: Representation of $\mathcal{L}_q(\omega)$, Hilbert spectral analysis of velocity intermittency, using different orders of moments (0, 1, 3, 4, 5 and 6). Power laws are observed on the range $10 < \omega < 1000\,\mathrm{Hz}$ for all spectra. The scaling exponent $\xi(q)$ are estimated on the inertial subrange, which are indicated by the vertical dashed lines.

heavy tail giving large probability to extrema events. We observe the power laws in range $10 < \omega < 1000\,\mathrm{Hz}$ for all order moments. The values of scaling exponents $\xi(q)$ are shown in each picture. This provides a way to estimate scaling exponents $\xi(q)$ for every order of moment $q \geq 0$[2] on a continuous range of scales in the frequency space. We show the corresponding scaling exponent $\xi(q)$ in Fig. 6.14, where the inset shows the departure from the K41 law. For comparison, we also display the scaling exponent provided by the Extended Self-Similarity (ESS) (Benzi *et al.*, 1993a,b, 1995) as dashed line. It can be seen that $\xi(q) - 1$ is nonlinear and is close to $\zeta(q)$, but departure from the K41 law shows that the curvature is not the same: $\xi(q)$ seems less concave than $\zeta(q)$. We thus recover the classical structure function scaling exponent $\zeta(q)$ in an amplitude-frequency space here for the first time.

[2]As we have already indicated in chapter 3, the order of moment q can belong to the on range $q \geq -1$. However, we only consider the case $q \geq 0$ here.

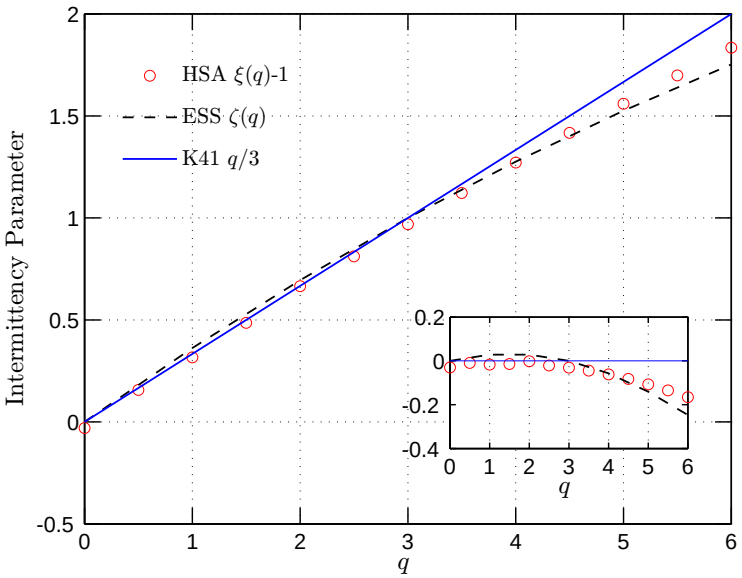

Figure 6.14: Comparison of the scaling exponents $\xi(q) - 1$ (○) with the classical $\zeta(q)$ obtained from structure functions analysis with the ESS method (dashed line) and K41 $q/3$ (solid line). The inset shows the departure from the K41 law.

6.5 Isotropy ratio and isotropy scaling exponent

In the database we consider here, for achieving high Reynolds number turbulent flow, an active-grid technique is performed (Kang *et al.*, 2003), which may cause the turbulent flow to violate the local isotropy hypothesis. In this section we check the scale dependent local isotropy ratio $\mathcal{I}(\omega)$ and the corresponding isotropy scaling exponent $\Gamma(q)$.

Scale Dependent Isotropy Ratio

A scale dependent isotropy ratio is defined as

$$\mathcal{I}(\omega) = \frac{\mathcal{L}_{u,2}(\omega)}{\mathcal{L}_{v,2}(\omega)} \tag{6.5.1}$$

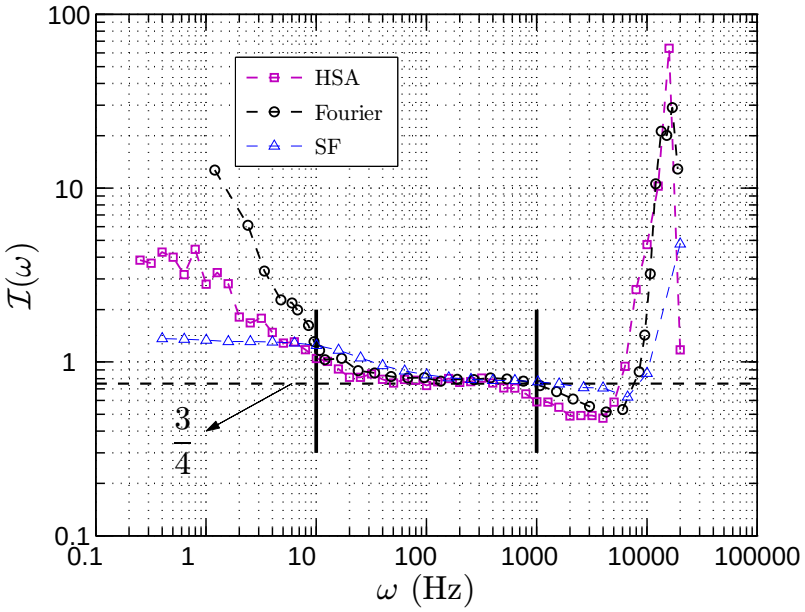

Figure 6.15: The scale dependent isotropy ratio $I(\omega) = \mathcal{L}_{u,2}(\omega)/\mathcal{L}_{v,2}(\omega)$ (□), where the vertical solid line indicates the inertial range $10 < \omega < 1000$ Hz. The horizontal dashed line indicates theoretical value 3/4 (Kolmogorov, 1941c). The direct estimation of the isotropy ratio is 1.16 (Kang *et al.*, 2003). For comparison, we also show the scale dependent isotropy ratio provided by Fourier spectrum (○) and structure function analysis (△), respectively. Except for the large scale part ($\omega \leq 10$ Hz), all these approaches provide almost the same shape. The Fourier spectrum is taken from Ref. Kang *et al.* (2003).

where $\mathcal{L}_{u,2}(\omega)$ and $\mathcal{L}_{v,2}(\omega)$ are the second order Hilbert marginal spectrum of the longitudinal and transverse velocity components. This is an isotropy ratio because it quantifies the scale dependent energy ratio between longitudinal and transverse velocity components. The Kolmogorov theory predicts that $\mathcal{I}(\omega)$ equals 3/4 if the scale ω in the inertial range (Kolmogorov, 1941c; Monin & Yaglom, 1971). Let us recall here how this isotropy ratio is obtained. The second order structure function of longitudinal and transverse velocities can be related as (Monin & Yaglom (1971)

p.352)

$$S_{\mathrm{T}}^2(r) = S_{\mathrm{L}}^2(r) + \frac{r}{2}\frac{\mathrm{d}S_{\mathrm{L}}^2(r)}{\mathrm{d}r} \tag{6.5.2}$$

It is a consequence of the continuity equation. Taking the Kolmogorov's second similarity hypothesis, we have in the inertial range

$$S_{\mathrm{L}}^2(r) \simeq Cr^{2/3}, \quad S_{\mathrm{T}}^2(r) \simeq C'r^{2/3} \tag{6.5.3}$$

where C and C' are the universal constants. From Eq. (6.5.2) and Eq. (6.5.3), it is easy to show that

$$\mathcal{I} = \frac{C}{C'} = \frac{3}{4} \tag{6.5.4}$$

A similar argument may apply to the Fourier power spectrum, see Monin & Yaglom (1971) for more details.

Figure 6.15 shows the scale dependent local isotropy ratio $\mathcal{I}(\omega)$ ($\square$), where the vertical solid lines demonstrate the location of the inertial range $10 < \omega < 1000\,\mathrm{Hz}$, and the horizontal dashed line indicates the Kolmogorov value 3/4. For comparison, we also show the scale dependent isotropy ratio provided by Fourier spectra ($\bigcirc$) and structure function analysis ($\triangle$) in the same figure (the structure function is converted from physical space into spectral space by taking $f = 1/\tau$). Except for the large scale part ($\omega < 10\,\mathrm{Hz}$), all these methods give almost the same shape. The direct estimation of the isotropy ratio at this location is 1.16, which is estimated by the ratio of r.m.s. velocity $u_{1\mathrm{r.m.s.}}/u_{2\mathrm{r.m.s.}}$, see Table 6.1. This value may be influenced by the large scale anisotropy. We note that the plateau range provided by the structure function is slightly different from the others, see also Fig. 6.16 (b). We have shown previously that the structure function is strongly influenced by the large scales. The difference shown here could be an effect of the large scale anisotropy on the structure functions, see chapter 5 for more discussion on the structure function.

The isotropy ratio has a different behaviour depending on the scale: the large scale forcing, the inertial range, where the local isotropy ratio is close to Kolmogorov value, and the dissipation range. Due to the grid and boundary effects, the large scale structure is strongly anisotropic. With the scale decreasing (or the frequency increasing), the structure becomes more and more isotropic and value asymptotically the theoretical value 3/4 in the inertial range. It then keeps this value until entering the dissipation range. In the dissipation range, the isotropy ratio deviates from its theoretical value and increases very fast, which is maybe also the effect of measurement noise. The mean isotropy ratio $\tilde{\mathcal{I}}$ are $\tilde{\mathcal{I}}^H = 0.77 \pm 0.05$, $\tilde{\mathcal{I}}^s = 0.79 \pm 0.03$, and $\tilde{\mathcal{I}}^F = 0.81 \pm 0.02$ for the HSA, structure function and Fourier estimators, respectively. It seems that the HSA approach provides the most isotropic prediction.

Generalized Isotropy Ratio

In order to quantify the evolution of the isotropy ratio for more and more intense events, and hence larger and larger moments we introduce the generalized isotropy ratio for arbitrary order Hilbert marginal spectra

$$\mathcal{I}_q(\omega) = \frac{\mathcal{L}_{u,q}(\omega)}{\mathcal{L}_{v,q}(\omega)} \sim \omega^{(\xi_T(q)-\xi_L(q))} \tag{6.5.5}$$

where $\xi_L(q)$ and $\xi_T(q)$ are the corresponding scaling exponent functions for longitudinal and transverse directions. We then expect $\mathcal{I}_q(\omega)$ to be independent from ω on the inertial range. Figure 6.16 (a) shows the $\mathcal{I}_q(\omega)$ for various q values in log-linear view on the range $8 < \omega < 2000$ Hz, where q =0 ($\bigcirc$), 2 ($\square$), 4 ($\triangle$) and 6 ($\diamondsuit$). The vertical solid lines indicate the plateau on the range $20 < \omega < 800$ Hz. The mean generalized isotropy ratio value $\tilde{\mathcal{I}}^H(q)$ is then estimated on this range, which are shown as thick horizontal dashed lines. The plateau range decreases with q. We apply the same idea

on structure function analysis. Figure 6.16 (b) shows the estimated $\mathcal{I}_q(f)$ on the range $8 < f(= 1/\tau) < 8000\,\mathrm{Hz}$ for various q. As we have mentioned previously, the structure function is strongly influenced by the large scales. The beginning of the flatness range is shifted of almost one decade. The range of plateau decreases with q. It seems that the structure function approach decreases faster than for the HSA approach. The mean isotropy ratio $\tilde{\mathcal{I}}^S(q)$ is estimated on the range $100 < f(= 1/\tau) < 2000\,\mathrm{Hz}$.

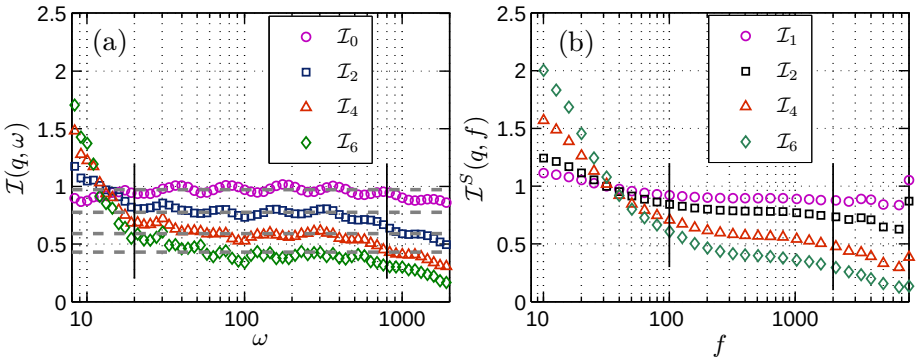

Figure 6.16: The scale dependent generalized isotropy ratio $\mathcal{I}$: (a) estimated by HSA approach on the range $8 < \omega < 2000\,\mathrm{Hz}$, where $q = 0$ (○), 2 (□), 4 (△) and 6 (♢); (b) estimated by structure function on the range $8 < f(= 1/\tau) < 8000\,\mathrm{Hz}$, where $q = 1$ (○), 2 (□), 4 (△) and 6 (♢). The vertical solid lines indicate the plateau range, where the mean isotropy ratio $\tilde{\mathcal{I}}(q)$ is estimated.

Before plotting the result, we estimate the generalized isotropy ratio using the skeleton representation. Figure 6.17 shows the isotropy ratio for the skeleton $\mathcal{A}_\mathrm{s}(\omega)$ (○) of the joint pdf $p(\omega, \mathcal{A})$ and the corresponding conditional pdf $p_\mathrm{max}(\omega)$ (□), the maxima amplitude $\mathcal{A}_\mathrm{max}(\omega)$ (△) and the corresponding conditional pdf $p_{\mathcal{A}_\mathrm{max}}(\omega)$ (solid line in inset). The ratio appears here noisy. However, except the conditional pdf $p_{\mathcal{A}_\mathrm{max}}(\omega)$ for the maxima amplitude, a flatness trend exists for the others on the inertial range. We estimate the mean isotropy ratio on the inertial range $10 < \omega < 1000\,\mathrm{Hz}$. We then plot in Fig. 6.18 the mean generalized isotropy ratio

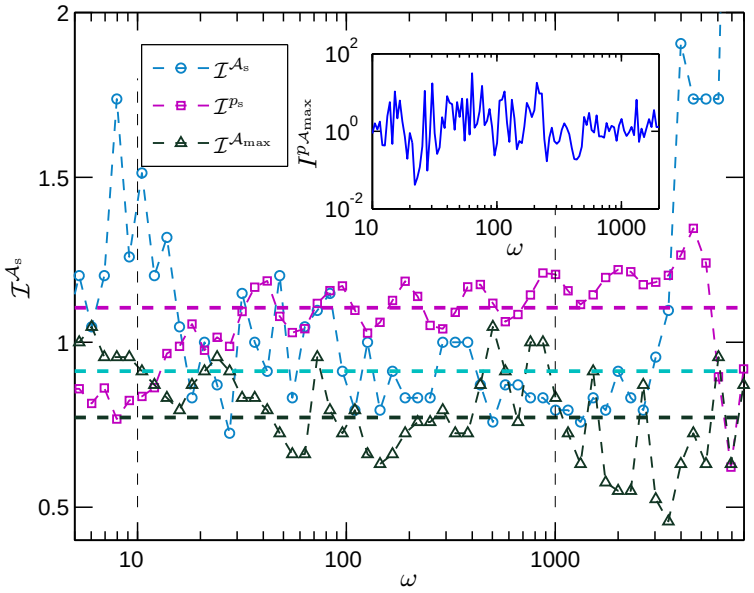

Figure 6.17: The scale dependent generalized isotropy ratio $\mathcal{I}(\omega)$ on range $5 < \omega < 8000$ Hz, where $\mathcal{A}_s$ ($\bigcirc$), $p_{max}(\omega)$ ($\square$) and $\mathcal{A}_{max}$ ($\triangle$), respectively. The inset shows the isotropy ratio for $p_{\mathcal{A}_{max}}$. The vertical dash lines indicate the inertial range $10 < \omega < 1000$ Hz. The mean isotropy ratio $\tilde{\mathcal{I}}$ is then estimated on this range.

$\tilde{\mathcal{I}}^H(q)$ ($\square$) estimated from the Hilbert spectra and the skeleton. A straight line trend seems compatible with the data. It suggests that the mean generalized isotropy ratio decreases linearly with q

$$\tilde{\mathcal{I}}(q) = \widehat{\alpha} q + \widehat{\beta} \tag{6.5.6}$$

where $\widehat{\alpha} \simeq -0.091$ and $\widehat{\beta} \simeq 0.96$ obtained from a least square fitting. Let us note that Antonia *et al.* (1997) provided a 9/16 isotropy ratio for the fourth order structure function. If we assume that the generalized isotropy ratio decreases linearly with q, and consider the two theoretical isotropy ratio values as boundary condition, we then have the equation

$$\tilde{\mathcal{I}}(q) = -\frac{3}{32} q + \frac{15}{16} \tag{6.5.7}$$

which is displayed as a dashed line in Fig. 6.18. It is rather good agreement with

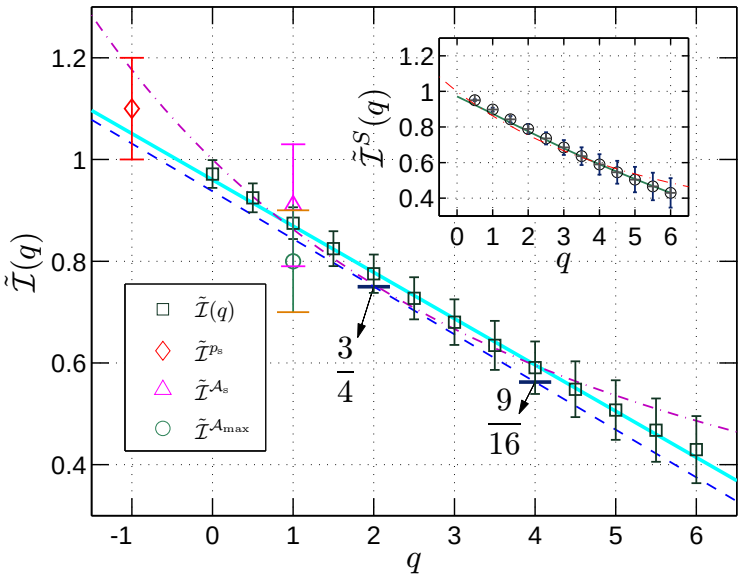

Figure 6.18: Representation of generalized isotropy ratio $\tilde{\mathcal{I}}(q)$, estimated from the arbitrary order Hilbert marginal spectra $\mathcal{L}_q(\omega)$ (□), the skeleton $\mathcal{A}_s$ (△), maxima amplitude (○) and the conditional pdf $p(\mathcal{A}_s)$ (♢). The dashed line indicates a linearity theoretical prediction by Eq. (6.5.7). The dashed-dotted line is an isotropy relation $\tilde{\mathcal{I}}(q) = (2/3)^{\zeta_L(q)}$ provided by Siefert *et al.* (2005). The inset shows the generalized isotropy ratio for the structure function.

experimental isotropy ratio. One interesting finding is that the mean isotropy ratio for the skeleton and the maxima amplitude are also in agreement with this linear prediction.

Other predications for the generalized isotropy ratio exist in the literature such as the one of Siefert *et al.* (2005). They assume of 2/3 rescaled factor between longitudinal and transverse velocity components, giving

$$\langle |u(r)|^q \rangle = \langle |v(\frac{2}{3}r)|^q \rangle = c_L^q r^{\zeta_L(q)} = c_T^q (\frac{2}{3}r)^{\zeta_T(q)} \tag{6.5.8}$$

where $\zeta_L(q)$ and $\zeta_T(q)$ are the scaling exponent function for the longitudinal and transverse velocities respectively, and the c^q constants are related to the Kolmogorov constants (Siefert *et al.*, 2005) . Assuming $\zeta_L(q) = \zeta_T(q)$, it then leads to the following

relation

$$\tilde{\mathcal{I}}(q) = \frac{c_L^q}{c_T^q} = \left(\frac{2}{3}\right)^{\zeta_{\mathrm{L}}(q)} \tag{6.5.9}$$

We show this relation as dashed-dotted line in the same figure, where the scaling exponent $\zeta_{\mathrm{L}}(q)$ correspond to mean values for experimental measurements (Schmitt, 2006). Both linear and convex relations are agreement with the experiment result on the range $0 < q < 5$. As a generalization of this approach, we can introduce $0 < a < 1$ for which

$$\tilde{\mathcal{I}}(q) = a^{\zeta_L(q)} \tag{6.5.10}$$

and try to find the best value of a. The best fitting vale of a is $a = 0.65 \pm 0.05$, quite close to $2/3$.

Isotropy Scaling Exponent

The existence of the plateau of the generalized isotropy ratio indicates that if we plot the longitudinal spectra $\mathcal{L}_{v,q}(\omega)$ against transverse one $\mathcal{L}_{u,q}(\omega)$, a power law behaviour with scaling exponent equal one should hold at least on the plateau range.

Figure 6.19 and 6.20 show respectively $\mathcal{L}_{v,q}(\omega)$ v.s. $\mathcal{L}_{u,q}(\omega)$ on the range $5 < \omega < 6000\,\mathrm{Hz}$, and $S_{v,q}(\tau)$ v.s. $S_{u,q}(\tau)$ on the range $5 < f(= 1/\tau) < 6000\,\mathrm{Hz}$ for various q. Graphically, power law behaviour holds as expected

$$\mathcal{L}_{v,q}(\omega) \sim (\mathcal{L}_{u,q}(\omega))^{\Gamma(q)}, \quad \xi_T(q) = \xi_L(q)\Gamma(q) \tag{6.5.11}$$

which provides

$$\xi_T(q) = \xi_L(q)\Gamma(q) \tag{6.5.12}$$

If the assumption of local isotropy holds, the scaling exponent $\Gamma(q)$ is then exactly equal to 1. Figure 6.21 shows the corresponding scaling exponent $\Gamma(q)$ estimated from

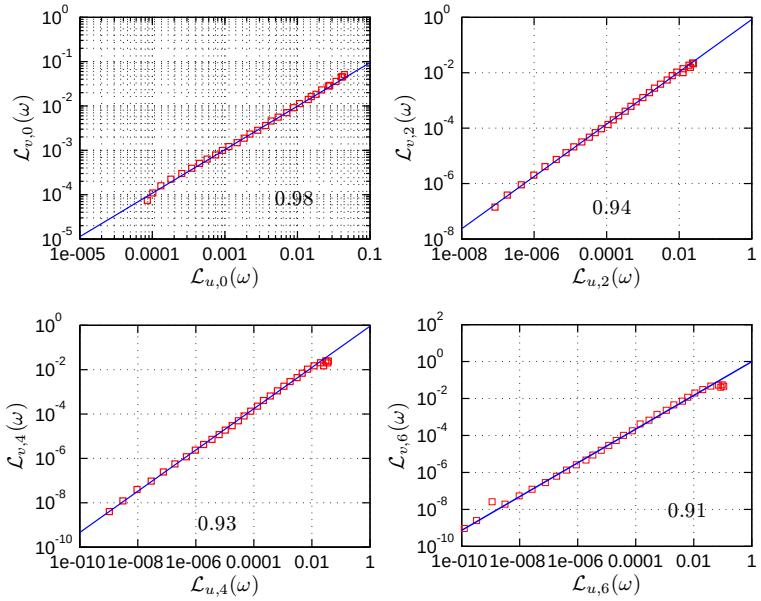

Figure 6.19: Representation of $\mathcal{L}_{v,q}(\omega)$ v.s. $\mathcal{L}_{u,q}(\omega)$ on the range $5 < \omega < 6000\,\mathrm{Hz}$, where $q = 0$, 2, 4 and 6, respectively. Power law behaviour is observed for all cases. The corresponding scaling exponent $\Gamma(q)$ is estimated on the inertial range $10 < \omega < 1000\,\mathrm{Hz}$.

the turbulent database. The isotropy scaling exponent $\Gamma(q)$ deviates from 1. The isotropy scaling exponent $\Gamma(q)$ decreases with the order q, which indicates that the anisotropy effect becomes more and more strong in high order statistical quantities. The HSA approach provides the larger scaling exponent, which may be linked to the local ability of the method. It may constrain the large scale anisotropy effect both in physical domain and frequency domain. However, for the high order q, $\Gamma(q)$ is significant less than 1 within statistical uncertainty. For structure function, it suggests an approximately linear expression

$$\Gamma^S(q) = -\hat{\gamma}q + \Gamma_o \tag{6.5.13}$$

where $\hat{\gamma} \simeq 0.018$ and $\Gamma_o \simeq 0.97$ are obtained experimentally. However, the influence of the large anisotropy scale on the structure function should be investigated

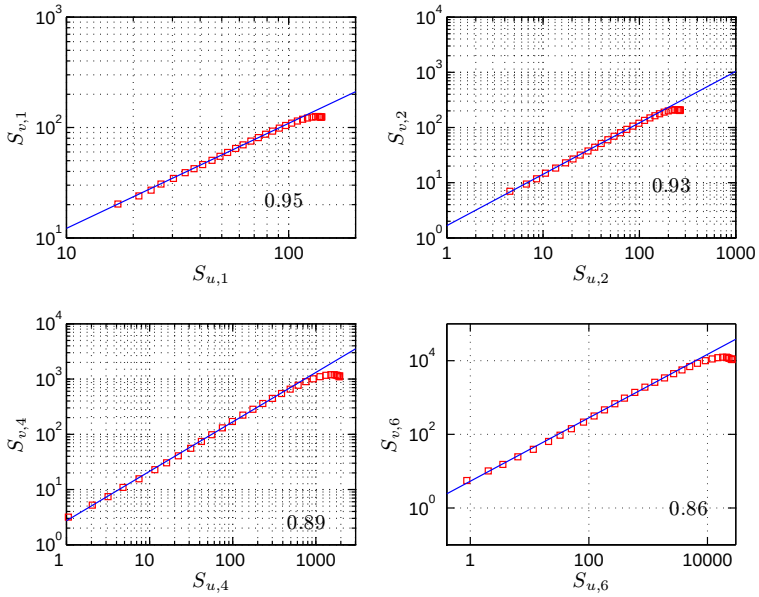

Figure 6.20: Representation of $S_{v,q}(\tau)$ v.s. $S_{u,q}(\tau)$ on the range $5 < f(= 1/\tau) < 6000\,\text{Hz}$, where $q = 0$, 2, 4 and 6. Power law behaviour is observed for all cases. The corresponding scaling exponent $\Gamma(q)$ is estimated on the inertial range $10 < f(= 1/\tau) < 1000\,\text{Hz}$.

systematically in the future studies.

Let us note that the two approaches we considered here are complementary, writting

$$\Gamma(q) = 1 - \beta(q) \tag{6.5.14}$$

We have

$$\zeta_T(q) = \zeta_L(q)(1 - \beta(q)) \tag{6.5.15}$$

and hence

$$\mathcal{I}(q)(\omega) \sim \omega^{\zeta_T(q) - \zeta_L(q)} \sim \omega^{-\beta(q)\zeta_L(q)} \tag{6.5.16}$$

This shows that if $\beta(q)$ is close to zero, $\mathcal{I}_q(\omega)$ has a flatness range and reciprocally if $\mathcal{I}_q(\omega)$ has a flatness range, $\beta(q)$ should close to zero. We cannot conclude on the best representation using the present experimental analysis.

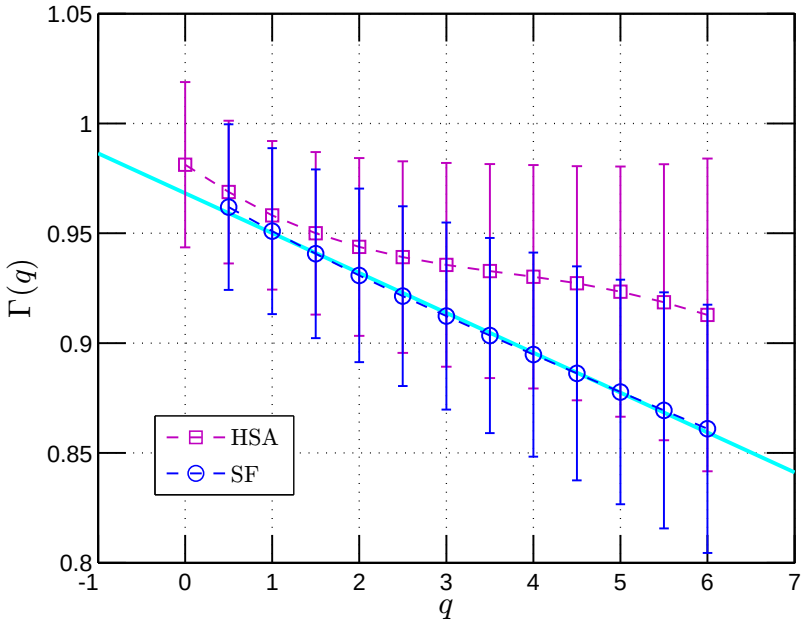

Figure 6.21: Representation of the isotropy scaling exponent $\Gamma(q)$, which are estimated from the arbitrary order Hilbert spectra $\mathcal{L}_q(\omega)$ ($\square$) and structure function ($\bigcirc$). For structure function, we have $\Gamma^S(q) \simeq -0.018q + 0.97$, which is obtained by the least square fitting.

Spatial Evolution

We may also consider the spatial evolution of these anisotropy indicators. Figure 6.22 shows the scale dependent isotropy ratio $\mathcal{I}$ at various downstream locations $x/M = 20$ ($\bigcirc$), $x/M = 30$ ($\square$), $x/M = 40$ ($\triangle$) and $x/M = 48$ ($\diamondsuit$), where the Kolmogorov isotropy ratio 3/4 is shown as horizontal solid line, and the vertical solid line illustrates the plateau range. The scale dependence isotropy ratio $\mathcal{I}$ are estimated by (a) the HSA approach, (b) the second order structure function and (c) the Fourier power spectrum. As we have shown above, the HSA approach and the Fourier power spectrum provide a similar shape of this ratio. The structure function is strongly influenced by the large scale anisotropy structure. We then show the mean isotropy

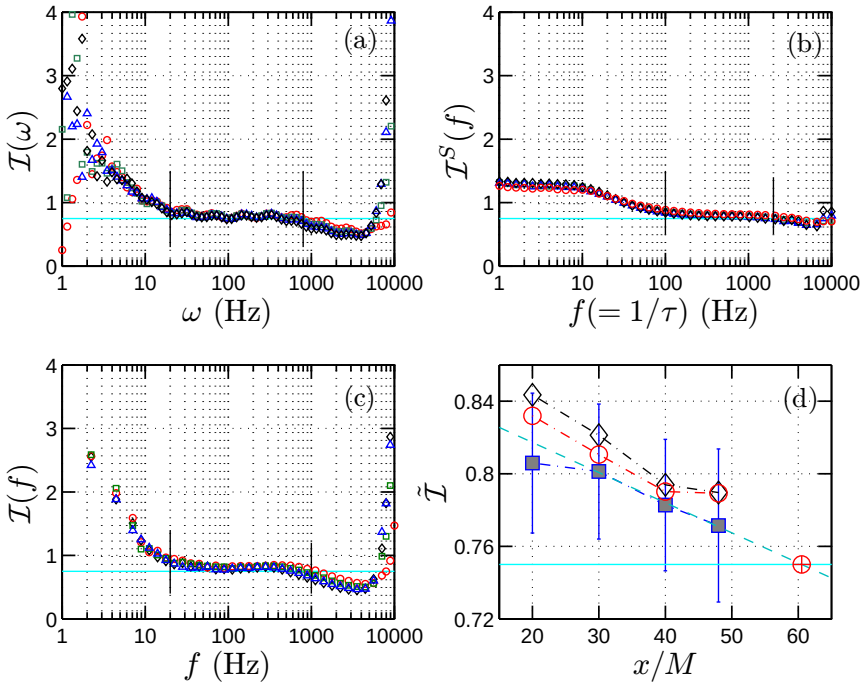

Figure 6.22: (a) The isotropy ratio $\mathcal{I}(\omega)$ estimated by the HSA approach at various downstream locations $x/M = 20$ (○), $x/M = 30$ (□), $x/M = 40$ (△) and $x/M = 48$ (♢); (b) the structure function; (c) the Fourier analysis. The vertical solid line indicates the plateau range, where the mean isotropy ratio $\tilde{\mathcal{I}}$ is estimated. The horizontal solid line illustrates the Kolmogorov value 3/4. (d) The mean isotropy ratio $\tilde{\mathcal{I}}$, provided by the HSA approach (□), the structure function (○) and the Fourier analysis (♢). The straight dashed line is the least square fit for the last three points of the HSA method. It predicts that the isotropy ratio may reach the Kolmogorov value at the downstream $x/M = 60.5$ (marked as ⊕).

ratio $\tilde{\mathcal{I}}$ in Fig. 6.22 (d), where the Kolmogorov isotropy value 3/4 is displayed as a horizontal solid line. It is interesting to note that both the Fourier approach and the structure function provide a similar spatial evolution trend: the isotropy ratio first decreases along the streamwise direction and reaches its minimum value at location $x/M = 40$ and then seems to saturate. The isotropy ratio seems to never reach the Kolmogorov value. The HSA approach gives a slightly different result. It seems that the isotropy ratio provided first decreases slowly and then decreases linearly along

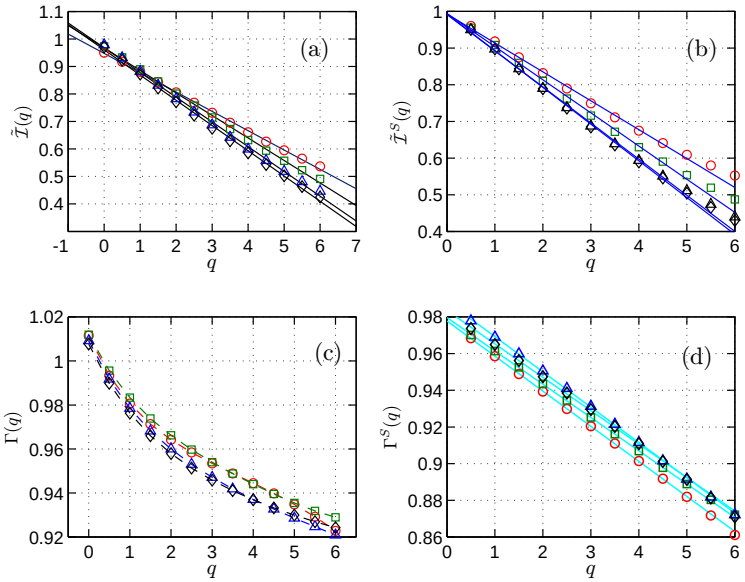

Figure 6.23: (a) The generalized mean isotropy ratio $\tilde{\mathcal{I}}(q)$ at various downstream, estimated by the HSA approach; (b) the structure function; (c) the isotropy scaling exponents $\Gamma(q)$ estimated by the HSA approach; (d) the structure function. The symbols are the same as Fig. 6.22 (a). The straight solid lines are the least square fit of each curve.

the downstream direction $\tilde{\mathcal{I}}(x) \simeq -0.017x/M + 0.85$. According to this linear trend, the isotropy ratio may reach its Kolmogorov value at the location $x/M = 60.5$, which is marked as $\oplus$ in Fig. 6.22 (d). Unfortunately, we do not have data on this location to check this prediction.

We now consider the downstream evolution for various orders q. Figure 6.23 shows the mean generalized isotropy ratio $\tilde{\mathcal{I}}$ provided by (a) the HSA approach, and (b) the structure function approach, and the isotropy scaling exponent $\Gamma(q)$ provided by (c) the HSA approach, and (d) the structure function approach for different 4 downstream values. The symbols are the same as Fig. 6.22 (a). Except for the Hilbert-based isotropy scaling exponent $\Gamma(q)$, see Fig. 6.23 (c), the others seem to linearly decrease with q with various slopes. We then show in Fig. 6.24 (a) the slope

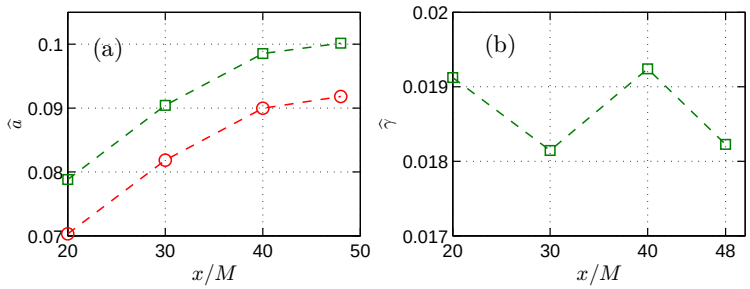

Figure 6.24: (a) The slope $\widehat{\alpha}$ of the generalization isotropy ratio estimated by the Hilbert-based approach (○) and the structure function (□); (b) The slope $\widehat{\gamma}$ of isotropy scaling exponents estimated by structure function approach. The mean value is $\widehat{\gamma} \simeq 0.187$.

$\hat{\alpha}$, and (b) the slope $\hat{\gamma}$. It seems that both Hilbert-based approach (○) and structure functions (□) provide the same evolution trend of $\hat{\alpha}$: they firstly increases with x/M and then seem to saturate at large x/M. However, the former one is small than the latter one. The slope of the isotropy scaling exponents is slight fluctuated around its mean value 0.187.

6.6 Summary

To summarize the main results of this chapter, we applied the EMD and the arbitrary order Hilbert spectral analysis methodology on an experimental homogeneous and nearly isotropy turbulence database. We found that the EMD acts as a dyadic filter bank for fully developed turbulence velocity time series. Based on the Fourier spectrum of each mode, we termed the IMF modes into different terms: measurement noise, dissipation range, inertial range and large forcing scale. We observed a scaling trend in the joint pdf $p(\omega, \mathcal{A})$ with a scaling exponent close to the Kolmogorov value. We then recovered the structure function scaling exponents $\zeta(q)$ in

amplitude-frequency space for the first time.

We tested the local isotropic hypothesis by considering the scale dependent isotropy ratio and the generalized isotropy ratio. The generalized isotropy ratio decreases linearly with q. The spatial evolution of the isotropy ratio shows that the isotropy ratio may reach the Kolmogorov value at downstream $x/M = 60.5$. The isotropy scaling exponent $\Gamma(q)$ suggested by the existence of the plateau of the scale dependent isotropy ratio is also studied. These scaling exponents deviate from 1, the value indicated by the local isotropy hypothesis. Furthermore, the scaling exponent provided by the structure function decreases linearly with order q. It implies that the high order structure function is strongly influenced by the large anisotropy scale part.

Chapter 7

Passive Scalar Turbulence

Another important issue in turbulence research is the passive scalar turbulence, which can be linked to many natural phenomena or engineering problems, such as pollutant diffusion, turbulent combustion, etc., see reviews by Sreenivasan (1996); Shraiman & Siggia (2000); Warhaft (2000). It has attracted huge interest during the last two decades (Antonia *et al.*, 1984; Sreenivasan, 1991, 1996; Ruiz-Chavarria *et al.*, 1996; Mydlarski & Warhaft, 1998; Shraiman & Siggia, 2000; Warhaft, 2000; Moisy *et al.*, 2001; Tsinober, 2001; Gylfason & Warhaft, 2004; Celani *et al.*, 2005; Schmitt, 2005). In the spirit of Kolmogorov, the relevant Obukhov-Corrsin law is a 1/3 scaling relation that predicts

$$S^q(\ell) = \langle |\Delta\theta(\ell)|^q \rangle \sim \ell^{\zeta_\theta(q)} \tag{7.0.1}$$

where $\Delta\theta(\ell) = \theta(x+\ell) - \theta(x)$, and $\zeta_\theta(q) = q/3$ is the corresponding scaling exponent. However, experimental evidence has shown that the scaling exponent $\zeta_\theta(q)$ is deviating from the simple KOC law, even with stronger deviation than the velocity field (Sreenivasan, 1991; Shraiman & Siggia, 2000; Warhaft, 2000). For example, it is found that the scaling exponent $\zeta_\Theta(q)$ is almost saturating for high order moments (Warhaft, 2000; Celani *et al.*, 2000). It is often believed that the so-called

"ramp-cliff" structures play an important role in scalar turbulent flows, see Fig. 7.1. For high order statistical moments, it seems that the statistical quantities, such as high order structure functions, are dominated by the ramp-cliff structure. Obviously, the ramp-cliff structure is a large scale structure with a ramp and a sharp cliff. It is believed that this structure couples with the small scales by the cliff structure. Thus it may have strong influence on both the small scales and large scales statistics.

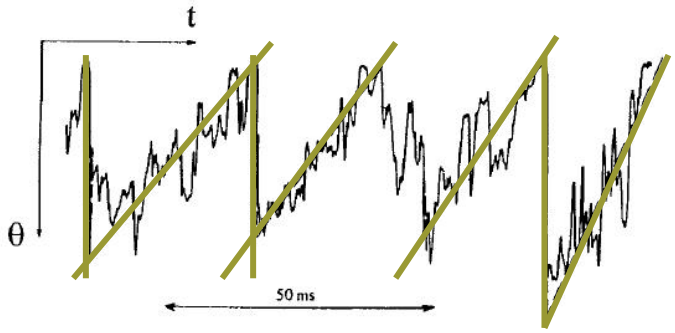

Figure 7.1: Illustration of the "ramp-cliff" structure. Graphically, the ramp-cliff structure is a large scale structure. Taken from Ref. Warhaft (2000)

We have shown previously that the structure functions are strongly influenced by large scales. It may then be that the saturation of scalar turbulence structure function is linked to the ramp-cliff structures. It could then be a shortcoming of the analysis approach instead of a real saturation of the scaling exponent associated to the most intense events. In this chapter, we check this hypothesis by considering scalar turbulence intermittency using arbitrary order Hilbert spectral analysis. The results presented in this chapter are not yet published. They will be in part included in a paper prepared for submission Huang *et al.* (2010b)[Y. Huang, *et al. Phy. Rev. Lett.*, 2009 (in preparation)].

7.1 Temperature data

The temperature data analyzed here are obtained from a jet experiment performed at Joseph Fourier University by Y. Gagne and P. Fougairolles, where a hot air jets from a nozzle into a cold ambient cross flow, see the sketch in Fig. 7.2. Along the flow direction, the jet may be separated into four different regions (A) potential core, (B) developing range, (C) developed range and (D) decaying range. The measurement

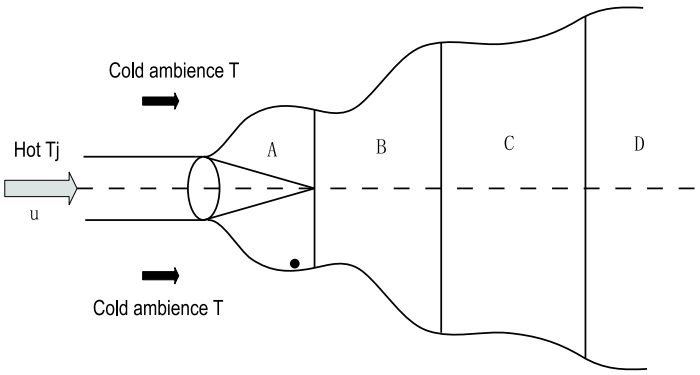

Figure 7.2: Sketch of the experiment. A hot air jets into the cold cross ambient flow from the nozzle: (A) potential core (B) developing range (C) developed range (D) decaying range. The measurement point (•) is close to the nozzle and the mixing layer. Therefore the flow here demonstrates strong intermittency properties.

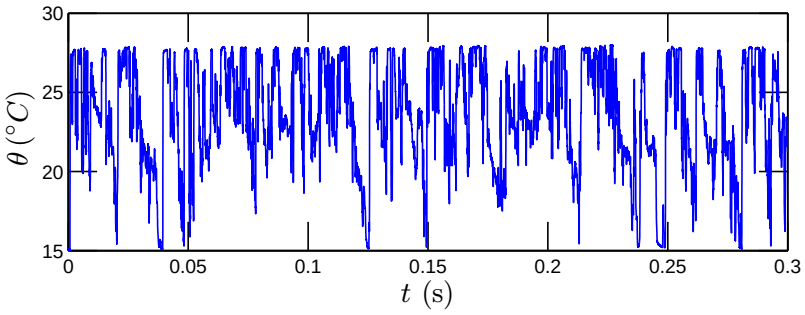

Figure 7.3: A 0.3 s portion of temperature time series. It illustrates the "ramp-cliff" structures and intermittent nature of passive scalar turbulence.

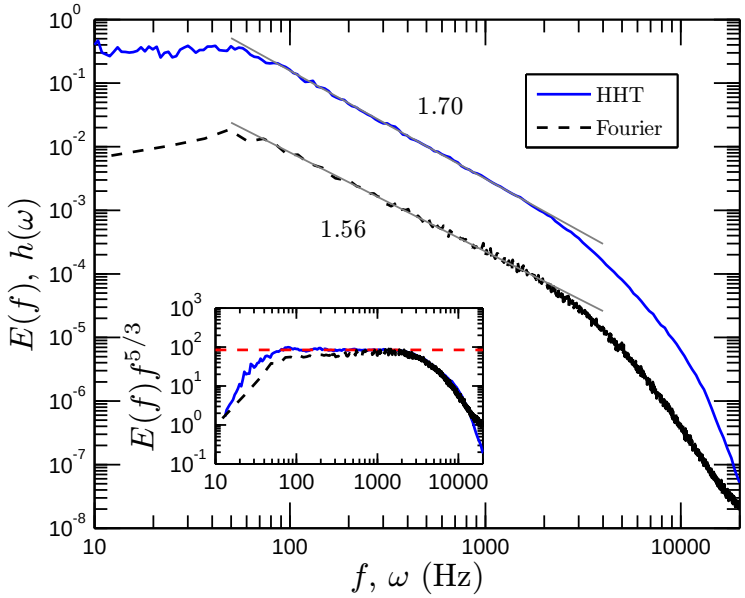

Figure 7.4: Comparison of the second order Hilbert marginal spectrum and Fourier spectrum. The inset shows the compensated spectrum $E(f)f^{5/3}$, which indicates a more than 1.4 decades of inertial range $80 < f < 2000$ Hz in both spectra. Since both EMD and HSA have very local abilities, they can constrain the ramp-cliff effects as much as they can, thus predict a steeper spectrum.

location is situated at the edge of the mixing layer and close to the nozzle. The initial temperature of the two flows are respectively T_J=27.8 °C and T=14.8 °C. The bulk Reynolds numbers are about $Re_J = 60000$ (based on the hydraulic diameter of the jet nozzle) and $Re_M = 1100$ (based on the mesh size of the turbulence grid of the cross flow channel). The Taylor-microscale based Reynolds number is estimated as $Re_\lambda = 250$. The sampling frequency is 50 kHz with a total 5×10^5 data points. A 0.3 s portion temperature time series is reproduced in Fig. 7.3. It illustrates a strong ramp-cliff structure and the intermittent nature of this passive scalar turbulence. Figure 7.4 shows the Fourier spectrum (dashed line) and Hilbert marginal spectrum (solid line), where the inset shows the corresponding compensated spectra. Power law behaviour is observed in both spectra on the range $80 < f(\text{ or } \omega) < 2000$ Hz, about 1.4 decades,

with scaling exponent 1.56 and 1.70 respectively for the Fourier power spectrum and the Hilbert spectrum. For the former one, it agrees with the value reported in other literatures, for example, see Refs. Sreenivasan (1996); Warhaft (2000). The latter is quite close to the scaling value of the longitude velocity in fully developed turbulent flows (Anselmet *et al.*, 1984; Benzi *et al.*, 1995; Frisch, 1995; Sreenivasan & Antonia, 1997).

7.2 EMD results

We divided the whole data into 122 segments (without overlapping), with 2^{12} data points each. After decomposition each segment is decomposed into several IMF modes, from 9 to 12 with one residual. We first check the mean frequency of each mode. The mean frequency $\overline{\omega}$ is defined by Eq. (6.2.1). Figure 7.5 shows the mean

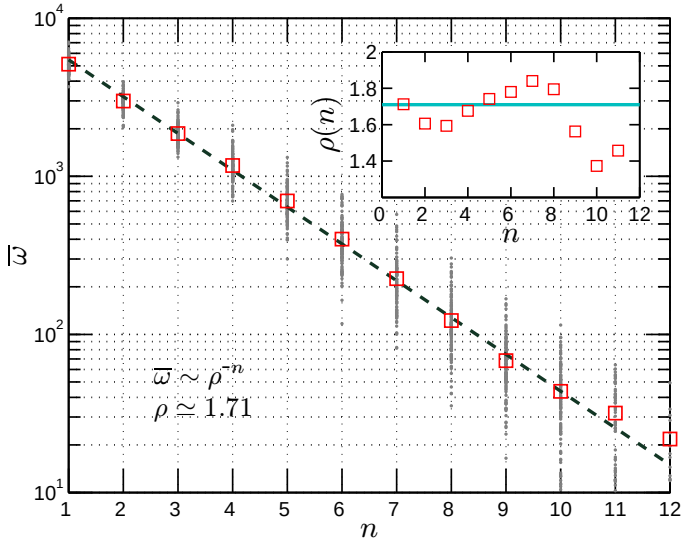

Figure 7.5: The mean frequency of IMF modes $\overline{\omega}$ vs modes n. Local slope $\rho(n)$ is shown as inset.

frequency $\overline{\omega}$, where the inset shows the local slope $\rho(n)$. One can find that, compared with the result for velocity, see Fig. 6.6, the mean frequency of each realization is rather scattered. However, the averaged mean value for all segments $\langle\overline{\omega}\rangle$ ($\square$) exponential decrease with mode index n as

$$\overline{\omega}(n) \sim \rho^{-n} \tag{7.2.1}$$

where $\rho \simeq 1.71$. This means that each mode is associated to a time scale almost 1.71 times larger than the previous one; this property is similar to a filter bank in the frequency domain (Flandrin & Gonçalvès, 2004; Wu & Huang, 2004; Huang *et al.*, 2008). We note that the deviation from a dyadic filter bank could be an effect of the ramp-cliff structure.

7.3 HSA results

Figure 7.6 shows the joint pdf $p(\omega, \mathcal{A})$, where the vertical dashed line illustrates the inertial range $80 < \omega < 2000\,\text{Hz}$. We observe a scaling trend. However, the length of data we have here is about 500,000 points. It is not long enough to get a smooth skeleton of this joint pdf. But nevertheless, as we show later, the arbitrary order Hilbert marginal spectrum is stable and convergent.

We provide here more comments on the marginal Hilbert spectrum and Fourier spectrum, see in Fig. 7.4. As mentioned previously, the Fourier transform is a linear asymptotic approach: it requires high order harmonic components to mimic nonlinear and nonstationary process. In this case, the high order harmonic component may lead an artificial energy transfer flux from a large scale (low frequency) to a small

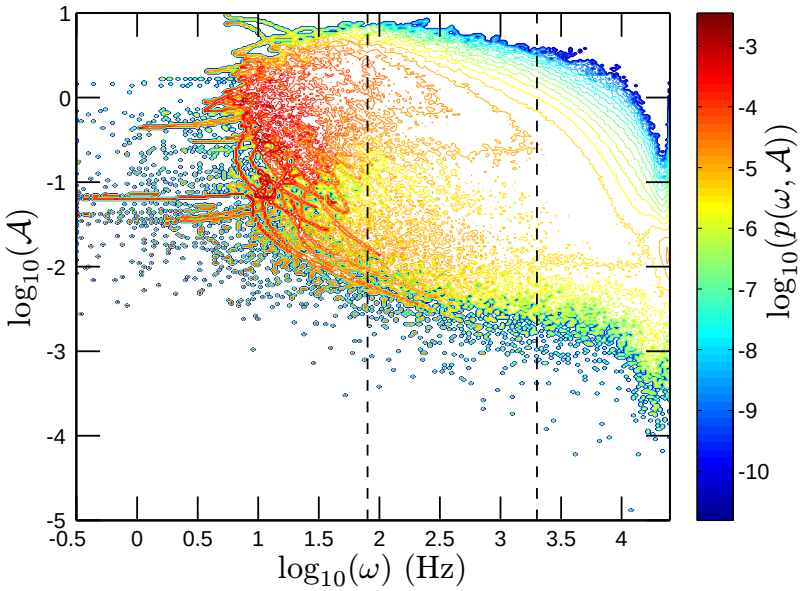

Figure 7.6: Representation of the joint pdf $p(\omega, \mathcal{A})$ for temperature fluctuations. The vertical dashed line indicates the inertial subrange. A scaling trend is observed in such presentation. However, due to the sample size, the skeleton of the joint pdf (not shown here) is rather scattered.

scale (high frequency). The artificial energy transfer may give a less steep power spectrum. We know that both EMD and HSA methodology have very local abilities both in physical and spectral domains: the Hilbert-based methodology can constrain the nonlinear and nonstationary effects (Huang *et al.*, 1998, 1999; Huang, 2005; Huang *et al.*, 2010a). In other words, it does not require any higher order harmonic components to simulate the nonlinear and nonstationary events. Thus, the Hilbert spectrum may reveal a less pertubated relation between the energy and the frequency.

Figure 7.7 shows the arbitrary order Hilbert marginal spectrum $\mathcal{L}_q(\omega)$, where $q = 0$, 1, 3, 4, 5 and 6. The vertical dashed line indicates the inertial subrange $80 < \omega < 2000$ Hz. Power law behaviour is observed in each plot on the inertial range, and the corresponding scaling exponents $\xi_\theta(q)$ are estimated on this range by

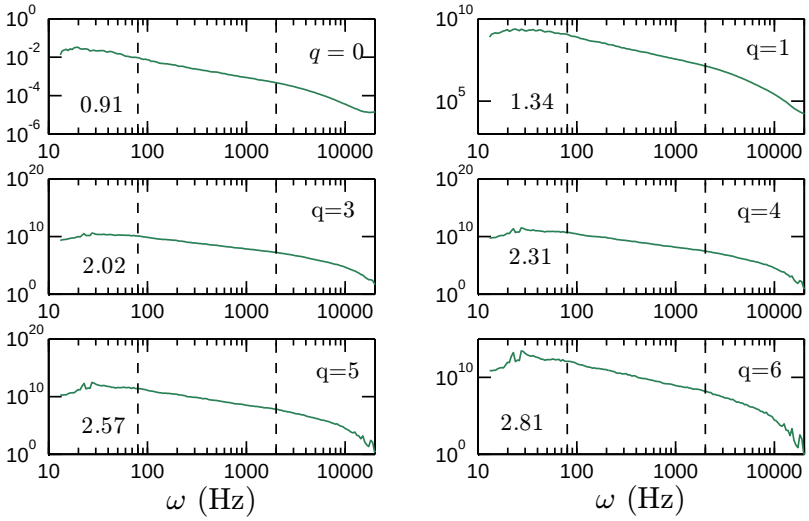

Figure 7.7: Arbitrary order Hilbert marginal spectrum $\mathcal{L}_q(\omega)$, where $q = 0$, 1, 3, 4, 5 and 6. Power law behaviour is observed on the range $80 < \omega < 2000$ Hz in all cases. The corresponding scaling exponents $\xi_\theta(q)$ is shown in each figure.

a least square fitting algorithm. We compare the scaling exponents $\xi_\theta(q) - 1$ ($\bigcirc$), $\zeta_\theta(q)$ from structure function ($\diamondsuit$), the value $\zeta_\theta(q)$ complied by Schmitt (2005) ($\square$ with error bar) with the theoretical value $q/3$ (solid line) in Fig. 7.8. The inset shows the scaling exponents departure from the theoretical KOC value. The classical structure function analysis method, as we will show in next section, it is strongly influenced by the ramp-cliff structure. The scaling exponent is then estimated by a least square fitting algorithm and by choosing the range case by case. The scaling exponent begins to be saturated when $q > 3$. It is usually interpreted as an evidence that the passive scalar field is more intermittent than the velocity field (Sreenivasan, 1991; Shraiman & Siggia, 2000; Warhaft, 2000). Using the HSA approach, a more clear inertial range holds for each plot, up to order 8. To compare with the velocity field, we plot the ESS result $\zeta(q)$ (dashed line) for longitude velocity (Benzi *et al.*, 1995) in the same figure. We find that the scaling exponent $\xi(q)$ is quite close to the ESS result for the

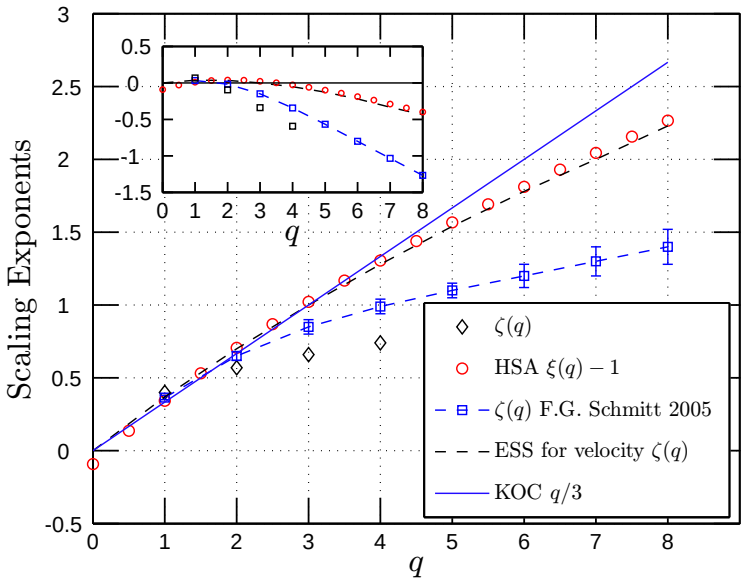

Figure 7.8: Comparison of the scaling exponents, which are estimated by the HSA $\xi_\theta(q)-1$ ($\bigcirc$), the structure functions $\zeta_\theta(q)$ ($\diamondsuit$), the value compiled by Schmitt (2005) ($\square$ with error bar) and the theoretical value $q/3$ (solid line). We also show the ESS result (dashed line) for longitudinal velocity (Benzi *et al.*, 1995). The inset shows the departure from the KOC theoretical value.

velocity, which may indicate that the scalar field is not so intermittent as what we have believed before. This is obtained here for one database, and should be confirmed using other database before a firm conclusion can be proposed.

7.4 Structure function analysis

As already noticed by several authors, for example, Antonia (Antonia *et al.*, 1984), Ruiz-Chavarria (Ruiz-Chavarria *et al.*, 1996) and Warhaft (Warhaft, 2000), for scalar turbulence, the scaling exponents of Fourier spectrum β_θ is not consistent with the second order structure function $\zeta_\theta(2)$: the relation $\zeta_\theta(2) = \beta_\theta - 1$ is not verified. This may be an effect of the ramp-cliff structure. Furthermore, it has been reported

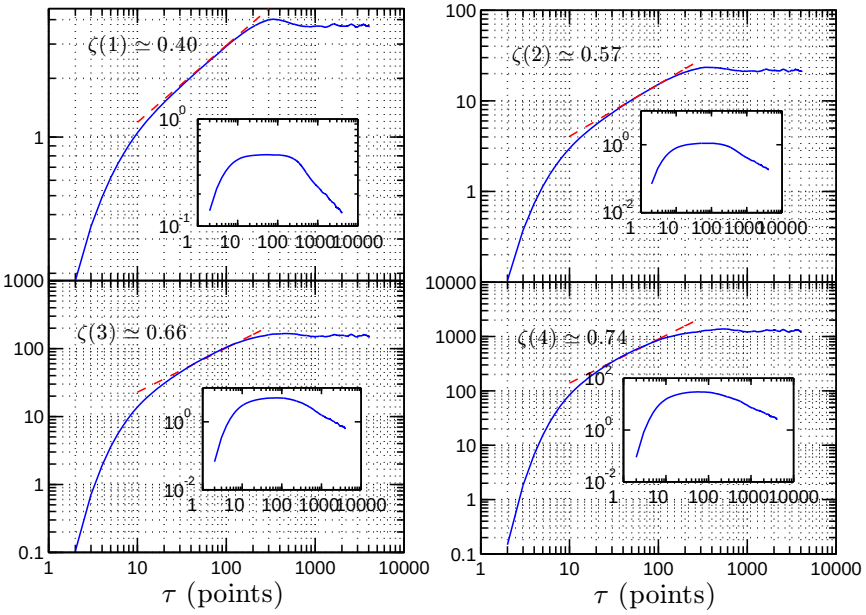

Figure 7.9: The structure function of temperature $S^q(\ell)$, $q = 1, 2, 3, 4$. The inset shows the corresponding compensated spectrum $S^q(\ell)\ell^{\zeta(q)}$. Power law range decreases with the order q, which may be interpreted as the effects of the ramp-cliff structure.

that the scalar spectrum has a larger scaling range than the velocity field at the same Re_λ (Jayesh & Warhaft, 1994; Gylfason & Warhaft, 2004). We have discussed previously that, in case of possessing large energetic nonlinear structures, the Fourier analysis needs high order harmonic components. Thus, both the inertial range and the scaling exponents may be contaminated by the ramp-cliff structure.

Figure 7.9 shows the first fourth order structure functions, where the insect shows the corresponding compensated spectrum by taking the estimated scaling exponent $\zeta_\theta(q)$. Due to the effect of the ramp-cliff structure, the inertial range decreases with the order q. When $q > 4$, there is no clear power law any more. It is believed that the structure function itself is then dominated by the ramp-cliff structure for high order structure function (Gylfason & Warhaft, 2004).

7.5 Summary

In this chapter, we applied the EMD and arbitrary order Hilbert spectral analysis to a temperature from a jet experiment. The data have very strong ramp-cliff structures, which have been considered as an important signature of passive turbulence. We find that the EMD algorithm acts a filter bank. Due to the effect of ramp-cliff structure, it deviates from a dyadic filter bank, which have been obtained previously using stochastic simulations of Gaussian noise, fractional Gaussian noise (fGn) and the fully developed turbulence velocity (Wu & Huang, 2004; Flandrin & Gonçalvès, 2004; Huang *et al.*, 2008).

We then considered the intermittency property of these data. It is found that the scaling exponent $\xi_\theta(q)$ provided by the Hilbert-based methodology is quite close to the ESS-based scaling exponent $\zeta(q)$ of the longitudinal velocity. Due to the very local ability of the Hilbert-based approach and the intrawave frequency modulation mechanism of the nonlinear process, the present method does not require high order harmonic components to mimic the ramp-cliff structure. Thus, the scalar turbulence may be not so intermittent as what we believed before. We should reconsider the role of the ramp-cliff structure in this framework. These results need to be confirmed using other passive scalar databases. This will be done in future work.

Chapter 8

Extended Self-Similarity and Hierarchy Model

During the last 2 or 3 decades, to extract the scaling exponents $\zeta(q)$ from various turbulent flows became a quite general approach in turbulent research (Anselmet *et al.*, 1984; Antonia *et al.*, 1984; Benzi *et al.*, 1993a; Frisch, 1995; Arneodo *et al.*, 1996; Sreenivasan & Antonia, 1997). One interesting improvement methodology is the so-called Extended-Self Similarity (ESS), which was proposed by Benzi *et al.* (1993a,b, 1995). It is believed that the ESS approach provides a more accuracy estimation of the scaling exponents $\zeta(q)$ and extends the power law range (Benzi *et al.*, 1993a). In this chapter, we will adapt the ESS idea into the Hilbert frame.

We recall Benzi's ESS theory here. According to Kolmogorov's refined similarity hypothesis (Kolmogorov, 1962; Frisch, 1995), the statistical properties of small scales are uniquely determined by the local energy dissipation rate ϵ_r and the scale r, where

$$\epsilon_r(x,t) = \frac{6}{\pi r^3} \int_{|r'|<r/2} \epsilon(x+r',t)\,\mathrm{d}r' \tag{8.0.1}$$

where $r/2$ is radius of the sphere. The qth order structure function is written

$$S^q(r) = \langle |u(x+r) - u(x)|^q \rangle \sim \langle \epsilon_r^{q/3} \rangle r^{q/3} \tag{8.0.2}$$

where $\langle\,\rangle$ is ensemble average. If the local energy dissipation rate ϵ_r itself has scaling law

$$\langle \epsilon_r^q \rangle \sim r^{K(q)} \tag{8.0.3}$$

where $K(0) = 0$. It then follows

$$\zeta(q) = q/3 - K(q/3) \tag{8.0.4}$$

The above equation connects the scaling exponents $\zeta(q)$ with the scaling intermittency of the dissipation since the mean dissipation is assumed to be conserved, $\langle \epsilon_\ell \rangle = \bar{\epsilon}$. So that $K(1) = 0$ and $\zeta(3) = 1$. This can be also obtained from the Kolmogorov (1941c) equation, for $r \gg \eta$ ($\eta \equiv \nu^{3/4}\epsilon^{-1/4}$ is Kolmogorov scale), one has

$$S^3(r) = -\frac{4}{5}\epsilon r \tag{8.0.5}$$

This is the famous Kolmogorov Four-Fifths law (Kolmogorov, 1941c; Monin & Yaglom, 1971; Frisch, 1995), which is the only one exactly statistical solution of Navier-Stokes equation for turbulence. It confirms the relation $K(1) = 0$ and $\zeta(3) = 1$, which means that the third order structure function $S^3(r)$ is free from the intermittency correction. Benzi *et al.* (1993a) suggested to plot $S^q(r)$ vs $S^3(r)$ instead of $S^q(r)$ vs r in structure function analysis, which reads

$$S^q(r) \sim S^3(r)^{\zeta^\star(q)} \tag{8.0.6}$$

Since $S^3(r)$ is proportional to r, the scaling exponent $\zeta^\star(q)$ is supposed to be the same as $\zeta(q)$. It has been found that ESS is valid not only for high Reynolds number turbulent flows but also for moderate Reynolds numbers, even when there is no clear inertial range (Benzi *et al.*, 1993a,b, 1995). The method was therefore extensively used in turbulence research and even in other fields such as natural science or finance. In the next section we consider this approach in the Hilbert spectral analysis framework.

8.1 Extended-Self similarity

Considering the Kolmogorov refined similarity hypothesis, we have the following relation for the arbitrary order Hilbert spectra in the Hilbert frame

$$\mathcal{L}_q(\omega) \sim \langle \epsilon_r^{q/3} \rangle \omega^{-(1+q/3)} \tag{8.1.1}$$

where $q \geq 0$. We have here two special cases $q = 0$[1] and $q = 3$, which are free from intermittency effect. Following the ESS idea of Benzi *et al.* (1993a,b), we link the arbitrary order Hilbert spectrum $\mathcal{L}_q(\omega)$ with these two special cases

$$\mathcal{L}_q(\omega) \sim (\mathcal{L}_p(\omega))^{\xi_p(q)/\xi(p)} \tag{8.1.2}$$

where $p = 0$ or $p = 3$. We denote $\xi_0(q)$ and $\xi_3(q)$ the corresponding scaling exponents.

Figure 8.1 shows a test of the ESS of the case $p = 0$ for various q on the range $10 < \omega < 6000\,\mathrm{Hz}$. The vertical dashed line illustrates the inertial range $10 < \omega < 1000\,\mathrm{Hz}$. A power law behaviour is observed in each plot on the inertial range , and the scaling exponents $\xi_0(q)$ is estimated on this range by using a least square fitting algorithm on the inertial range. Figure 8.2 shows the case $p = 3$, where the vertical dashed line demonstrates the inertial range $10 < \omega < 1000\,\mathrm{Hz}$, and the thick solid line indicates the location $\omega = 3000\,\mathrm{Hz}$. It seems that, except the zeroth order Hilbert marginal spectrum, the power law range extends as expected. We take the $\mathcal{L}_7(\omega)$ as example: the scaling range extends to $\omega = 3000\,\mathrm{Hz}$. This is similar with the observations done for the traditional ESS (Benzi *et al.*, 1993b, 1995). The corresponding scaling exponent $\xi_3(q)$ is then estimated on the range $10 < \omega < 3000\,\mathrm{Hz}$.

[1] As mentioned in chapter 3, the zeroth order Hilbert marginal spectrum is the marginal pdf of the instantaneous frequency. We have found the general property that such marginal pdf itself has a power law behaviour, and the corresponding scaling exponent $\xi(0)$ is close to 1, which is rather natural since it corresponds to $\zeta(0) = 0$.

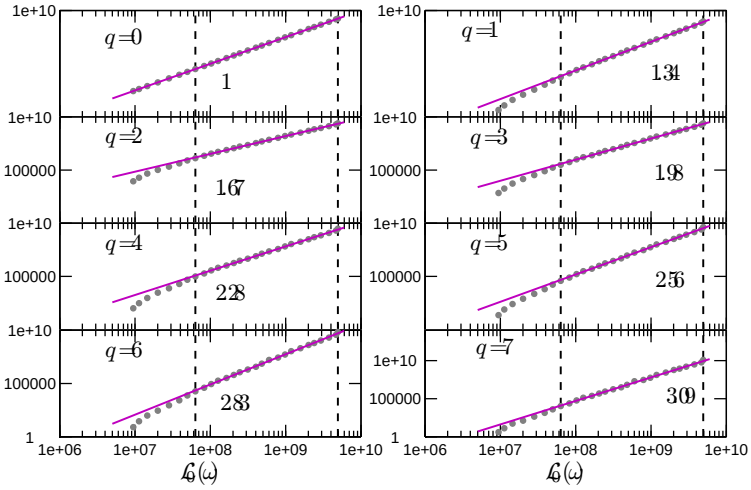

Figure 8.1: A test of Extended Self-Similarity of arbitrary order Hilbert spectra $\mathcal{L}_q(\omega)$ V.S. $\mathcal{L}_0(\omega)$ for the longitudinal velocity, $q = 0$, 1, 2, 3, 4, 5, 6 and 7 on the range $10 < \omega < 6000\,\mathrm{Hz}$. The dashed line indicates the inertial range $10 < \omega < 1000\,\mathrm{Hz}$. The scaling exponent $\xi(q)$ is then estimated on this range.

We then compare the scaling exponents $\xi(q)$ in Fig. 8.3 for different estimators[2], HSA result $\xi(q) - 1$ ($\times$), Hilbert-based ESS $\xi_0(q) - 1$ ($\square$) and $\xi_3(q) - 1$ ($\triangleleft$), $\zeta(q)$ (dashed line) provided by the traditional ESS (Benzi *et al.*, 1995), and the K41 prediction (solid line), see also Tab. 8.1. The inset shows the departure from the K41 $q/3$ law. The scaling exponents $\xi_0(q)$ and $\xi_3(q)$ are in good agreement with $\zeta(q)$ when $q \leq 4$. When $q < 4$, the Hilbert-based estimators display a larger scaling exponents than the structure function based ESS $\zeta(q)$.

For comparison, we consider the log-Lévy model and the log-normal model here (Frisch, 1995; Schertzer *et al.*, 1997). The log-Lévy model (Schertzer & Lovejoy, 1987; Kida, 1991; Schmitt *et al.*, 1992; Schertzer *et al.*, 1997) predicts a scaling exponent

$$\zeta(q) = q/3 - \frac{C_1}{\alpha - 1}\left[(q/3)^\alpha - q/3\right] \tag{8.1.3}$$

where C_1 is the codimension of the mean events ($0 \leq C_1 \leq d$, where d is the dimension

[2]We do not apply here the structure function analysis on these database.

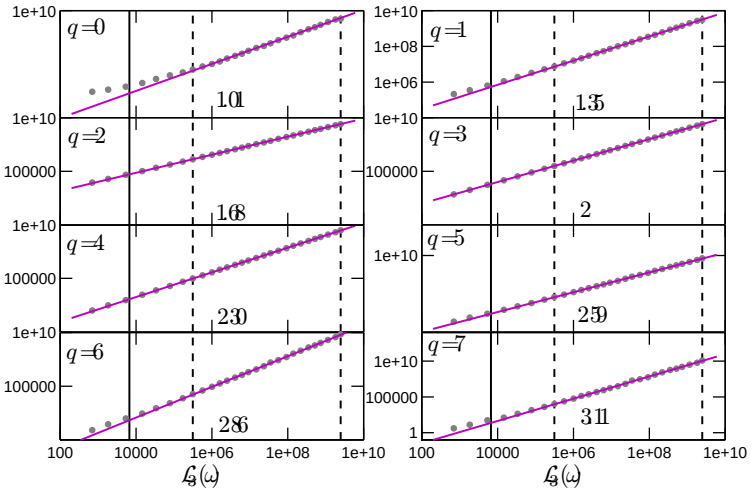

Figure 8.2: A test of Extended Self-Similarity of arbitrary order Hilbert spectra $\mathcal{L}_q(\omega)$ V.S. $\mathcal{L}_3(\omega)$ for the longitudinal velocity, $q = 0$, 1, 2, 3, 4, 5, 6 and 7 on the range $10 < \omega < 6000$ Hz, where the dash line indicates the inertial range $10 < \omega < 1000$ Hz. The vertical thick solid line indicates the location of 3000 Hz. The scaling exponent $\xi(q)$ is then estimated on this range.

of the observation space), and α is the Lévy index, bounded between 0 and 2. We fix $\alpha = 1.5$ (Schertzer *et al.*, 1997) and consider C_1 as a free parameter. We fit experimental data by a least square fitting algorithm. C_1 is found to be 0.095 for Hilbert-based ESS scaling exponent. The log-normal model predicts

$$\zeta(q) = \frac{q}{3} - \frac{\mu}{18}\left(q^2 - 3q\right) \tag{8.1.4}$$

where μ is the so-called intermittency parameter (Frisch, 1995; Schertzer *et al.*, 1997). We take here μ as a free parameter. The μ is found to be 0.15, which is comparable with 0.2, an estimation value provided by Anselmet *et al.* (1984). Graphically, both of these two models with the present chosen parameter predict the same scaling exponents.

As we have mentioned previously, the data we used here are generated by the active-grid technique. The results presented here may be influenced by a lack of

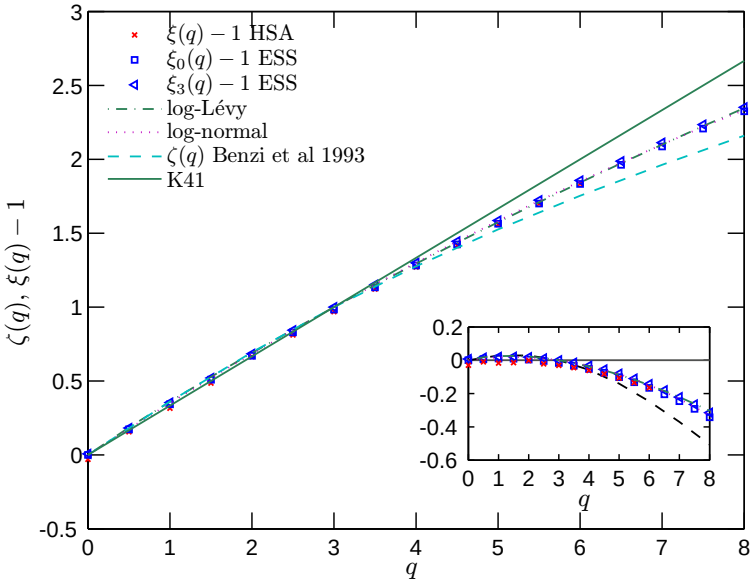

Figure 8.3: Comparison of the scaling exponents $\xi(q) - 1$ ($\times$), ESS $\xi_0(q) - 1$ ($\square$), ESS $\xi_3(q) - 1$ ($\triangleleft$), the $\zeta(q)$ provided by the ESS method (Benzi *et al.*, 1995) (dashed line) and K41 $q/3$ (solid line). We also show a best fitting of the data by log-Lévy model (dashed-dotted line) with $C_1 = 0.095$ and $\alpha = 1.5$, log-normal model (dotted line) with $\mu = 0.15$. The inset shows the departure from the K41 law.

isotropy, see chapter 6, we thus should check this ESS idea on more databases.

8.2 Hierarchy model

We have shown in chapter 6 that the skeleton $\mathcal{A}_s(\omega)$ and its corresponding conditional pdf $p_{\max}(\omega)$ of the joint pdf $p(\omega, \mathcal{A})$ have a power law behaviour on the inertial range $10 < \omega < 1000\,\text{Hz}$, where ω is the instantaneous frequency and $\mathcal{A}$ is the amplitude. This power law is written as

$$\mathcal{A}_s(\omega) \sim \omega^{-\beta_1}, \quad p_{\max}(\omega) \sim \omega^{-\beta_2} \tag{8.2.1}$$

where $\beta_1 = 0.38 \pm 0.05$ and $\beta_2 = 0.63 \pm 0.05$, see Fig. 6.10. We also found dimensionally that without intermittency we have

$$\beta_1 = \frac{1}{3}, \quad \beta_2 = \frac{2}{3} \tag{8.2.2}$$

see chapter 6. Following She and Lévêque's hierarchy model (She & Lévêque, 1994), we present a hierarchy model in the following.

A Weighted Function For Hilbert Marginal Spectra

We have shown previously that the joint pdf $p(\omega, \mathcal{A})$ is strongly peaked around $\mathcal{A}_s(\omega)$, see Fig. 6.12. The arbitrary order Hilbert marginal spectrum $\mathcal{L}_q(\omega)$ can be rewritten as

$$\mathcal{L}_q(\omega) = \mathcal{G}(\omega, q) p_{\max}(\omega) \mathcal{A}_s(\omega)^{1+q} \tag{8.2.3}$$

where $\mathcal{G}(\omega, q)$ is a weighted function. It may be determined by different distribution functions for $p(\omega, \mathcal{A})$. For high Reynolds number turbulent flows, where the local homogeneous and isotropy hypotheses hold, we assume that Eq. (8.2.1) is valid at least on the inertial subrange. It indicates that

$$\mathcal{L}_q(\omega) \sim \mathcal{G}(\omega, q) \omega^{-((1+q)\beta_1 + \beta_2)} \tag{8.2.4}$$

For discussion convenience, we assume that the intermittency does not affect the skeleton $\mathcal{A}_s(\omega)$ and the corresponding conditional pdf $p_{\max}(\omega)$.[3] We then have

$$\mathcal{L}_q(\omega) \sim \mathcal{G}(\omega, q) \omega^{-(1+q/3)} \tag{8.2.5}$$

For different distribution models of the joint pdf $p(\omega, \mathcal{A})$, the weight function $\mathcal{G}(\omega, q)$ may have different forms. It may be universal for high Reynolds turbulent flow. For

[3] Based on the observation of the joint pdf $p(\omega, \mathcal{A})$, the intermittency does influence on $\mathcal{A}_s(\omega)$ and $p_{\max}(\omega)$, see Fig. 6.10.

example, if $\mathcal{G}(\omega, q)$ is independent from ω and q, Eq. (8.2.5) then one recovers the K41 prediction.

The weighted function $\mathcal{G}(\omega, q)$ may be determined by considering the compensated arbitrary order Hilbert marginal spectrum

$$\mathcal{G}(\omega, q) \sim \mathcal{L}_q(\omega)\omega^{1+q/3} \sim \omega^{-\Lambda(q)} \tag{8.2.6}$$

Thus $\Lambda(q)$ measures the departure from the K41 theory. This finally give

$$\Lambda(q) = \xi(q) - (1 + \frac{q}{3}) \tag{8.2.7}$$

According to Kolmogorov's 1962 refined similarity hypothesis (Kolmogorov, 1962), we have $\Lambda(0) = \Lambda(3) = 0$, which means they are free with the intermittency effect.

A Hierarchical Model

Following the hierarchical model idea of She & Lévêque (1994), we define a hierarchical spectral function $\mathcal{L}^{(q)}(\omega)$ by the ratio of two successive arbitrary order Hilbert spectra

$$\mathcal{L}^{(q)}(\omega) \quad = \quad \frac{\int p(\omega, \mathcal{A})\mathcal{A}^{q+1}\,\mathrm{d}\mathcal{A}}{\int p(\omega, \mathcal{A})\mathcal{A}^{q}\,\mathrm{d}\mathcal{A}} = \int \mathcal{Q}_q(\omega, \mathcal{A})\mathcal{A}\,\mathrm{d}\mathcal{A} \tag{8.2.8}$$

where $q \geq 0$, and $\mathcal{Q}_q(\omega, \mathcal{A}) = p(\omega, \mathcal{A})\mathcal{A}^{q+1} / \int p(\omega, \mathcal{A})\mathcal{A}^q\,\mathrm{d}\mathcal{A}$ is weighted pdf for which $\mathcal{L}^{(q)}(\omega)$ is a mathematical expectation. Similar with $\epsilon_r^{(q)} = < \epsilon_r^{q+1} > / < \epsilon_r^q >$, when $q \to \infty$, $\mathcal{L}^{(\infty)}(\omega)$ measures the most intermittent structures (She & Lévêque, 1994). We then expect that the power law behaviour holds at least in the inertial range

$$\mathcal{L}^{(q)}(\omega) \sim \omega^{-\Pi(q)} \tag{8.2.9}$$

where

$$\Pi(q) = \xi(q+1) - \xi(q) \tag{8.2.10}$$

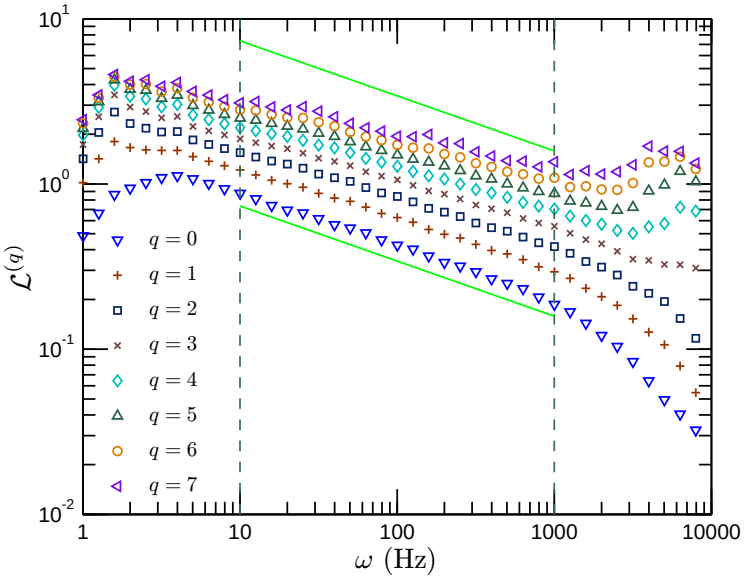

Figure 8.4: Representation of the hierarchical spectral function $\mathcal{L}^{(q)}(\omega)$, where q =0 ($\triangledown$), 1 (+), 2 ($\square$), 3 ($\times$), 4 ($\diamondsuit$), 5 ($\triangle$), 6 ($\bigcirc$) and 7 ($\triangleleft$). A power law behaviour is observed in the inertial range $10 < \omega < 1000\,\mathrm{Hz}$, which is indicated by the vertical dashed line. The solid line demonstrates the Kolmogorov value 1/3.

The dimensional consideration indicates for the non-intermittency case

$$[\mathcal{L}^{(q)}] = [\mathcal{A}], \quad \Pi(q) = \frac{1}{3} \tag{8.2.11}$$

Figure 8.4 shows the hierarchical spectral function $\mathcal{L}^{(q)}(\omega)$ for various $q = 0$ ($\triangledown$), 1 (+), 2 ($\square$), 3 ($\times$), 4 ($\diamondsuit$), 5 ($\triangle$), 6 ($\bigcirc$) and 7 ($\triangleleft$). The solid line indicates the Kolmogorov value 1/3 for the nonintermittent case, and the vertical dashed line illustrates the inertial range $10 < \omega < 1000\,\mathrm{Hz}$. A power law behaviour is observed on this inertial range for all curves. The slope shows departure from the nonintermittent value when q is increasing. We estimate the scaling exponent $\Pi(q)$ on the inertial range. The corresponding scaling value $\Pi(q)$ ($\bigcirc$) is shown in Fig. 8.5, where the horizontal thick solid line indicates the Kolmogorov value 1/3. For comparison, we also show the corresponding $\Pi(q)$ estimated from the Hilbert-based ESS $\xi_3(q)$ ($\square$), the

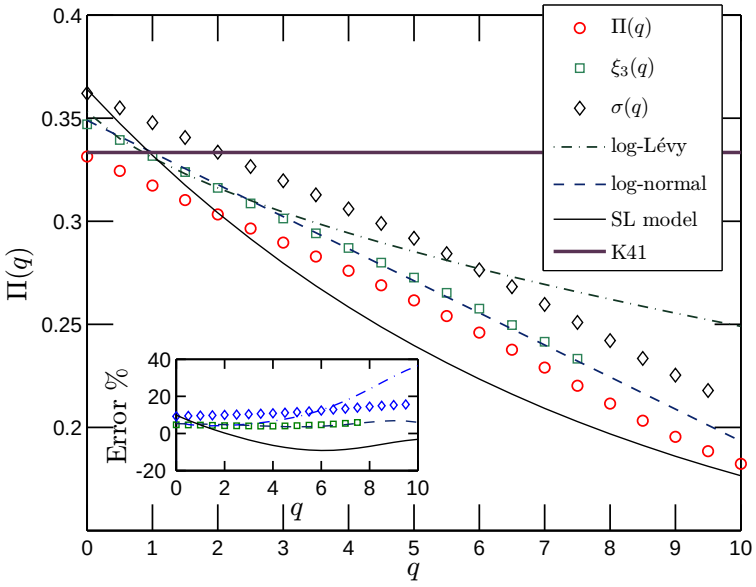

Figure 8.5: Representation of the scaling exponents $\Pi(q)$ ($\bigcirc$) for the hierarchical spectral function $\mathcal{L}^{(q)}(\omega)$. The horizontal thick line indicates Kolmogorov value 1/3. The corresponding scaling exponent $\Pi(q)$ is estimated on the inertial subrange $10 < \omega < 1000\,\text{Hz}$. For comparison, we also show the corresponding scaling exponents from $\xi_3(q)$ ($\square$), $\sigma(q)$ ($\diamondsuit$), the log-Lévy model with $C_1 = 0.07$, $\alpha = 1.5$ (dashed-dotted line), log-normal model with $\mu = 0.11$ (dashed line) and SL model (solid line). The inset shows the relative error from $\Pi(q)$.

Hilbert-based generalized ESS $\sigma(q)$ ($\diamondsuit$) (see below), log-Lévy model with $C_1 = 0.07$ and $\alpha = 1.5$ (dashed-dotted line), log-normal model with $\mu = 0.11$ (dashed line)[4] and SL model (thin solid line). The relative error from the direct estimated $\Pi(q)$ is shown as inset. The estimated $\Pi(q)$ decreases linearly with q with the same 0.015 obtained graphically. In this case, only log-normal model provides a linear prediction of $\Pi(q)$. Based on this observation, the log-normal model with such chosen parameter seems to give the best fitting among these three models.

[4]The parameters we choose here is based on the Hilbert-based ESS $\xi_3(q)$. This means that we fit $\xi_3(q)$-based $\Pi(q)$ to determine the parameters C_1 and μ.

8.3 Generalized Extended-Self similarity

Following the idea of generalized extended self-similarity of Benzi *et al.* (1996), let us introduce a dimensionless arbitrary order Hilbert marginal spectrum

$$\mathcal{Z}_q(\omega) = \frac{\mathcal{L}_q(\omega)}{\mathcal{L}_3(\omega)^{q/3}} \sim \omega^{-\sigma(q)} \tag{8.3.1}$$

in which

$$\sigma(q) = \xi(q) - \frac{\xi(3)q}{3} \tag{8.3.2}$$

where $\xi(q)$ is the scaling exponent. We expect that the dimensionless arbitrary order Hilbert marginal spectrum $\mathcal{Z}_q(\omega)$ itself has power law behaviour. We postulate a Generalized Extended-Self Similarity (GESS) (Benzi *et al.*, 1996), which is written as

$$\mathcal{Z}_q(\omega) \sim (\mathcal{Z}_p(\omega))^{\rho(q,p)} \tag{8.3.3}$$

By the definition we have

$$\rho(q,p) = \frac{\sigma(q)}{\sigma(p)},\ p \neq 3 \tag{8.3.4}$$

Figure 8.6 shows the dimensionless arbitrary order Hilbert marginal spectrum $\mathcal{Z}_q(\omega)$ for various q, 0 ($\bigcirc$), 2 ($\square$), 4 ($\triangle$), 6 ($\diamondsuit$), 8 ($\triangleleft$), 10 ($\triangleright$). The vertical dashed line demonstrates the inertial subrange $10 < \omega < 1000$ Hz. A power law behaviour is observed in each representation. We estimate the corresponding $\sigma(q)$ on the inertial range by using a least square fitting algorithm. The scaling exponent $\sigma(q)$ ($\bigcirc$) is shown in Fig. 8.7. For comparison, we also show the corresponding scaling value in the same figure, provided by the Hilbert-based ESS $\xi_3(q)$ ($\triangleleft$), the log-Lévy model with $C_1 = 0.07$ and $\alpha = 1.5$ (dashed line), the log-normal model with $\mu = 0.11$ (dashed-dotted line) and the SL model (solid line). The inset shows the relative error from $\sigma(q)$. The Hilbert-based ESS predicts almost the same value $\sigma(q)$ as the

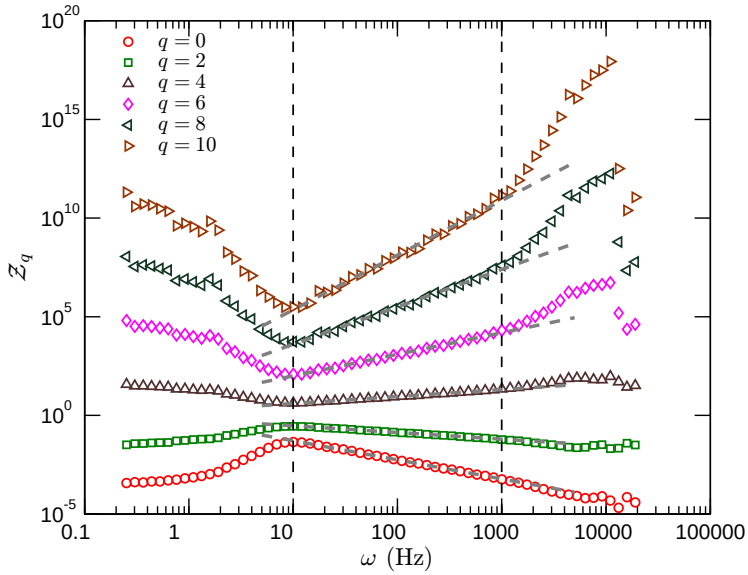

Figure 8.6: Representation of the dimensionless arbitrary order Hilbert marginal spectra function $\mathcal{Z}_q(\omega)$, where $q = 0$ (○), 2 (□), 4 (△), 6 (♢), 8 (◁) and 10 (▷). The vertical dashed line demonstrates the inertial subrange $10 < \omega < 1000\,\mathrm{Hz}$. The dashed line is the least square fitting on the inertial range.

dimensionless arbitrary order Hilbert marginal spectrum $\mathcal{Z}_q(\omega)$. We also note that the log-normal model with the parameter $\mu = 0.11$ gives the best fit of $\sigma(q)$.

We represent the dimensionless arbitrary order Hilbert marginal spectrum $\mathcal{Z}_q(\omega)$ vs $\mathcal{Z}_p(\omega)$ on the range $10 < \omega < 7000\,\mathrm{Hz}$ in Fig. 8.8 for various p (a) $p = 0$, (b) $p = 1$, (c) $p = 2$ and (d) $p = 4$, where $q = 0$ (○), 2 (□), 4 (△), 6 (♢), 8 (▷) and 10 (▽). The vertical dashed line indicates the inertial subrange $10 < \omega < 1000\,\mathrm{Hz}$. A power law behaviour is observed as expected in all cases. The power law range is also extended as expected, which may depend on each case. However, we estimate the scaling exponent $\rho(q, p)$ on the inertial subrange by using a least square fitting. Figure 8.9 shows the corresponding $\rho(q, p)$ for various p, 0 (△), 1 (○), 2 (□), 4 (♢) and 5 (◁). We compare the experimental result with (a) the SL model, (b) the log-Lévy model with $C_1 = 0.07$ and $\alpha = 1.5$, and (c) the log-normal model with $\mu = 0.11$. We

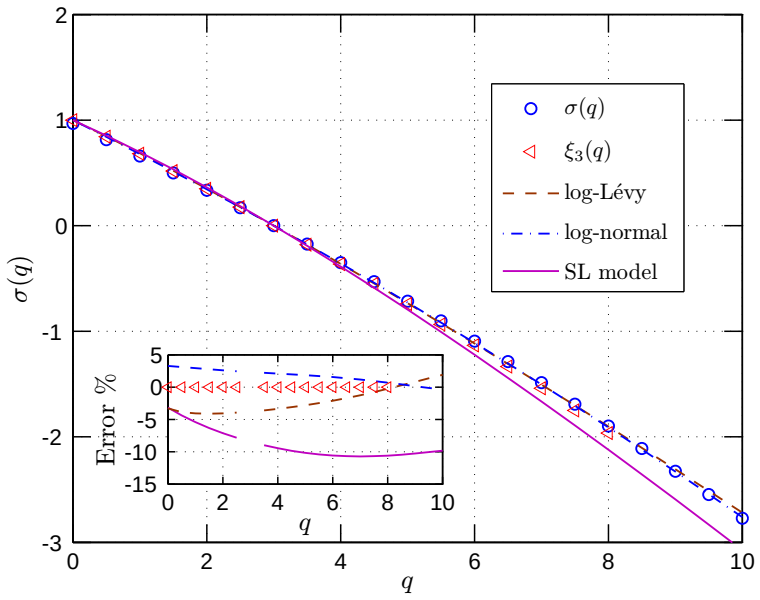

Figure 8.7: Representation of the scaling exponent $\sigma(q)$ ($\bigcirc$), where q goes from 0 to 10. For comparison, we also show the corresponding scaling exponent estimated from the Hilbert-based ESS $\xi_3(q)$ ($\triangleleft$), the log-Lévy model with $C_1 = 0.07$, $\alpha = 1.5$ (dashed line), the log-normal model with $\mu = 0.11$ (dashed-dotted line) and the SL model (solid line). The inset shows the relative error from $\sigma(q)$.

show the relative error in the right part of these figures. For each model, the relative error have a similar shape and is parallel with each other. We also note that the log-normal model with present choice of μ has smaller relative error.

Figure 8.10 shows $\mathcal{Z}_q$ v.s. $\mathcal{Z}_{q-1}$ for various q (1, 5, 8 and 10) on the range $10 < \omega < 7000\,\text{Hz}$. A power law behaviour holds on this range for each plot, which is significant larger than the inertial range $10 < \omega < 1000\,\text{Hz}$. We still estimate the scaling exponent $\rho(q, q-1)$ on the inertial range. The estimated $\rho(q, q-1)$ ($\square$) are shown in Fig. 8.11. For comparison, the log-Lévy model with $C_1 = 0.07$ and $\alpha = 1.5$ (dashed-dotted line), log-normal model with $\mu = 0.11$ (dashed line) and the SL model (solid line) are also shown. The inset shows the relative error from experimental value $\rho(q, q-1)$. There is no significant different among these three models. However, it

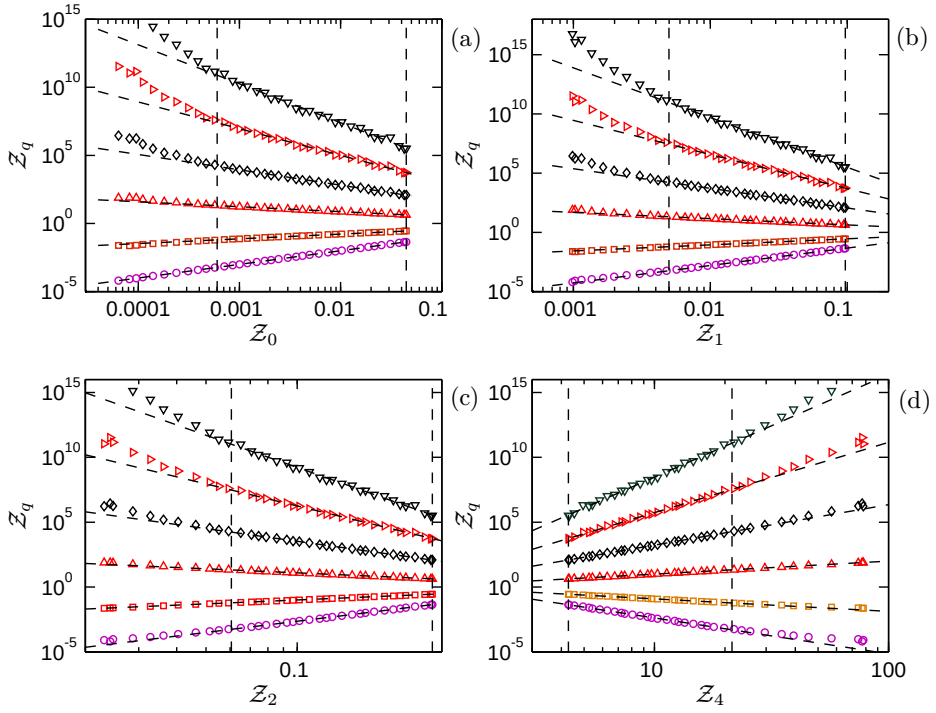

Figure 8.8: Representation of GESS $\mathcal{Z}_q(\omega)$ vs $\mathcal{Z}_p(\omega)$ for various p (a) $p = 0$, (b) $p = 1$, (c) $p = 2$ and (d) $p = 4$, where $q = 0$ (○), 2 (□), 4 (△), 6 (◇), 8 (▷) and 10 (▽). The vertical dashed line demonstrates the inertial subrange $10 < \omega < 1000\,\mathrm{Hz}$. The dashed line is the least square fitting on inertial range.

seems that the log-normal model with present parameter provides the smallest relative error.

Considering Eq. (8.2.7) and Eq. (8.3.2), we may link $\sigma(q)$ and $\rho(q,p)$ to the scaling exponent $\xi(q)$, which is written as

$$\xi(q) = \frac{2q}{3} + \sigma(q) \tag{8.3.5a}$$

and

$$\xi(q) = \frac{2q}{3} + \rho(q,p)\sigma(p),\ p \neq 3 \tag{8.3.5b}$$

A potential application of $\rho(q, q-1)$ is to estimate $\xi(q)$ for high order q, if the quantity

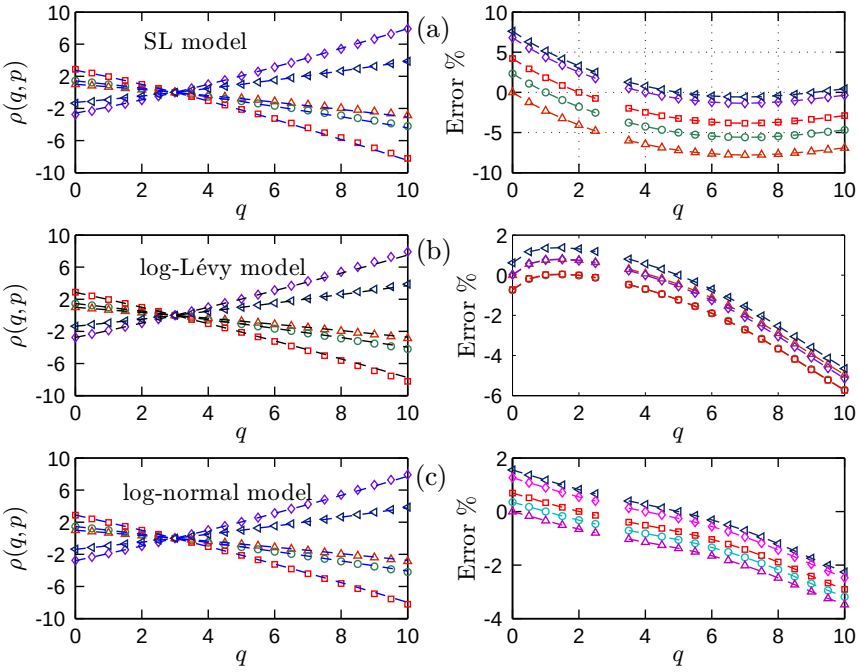

Figure 8.9: Representation of the scaling ratio $\rho(q,p)$ of GESS, where q goes from 0 to 10, $p = 0$ ($\triangle$), 1 ($\bigcirc$), 2 ($\square$), 4 ($\diamondsuit$) and 5 ($\triangleleft$). For comparison, we present three different model, (a) SL model, (b) log-Lévy model, and (c) log-normal model. The right part shows the relative error.

of the data is available. One may estimate $\sigma(q)$ and $\xi(q)$ by the following formula

$$\sigma(q) = \prod_{i=5}^{q} \rho(i, i-1)\sigma(4),\ q \geq 5 \tag{8.3.6}$$

and

$$\xi(q) = \frac{2q}{3} + \prod_{i=5}^{q} \rho(i, i-1)\sigma(4),\ q \geq 5 \tag{8.3.7}$$

We show the estimated $\zeta(q)$ (corresponding to $\xi(q) - 1$) in Fig. 8.12, based on $\sigma(q)$ (dashed-dotted line), $\rho(q,p)$ ($\diamondsuit$)[5] and Hilbert-based ESS ($\triangleleft$). For comparison, we show the log-normal model with two different intermittency parameter $\mu = 0.11$ (dashed-dotted line) fitting for $\sigma(q)$ and $\mu = 0.15$ (dashed line) fitting for $\xi(q) - 1$

[5]Here different p gives almost the same $\xi(q)$. Therefore, we only present the mean value of them, which is denoted as $\rho(q,p)$.

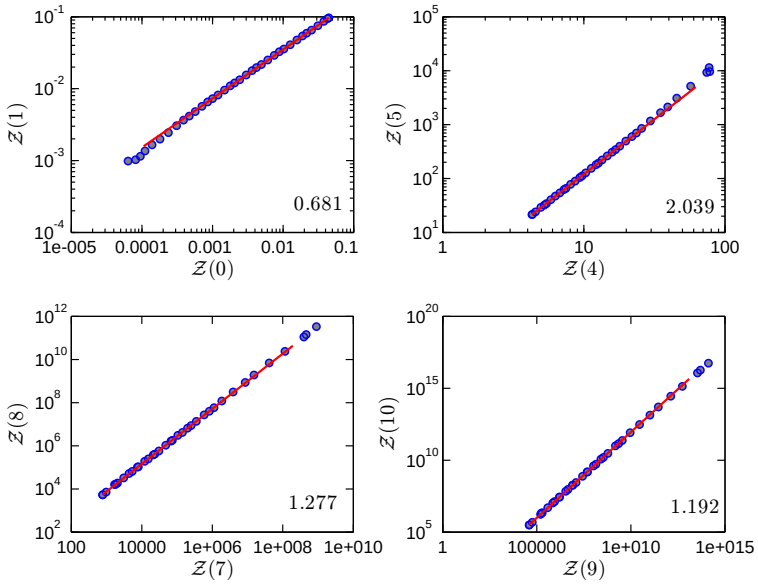

Figure 8.10: Representation of the GESS $\mathcal{Z}_{(q)}$ vs $\mathcal{Z}_{(q-1)}$ on the range $10 < \omega < 7000$ Hz, where $q = 1$, 5, 8 and 10. Power law is observed in all cases.

from Hilbert-based ESS $\xi_0(q)$ and $\xi_3(q)$. The SL model is shown in the same picture as thin solid line. The GESS scaling exponent is quite close to the Hilbert-based ESS one, and significantly larger than SL model when q is greater than 5. We reproduce these scaling exponents from different approaches in Tab. 8.1.

Taking Benzi's ESS result (Benzi *et al.*, 1993a,b; Arneodo *et al.*, 1996) as a reference line, we show in Fig. 8.13 the absolute error and relative error from $\zeta(q)$ for different estimators $\xi(q)$ ($\triangleright$), $\xi_0(q)$ ($\square$), $\xi_3(q)$ ($\diamondsuit$), $\Pi(q)$ ($\bigcirc$), $\sigma(q)$ ($\triangleleft$) and $\rho(q,p)$ ($\triangle$). One can find that the relative error is decreasing with q when $q \leq 4$. When $q \geq 4$, the relative error is then increasing with q. However, the relative error is less than 10% when $2 \leq q \leq 8$.

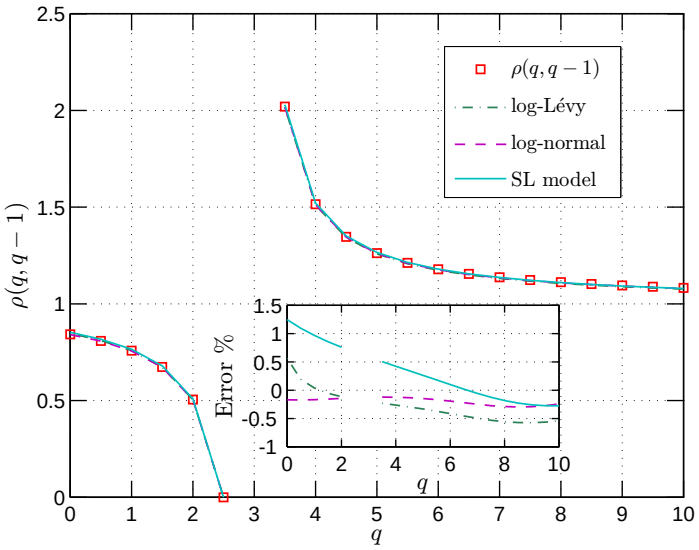

Figure 8.11: Representation of the scaling exponent ratio $\rho(q, q-1)$ from GESS (□), where q goes from 0 to 10. For comparison, log-Lévy model with $C_1 = 0.07$ and $\alpha = 1.5$ (dashed-dotted line), log-normal model with $\mu = 0.11$ (dashed line) and SL model (solid line) are also presented. The inset shows the relative error.

8.4 Summary

In this chapter, we extended Benzi's idea of Extended Self-Similarity into the Hilbert frame. According to Kolmogorov's refined similarity hypothesis (Kolmogorov, 1962; Monin & Yaglom, 1971; Frisch, 1995), we have two special cases, $\mathcal{L}_0(\omega)$ and $\mathcal{L}_3(\omega)$, which are free from the intermittency effect. We therefore use $\mathcal{L}_0(\omega)$ and $\mathcal{L}_3(\omega)$ to define the so-called ESS. They provide almost the same scaling exponents $\xi(q)$, which are slightly larger than SL model for high order q. We then proposed a hierarchy model by defining a hierarchical spectral function. The scaling exponent $\Pi(q)$ of the hierarchical spectral function decreases linearly with q. We finally presented a generalized ESS by considering a dimensionless arbitrary order Hilbert spectrum. The scaling exponents provided by the dimensionless spectrum and the GESS are in good agreement with each other.

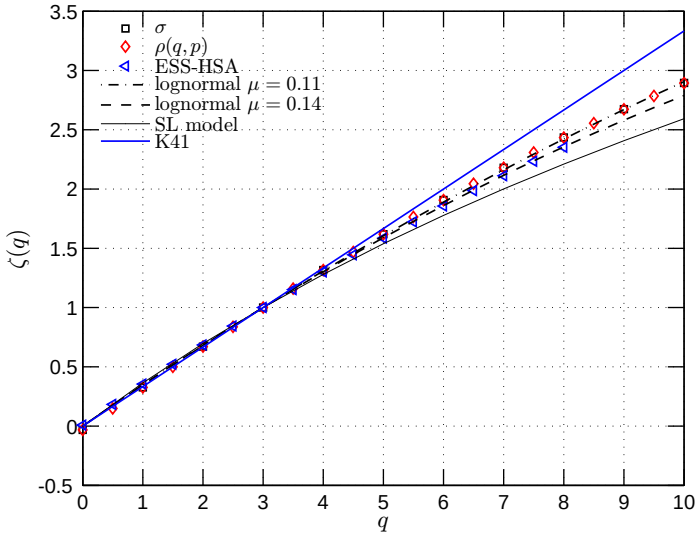

Figure 8.12: Comparison of the scaling exponents $\zeta(q)$ from GESS, $\sigma(q)$ ($\square$), $\rho(q,p)$ ($\diamondsuit$), and the direct estimation by ESS-HSA ($\triangleleft$). For comparison, the SL model is also shown in the same picture as thin solid line. We also fit the data by the log-normal model with $\mu = 0.11$ (dashed-dotted line) and $\mu = 0.15$ (thin dashed line)

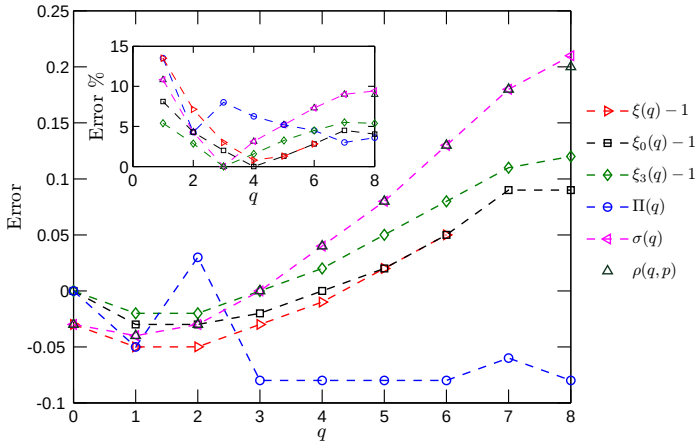

Figure 8.13: Absolute error from $\zeta(q)$ (Benzi *et al.*, 1993b), where the scaling exponents are estimated by $\xi(q) - 1$ ($\triangleright$), $\xi_0(q) - 1$ ($\square$), $\xi_3(q) - 1$ ($\diamondsuit$), $\Pi(q)$ ($\bigcirc$), $\sigma(q)$ ($\triangleleft$) and $\rho(q,p)$ ($\triangle$). The inset shows the relative error.

Table 8.1: Scaling exponents $\zeta(q)$ from different approaches: the ESS $\zeta(q)$ (Benzi *et al.*, 1996), the Hilbert-based $\xi(q)-1$ (Eq. (3.1.3)), the Hilbert-based ESS $\xi_0(q)-1$ (Eq. (8.1.2)), the Hilbert-based ESS $\xi_3(q)-1$ (Eq. (8.1.2)), the dimensionless Hilbert spectrum $\sigma(q)$ (Eq. (8.3.5a)) and the GESS $\rho(q,p)$ (Eq. (8.3.5b)).

q	$\zeta(q)$	$\xi(q)-1$	$\xi_0(q)-1$	$\xi_3(q)-1$	$\sigma(q)$	$\rho(q,p)$
0	0.00	-0.03	0.00	0.00	-0.03	-0.03
1	0.37	0.32	0.34	0.35	0.33	0.33
2	0.70	0.65	0.67	0.68	0.67	0.67
3	1.00	0.97	0.98	1.00	1.00	1.00
4	1.28	1.27	1.28	1.30	1.32	1.32
5	1.54	1.56	1.56	1.59	1.62	1.62
6	1.78	1.83	1.83	1.86	1.91	1.91
7	2.00		2.09	2.11	2.18	2.18
8	2.23		2.32	2.35	2.44	2.43

Part III

Application to Environmental Time Series

Chapter 9

Analysis of River Flow Fluctuations

A better understanding of river flow fluctuations is of sharp practical importance, e.g. for ecosystem studies (transport properties), and for flood understanding and forecasting. River flows fluctuate on many different scales: at small scales, river turbulence induces stochastic fluctuations and at larger scales (from days to years) the river flow fluctuations are the result of complex nonlinear interactions between rainfall processes, topography and geography (Schumm, 2005). They are also impacted by solar forcing and other large scale variations of the climate system (Mauas *et al.*, 2008). Daily river flow time series thus show fluctuations possessing stochastic properties, as well as deterministic forcing resulting from seasonal or annual meteorological and climatic cycles.

In this chapter, we apply the empirical mode decomposition (EMD) and the arbitrary order Hilbert spectral analysis (HSA) on river flow discharge fluctuations data. to characterize the scale invariant properties of small scale in amplitude-frequency space. The results presented in this chapter are published in Huang *et al.* (2009b)[Y. Huang, *et al. J. Hydrol.*, 373, 103-111, 2009.].

9.1 Introduction

Since Hurst (1951) revealed the long-range dependent properties in river flow, associated to scaling properties, researchers have tried different methods to characterize the (multi)scaling properties in river flows (Hurst *et al.*, 1965; Tessier *et al.*, 1996; Pandey *et al.*, 1998; Jánosi & Gallas, 1999; Kantelhardt *et al.*, 2003, 2006; Livina *et al.*, 2003b,a; Koscielny-Bunde *et al.*, 2006; Mauas *et al.*, 2008). Below we quickly review the approaches undertaken in these studies.

Tessier *et al.* (1996) analyzed the relation between rainfall and river flow of 30 rivers and basins in France. They used the double trace moment technique to characterize the multifractal properties. They found that a scaling break occurs at a scale about 16 days. They argued that the rain field itself is the source of the river flow, therefore typical scales in the rain field will also be present in the river flow.

Dahlstedt & Jensen (2005) investigated the Danube and the Mississippi river flows and levels by using finite-size-scaling hypothesis (Aji & Goldenfeld, 2001). They considered the river flow basin size L from different locations. They characterized the multiscaling properties of river flow and level records by considering the relative and general relative scaling (or Extended-Self-Similarity and Generalized Extended-Self-Similarity in the turbulent community). They found that the Fourier spectrum may be different from location to location due to the size effect of the basin area.

More recently, several authors applied the so-called detrended fluctuation analysis (DFA) and its multifractal version to describe the scaling and multiscaling properties of river flows (Kantelhardt *et al.*, 2003; Livina *et al.*, 2003b,b; Kantelhardt *et al.*, 2006; Koscielny-Bunde *et al.*, 2006; Livina *et al.*, 2007; Zhang *et al.*, 2008, 2009). Livina *et al.* (2003a,b) argued that the climate is strongly forced by the periodic variations

of the Earth with respect to the state of the solar system. The seasonal variations in the solar radiation cause periodic changes in temperature and precipitations, which eventually lead to a seasonal periodicity of river flows. The Fourier and structure function analyses are impacted by this strong periodicity (Livina *et al.*, 2003a,b; Kantelhardt *et al.*, 2003; Koscielny-Bunde *et al.*, 2006). According to these authors, the DFA approach is an efficient method to eliminate the trend effects.

Koscielny-Bunde *et al.* (2006) found that the Hurst number H varies from river to river between $0.55 \sim 0.95$ in a non-universal manner independent of the size of the basin. They found that at large time scales, $F_q(s)$ scales as $s^{h(q)}$, and they further proposed a simple function form with two parameters a and b, $h(q) = 1/q - [\ln a^q + b^q]/[q \ln(2)]$ to describe the scaling exponent $h(q)$ of all moments (Kantelhardt *et al.*, 2003). Kantelhardt *et al.* (2006) also found that the Hurst number H estimated from 99 precipitation and 42 river runoff records data are not consistent with the hypothesis that the scaling is universal with an exponent close to 0.75 (Hurst *et al.*, 1965; Peters *et al.*, 2002).

9.2 Seine River and Wimereux River

The Seine river is the third largest river in France. Its length is 776 km, and its basin is 78650 km^2. It is economically important for France, with 25% of its population as well as 40% of its industry and agriculture concentrated in and around it (Dauvin, 2007). The flow data is provided by the Service de Navigation de la Seine (SNS). This corresponds to daily flow data Q ($\mathrm{m}^3\mathrm{s}^{-1}$), recorded from 1 January 1976 to 28 April 2008. There are 11828 data values, with some missing values due to interruptions for maintenance or because of the failure of measuring devices. Due to the local ability

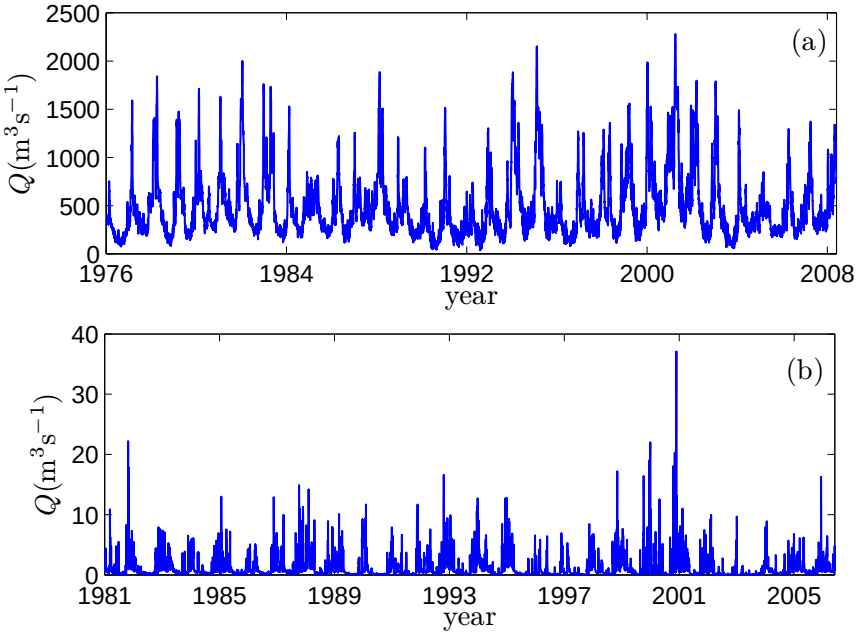

Figure 9.1: The river flow discharge time series of (a) Seine River, recorded from 1 January 1976 to 28 April 2008, (b) Wimereux river, recorded from 1 January 1981 to 27 May 2006. The data illustrate clear strong annual cycles with huge fluctuations. The total lengths are 11828 and 9278 data points for the Seine river and the Wimereux river, respectively.

of HSA approach, which is performed through spline interpolation, the missing values in the time series do not change the results, since the method can be applied even for irregular sampling. The data are shown in Fig. 9.1 (a), demonstrating some large fluctuations at all scales. The mean and standard deviation of the discharge are $488\,\mathrm{m^3s^{-1}}$ and $349\,\mathrm{m^3s^{-1}}$, respectively. This figure shows a complex and stochastic behavior, with a visible strong annual cycle.

The Wimereux river is a small river in the North of France[1]. Its length is 22 km, and its basin is $78\,\mathrm{km^2}$. It can have strong fluctuations due to fast increase of the flow in case of heavy rain. The daily flow discharge is recorded from 1 January 1981

[1]The Wimereux river is the local river in Wimereux city, the coastal host city of the laboratory of Oceanology and Geosciences.

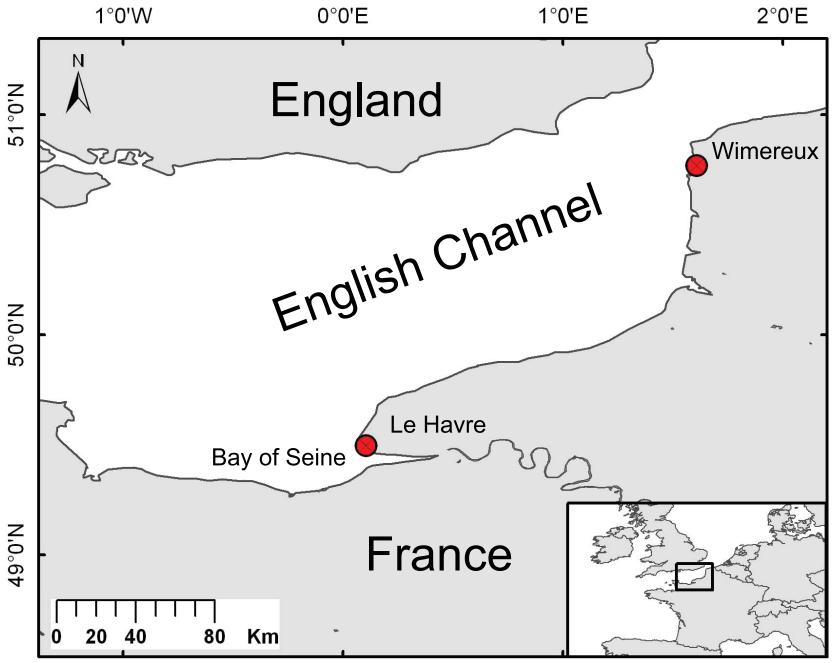

Figure 9.2: A map showing the location of the Seine river and the Wimereux river, in the eastern English Channel. The distance between them is about 300 km.

to 27 May 2006, with a total length of 9278 points values with some missing, see Fig. 9.1 (b). The mean and standard deviation of the discharge data are $1.02\,\mathrm{m^3 s^{-1}}$ and $1.73\,\mathrm{m^3 s^{-1}}$.

Figure 9.2 shows the location of these two rivers, where the Seine river is represented as a solid line. The Wimereux river is too small to be displayed in the same figure. The difference between these two rivers is clear: the Seine river is a real big one, and the Wimereux river is much smaller and strongly influenced by the local rainfall conditions. The distance between them is about 300 km, see Fig. 9.2. Both of them are affected by the same large scale climatic factors and belong to the marine west coast climate of Northern France. This climate is found on the west coast of middle latitude regions and can be quite humid. Indeed it is subject to western wind

bringing important variability and intermittent clouds, important precipitation and temperate temperatures. The direct estimation of the cross correlation between these two recorded data is about 0.256, a value that may be contaminated by the small scale fluctuations. We will apply to these two data sets by the EMD method in the following section.

9.3 EMD Results

After the application of the EMD method, the original data are separated into several IMF modes. We then represent the IMF modes in Fig. 9.3 and Fig. 9.4 for the Seine river and the Wimereux river, respectively. For display convenience, we exclude the residual for the Seine river. Graphically, one can see that the characteristic scale is increasing with the mode index n. Let us note that the number of IMF modes is produced by the algorithm and depends on the length and the complexity of the data. In practice, based on the dyadic filter bank property of the EMD method, this number is usually less than $\log_2(N)$, where N is the length of the data (Flandrin & Gonçalvès, 2004; Flandrin *et al.*, 2004; Wu & Huang, 2004; Huang *et al.*, 2008). First, we estimate the mean frequency $\overline{\omega}$ of each IMF mode. We use the following three definitions of mean frequency $\overline{\omega}$. The first one was proposed by Huang *et al.* (1998), which is written as

$$\overline{\omega}_i = \frac{\int_0^\infty f S_i(f)\,\mathrm{d}f}{\int_0^\infty S_i(f)\,\mathrm{d}f} \tag{9.3.1}$$

where $S_i(f)$ is Fourier spectrum of $\mathbb{C}_i$. It is an energy weighted average in Fourier space. The second one was given by Flandrin (Flandrin *et al.*, 2004; Flandrin &

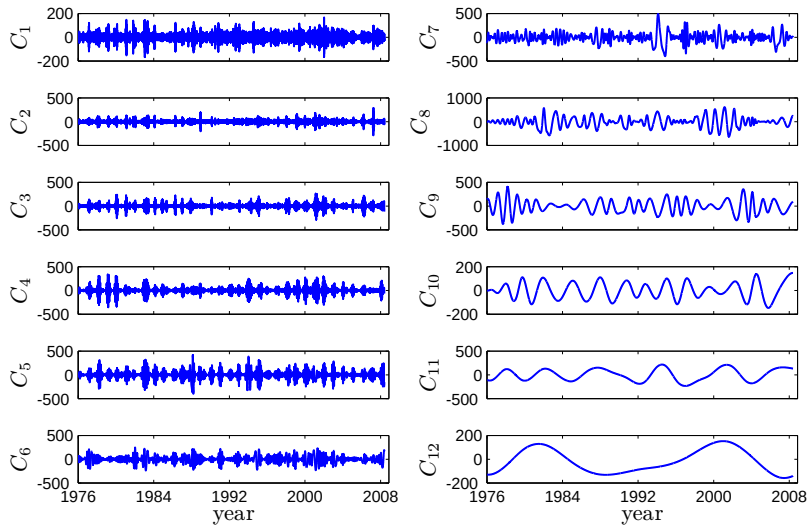

Figure 9.3: IMF modes (excluding the residual) from EMD for the Seine river. Here the data are taken from 1 January 1976 to 28 April 2008. The characteristic scale is increasing with the mode index number n.

Gonçalvès, 2004), and is written as

$$\overline{\omega}_i = \frac{\mathbb{N}^0 - 1}{\mathbb{L}^0} \tag{9.3.2}$$

where $\mathbb{N}^0$ is the zero-crossing number, and $\mathbb{L}^0$ is the distance between the first and last zero-crossing. The third one is introduced here for the first time, and is defined

Table 9.1: The mean period (in days) of each IMF mode (excluding the residual) of the Seine river and the Wimereux river, respectively. Here the mean period is estimated as $\overline{T} = 1/\overline{\omega}$, where $\overline{\omega}$ is calculated by Eq. (9.3.1). The 8^{th} and 9^{th} IMF modes of the Seine river and Wimereux river, respectively, are close to the annual cycle.

	1	2	3	4	5	6	7	8	9	10	11	12	13
Seine	3	8	19	33	55	86	185	358	452	869	1823	5551	
Wimereux	5	9	16	25	36	58	103	182	376	574	2149	2785	3125

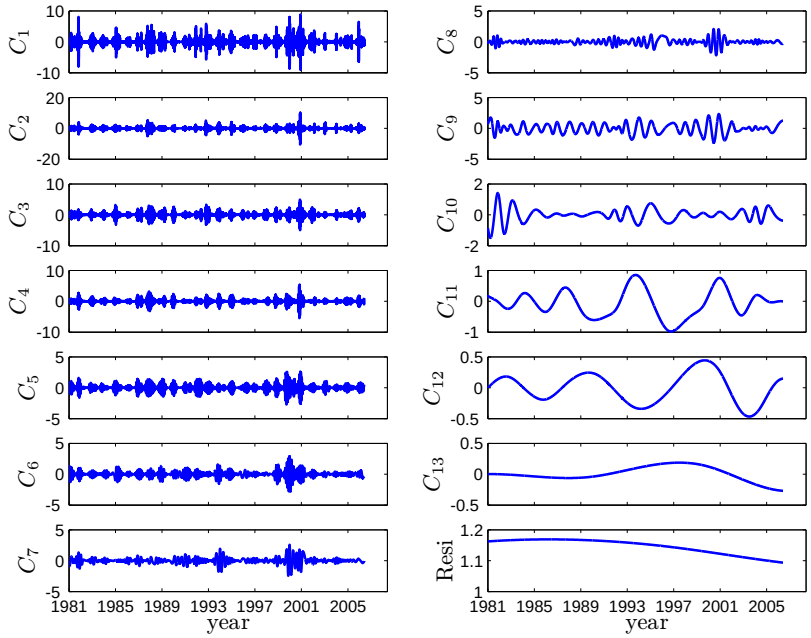

Figure 9.4: IMF modes from EMD for Wimereux river. Here the data are taken from 1 January 1981 to 27 May 2006.

as

$$\overline{\omega}_i = \frac{\int_0^\infty \omega h_i(\omega)\,\mathrm{d}\omega}{\int_0^\infty h_i(\omega)\,\mathrm{d}\omega} \tag{9.3.3}$$

where $h_i(\omega)$ is the Hilbert marginal spectrum for the i^{th} mode. This definition is similar to the first one: it is an energy weighted measurement of the mean frequency in Hilbert space. We then represent the mean frequency $\overline{\omega}$ estimated by these three definitions Eq. (9.3.1) (○), (9.3.2) (□) and (9.3.3) (×) for each mode in Fig. 9.5 for (a) the Seine river, and (b) the Wimereux river. One can see that the two energy weighted estimators give almost the same mean frequency. However, they are slightly smaller than the zero-crossing based estimator. Graphically, all these three estimators suggest the following exponential law

$$\overline{\omega}(n) \sim \gamma^{-n} \tag{9.3.4}$$

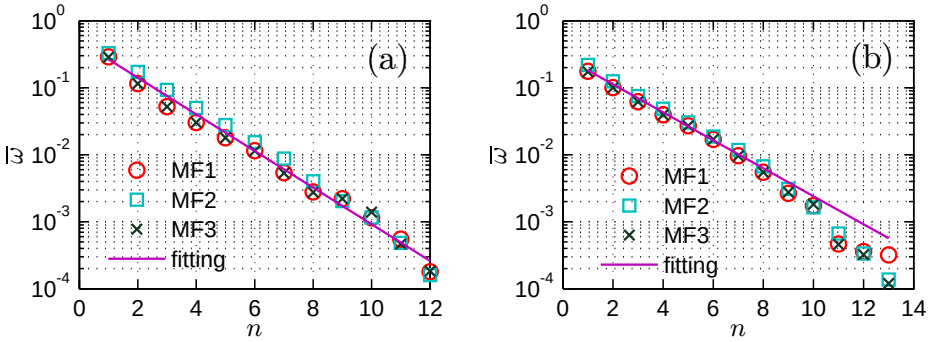

Figure 9.5: Representation of the mean frequency $\overline{\omega}$ vs the mode index n in log-linear view: (a) Seine river, (b) Wimereux river, where the mean frequency $\overline{\omega}$ are estimated by using Eqs. (9.3.1) (○), (9.3.2) (□) and (9.3.3) (×), respectively. An exponential law is observed for each representation. The straight line is the least square fit of the data.

where $\gamma_s \simeq 1.88$, $\gamma_w \simeq 1.62$ are estimated by using the least square fitting for the Seine river and the Wimereux river, respectively. This result implies that the mean frequency of a given mode is γ times larger than the mean frequency of next one. We notice that these values are significantly different from 2, which would correspond to a dyadic filter bank, which are reported for white noise (Wu & Huang, 2004), fractional Gaussian noise (Flandrin *et al.*, 2004; Flandrin & Gonçalvès, 2004) and turbulence time series (Huang *et al.*, 2008). However, it still indicates that the EMD algorithm acts a filter bank here.

We list the mean period $\overline{T}$ (in days) in Table 9.1, where $\overline{T} = 1/\overline{\omega}$. Since the three above mentioned mean frequency estimators give almost the same value, we thus only present the value estimated by Eq. (9.3.1). One can find that the EMD approach captures the annual cycle, which is the 8^{th} and 9^{th} mode for the Seine river and Wimereux river, respectively. Both rivers belong to the same climate and it is expected that large scale modes are correlated. However, the data at daily scale are not (the cross-correlation at this scale is 0.256); this is due to the influence of small

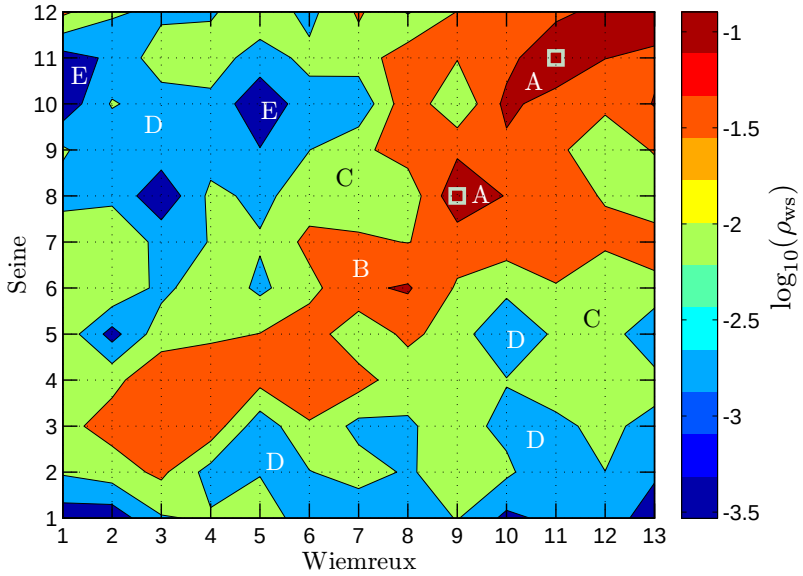

Figure 9.6: Representation of the cross-correlation ρ_{ws} between IMF modes from the Seine and Wimereux rivers. The data span is taken from 1 January 1981 to 27 May 2006 for both series. For convenience, we consider the coefficient value $\log_{10}(\rho_{ws}(i,j))$. As expected, the annual cycle shows a strong correlation with a coefficient $\rho_{ws}(9,8) = 0.426$. The coefficient of the most correlated modes is $\rho_{ws}(11,11) = 0.579$. These two strong correlations are then marked by □.

scales. The cross-correlation between two IMF modes is defined as

$$\rho_{ws}(i,j) = \frac{\langle C_{w,i} C_{s,j} \rangle}{\langle C_{w,i}^2 \rangle^{1/2} \langle C_{w,i}^2 \rangle^{1/2}} \tag{9.3.5}$$

where $\langle \cdot \rangle$ means ensemble average. The corresponding cross-correlation $\rho_{ws}(i,j)$ is then plotted in Fig. 9.6, where the most correlated modes are marked by □. The large scale modes are correlated as expected. More precisely, we observe a larger cross-correlation between the annual cycle modes, $\rho_{ws}(9,8) = 0.426$, and the most correlation coefficient is $\rho_{ws}(11,11) = 0.579$, with mean periods of about 6 and 8 years for the Seine river and the Wimereux river, respectively.

We then replot the annual cycle for the Seine river (thin solid line) and Wimereux river (thick solid line) in Fig. 9.7 (a). One can find that their shapes are almost the

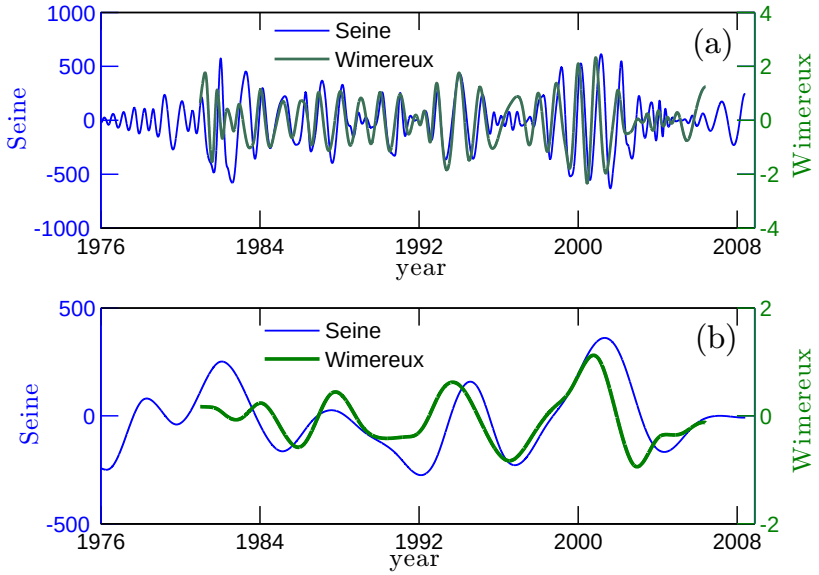

Figure 9.7: Most correlated IMF modes: (a) the annual cycle mode for the Seine river (thin solid line) and the Wimereux river (thick solid line), (b) the reconstruction of the large scale part for the Seine river (thin solid line) and the Wimereux river (thick solid line). We took the IMF modes $11 \sim 12$ from the Seine river and $11 \sim 13$ from the Wimereux river, which means periods larger than 3 years, to reconstruct the large scale part. Graphically, they have the same evolution trend on range 1 January 1981 to 28 May 2006.

same on the range from 1 January 1981 to 28 May 2006. We also reconstruct the large scale signal from those modes, with mean period larger than 3 years, 11^{th} and 12^{th} from the Seine river (thin solid line), and 11^{th} to 13^{th} from the Wimereux river (thick solid line). The result is shown in Fig. 9.7 (b): they have almost the same shape and evolution trend.

9.4 HSA Results

In order to characterize the intermittent properties of river flow fluctuations, we consider here HSA and arbitrary order HSA analysis. We first compare the Hilbert

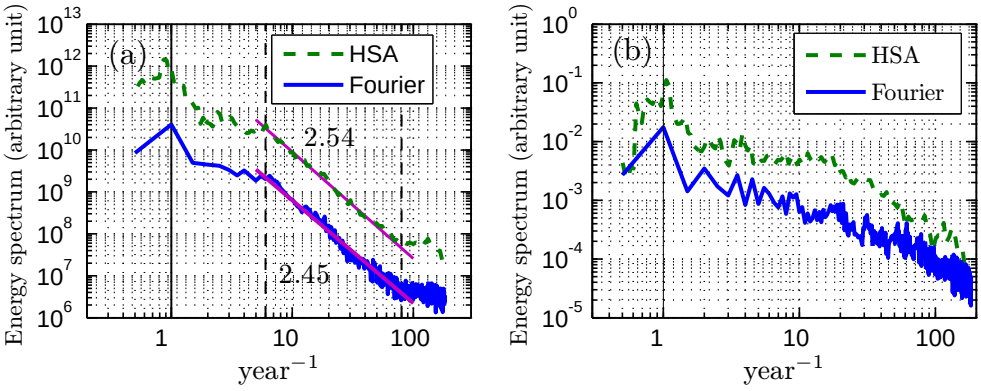

Figure 9.8: Comparison of the Hilbert marginal spectrum (dashed line) and Fourier spectrum (solid line) for (a) the Seine river, (b) the Wimereux river. For the Seine river, a power law behaviour is observed on the range $6 < \omega < 80\,\text{year}^{-1}$, or $4.5 \sim 60$ days: this range is marked by the vertical dashed lines. The scaling values are 2.54 and 2.45 for Hilbert spectrum and Fourier spectrum, respectively. The vertical solid line indicates the annual cycle.

marginal spectrum (dashed line) and Fourier spectrum (solid line) in Fig. 9.8 for (a) the Seine river, and (b) the Wimereux river to identify the power law range, where the scale invariance holds. For the Seine river, both methods capture the annual cycle (vertical solid line) and show power law behaviour on the range $6 < \omega < 80\,\text{year}^{-1}$ or from 4.5 to 60 days, with scaling exponent 2.54 and 2.45, respectively. The power law range is between synoptic and intraseasonal scales (Zhang, 2005). The latter may be linked to the Madden-Julian Oscillation (MJO), since some connection between and the North Atlantic Oscillation (NAO) and MJO have been found (Cassou, 2008). For the Wimereux river, the power law range is less clear. We therefore only apply below the arbitrary order HSA analysis on the Seine river.

Since we are concerned with the scaling property in the above range, we thus divide the entire time series into 16 segments, each one has 2×365 points, 2 years each. The arbitrary order Hilbert marginal spectra are shown in Fig. 9.9, for $q = 0$,

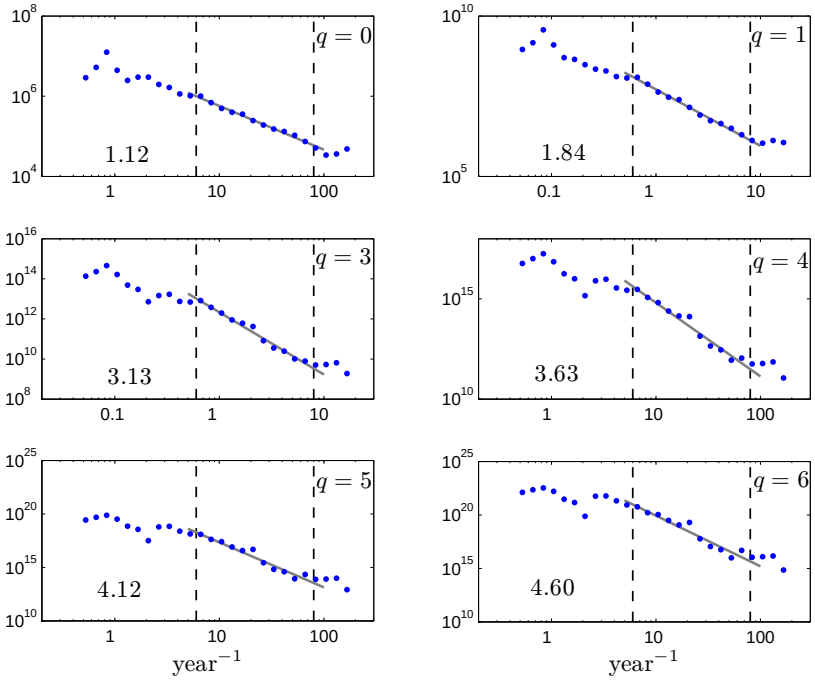

Figure 9.9: Representation of arbitrary order Hilbert marginal amplitude spectra $\mathcal{L}_q(\omega)$ for the Seine river, where $q = 0$, 1, 3, 4, 5 and 6. A power law behaviour is observed in all cases on the range $6 < \omega < 80\,\text{year}^{-1}$. The vertical dashed lines indicate the power law range. The corresponding scaling values are shown in each figure.

1, 3, 4, 5 and 6. Power law behaviour is then observed in all cases on the range $6 < \omega < 80\,\text{year}^{-1}$. The corresponding scaling exponents $\xi(q)$ are estimated on this range by using least square fitting with 95% confidence limit, Fig. 9.10 shows the scaling exponents $\xi(q)$ ($\bigcirc$). This curve is concave, which indicates the multifractal properties of the river flow discharge (Pandey *et al.*, 1998; Kantelhardt *et al.*, 2003, 2006). For comparison, we also show a reference line $qH + 1$ (solid line), where $H = \xi(1) - 1 = 0.84 \pm 0.08$, which corresponds to the mono-scaling case. The departure from this reference mono-scaling line is then shown in inset.

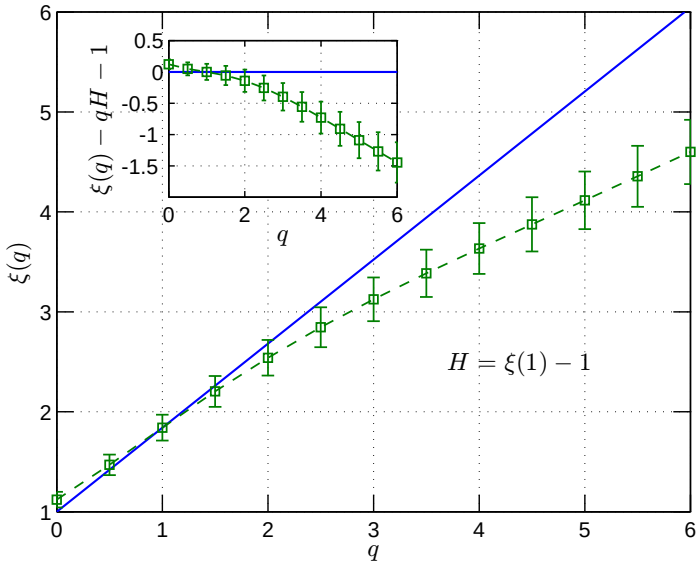

Figure 9.10: Scaling exponents $\xi(q)$ (○) for the Seine river. The inset shows the departure from the reference line $qH + 1$, where $H = \xi(1) - 1$. The shape of these scaling exponents is concave, which indicates the small scale intermittency nature of river flow.

9.5 Discussion

We compare the above observation with the conventional structure function analysis, the traditional way to extract the scaling exponents. We plot the result in Fig. 9.11, where $q = 1$ (□), 2 (○) and 3 (♢), respectively. Some scaling portion are visible on these figures, of a relatively limited amplitude. To reveal the scale invariance more clearly, we consider the Extended Self-Similarity (ESS) properties, a relative scaling expressed as (Benzi *et al.*, 1993b)

$$\langle \Delta x^q \rangle \sim \langle \Delta x \rangle^{\psi(q)} \tag{9.5.1}$$

where in case of scaling, we have $\zeta(q) = H\psi(q)$. Eq. (9.5.1) can be used to estimate more accurately the exponents $\psi(q)$. The ESS is verified for the Seine river on range $2 < \tau < 60$ days, see Fig. 9.12. Figure 9.13 shows the ESS result for the Wimereux

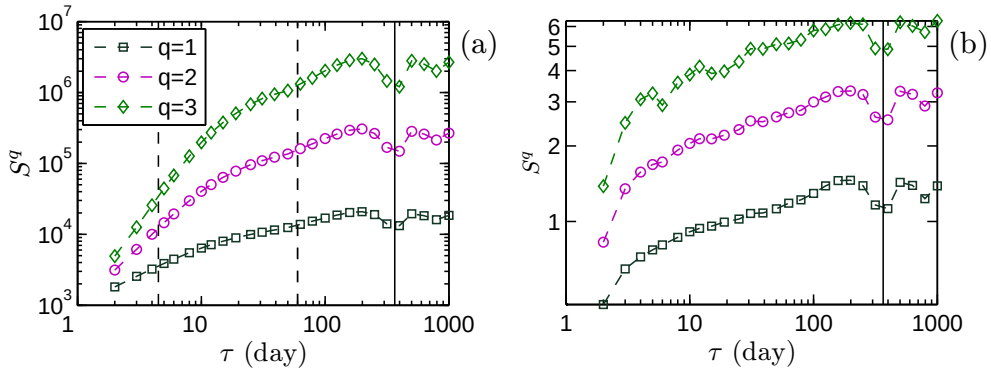

Figure 9.11: Structure function for (a) the Seine river, and (b) the Wimereux river, where $q = 1$ (□), 2 (○) and 3 (◇). The vertical dashed lines indicate the range $4.5 \sim 60$ days. The annual cycle influence is also indicated by the solid line.

river. It is scaling and is rather scattered. We then show the relative scaling exponents $\psi(q)$ and the normalized scaling exponents $(\xi(q) - 1)/(\xi(1) - 1)$ in Fig. 9.14. In the mono-scaling case and when there is no large scale forcing, they should collapse on a solid line $\psi(q) = q$. The same approach is applied to the Wimereux river. In this case the HSA approach is not displaying any clear scaling range. We thus use the ESS approach and compare the resulting curve $\psi(q)$ to the one obtained from the Seine river. The Wimereux river scaling exponents are saturating at $\psi(q = 1)$, and the curve is quite different from the Seine river. This shows that the Wimereux river is more intermittent than the Seine river: which may come from the fact that its catchment basin is much smaller, hence its discharge variation can be more rapid. This may also be an effect of strong oscillations that reduce the multifractal degree (see Telesca & Macchiato (2004); Bolzan *et al.* (2009)). It is also interesting to see in the same graph the difference between the HSA based exponents and structure function's exponents for the Seine river. The discrepancy can be interpreted as coming from the influence of the periodic component in the time series. Indeed we have shown

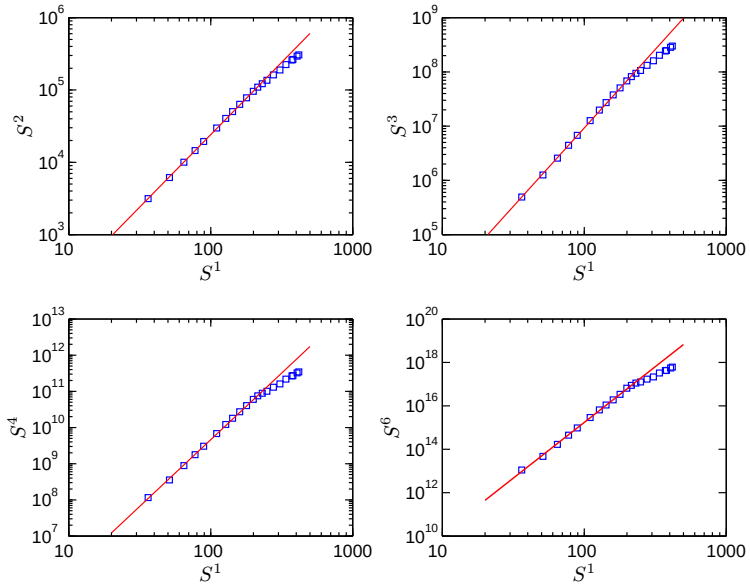

Figure 9.12: Extended self-similarity test of the Seine river on range $2 < \tau < 300$ day. The relative scaling is very well captured for all moments.

in Huang *et al.* (2010a, 2009a), see also chapter 5, that the influence of periodic components is stronger on structure function than on HSA exponents, which can be linked to the fact that EMD acts a filter bank (Flandrin & Gonçalvès, 2004; Flandrin *et al.*, 2004; Huang *et al.*, 2008; Wu & Huang, 2004). Periodic components tend to increase the value of $\zeta(q)$ relative to the real theoretical curve.

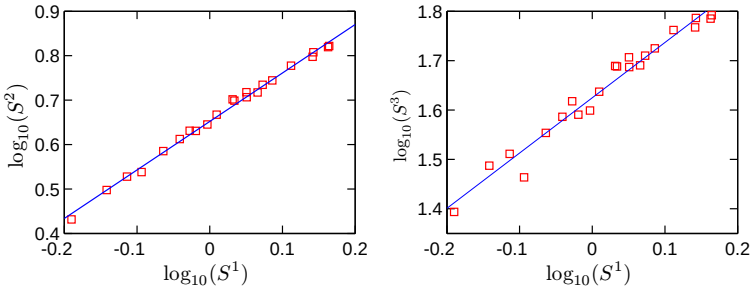

Figure 9.13: Extended self-similarity test of the Wimereux river on range $2 < \tau < 300$ day.

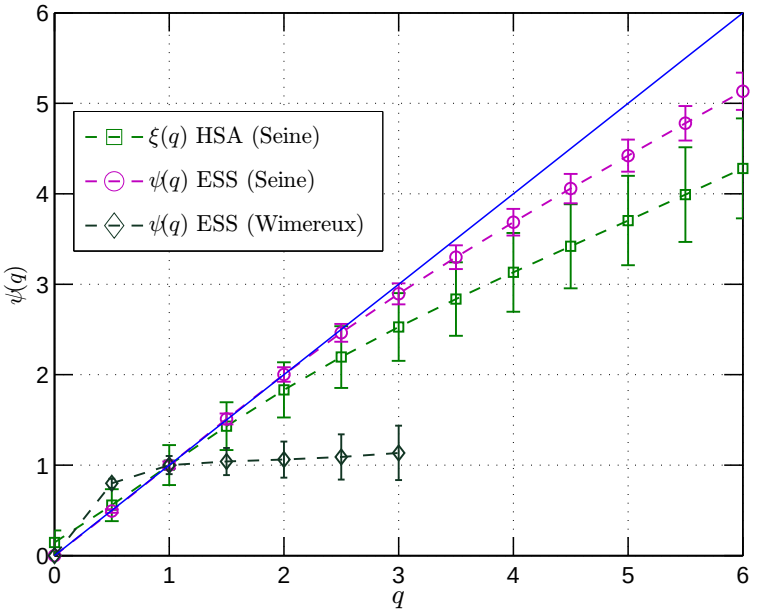

Figure 9.14: Comparison of the relative scaling exponents $\psi(q)$ ($\square$) and $(\xi(q)-1)/(\xi(1)-1)$ ($\bigcirc$).

9.6 Summary

In this chapter we applied for the first time the EMD methodology to river flow time series. Using daily river flow discharge data, 32 years recorded in the Seine river (France), and 25 years recorded in the Wimereux river (France), we have shown that the time series can be successfully separated into several IMF modes. Exponential laws for the mean frequency of each mode have been found, with exponents $\gamma_s = 1.88$ and $\gamma_w = 1.62$ for the Seine river and the Wimereux river, respectively. These values are smaller than 2, the value for dyadic filter bank. Even though, it still confirmed that the EMD algorithm acts as a filter bank for river flow data. Furthermore, strong cross-correlation have been observed between annual cycles and the large scale modes having a mean period larger than 3 years. Based on the correlation analysis results, we have found that the annual cycle mode and the reconstructed large scale part have

almost the same evolution trends.

We have also characterized the intermittency of the time series over the ranges showing scaling properties. For the Seine river, we observed power laws for the first six order Hilbert marginal spectra on the range $6 < \omega < 80\,\mathrm{year}^{-1}$ or 4.5∼60 days, between synoptic and intraseasonal scales. The corresponding scaling exponents $\xi(q)$ indicate the small scale multifractal nature of the river flow data analyzed here. The differences obtained using the structure functions approach and the frequency based HSA approach have been emphasized, which is especially clear for large order moments associated to the more active fluctuations. We have interpreted this difference as coming from the strong annual cycle which has more influence on structure functions scaling exponents than on the Hilbert-based approach. We have also compared the scaling exponents estimated from the ESS method, for the Seine river and Wimereux river; the much smaller exponents obtained for the Wimereux river express a higher degree of multifractality, which was interpreted as coming from the inertia associated to the large scale basin for the Seine river, whereas small rivers such as the Wimereux river may be more sensitive to local precipitation events.

Several previous studies have considered scaling properties of river flows using other methods such as rescaled range analysis, trace moments, double trace moments, wavelet analysis, multifractal detrended fluctuation analysis (MFDA). We applied here a new method which gives results similar to the classical methods (structure functions, wavelet analysis, MFDA) for fractional Brownian motion or pure multifractal processes (Huang *et al.*, 2009a), see also chapter 3. However, we have shown in the same chapter that strong deterministic forcing had important influence on classical methods, whereas the Hilbert-based approach was much more stable and

presented less influence (Huang *et al.*, 2010a, 2009a), see also chapter 3. This method seems hence more appropriate for environmental time series that possess often strong periodic components superposed to scaling regimes. The origin of this stability property is the adaptative and local approach which is at the heart of the Hilbert-based method.

We have compared here two rivers of very different size and catchment basin in order to compare their scaling properties. One of the objectives of scaling analyses of river flow time series is indeed to detect some differences among rivers, but also to evaluate some universality, i.e. some general similarity in statistical properties. This was done for normalized pdfs (Dahlstedt & Jensen, 2005), for river flow volatilities (Livina *et al.*, 2003b,a), and for scaling regimes (Tessier *et al.*, 1996) or multifractal parameters (Pandey *et al.*, 1998). We hope that the method presented in this paper, which we claim to be well adapted to environmental time series, will help this quest for universal properties of river flow scaling statistics.

Chapter 10

Marine Turbulence in the Surf Zone

One of the main properties of fully developed turbulence is its inertial range intermittent properties, between a large-scale injection of energy and a small-scale dissipation (Frisch, 1995; Pope, 2000). In the surf zone, when waves break, the wave energy is transferred into turbulent motions through a violent, highly energetic process associated with breaking wave times scales, typically a few seconds, and then turbulence is dissipated at smaller scales (Svendsen, 1987; Battjes, 1988; Svendsen, 2005). The surf zone environment is a complex system: there are water turbulent motion at different scales, breaking waves feeding turbulence at the surface, and residual turbulence persisting from one wave to the next (Svendsen, 1987; Jaffe & Rubin, 1996). This highly energetic system has a strong effect on sediment transport dynamics, morphological changes associated with it, and shoreline evolution processes (Jaffe & Rubin, 1996; Cox *et al.*, 1996; Trowbridge & Elgar, 2001; Masselink & Russell, 2006; Torres-Freyermuth *et al.*, 2007), and also on ecological processes through influences

on feeding, settlement, fertilization, bloom dynamics, etc. (Denny & Shibata, 1989; Du Preez *et al.*, 1990; Mead & Denny, 1995).

In the intertidal zone, transport models for either sediments or living organisms need the description of surf zone velocity fluctuations. It is then important in this context to be able to characterize these velocity fluctuations for a wide range of scales, including highly energetic breaking waves scales and smaller turbulent scales. This is not an easy task because of the unsteadiness of breaking waves: phase-average methods are not straightforward since the wave forcing is not monochromatic; ocean breaking waves are nonlinear and present random components.

We use here for this the Empirical Mode Decomposition method and the Hilbert spectral analysis. It has already been applied to nonstationary ocean wave data (Hwang *et al.*, 2003; Veltcheva & Soares, 2004), but these studies focus on deep water ocean waves, which are different from surf zone breaking waves. Here we consider experimental turbulent velocity time series recorded in the surf zone. The results presented in this chapter are published in Schmitt *et al.* (2009)[Schmitt, *et al. J. Mar. Sys.*, 77, 473-481, 2009.]

10.1 Characterization of intermittency using cumulants

Structure Functions and Cumulants

One of the characteristic features of fully developed turbulence is the intermittent nature of velocity fluctuations (Frisch, 1995). Intermittency provides corrections to Kolmogorov's scaling law (Kolmogorov, 1941a), which are now well established and

received considerable attention in the last twenty years. Let us recall how to quantify intermittency effects on scaling laws for Eulerian isotropic turbulence. Denoting $\Delta V_\ell = V(x+\ell) - V(x)$ the longitudinal increments of the Eulerian velocity field at a spatial scale ℓ, their fluctuations are characterized, in the inertial range, using the scale invariant moment function $\zeta(q)$

$$\langle |\Delta V_\ell|^q \rangle = A_q \ell^{\zeta(q)} \tag{10.1.1}$$

where $q > 0$ is the order of moment and A_q is a constant that may depend on q. Kolmogorov's initial proposal, for a non-intermittent constant dissipation, leads to $\zeta(q) = q/3$ (Kolmogorov, 1941a). For intermittent turbulence, $\zeta(q)$ is proportional to a cumulant generating function, and is nonlinear and concave; only the third order moment has no intermittency correction: $\zeta(3) = 1$. The accuracy of the scaling of Eq. (10.1.1) is usually tested for each order of moment, for various values of ℓ in log-log plot, using a least-square regression (Anselmet *et al.*, 1984). The values of $\zeta(q)$ which are then obtained may be compared and fitted to different multifractal models (among many studies, see She & Lévêque (1994); Chen & Cao (1995); Arneodo *et al.* (1996); Boratav (1997); Schertzer *et al.* (1997); van de Water & Herwijer (1999); Anselmet *et al.* (2001)). This way of estimating $\zeta(q)$ depends on the choice of the scaling range: one usually estimates $\zeta(q)$ for the range of scales where the exact relation $\zeta(3) = 1$ is verified, assuming that the scaling range is the same for each order of moment.

Here there is no large scaling range: we therefore consider another approach: instead of studying the scale dependence for each moment, we focus on the moment dependence using cumulants at a given scale. The cumulant approach has already been undertaken in the scaling turbulence framework in a few studies (see e.g. Delour *et al.* (2001); Eggers *et al.* (2001); Chevillard *et al.* (2005)), where the cumulants of

the cascade process (Eggers *et al.*, 2001) or a polynomial development of the cumulant generating function (Delour *et al.*, 2001; Chevillard *et al.*, 2005) have been considered; see also Ref. Venugopal *et al.* (2006) for an application to multifractal properties of rainfall.

Non Analytical Cumulant Generating Functions

We consider here a random variable X. The cumulant generating function of its generator $g = \log|X|$ is defined as (Gardiner, 2004)

$$\Psi(q) = \log\langle|X|^q\rangle \tag{10.1.2}$$

The function $\Psi(q)$ is also the second Laplace characteristic function of the generator: $\Psi(q) = \log\langle e^{qg}\rangle$. As a second characteristic function, it is convex (Feller, 1971), and can be developed using the cumulants

$$\Psi(q) = \sum_{p=1}^{\infty} c_p \frac{q^p}{p!} \tag{10.1.3}$$

where c_p is the p^{th} cumulant. Let us recall the expression for the first cumulant

$$c_1 = \langle g\rangle = \langle\log|X|\rangle \tag{10.1.4}$$

We also know that $c_2 = \langle g^2\rangle - c_1^2$, and c_n depends on all moments $\langle g^p\rangle$ $(1 \leq p \leq n)$. The theorem of Marcienkiewicz states that, if it exists, the development in Eq. (10.1.3) is either infinite, or if finite, of degree not higher than 2 (Gardiner, 2004). In fact, the development in Eq. (10.1.3) may not exist in case of non-analycity of $\Psi(q)$. This is the case when g is a stable process whose second order moment (and hence second order cumulant) diverges (Feller, 1971; Taqqu & Samorodnisky, 1994). Stable random

variables (sometimes also called "Lévy" in the physics literature) correspond to variables that have a domain of attraction and being stable under addition (Feller, 1971; Taqqu & Samorodnisky, 1994; Janicki & Weron, 1994). They have been introduced in the 1930s by Paul Lévy and correspond to a generalisation of the Gaussian law. The main parameter is the index α bounded between 0 and 2. The case $\alpha = 2$ corresponds to the Gaussian law. Log-stable models for turbulent intermittency (Schertzer & Lovejoy, 1987; Kida, 1991) correspond to a nonanalytic scaling moment function (see also Schertzer *et al.* (1997)). In this case, we have instead of Eq. (10.1.3)

$$\Psi(q) = c_1 q + c_\alpha q^\alpha \tag{10.1.5}$$

where $0 \leq \alpha \leq 2$ is the index of the stable process and c_α is the cumulant of order α. When $\alpha = 2$ the generator is a Gaussian process and there are only two cumulants in the development of Eq. (10.1.3). To check this model, we consider in the following the function

$$\Phi(q) = \Psi(q) - c_1 q \tag{10.1.6}$$

For a stable law, $\Phi(q)$ should be proportional to q^α; we check this below in log-log plot using experimental data, for a given time or frequency scale.

Concerning the choice of the random variable w, we will compare the structure function approach ($X = |\Delta V_\ell|$, where ℓ is the time scale) and the EMD-Hilbert spectral analysis approach ($X = \mathcal{A}$, the moments being estimated from the pdf $p(\mathcal{A}|\omega)$ for a given frequency value ω).

10.2 Presentation of the experimental database

The data analyzed here have been recorded using an Acoustic Doppler Velocimeter (ADV) from Sontek/YSI, operating under autonomous operation conditions, at a 25 Hz sampling rate, and providing the 3D velocity vector averaged over a small volume of about 250 mm^3 at a 5 cm distance from the ADV probe, with an accuracy of 1% of the measured value. Measurements have been performed in the beach in front of the research laboratory for Littoral and Coastal Ecosystems (ELICO): Eastern English Channel at Wimereux city (North of France, near Boulogne-sur-mer): this is a flat sand beach with a megatidal regime that varies between 8 to 11 m (see Fig. 10.1). A heavy metallic structure has been built in the laboratory ELICO as a support for the ADV, its electronics canister, and its battery canister (see Fig. 10.2). The measurement location is the intertidal zone in the beach, corresponding to the surf zone. The Eastern English Channel is a megatidal sea with strong currents. The metallic structure has been fixed to the ground using hooks; it was built in thin tubes to avoid a too strong stress on the structure from the tide and currents.

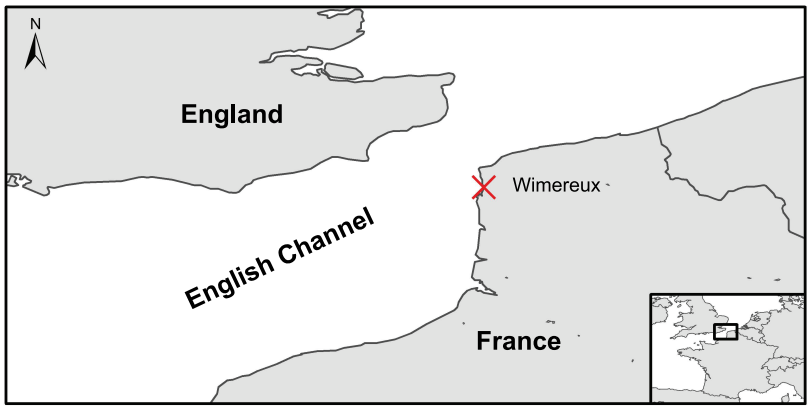

Figure 10.1: A map showing the location of the measurements, in the French coast of the Eastern English Channel (marked "X" in the map).

Figure 10.2: A photography of the ADV measuring device and its support, in the intertidal zone, before being submerged by the tide.

The measurements have been done on 9 and 10 June, 2004, during 2 tidal cycles, at a height of 50 cm from the bottom. Measurements have been considered when there was approximately at least 1 m of water above the experimental device. Due to the tidal activity, this distance was between 1 to 3 m. We considered 27 m sections of the U component of the velocity vector, corresponding to the direction perpendicular to the shore, each of length $32,000$ data points (each of 21 min duration). We cannot consider longer sections, since the internal programming of the ADV interrupts the continuous recording of data, to synchronise the different clocks. The 27 sections have been chosen among the whole data set, in order to have a large enough internal correlation of bursts, corresponding to a precise enough estimation of the velocity. We have thus a total of $864,000$ data points, separated into 27 sections. A one minute portion is shown in Fig. 10.3: strong fluctuations at small scales are visible, but the whole time series seems stationary. In the following we analyze the

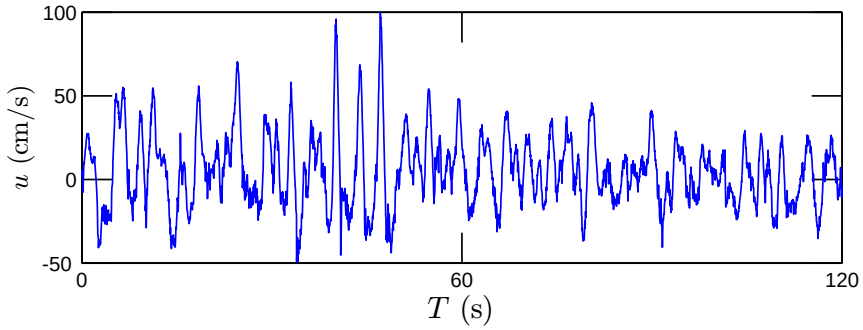

Figure 10.3: A two minutes portion of the experimental velocity data, showing their high variability at small scales.

data using the EMD method, the Hilbert-based amplitude-frequency method, and cumulant generating functions.

10.3 EMD and HSA results

EMD Results

The analyses below are performed over the entire dataset, and the results displayed after performing an ensemble average over 27 realizations, where each segment of length $32,000$ data points is one realization. After decomposition, the original velocity series is decomposed into several IMFs (see Fig. 10.4), from 13 to 16 modes (depending on the segment) with one residual. As visible in this figure, the time scale is increasing with the mode; each mode has a different mean frequency, which is estimated by considering the energy weighted mean frequency in the Fourier power spectrum of each mode time series; the relation between mode number m and mean time scale is displayed in Fig. 10.5. The straight line which is obtained in log-linear plot suggests the following relation between the mean time scale T and m, for modes

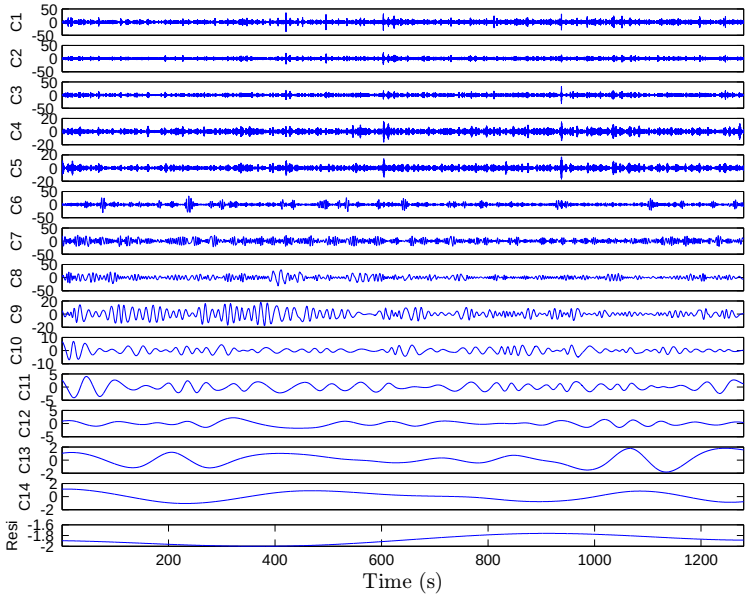

Figure 10.4: IMFs estimated from one 32,000 data points segment of the velocity time series: mode number increasing from top to below. The time scale is increasing with the mode. The residual time series is also plotted.

between 4 and 13

$$T = T_0 e^{\lambda m} \tag{10.3.1}$$

where $T_0 = 0.038$ is a constant and the coefficient $\lambda = 0.667$ is graphically estimated. We remark that $e^{\lambda} = 1.94$ is close to 2, showing that each mode is associated with a time scale almost twice as large as the time scale of the preceding mode; this property corresponds to a dyadic filter bank in the time domain. This property was shown previously using stochastic simulations of Gaussian noise and fractional Gaussian noise (fGn) (Flandrin & Gonçalvès, 2004; Wu & Huang, 2004), and also for fully developed turbulence data (Huang *et al.*, 2008). It is interesting to note here that this is still verified for surf zone turbulence data possessing a strong forcing in the middle of the studied range.

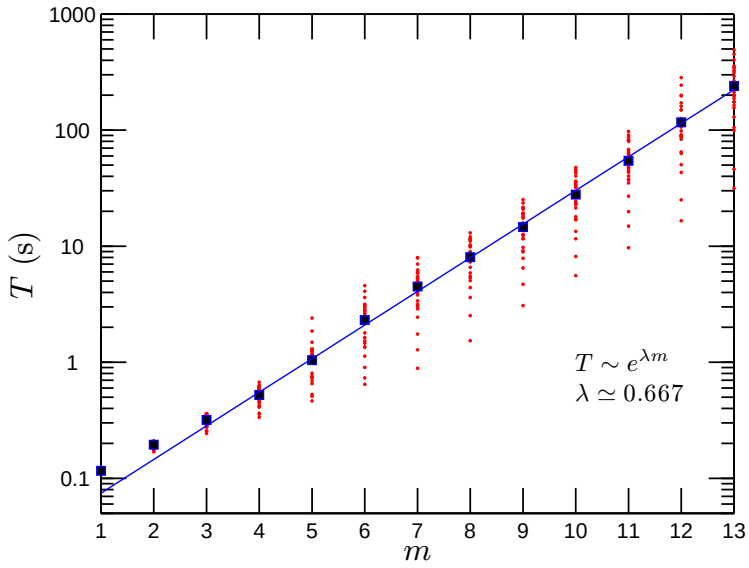

Figure 10.5: Mean time scales associated with each mode. There is an exponential increase for mode numbers between 4 and 13.

HSA Results

Figure 10.6 represents the averaged Fourier power spectrum of the data, superposed with the Hilbert-Huang power spectrum. It is visible that the wind wave breaking scales (between 2 and 16 s) correspond to a strong forcing of the data. This power spectrum is similar to power spectra presented by Trowbridge & Elgar (2001) for surf zone turbulent data recorded in a sandy Atlantic beach near Duck, North Carolina. A $-5/3$ power spectrum can be found for large scales (minutes or larger) and scales smaller than 1 s could also be characterized by such spectrum: the range is too small to be affirmative on this last point. The Hilbert-Huang spectrum which is superposed presents a similar shape, despite its different mathematical definition for the frequency as well as for the spectrum. For the smaller scales, the shape is different, since the Hilbert-Huang power spectrum falls down very quickly.

The EMD and Hilbert spectral analysis methodological frameworks provide a way

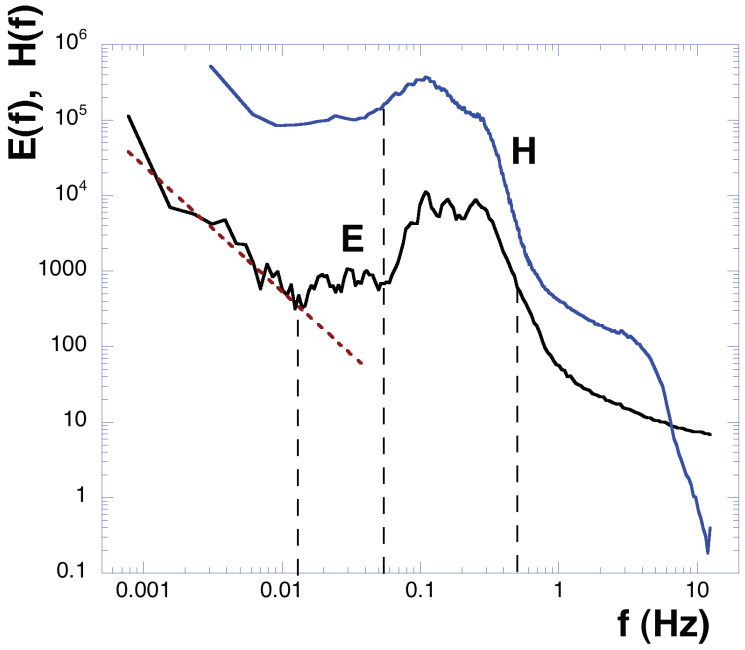

Figure 10.6: Fourier spectrum of the data ($E(f)$), superposed to the Hilbert marginal spectrum ($H(f)$). The latter has been vertically shifted for clarity. A strong wind wave breaking at scales between 2 and 16 s is clearly visible on both power spectra. It is interesting to notice that except for the smaller scales, they have the same shape, despite a different mathematical definition. The dotted straight line has a slope of $-5/3$.

to represent the fluctuations in an amplitude-frequency space: the joint pdf $p(\omega, \mathcal{A})$ is shown in Fig. 10.7. It can be seen graphically that the amplitudes decrease with increasing frequencies. This pdf can be used to estimate many statistical information such as the Hilbert spectrum, and the cumulants as shown below. It can also be used to estimate the skeleton $\mathcal{A}_s(\omega)$ which corresponds to the amplitude for which the conditional pdf $p(\mathcal{A}|\omega)$ is maximum:

$$\mathcal{A}_s(\omega) = \mathcal{A}_0 \,;\, p(\mathcal{A}_0, \omega) = \max_{\mathcal{A}}\{p(\mathcal{A}|\omega)\} \tag{10.3.2}$$

and the skeleton pdf $p_{\max}(\omega) = p(\mathcal{A}_s(\omega), \omega) = \max_{\mathcal{A}}\{p(\mathcal{A}|\omega)\}$, which is shown in

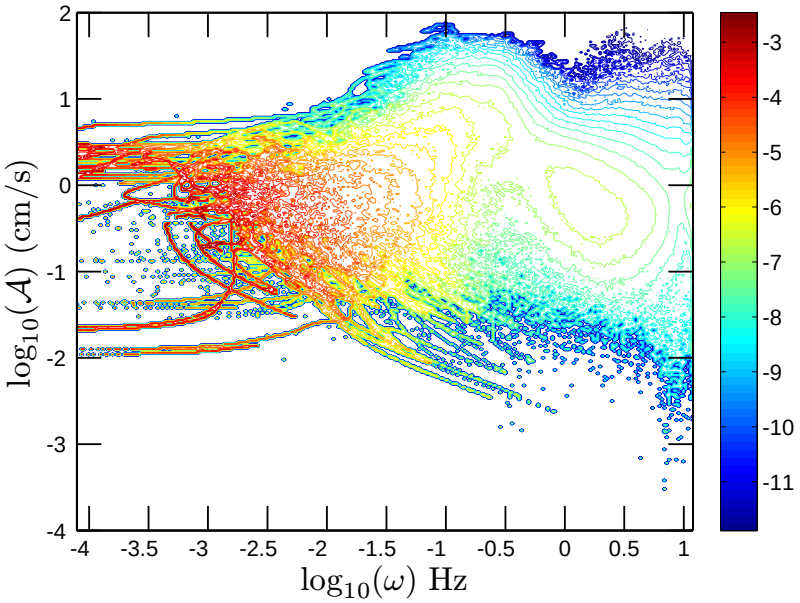

Figure 10.7: Representation of the joint pdf $p(\omega, \mathcal{A})$ (in log scale) of velocity fluctuations in an amplitude-frequency space.

Fig. 10.8. A power law behaviour is found :

$$p_{\max}(\omega) \sim \omega^{-\beta_2} \tag{10.3.3}$$

where $\beta_2 \simeq 1.7$, close to the Kolmogorov value $5/3$. This new result corresponds to an experimental fact that needs further investigation in future studies.

10.4 Non analytic cumulant generating function

We consider here the cumulant analysis applied to the velocity fluctuations, using the EMD and Hilbert spectral analysis described above, and compare this to the same analysis using structure functions.

We first show the estimation of the first cumulant c_1 in Fig. 10.9. In this figure, the first cumulant is estimated as given by Eq. (10.1.4), using on the one hand, the

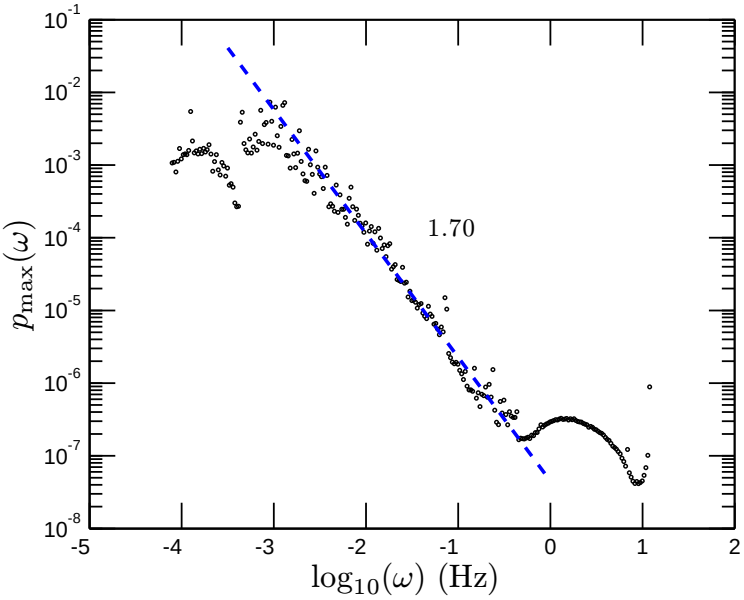

Figure 10.8: The skeleton of the joint pdf $p_{\max}(\omega)$ in log-log plot. A power law behaviour is observed in the inertial subrange with scaling exponent 1.70.

amplitude-frequency pdf for a given value of ω, and taking the time scale $\ell = 1/\omega$ (denoted "HSA" on the figure). On the other hand, it is superposed to the estimate of the first cumulants estimated for all modes separately, as function of scale, through the correspondence given by Fig. 10.5 (denoted "EMD" in the figure). It is also superposed to the first cumulants estimated using the structure function approach, where the scale is the time increment: this value of c_1 has been vertically shifted by 0.6 to be compared to the other curves. Figure 10.9 shows that c_1 increases strongly for energetic scales associated with wave breaking, between 2 and 20 s. It also shows that the EMD-based first cumulant is very close to the Hilbert spectral analysis one (HSA). However the HSA approach is able to provide the first cumulant on a continuous range, since it is based on a frequency estimation, whereas the EMD curve is discrete in scale, being associated with the characteristic scale of each mode.

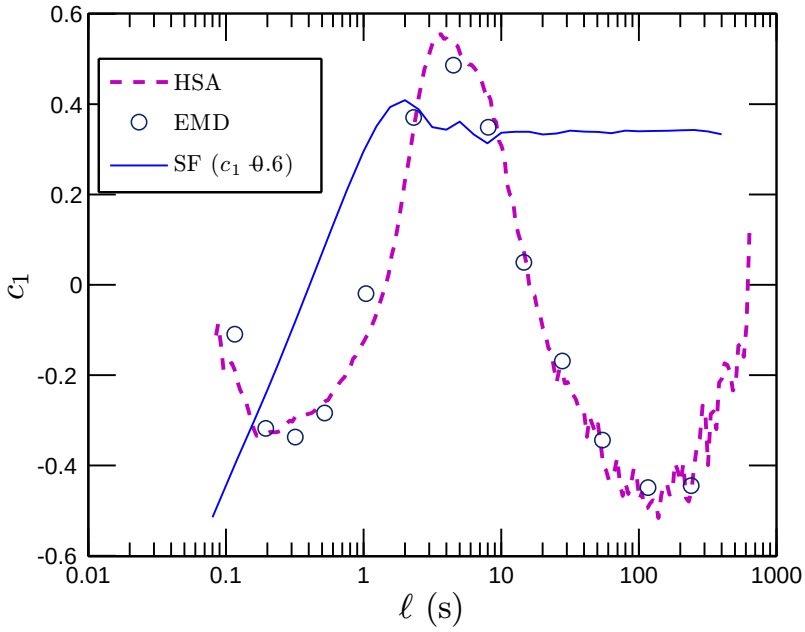

Figure 10.9: Estimation of the first cumulant c_1, using three different methods: (i) estimation in frequency space using the joint amplitude-frequency pdf (dotted line denoted HSA); (ii) estimation using the empirical mode decomposition, done for each mode, where the time scale is estimated using the mode-scale correspondence (open dots, denoted EMD); and (iii) estimation using the structure functions.

We also see from this figure that the first cumulant estimated using the structure function is quite far from the other estimates: the plateau obtained at large scales comes from the fact that the difference $V(t+\ell) - V(t)$ is not removing the forcing when the scale ℓ is larger than the forcing scale. This shows that for such data, the EMD and HSA methods provide a more reliable estimation of the first cumulant.

The functions $\Phi(q)$ are then estimated, for moments from 0 to 8, for scales between 1/25 s to 10 minutes. For comparison purposes, the analysis is done using the HSA approach in Eq. (3.1.3) and using the structure functions. An example is shown in Figures 10a-d, for fluctuations at the scale of 2 s. Figures 10a-b show the analyses using the HSA approach, in lin-lin and log-log plots, and Fig. 10.10 c-d show the same

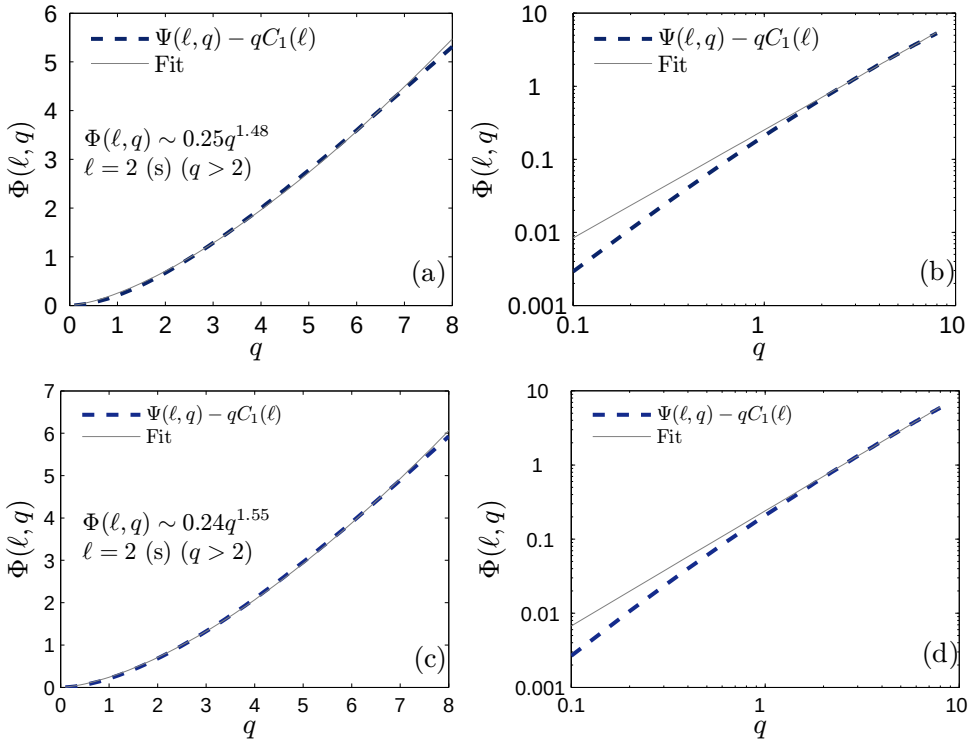

Figure 10.10: $\Phi(q)$ vs. q estimated for q between 0 and 8 for a scale $\ell = 2$ s, chosen here for illustration purpose. Experimental values are given by continuous lines whereas dotted lines correspond to power-law fits. The proportionalities of $\Phi_\ell(q)$ to q^α confirm the nonanalytic framework applied here. (a): lin-lin plot using HSA mehod; (b): log-log plot using HSA method; (c) lin-lin plot using the structure functions; (d) log-log plot using the structure functions.

for the structure functions. Figures 10.10a and 10.10c show convex and increasing functions. The non-analytical behaviour of these curves are emphasized in log-log plots (Fig. 10.10 b and d). The straight lines which are obtained confirm the non-analycity. Using a best fit, the slopes of these straight lines are estimated for all scales, giving directly the exponent α in Eq. (10.1.6). Figure 10.11 shows the values of α estimated for different scales ℓ, for both the HSA and the structure function methods. Except at both ends, the values are relatively independent of scale, and we can estimate a mean value: we find $\alpha = 1.52 \pm 0.07$ for the HSA estimates

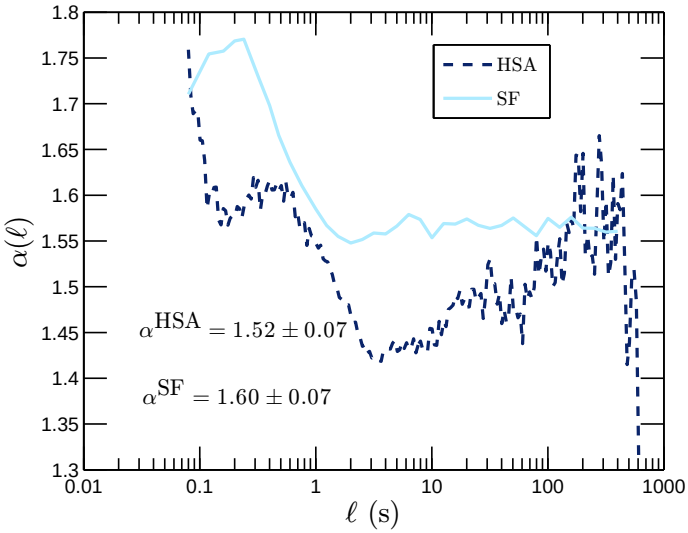

Figure 10.11: Values of α estimated for different scales ℓ: comparison between the HSA and structure functions methods.

and $\alpha = 1.60 \pm 0.07$ for the structure functions estimates, where error bars are coming from different scales. These values are below 2 and approximately compatible between the two methods. Figure 10.12 shows the non-analytical cumulant (it cannot be denoted second cumulant) $c_\alpha(\ell)$ given by Eq. (10.1.5). The curves are different for both methods, but their mean values are close. These results show that the log-normal framework is not adequate, to be replaced by a log-Lévy stochastic modelling. Simulations of such random variables can be performed using available stochastic simulation algorithms (Janicki & Weron, 1994).

10.5 Summary

We have considered here surf zone velocity measurements recorded in the Eastern English Channel using a 25 Hz sampling sonic anemometer. Such data is characterized by the transformation of wave motion into small-scale turbulent motion (Battjes,

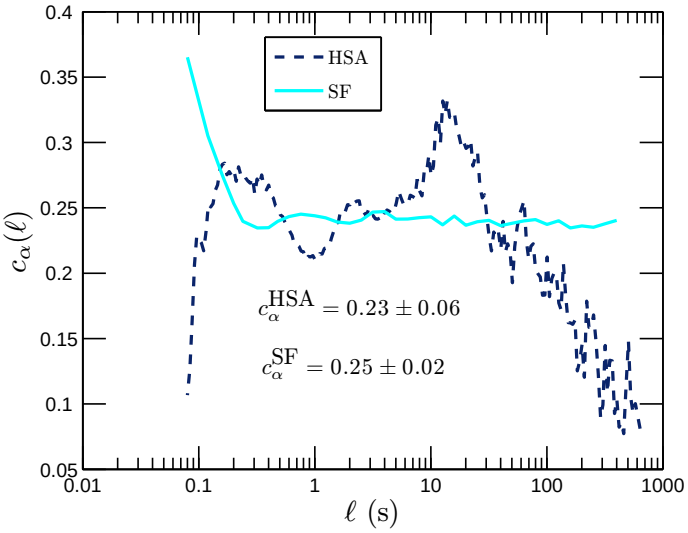

Figure 10.12: Values of $c_\alpha(\ell)$ estimated for different scales ℓ: comparison between the HSA and structure functions methods.

1988). An important issue in this complex framework is to be able to characterize the contribution of each scale to velocity fluctuations, since the modelling of sediment and living organisms transport and suspension is associated with such velocity fluctuations (Cox *et al.*, 1996; Svendsen, 2005; Torres-Freyermuth *et al.*, 2007). We have analysed this series here using the EMD methodology, associated with Hilbert spectral analysis. We have provided the mode versus time scale relationship, showing that for such data base, the dyadic mode decomposition which has been found in Gaussian noise is still valid. We have also provided the Fourier and Hilbert Huang marginal spectrum, showing the high energy associated with wave breaking scales, between 2 and 20 s. In another section, we have analyzed the fluctuations at each scale using cumulants. The cumulants could be estimated on a continuous range of scales using the joint amplitude-frequency pdf of velocity fluctuations that was estimated using the EMD-HSA framework. The non-analytical properties of cumulants was shown for

each scale, for both methods. We showed, using the first cumulant, that the structure function approach saturates at large scales, whereas the HSA based method is more precise in its scale approach; this therefore shows the strength and usefulness of this new EMD-HSA method combined to cumulant analysis. It was shown here to be efficient for surf zone velocity analysis, but could be also applied to other time series.

Let us note that our approach has considered the time series globally, while the depth of the water varied between 1 and 3 meters. It may be that some statistical properties depend on the depth of the water, requesting a more precise analysis, considering separately different sections of the time series. We have checked that this is indeed the case (not shown here), considering the power spectra; however, the shape of the latter did not vary much. We then keep for future studies a more precise analysis of the depth relation, noting here that the results we obtained must be considered as a mean value for different depths between 1 and 3 meters.

We have shown that the log-stable model applies very well, with a characteristic exponent of $\alpha = 1.60 \pm 0.07$ valid for all scales. This property may be used for stochastic simulations. Such modelling in the surf zone may be useful for several applications, such as plankton-turbulence coupling, energetics studies associated with bloom formation, to fertilization processes, or feeding rate of small fishes, or also sediment transport characterization and modelling.

Part IV

Conclusion and Discussion

Discussion and Conclusion

In this chapter, we summarize the main results and conclusions of this thesis. We provide also some comments on these results.

Main Results

The Hilbert-Huang transform is a scale dependent decomposition method with very local ability in both physical and spectral domains. The method, we proposed here, arbitrary order Hilbert spectral analysis, is an extended version of the HHT devoted to take into account intermittency in a scaling framework. It inherits all the advantages and shortcomings of the HHT. The main advantages of the present methodology are the very local abilities both in physical and spectral domains, and the fully adaptiveness. The main drawback is its lack of rigorous mathematical foundation.

Arbitrary Order Hilbert Spectral Analysis

We validated the idea of the arbitrary order Hilbert spectral analysis by using a simulated fractional Brownian motion time series and synthesized multifractal time series. We found that the Hilbert-based approach provides a more precise estimator of the scaling exponents than the classical structure function. We also found a general property of the zeroth order Hilbert marginal spectrum $\mathcal{L}_0(\omega)$, the marginal probability density function (pdf) of the instantaneous frequency ω, with a scaling exponent

$\xi(0) \simeq 1$. This implies that not only the amplitude has a distribution law, but also the scale (instantaneous frequency) itself has a distribution law. However, we still need more theoretical work to fully understand the empirical mode decomposition, the first step of the present methodology, and the arbitrary order Hilbert spectral analysis.

Structure Function and Autocorrelation Function of Velocity Increments

We investigated the structure function and the autocorrelation function of the velocity increments time series $\Delta u_\ell(t)$. Based on statistical stationarity assumption, we proposed an analytical model for them. By a definition of a cumulative function, we found that the structure function is strongly influenced by the large scales. We also shown experimentally that it is also strongly influenced by a single scale (or large scale deterministic forcing). We proved analytically that the autocorrelation function of the velocity increments has its minima value at the separation scale ℓ. A power law relation is also suggested by our analytical model. The power law is then verified by fractional Brownian motion and confirmed by the turbulent database.

Experimental Homogeneous and isotropy Turbulent Database

We applied the empirical mode decomposition and arbitrary order Hilbert spectral analysis to an experimental homogeneous and isotropy turbulent database. We found that the EMD algorithm acts a dyadic filter bank. We observed a scaling trend on the joint pdf of the velocity fluctuations with the scaling exponent quite close to the Kolmogorov value. We recovered the structure function scaling exponent in an amplitude-frequency space for the first time. We then tested the isotropy ratio in Hilbert frame. It is found that the generalized isotropy ratio decreases linearly with

q.

Passive Scalar

We applied the empirical mode decomposition and arbitrary order Hilbert spectral analysis to a passive scalar (temperature). Due to the strong ramp-cliff structures, the classical structure function fails. The Hilbert-based approach provides a scaling exponent $\xi_\Theta(q) - 1$ quite close to the scaling exponent $\zeta(q)$ of the fully developed turbulent velocity field. It indicates that the scalar field may be not so intermittent as what we believed before. However, more passive database should be investigated under the present Hilbert framework to confirm the role of the ramp-cliff structures.

Extended Self-Similarity and Hierarchical Model

We generalized the traditional extended self-similarity into Hilbert frame. In the present framework, according to the Kolmogorov 1962 theory, we have two special case $q = 0$ and $q = 3$, which are not influenced by the intermittent effect. We therefore proposed two ESS formula by plotting the arbitrary order Hilbert spectra $\mathcal{L}_q(\omega)$ against $\mathcal{L}_p(\omega)$, where $p = 0$ or $p = 3$. It is found experimentally that both of them provide the same scaling exponents. We then define a hierarchical spectral function $\mathcal{L}^q(\omega)$ by considering the ratio of two successive arbitrary order Hilbert spectra $\mathcal{L}_p(\omega)$. The scaling exponents $\Pi(q)$ of the hierarchical functions decrease linearly with q.

River Flow Discharge

We applied the Hilbert-based methodology to the daily river flow discharges of the Seine river and Wimereux river. Both rivers are controlled by the marine west coast climate of Northern France. After EMD decomposition, the original time series are

separated into several IMF modes. We observed large correlation among the large scale IMF modes. We found the same evolution trend for the annual cycles and the reconstructed large scale between the Seine river and Wimereux river. We then characterized the small scale intermittent property in the Hilbert frame. Due to the effect of the strong annual cycle, the structure functions fail.

Surf Zone Marine Turbulence

We analyzed a surf zone marine turbulence time series. We characterized the scale invariant properties by considering the nonanalytical cumulant analysis. The log-stable model provides a characteristic exponent of $\alpha = 1.6 \pm 0.07$ for all scales. These results may provide a new approach to separate waves from small scale turbulent motions.

Future studies

The results we shown in this thesis may be useful for modelling, which we do not consider here. However, it should be done in future studies. We list here some topics we may consider in future studies.

1. **Skeleton of the joint pdf $p(\omega, \mathcal{A})$**

   We found experimentally a skeleton of the joint pdf with a scaling behaviour. However, the exactly physical/mathematical meaning of this skeleton is not understood. We need more experimental and theoretical work on this topic to provide more understanding of the scaling property of the skeleton.

2. **Zeroth order Hilbert marginal spectrum $\mathcal{L}_0(\omega)$**

   The corresponding scaling exponent $\xi(0)$ of the zeroth order Hilbert marginal

spectrum is found to be approximately equal to 1. The mathematical meaning of the zeroth order Hilbert marginal spectrum is the marginal pdf of the instantaneous frequency. It seems that it is a general property of the present methodology. It implies that not only the amplitude, but also the scale (instantaneous frequency) has a distribution law. But what is the exactly physical meaning of this $\xi(0) = 1$ scaling exponent?

3. **Kolmogorov 4/5 law**

   The famous Kolmogorov 4/5 law for the third order structure function is an exact statistical solution of the Navier-Stokes equations. Does it hold for the third order Hilbert marginal spectrum? The turbulent database we considered in this thesis has no resolution on Kolmogorov scale. Thus we did not check this topic in this thesis. It should be checked using other databases.

4. **Turbulence modelling**

   We believe that the results presented in this thesis provide useful information for turbulence modelling. We will link our results with turbulence modelling in future studies. We need for this to be able to extend the present 1D to tensorial quantities.

5. **Passive scalar: ramp-cliff structure**

   The ramp-cliff structure is an important signature of passive scalar turbulence. The structure functions, especially for high order moments, are strongly influenced by this large scale structure. Thus, we should check more passive scalar turbulence databases under the present framework in future studies.

Appendix A

List of Publications

Publications before the Ph.D thesis or in other subjects

1. **Y. Huang**, and Z. Lu. Application of Hilbert-Huang Transform in analysis of Duffing equation and wake flow over a cylinder. *Chinese Quarterly of Mechanics*, (in Chinese) 26(2), 2005.

2. **Y. Huang**, Z. Lu, and Y. Liu. Analysis of an atmospheric turbulence data by Hilbert-Huang Transform. *Journal of Hydrodynamics*, (in Chinese) 21(3), 2006.

3. X. Qiu, **Y. Huang**, Z. Lu, and Y. Liu. Application of LIF and PIV in Experimental Measurements of Stratified Turbulence. *Journal of Experiments in Fluid Mechanics*, (in Chinese) 22(2):1-9, 2008.

4. X. Qiu, **Y. Huang**, Z. Lu, Y. Liu. Large eddy simulation of turbulent statistical and transport properties in stably stratified flows. *Applied Mathematics and Mechanics*, 30(2),153-162, 2009.

Publications directly with the Ph.D thesis

1. F.G. Schmitt, **Y. Huang**, Z. Lu, S.B. Zongo, J.C. Molinero, and Y. Liu. Analysis of nonlinear biophysical time series in aquatic environments : scaling properties and empirical mode decomposition. *Nonlinear Dynamics in Geosciences*, edited by A. Tsonis and J. Elsner, pp. 261-290, Springer, 2007.

2. **Y. Huang**, F.G. Schmitt, Z. Lu, and Y. Liu. An amplitude-frequency study of turbulent scaling intermittency using Empirical Mode Decomposition and Hilbert Spectral Analysis. *Europhysics Letters*, 84, 40010, 2008.

3. F.G. Schmitt, **Y. Huang**, Z. Lu, Y. Liu, and Nicolas Fernandez. Analysis of velocity fluctuations and their intermittency properties in the surf zone using empirical mode decomposition. *Journal of Marine System*, 77, 473-481, 2009.

4. **Y. Huang**, F.G. Schmitt, Z. Lu, and Y. Liu. Analysis of daily river flow fluctuations using empirical mode decomposition and arbitrary order Hilbert spectral analysis, *Journal of Hydrology*, 373, 103-111, 2009.

5. **Y. Huang**, F.G. Schmitt, Z. Lu, and Y. Liu. Autocorrelation function of velocity increments in fully developed turbulence, *Europhysics Letters*,86, 40010, 2009.

6. **Y. Huang**, F.G. Schmitt, Z. Lu, and Y. Liu. Analyse de l'invariance d'échelle de séries temporelles par la décomposition modale empirique et l'analyse spectrale de Hilbert . *Traitement du Signal*, (in French) 25, 481-492, 2008.

7. **Y. Huang**, F.G. Schmitt, Z. Lu, and Y. Liu. Arbitrary order Hilbert spectral analysis for time series possessing scaling statistic: definition and validation,

Physical Review E, 2010 (submitted).

8. **Y. Huang**, F.G. Schmitt, Z. Lu, and Y. Liu. Second order structure function in fully developed turbulence, *Physical Review E*, 2010 (submitted).

Bibliography

Abry, P., & Sellan, F. 1996. The Wavelet-Based Synthesis for Fractional Brownian Motion Proposed by F. Sellan and Y. Meyer: Remarks and Fast Implementation. *Appl. Comput. Harmon. Anal.*, **3**(4), 377–383.

Aji, V., & Goldenfeld, N. 2001. Fluctuations in Finite Critical and Turbulent Systems. *Phys. Rev. Lett.*, **86**(6), 1007–1010.

Anselmet, F., Gagne, Y., Hopfinger, E. J., & Antonia, R. A. 1984. High-order velocity structure functions in turbulent shear flows. *J. Fluid Mech.*, **140**, 63–89.

Anselmet, F., Antonia, R. A., & Danaila, L. 2001. Turbulent flows and intermittency in laboratory experiments. *Plan. Space Sci.*, **49**(12), 1177–1191.

Antonia, RA, Hopfinger, EJ, Gagne, Y., & Anselmet, F. 1984. Temperature structure functions in turbulent shear flows. *Phys. Rev. A*, **30**(5), 2704–2707.

Antonia, RA, Ould-Rouis, M., Zhu, Y., & Anselmet, F. 1997. Fourth-order moments of longitudinal-and transverse-velocity structure functions. *Europhys. Lett.*, **37**(2), 85–90.

Arneodo, A., Baudet, C., Belin, F., Benzi, R., Castaing, B., Chabaud, B., Chavarria, R., Ciliberto, S., Camussi, R., & Chilla, F. 1996. Structure functions in turbulence, in various flow configurations, at Reynolds number between 30 and 5000, using extended self-similarity. *Europhys. Lett.*, **34**(6), 411–416.

Bacry, E., Delour, J., & Muzy, JF. 2001. Multifractal random walk. *Phys. Rev. E*, **64**(2).

Balocchi, R., Menicucci, D., Santarcangelo, E., Sebastiani, L., Gemignani, A., Ghelarducci, B., & Varanini, M. 2004. Deriving the respiratory sinus arrhythmia from the heartbeat time series using empirical mode decomposition. *Chaos Soliton Fract.*, **20**(1), 171–177.

Batchelor, GK, & Townsend, AA. 1949. The nature of turbulent motion at large wave-numbers. *Proc. R. Soc. London, Ser. A*, 238–255.

Battjes, J. A. 1988. Surf Zone Dynamics. *Annu. Rev. Fluid Mech.*, **20**(1), 257–291.

Benzi, R., Paladin, G., Vulpiani, A., & Parisi, G. 1984. On the multifractal nature of fully developed turbulence and chaotic systems. *J. Phys. A*, **17**, 3521–3531.

Benzi, R., Ciliberto, S., Baudet, C., Chavarria, G.R., & Tripiccione, R. 1993a. Extended self-similarity in the dissipation range of fully developed turbulence. *Europhys. Lett*, **24**(4), 275–279.

Benzi, R., Ciliberto, S., Tripiccione, R., Baudet, C., Massaioli, F., & Succi, S. 1993b. Extended self-similarity in turbulent flows. *Phys. Rev. E*, **48**(1), 29–32.

Benzi, R., Ciliberto, S., Baudet, C., & Chavarria, GR. 1995. On the scaling of three-dimensional homogeneous and isotropic turbulence. *Physica D*, **80**(4), 385–398.

Benzi, R., Biferale, L., Ciliberto, S., Struglia, MV, & Tripiccione, R. 1996. Generalized scaling in fully developed turbulence. *Physica D*, **96**(1-4), 162–181.

Beran, J. 1994. *Statistics for Long-Memory Processes*. CRC Press.

Biagini, F., Hu, Y., Oksendal, B., & Zhang, T. 2008. *Stochastic calculus for fractional Brownian motion and applications*. Springer Verlag.

Bohr, T., Jensen, MH, Paladin, G., & Vulpiani, A. 1998. Dynamical systems approach to turbulence.

Bolzan, MJA, Rosa, RR, & Sahai, Y. 2009. Multifractal analysis of low-latitude geomagnetic fluctuations. *Ann. Geophys*, **27**, 569–576.

Boratav, O. N. 1997. On recent intermittency models of turbulence. *Phys. Fluids*, **9**, 1206.

Calvet, L., & Fisher, A. 2002. Multifractality in asset returns: theory and evidence. *Rev. Econ. Statist.*, **84**(3), 381–406.

Cassou, C. 2008. Intraseasonal interaction between the Madden–Julian Oscillation and the North Atlantic Oscillation. *Nature*, **455**(7212), 523–527.

Celani, A., Lanotte, A., Mazzino, A., & M., Vergassola. 2000. Universality and Saturation of Intermittency in Passive Scalar Turbulence. *Phys. Rev. Lett.*, **84**, 2385–2388.

Celani, A., Cencini, M., Vergassola, M., Villermaux, E., & Vincenzi, D. 2005. Shear effects on passive scalar spectra. *J. Fluid Mech.*, **523**, 99–108.

Chen, J., Xu, Y. L., & Zhang, R. C. 2004. Modal parameter identification of Tsing Ma suspension bridge under Typhoon Victor: EMD-HT method. *J. Wind Eng. Ind. Aerodyn.*, **92**(10), 805–827.

Chen, S., & Cao, N. 1995. Inertial range scaling in turbulence. *Phys. Rev. E*, **52**(6), 5757–5759.

Chevillard, L., Roux, SG, Lévêque, E., Mordant, N., Pinton, J. F., & Arnéodo, A. 2005. Intermittency of Velocity Time Increments in Turbulence. *Phys. Rev. Lett.*, **95**(6), 64501.

Cohen, L. 1995. *Time-frequency analysis*. Prentice Hall PTR Englewood Cliffs, NJ.

Comte-Bellot, G., & Corrsin, S. 1966. The use of a contraction to improve the isotropy of grid-generated turbulence. *J. Fluid. Mech.*, **25**(04), 657–682.

Comte-Bellot, G., & Corrsin, S. 1971. Simple Eulerian time correlation of full-and narrow-band velocity signals in grid-generated, 'isotropic' turbulence. *J. Fluid. Mech.*, **48**(02), 273–337.

Corrsin, S. 1951. On the spectrum of isotropic temperature fluctuations in an isotropic turbulence. *J. Appl. Phys.*, **22**, 469.

Coughlin, K. T., & Tung, K. K. 2004. 11-Year solar cycle in the stratosphere extracted by the empirical mode decomposition method. *Adv. Space Res.*, **34**(2), 323–329.

Cox, D.T., Kobayashi, N., & Okayasu, A. 1996. Bottom shear stress in the surf zone. *J. Geophys. Res.*, **101**(C6), 14337–14348.

Dahlstedt, K., & Jensen, H.J. 2005. Fluctuation spectrum and size scaling of river flow and level. *Physica A*, **348**, 596–610.

Daubechies, I. 1992. *Ten lectures on wavelets.*

Dauvin, J. C. 2007. Paradox of estuarine quality: Benthic indicators and indices, consensus or debate for the future. *Mar. Pollut. Bull.*, **55**(1-6), 271–281.

De Lima, M., & Grasman, J. 1999. Multifractal analysis of 15-min and daily rainfall from a semi-arid region in Portugal. *J. Hydrol.*, **220**(1-2), 1–11.

Delour, J., Muzy, JF, & Arnéodo, A. 2001. Intermittency of 1D velocity spatial profiles in turbulence: a magnitude cumulant analysis. *Eur. Phys. J. B*, **23**(2), 243–248.

Denny, M. W., & Shibata, M. F. 1989. Consequences of Surf-Zone Turbulence for Settlement and External Fertilization. *Am. Nat.*, **134**(6), 859–889.

Doukhan, P., Taqqu, M.S., & Oppenheim, G. 2003. *Theory and Applications of Long-Range Dependence.* Birkhauser.

Du Preez, H. H., McLachlan, A., Marais, J. F. K., & Cockcroft, A. C. 1990. Bioenergetics of fishes in a high-energy surf-zone. *Mar. Biol.*, **106**(1), 1–12.

Dubrulle, B. 1994. Intermittency in fully developed turbulence: Log-Poisson statistics and generalized scale covariance. *Phys. Rev. Lett.*, **73**(7), 959–962.

Dur, G., Schmitt, F. G., & Souissi, S. 2007. Analysis of high frequency temperature time series in the Seine estuary from the Marel autonomous monitoring buoy. *Hydrobiologia*, **588**, 5968.

Echeverria, J. C., Crowe, J. A., Woolfson, M. S., & Hayes-Gill, B. R. 2001. Application of empirical mode decomposition to heart rate variability analysis. *Med. Biol. Eng. Comput.*, **39**(4), 471–479.

Eggers, H. C., Dziekan, T., & Greiner, M. 2001. Translationally invariant cumulants in energy cascade models of turbulence. *Phys. Lett. A*, **281**, 249–255.

Feller, W. 1971. *An introduction to probalitity theory and its applications.* New York: Wiley.

Feynman, R.P. 1964. *The Feynman lectures on physics.* Vol. 6. by Leighton, R.B. and Sands, M., Addison-Wesley, Redwood City.

Flandrin, P. 1992. Wavelet analysis and synthesis of fractional Brownian motion. *IEEE Trans. Inf. Theory*, **38**(2 Part 2), 910–917.

Flandrin, P. 1998. *Time-frequency/time-scale analysis.* Academic Press.

Flandrin, P., & Gonçalvès, P. 2004. Empirical Mode Decompositions as Data-Driven Wavelet-Like Expansions. *Int. J. Wavelets, Multires. Info. Proc.*, **2**(4), 477–496.

Flandrin, P., Rilling, G., & Gonçalvès, P. 2004. Empirical mode decomposition as a filter bank. *IEEE Sig. Proc. Lett.*, **11**(2), 112–114.

Frisch, U. 1995. *Turbulence: the legacy of AN Kolmogorov*. Cambridge University Press.

Frisch, U., Sulem, P.L., & Nelkin, M. 1978. A simple dynamical model of intermittent fully developed turbulence. *J. Fluid Mech.*, **87**(04), 719–736.

Gardiner, C. W. 2004. *Handbook of Stochastic Methods* . Springer, Berlin, third edition.

Ghashghaie, S., & Dodge, Y. 1996. Turbulent cascades in foreign exchange markets. *Nature*, **381**, 27.

Grant, HL, Stewart, RW, & Moilliet, A. 1962. Turbulence spectra from a tidal channel. *J. Fluid. Mech.*, **12**(02), 241–268.

Grassberger, P. 1986. Estimating the fractal dimensions and entropies of strange attractors. *Chaos*, 291.

Grassberger, P., & Procaccia, I. 1983. Generalized dimensions of strange attractors. *Phy. Rev. Lett.*, **50**(6), 346.

Gurvich, AS, & Zubkovskii, SL. 1963. Experimental estimate of fluctuations in the turbulent energy dissipation. *Izv. Akad. Nauk SSSR, Ser. Geofiz*, **12**, 1856–1858.

Gylfason, A., & Warhaft, Z. 2004. On higher order passive scalar structure functions in grid turbulence. *Phys. Fluids*, **16**, 4012.

Halsey, T.C., Jensen, M.H., Kadanoff, L.P., Procaccia, I., & Shraiman, B.I. 1986. Fractal measures and their singularities: the characterization of strange sets. *Phys. Rev. A*, **33**(2), 1141–1151.

Hentschel, HGE, & Procaccia, I. 1983. The infinite number of generalized dimensions of fractals and strange attractors. *Physica. D*, **8**(3), 435–444.

Hou, T.Y., Wu, X.H., Chen, S., & Zhou, Y. 1998. Effect of finite computational domain on turbulence scaling law in both physical and spectral spaces. *Phys. Rev. E*, **58**(5), 5841–5844.

Huang, N. E. 2005. *Hilbert-Huang Transform and Its Applications*. World Scientific. Chap. 1. Introduction to the Hilbert-Huang transform and its related mathematical problems, pages 1–26.

Huang, N. E., Shen, Z., Long, S. R., Wu, M. C., Shih, H. H., Zheng, Q., Yen, N.C., Tung, C. C., & Liu, H. H. 1998. The empirical mode decomposition and the Hilbert spectrum for nonlinear and non-stationary time series analysis. *Proc. R. Soc. London, Ser. A*, **454**(1971), 903–995.

Huang, N. E., Shen, Z., Long, S. R., *et al.* 1999. A new view of nonlinear water waves: The Hilbert Spectrum . *Annu. Rev. Fluid Mech.*, **31**(1), 417–457.

Huang, N. E., Wu, M. L., Long, S. R., Shen, S. S. P., Qu, W., Gloersen, P., & Fan, K. L/. 2003a. A confidence limit for the empirical mode decomposition and Hilbert spectral analysis. *Proc. R. Soc. London, Ser. A*, **459**(2037), 2317–2345.

Huang, N. E., Wu, M. L., Qu, W., Long, S. R., & Shen, S. S. P. 2003b. Applications of Hilbert-Huang transform to non-stationary financial time series analysis. *Appl. Stoch. Model Bus.*, **19**(3), 245–268.

Huang, Y., Schmitt, F. G., Lu, Z., & Liu, Y. 2009a. Analyse de l'invariance d'échelle de séries temporelles par la décomposition modale empirique et l'analyse spectrale de Hilbert. *Traitement du Signal*, **25**, 481-492.

Huang, Y., Schmitt, F. G., Lu, Z., & Liu, Y. 2009b. Analysis of Daily River Flow Fluctuations Using Empirical Mode Decomposition and Arbitrary Order Hilbert Spectral Analysis. *J. Hydrol.*, **373**, 103-111.

Huang, Y., Schmitt, F. G., Lu, Z., & Liu, Y. 2009c. Autocorrelation function of velocity increments in fully developed turbulence. *Europhys. Lett.* **86**, 40010, 2009.

Huang, Y., Schmitt, F. G., Lu, Z., & Liu, Y. 2010a. Arbitrary order Hilbert spectral analysis for time series possessing scaling statistics: definition and validation. *Phys. Rev. E (submitted).*

Huang, Y., Schmitt, F. G., Lu, Z., & Liu, Y. 2010b. Second order structure function in fully developed turbulence. *Phys. Rev. E (submitted).*

Huang, Y., Schmitt, F. G., Lu, Z., & Liu, Y. 2008. An amplitude-frequency study of turbulent scaling intermittency using Hilbert spectral analysis. *Europhys. Lett.*, **84**, 40010.

Hurst, H. E. 1951. Long-term Storage Capacity of Reservoirs. *Trans. Am. Soc. Civ. Eng.*, **116**, 770–808.

Hurst, H.E., Black, RP, & Simaika, YM. 1965. Long-term storage: an experimental study.

Hwang, P. A., Huang, N. E., & Wang, D. W. 2003. A note on analyzing nonlinear and nonstationary ocean wave data. *Appl. Ocean Res.*, **25**(4), 187–193.

Ivanov, P.C., Bunde, A., Amaral, LAN, Havlin, S., Fritsch-Yelle, J., Baevsky, RM, Stanley, HE, & Goldberger, AL. 1999. Sleep-wake differences in scaling behavior of the human heartbeat: Analysis of terrestrial and long-term space flight data. *Europhys. Lett.*, **48**(5), 594–600.

Jaffe, B.E., & Rubin, D.M. 1996. Using nonlinear forecasting to learn the magnitude and phasing of time-varying sediment suspension in the surf zone. *J. Geophys. Res.*, **101**(C6), 14283–14296.

Janicki, A., & Weron, A. 1994. *Simulation and chaotic behavior of alpha-stable stochastic processes*. New York: Marcel Dekker.

Jánosi, I.M., & Gallas, J.A.C. 1999. Growth of companies and waterlevel fluctuations of the river Danube. *Physica A*, **271**(3), 448–457.

Jánosi, I.M., & Müller, R. 2005. Empirical mode decomposition and correlation properties of long daily ozone records. *Phys. Rev. E*, **71**(5), 56126.

Jayesh, C.T., & Warhaft, Z. 1994. On temperature spectra in grid turbulence. *Phys. Fluids*, **6**, 306.

Kahalerras, H., Malécot, Y., Gagne, Y., & Castaing, B. 1998. Intermittency and Reynolds number. *Phys. Fluids*, **10**, 910.

Kang, H., & Meneveau, C. 2001. Passive scalar anisotropy in a heated turbulent wake: new observations and implications for large-eddy simulations. *J. Fluid Mech.*, **442**, 161–170.

Kang, H., Chester, S., & Meneveau, C. 2003. Decaying turbulence in an active-grid-generated flow and comparisons with large-eddy simulation. *J. Fluid Mech.*, **480**, 129–160.

Kantelhardt, J.W., Rybski, D., Zschiegner, S.A., Braun, P., Koscielny-Bunde, E., Livina, V., Havlin, S., & Bunde, A. 2003. Multifractality of river runoff and precipitation: comparison of fluctuation analysis and wavelet methods. *Physica A*, **330**(1-2), 240–245.

Kantelhardt, J.W., Koscielny-Bunde, E., Rybski, D., Braun, P., Bunde, A., & Havlin, S. 2006. Long-term persistence and multifractality of precipitation and river runoff records. *J. Geophys. Res.*, **111**.

Kida, S. 1991. Log-stable distribution and intermittency of turbulence. *J. Phys. Soc. Japan*, **60**(5).

Kolmogorov, A. N. 1941a. Local structure of turbulence in an incompressible fluid at very high Reynolds numbers. *Dokl. Akad. Nauk SSSR*, **30**, 299–303.

Kolmogorov, A. N. 1941b. On decay of isotropic turbulence in an incompressible viscous fluid. *Dokl. Akad. Nauk SSSR*, **31**, 538–540.

Kolmogorov, A. N. 1941c. Energy dissipation in locally isotropic turbulence. *Dokl. Akad. Nauk SSSR*, **32**(1), 19–21.

Kolmogorov, A. N. 1962. A refinement of previous hypotheses concerning the local structure of turbulence in a viscous incompressible fluid at high Reynolds number. *J. Fluid Mech.*, **13**, 82–85.

Kolmogorov, AN. 1940. The Wiener spiral and some other interesting curves in Hilbert space. *Dokl. Akad. Nauk SSSR*, **26**(2), 115–118.

Koscielny-Bunde, E., Kantelhardt, J.W., Braun, P., Bunde, A., & Havlin, S. 2006. Long-term persistence and multifractality of river runoff records: Detrended fluctuation studies. *J. Hydrol.*, **322**(1-4), 120–137.

Kraichnan, R. H. 1991. Turbulent cascade and intermittency growth. *Proc. R. Soc. London, Ser. A*, **434**(1890), 65–78.

Landau, L.D., & Lifshitz, E.M. 1987. Fluid Mechanics. *New York*.

Livina, V., Ashkenazy, Y., Kizner, Z., Strygin, V., Bunde, A., & Havlin, S. 2003a. A stochastic model of river discharge fluctuations. *Physica A*, **330**(1-2), 283–290.

Livina, V., Kizner, Z., Braun, P., Molnar, T., Bunde, A., & Havlin, S. 2007. Temporal scaling comparison of real hydrological data and model runoff records. *J. Hydrol.*, **336**(1-2), 186–198.

Livina, V.N., Ashkenazy, Y., Braun, P., Monetti, R., Bunde, A., & Havlin, S. 2003b. Nonlinear volatility of river flux fluctuations. *Phys. Rev. E*, **67**(4), 42101.

Loh, C. H., Wu, T. C., & Huang, N. E. 2001. Application of the Empirical Mode Decomposition-Hilbert Spectrum Method to Identify Near-Fault Ground-Motion Characteristics and Structural Responses. *BSSA*, **91**(5), 1339–1357.

Long, S. R., Huang, N. E., Tung, C. C., Wu, M. L., Lin, R. Q., Mollo-Christensen, E., & Yuan, Y. 1995. The Hilbert techniques: an alternate approach for non-steady time series analysis. *IEEE Geoscience and Remote Sensing Soc. Lett.*, **3**, 6–11.

Loutridis, S. J. 2005. Resonance identification in loudspeaker driver units: A comparison of techniques. *Appl. Acoust.*, **66**(12), 1399–1426.

Lumley, J. L. 1992. Some comments on turbulence. *Phys. Fluids*, **4**(2), 203–211.

Lumley, J. L., & Yaglom, A. M. 2001. A Century of Turbulence. *Flow Turbul. Combust.*, **66**(3), 241–286.

Lux, T. 2001. Power laws and long memory. *Quant. Finance*, **1**(6), 560–562.

L'vov, Victor, & Procaccia, Itamar. 1997. Hydrodynamic Turbulence: a 19th Century Problem with a challenge for the 21st Century. *Turbulence Modeling and Vortex Dynamics, Lecture Notes in Physics.*

Makita, H. 1991. Realization of a large-scale turbulence field in a small wind tunnel. *Fluid Dynamics Research*, **8**, 53–64.

Malik, SC, & Arora, S. 1992. *Mathematical Analysis.* John Wiley & Sons Inc.

Mandelbrot, B.B. 1974. Intermittent turbulence in self-similar cascades: divergence of high moments and dimension of the carrier. *J. Fluid Mech.*, **62**(02), 331–358.

Mandelbrot, B.B., & Van Ness, J.W. 1968. Fractional Brownian Motions, Fractional Noises and Applications. *SIAM Review*, **10**, 422.

Marple Jr, L. 1999. Computing the discrete-time analytic signal via FFT. *IEEE T. Signal. Proces.*, **47**(9), 2600–2603.

Masselink, Gerhard, & Russell, Paul. 2006. Flow velocities, sediment transport and morphological change in the swash zone of two contrasting beaches. *Mar. Geol.*, **227**(3-4), 227–240.

Mauas, Pablo J. D., Flamenco, Eduardo, & Buccino, Andrea P. 2008. solar forcing of the stream flow of a continental scale south american river. *Phys. Rev. Lett.*, **101**, 168501.

Mead, K. S., & Denny, M. W. 1995. The effects of hydrodynamic shear stress on fertilization and early development of the purple sea urchin *Strongylocentrotus purpuratus*. *Biol. Bull*, **188**(1), 46–56.

Meyer, Y. Lecture notes for the Montréal splines and wavelets coneference. *Université de Montréal, Canada, Mars 1996, unpublished*.

Moisy, F., Willaime, H., Andersen, JS, & Tabeling, P. 2001. Passive Scalar Intermittency in Low Temperature Helium Flows. *Phys. Rev. Lett.*, **86**(21), 4827–4830.

Molla, Md. Khademul Islam, Rahman, M. Sayedur, Sumi, Akimasa, & Banik, Pabitra. 2006. Empirical mode decomposition analysis of climate changes with special reference to rainfall data. *Discrete Dyn. Nat. Soc.*, **2006**, Article ID 45348, 17 pages. doi:10.1155/DDNS/2006/45348.

Monin, A. S., & Yaglom, A. M. 1971. *Statistical fluid mechanics vd II.* MIT Press Cambridge, Mass.

Muzy, J.F., & Bacry, E. 2002. Multifractal stationary random measures and multifractal random walks with log infinitely divisible scaling laws. *Phys. Rev. E*, **66**(5), 056121.

Mydlarski, L., & Warhaft, Z. 1996. On the onset of high-Reynolds-number grid-generated wind tunnel turbulence. *J. Fluid. Mech.*, **320**, 331–368.

Mydlarski, L., & Warhaft, Z. 1998. Passive scalar statistics in high-Péclet-number grid turbulence. *J. Fluid Mech.*, **358**, 135–175.

Nelkin, M. 1994. Universality and scaling in fully developed turbulence. *Adv. Phys.*, **43**(2), 143–181.

Nichols Pagel, G.A., Percival, D.B., Reinhall, P.G., & Riley, J.J. 2008. Should structure functions be used to estimate power laws in turbulence? A comparative study. *Physica D*, **237**(5), 665–677.

Novikov, EA. 1969. Scale similarity for random fields. **14**, 104–107.

Obukhov, AM. 1941. Spectral energy distribution in a turbulent flow. *Dokl. Akad. Nauk SSSR*, **32**(1), 22–24.

Obukhov, AM. 1949. Structure of the temperature field in a turbulent flow. *Izv. Acad. Nauk SSSR Ser. Geog. Geofiz*, **13**, 58–69.

Obukhov, AM. 1962. Some Specific Features of Atmospheric Turbulence. *J. Geophys. Res.*, **67**, 3011–3014.

Pandey, G., Lovejoy, S., & Schertzer, D. 1998. Multifractal analysis of daily river flows including extremes for basins of five to two million square kilometres, one day to 75 years. *J. Hydrol.*, **208**(1-2), 62–81.

Parisi, G., & Frisch, U. 1985. On the singularity spectrum of fully developed turbulence. *Turbulence and predictability in geophysical fluid dynamics, North Holland, Proceedings of the International Summer School in Physics Enrico Fermi*, 84–87.

Percival, D.B., & Walden, A.T. 1993. *Spectral Analysis for Physical Applications: Multitaper and Conventional Univariate Techniques.* Cambridge University Press.

Peters, O., Hertlein, C., & Christensen, K. 2002. A complexity view of rainfall. *Phys. Rev. Lett.*, **88**(1), 018701.

Podesta, J. J., Forman, M. A, Smith, C W, Elton, D C, Malecot, Y., & Gagne, Y. 2009. Accurate estimation of third-order moments from turbulence measurements. *Nonlin. Processes Geophys.*, **16**, 99–110.

Pond, S., & Stewart, RW. 1965. Measurements of the statistical characteristics of small-scale turbulent motions. *Izv. Atmos. Oceanic Phys*, **1**, 914–919.

Ponomarenko, V. I., Prokhorov, M. D., Bespyatov, A. B., Bodrov, M. B., & Gridnev, V. I. 2005. Deriving main rhythms of the human cardiovascular system from the heartbeat time series and detecting their synchronization. *Chaos Soliton Fract.*, **23**, 1429–1438.

Pope, S. B. 2000. *Turbulent Flows.* Cambridge University Press.

Reynolds, O. 1883. An experimental investigation of the circumstances which determine whether the motion of water shall be direct or sinuous, and the law of resistance in parallel channels. *Proc. R. Soc. London, Ser. A*, **174.**, 935–982.

Reynolds, O. 1894. On the dynamical theory of turbulent incompressible viscous fluids and the determination of the criterion. *Proc. R. Soc. London, Ser. A*, **186**, 123–161.

Richardson, L.F. 1922. *Weather prediction by numerical process.* Cambridge University Press, Cambridge, England,.

Rilling, G., & Flandrin, P. 2006. on the Influence of Sampling on the Empirical Mode Decomposition. *IEEE International Conference on Acoustics, Speech and Signal Processing, 2006. ICASSP 2006 Proceedings. 2006*, **3**, 444.

Rilling, G., & Flandrin, P. 2008. One or two frequencies? The empirical mode decomposition answers. *IEEE Trans. Signal Process.*

Rilling, G., & Flandrin, P. 2009. Sampling effects on the empirical mode decomposition. *Adv. Adapt. Data Anal.*, **1**, 43–59.

Rilling, G., Flandrin, P., & Gonçalvès, P. 2003. On empirical mode decomposition and its algorithms. *IEEE-EURASIP Workshop on Nonlinear Signal and Image Processing.*

Rilling, G., Flandrin, P., & Gonçalvès, P. 2005. Empirical Mode Decomposition, fractional Gaussian noise and Hurst exponent estimation. *Acoustics, Speech, and Signal Processing, 2005. Proceedings.(ICASSP'05). IEEE International Conference on*, **4**.

Rogers, L. 1997. Arbitrage with Fractional Brownian Motion. *Math. Finance*, **7**(1), 95–105.

Ruiz-Chavarria, G., Baudet, C., & Ciliberto, S. 1996. Scaling laws and dissipation scale of a passive scalar in fully developed turbulence. *Physica D*, **99**(2-3), 369–380.

Samorodnitsky, G., & Taqqu, M.S. 1994. *Stable Non-Gaussian Random Processes: stochastic models with infinite variance.* Chapman & Hall.

Schertzer, D., & Lovejoy, S. 1987. Physical modeling and analysis of rain and clouds by anisotropic scaling multiplicative processes. *J. Geophys. Res*, **92**(D8), 9693–9714.

Schertzer, D., Lovejoy, S., Schmitt, F. G., Chigirinskaya, Y., & Marsan, D. 1997. Multifractal cascade dynamics and turbulent intermittency. *Fractals*, **5**(3), 427–471.

Schmitt, F. G. 2003. A causal multifractal stochastic equation and its statistical properties. *Eur. Phys. J. B*, **34**(1), 85–98.

Schmitt, F. G. 2005. Relating Lagrangian passive scalar scaling exponents to Eulerian scaling exponents in turbulence. *Eur. Phys. J. B*, **48**(1), 129–137.

Schmitt, F. G. 2006. Linking Eulerian and Lagrangian structure functions? scaling exponents in turbulence. *Physica A*, **368**(2), 377–386.

Schmitt, F. G., Lavallee, D., Schertzer, D., & Lovejoy, S. 1992. Empirical determination of universal multifractal exponents in turbulent velocity fields. *Phys. Rev. Lett.*, **68**(3), 305–308.

Schmitt, F. G., Vannitsem, S., & Barbosa, A. 1998. Modeling of rainfall time series using two-state renewal processes and multifractals. *J. Geophys. Res.*, **103**(D18), 23181–23193.

Schmitt, F. G., Schertzer, D., & Lovejoy, S. 1999. Multifractal analysis of foreign exchange data. *Appl. Stoch. Models and Data Anal.*, **15**(1), 29–53.

Schmitt, F. G., Huang, Y., Lu, Z., Zongo, S. B., Molinero, J. C., & Liu, Y. 2007. Analysis of nonliner biophysical time series in aquatic environments: scaling properties and empirical mode decomposition. *Pages 261–280 of: Nonlinear Dynamics in Geosciences. edited by A. Tsonis and J. Elsner.* Springer.

Schmitt, F. G., Dur, G., Souissi, S., & Brizard Zongo, S. 2008. Statistical properties of turbidity, oxygen and pH fluctuations in the Seine river estuary (France). *Physica A*, **387**(26), 6613–6623.

Schmitt, F. G., Huang, Y., Lu, Z., Y., Liu, & Fernandez, N. 2009. Analysis of velocity fluctuations and their intermittency properties in the surf zone using empirical mode decomposition. *J. Mar. Sys.*, 77, 473-481, doi:10.1016/j.jmarsys.2008.11.012.

Schumm, S.A. 2005. *River Variability and Complexity.* Cambridge University Press.

Sellan, F. 1995. Synthèse de mouvements browniens fractionnaires à l' aide de la transformation par ondelettes. *C. R. Acad. Sci. Paris Sé r. I Math*, **321**, 351358.

She, Z. S., & Lévêque, E. 1994. Universal scaling laws in fully developed turbulence. *Phys. Rev. Lett.*, **72**(3), 336–339.

She, Z.S., & Waymire, E.C. 1995. Quantized Energy Cascade and Log-Poisson Statistics in Fully Developed Turbulence. *Phys. Rev. Lett.*, **74**(2), 262–265.

Shraiman, B.I., & Siggia, E.D. 2000. Scalar turbulence. *Nature*, **405**(6787), 639–646.

Siefert, M., Peinke, J., & Friedrich, R. 2005. A Simple Relation Between Longitudinal and Transverse Increments. *Progress in Turbulence*, **101**, 63–66.

Solé, J., Turiel, A., & Llebot, JE. 2007. Using empirical mode decomposition to correlate paleoclimatic time-series. *Nat. Hazard Earth Sys. Sci.*, **7**, 299–307.

Sreenivasan, KR. 1991. On Local Isotropy of Passive Scalars in Turbulent Shear Flows. *Proc. R. Soc. Lond. A*, **434**(1890), 165–182.

Sreenivasan, K.R. 1996. The passive scalar spectrum and the Obukhov–Corrsin constant. *Phys. Fluids*, **8**, 189.

Sreenivasan, K.R., & Antonia, RA. 1997. The phenomenology of small-scale turbulence. *Annu. Rev. Fluid Mech.*, **29**, 435–472.

Staicu, A., & van de Water, W. 2003. Small Scale Velocity Jumps in Shear Turbulence. *Phys. Rev. Lett.*, **90**(9), 94501.

Stolovitzky, G., & Sreenivasan, K. R. 1994. Kolmogorov's refined similarity hypotheses for turbulence and general stochastic processes. *Rev. Mod. Phys.*, **66**(1), 229–240.

Svendsen, I. A. 1987. Analysis of surf zone turbulence. *J. Geophys. Res.*, **92**(C5), 5115–5124.

Svendsen, I.A. 2005. Introduction to Nearshore Hydrodynamics. *Adv. Series on Ocean Eng.*, **24**.

Taqqu, M. S., & Samorodnisky, G. 1994. *Stable Non-Gaussian Random Processes.* Chapman & Hall, New York.

Taylor, G. I. 1935. Statistical Theory of Turbulence. *Proc. R. Soc. London, Ser. A*, **151**(873), 421–444.

Taylor, G. I. 1938. The Spectrum of Turbulence. *Proc. R. Soc. London, Ser. A*, **164**(919), 476–490.

Telesca, L., & Macchiato, M. 2004. Time-scaling properties of the Umbria-Marche 1997–1998 seismic crisis, investigated by the detrended fluctuation analysis of interevent time series. *Chaos Soliton Fract.*, **19**(2), 377–385.

Tessier, Y., Lovejoy, S., Hubert, P., Schertzer, D., & Pecknold, S. 1996. Multifractal analysis and modeling of rainfall and river flows and scaling, causal transfer functions. *J. Geophys. Res.*, **101**, 26427–26440.

Torres-Freyermuth, A., Losada, I. J., & Lara, J. L. 2007. Modeling of surf zone processes on a natural beach using Reynolds-Averaged Navier-Stokes equations. *J. Geophys. Res.*, **112**, C09014.

Trowbridge, J., & Elgar, S. 2001. Turbulence Measurements in the Surf Zone. *J. Phys. Oceanogr.*, **31**(8), 2403–2417.

Tsinober, A. 2001. *An Informal Introduction to Turbulence*. Kluwer Academic Publishers, Amsterdam.

Tsuji, Y. 2004. Intermittency effect on energy spectrum in high-Reynolds number turbulence. *Phys. Fluids*, **16**, L43–L46.

Vainshtein, SI. 2003. Most singular vortex structures in fully developed turbulence. *Arxiv preprint physics/0310008*.

van de Water, W., & Herwijer, J. A. 1999. High-order structure functions of turbulence. *J. Fluid Mech.*, **387**, 3–37.

Veltcheva, A. D., & Soares, C. G. 2004. Identification of the components of wave spectra by the Hilbert Huang transform method. *Appl. Ocean Res.*, **26**(1-2), 1–12.

Venugopal, V., Roux, S. G., Foufoula-Georgiou, E., & Arnéodo, A. 2006. Scaling behavior of high resolution temporal rainfall: New insights from a wavelet-based cumulant analysis. *Phys. Lett. A*, **348**(3-6), 335–345.

Warhaft, Z. 2000. Passive scalars in turbulent flows. *Annu. Rev. Fluid Mech.*, **32**(1), 203–240.

Wood, A.T.A., & Chan, G. 1994. Simulation of stationary Gaussian processes in [0, 1] d. *J Comput. Graph. Stat.*, **3**(4), 409–432.

Wu, Z., & Huang, N. E. 2004. A study of the characteristics of white noise using the empirical mode decomposition method. *Proc. R. Soc. London, Ser. A*, **460**, 1597–1611.

Wu, Z., Huang, N.E., Long, S.R., & Peng, C.K. 2007. On the trend, detrending, and variability of nonlinear and nonstationary time series. *PNAS*, **104**(38), 14889.

Xia, H., Punzmann, H., Falkovich, G., & Shats, MG. 2008. Turbulence-condensate interaction in two dimensions. *Phys. Rev. Lett.*, **101**(19), 194504.

Yaglom, A. M. 1957. Some classes of random fields in n-dimensional space, related to stationary random processes. *Theor. Probab. App+*, **2**, 273.

Yaglom, A. M. 1966. The influence on the fluctuation in energy dissipation on the shape of turbulent characteristics in the inertial interval. *Sov. Phys. Dokl*, **2**, 26–30.

Yaglom, A. M. 2001. The century of turbulence theory: The main achievements and unsolved problems. *New Trends in Turbulence, Springer-Verlag, Berlin, Heidelberg, New York*, 1–52.

Zhang, C. 2005. Madden-Julian Oscillation. *Rev. Geophys.*, **43**, 36.

Zhang, Q., Xu, C., Chen, Y.D., & Yu, Z. 2008. Multifractal detrended fluctuation analysis of streamflow series of the Yangtze River basin, China. *Hydrol. Process.*, **22**, 4997–5003.

Zhang, Q., Xu, C., Liu, C., & D., Chen Y. 2009. Multifractal analysis of streamflow records of the East River basin (Pearl River), China. *Physica A*, **388 (6)**, 927–934.